Modélisation bidimensionnelle de la décharge plasma dans un propulseur de Hall

Vivien Croes

NNT : 2017SACLX060

Thèse de doctorat de l'Université Paris-Saclay préparée à l'École Polytechnique

École doctorale n°572
École Doctorale Onde et Matière
Spécialité de doctorat : Physique des Plasmas

par

M. Vivien CROES

Modélisation de la décharge plasma d'un propulseur à effet Hall.

Soutenance faite à Palaiseau, le 24 octobre 2017.

Composition du Jury :

Prof.	Marc Massot	Professeur École Polytechnique	(Président)
Prof.	Miles Turner	Professeur NCPST / DCU	(Rapporteur)
Dr.	Francesco Taccogna	Chercheur IMIP / CNR	(Rapporteur)
Dr.	Jean-Marc Charbonnier	Dir. R&T CNES	(Examinateur)
Dr.	Jean-Claude Adam	Dir. de recherche émérite CPhT / CNRS	(Examinateur)
Dr.	Stephan Zurbach	Ing. expert senior Safran Aircraft Engines	(Référent)
Dr.	Pascal Chabert	Dir. de recherche LPP / CNRS	(Dir. de thèse)
Dr.	Anne Bourdon	Dir. de recherche LPP / CNRS	(Co-dir. de thèse)

II

“Ne pas s'imaginer que le monde tourne vers nous un visage lisible que nous n'aurions plus qu'à déchiffrer ; il n'est pas complice de notre connaissance ; il n'y a pas de providence prédiscursive qui le dispose en notre faveur.”
L'ordre du discours (1970), Michel Foucault

“Voyez-vous, Robineau, dans la vie il n’y a pas de solutions. Il y a des forces en marche : il faut les créer et les solutions suivent.”
Vol de nuit (1931), Antoine de Saint-Exupéry

Résumé

Les applications découlant de technologies spatiales sont de plus en plus présentes et essentielles dans nos vies de tous les jours. Alors que les coûts de lancement de satellites sont actuellement en chute libre grâce au développement de lanceurs ré-utilisables *low-cost*, et que de nouvelles applications sorties de l'élan *new space* émergent, les coûts d'utilisation et d'opération des satellites doivent être drastiquement diminués. Cet objectif peut être atteint, entre autres, grâce à l'utilisation de systèmes de propulsion électriques, plus efficaces que leurs équivalents chimiques traditionnels. En effet, grâce à une plus importante vitesse d'expulsion des gaz, ces propulseurs offrent une bien meilleure efficacité.

Bien que de nombreux systèmes de propulsion spatiale électrique existent, le présent travail se concentre sur un type de propulseur : le propulseur à effet Hall, aussi appelé propulseur à courant de Hall ou propulseur à plasma stationnaire. Ce type de propulseur est l'un des plus utilisés et des plus performants aujourd'hui. Toutefois, ces systèmes propulsifs restent complexes et relativement peu compris. En effet, certaines questions clefs restent ouvertes, que ce soit au sujet du transport anormal des électrons ou des intéractions plasma/paroi.

Les réponses à ces deux questions sont basées sur des mécanismes cinétiques, et donc ne peuvent être étudiées au travers de codes de simulation fluides. De plus les échelles caractéristiques de temps et d'espace de ces mécanismes les rendent difficiles à étudier expérimentallement de manière exhaustive. Ainsi, afin de répondre à ces questions et compléter les travaux expérimentaux menés jusqu'ici, un code de simulation cinétique bi-dimensionel a été développé *ex nihilo*.

Le développement de ce code de simulation a été caractérisé par une attention toute particulière aportée à la fiabilité des résultats grâce à l'utilisation de cas-tests bien documentés. De plus, cet outil de simulation a été conçu afin d'utiliser efficacement les puissances de calcul aujourd'hui disponibles. Cet effort a mené à une architecture massivement parallélisée de l'outil informatique, permettant ainsi de nombreuses études paramétriques.

Grâce à l'utilisation d'un modèle simplifié de propulseur à effet Hall, il nous a été possible d'étudier les différents phénomènes physiques ayant lieu dans la décharge plasma d'un propulseur. S'appuyant sur les récents résultats d'une théorie cinétique développée spécifiquement pour décrire la décharge plasmas des propulseurs à effet Hall et le transport anormal des électrons, il a été possible de mettre en valeur l'importance de l'instabilité de dérive électronique concernant le transport anormal des électrons dans le canal de décharge.

Ensuite, en raffinant le modèle utilié afin de simuler de façon plus réaliste la décharge plasma, il a été possible de quantifier l'apport des parois au transport anormal des électrons. L'effet des parois sur la décharge et son comportement a pu être confirmé et son intrication avec l'instabilité de dérive électronique a été mise en valeur. Grâce à une étude paramétrique exhaustive, l'impact de l'émissivité des parois sur la décharge plasma a pu être quantifié, permettant l'identification de trois régimes de décharge distincts.

Enfin de nombreuses études paramétriques ont pu être faites autour de l'impact des parois diélectriques, des modèles d'émission secondaire, et des ergols alternatifs. Ces études paramétriques ont été rendues possibles par la flexibilité et la performance de l'outil de simulation développé au cours de ce travail. Grâce à des modèles réalistes (diélectriques modélisés de façon autonome et cohérente, processus collisionnels tirés de mesures expérimentales), ces études ont confirmé les résultats antérieurs.

De plus, les différentes études paramétriques conduites ont permis de développer un modèle global permettant de mieux comprendre le fonctionnement de la décharge plasma dans un propulseur à effet Hall. Grâce à ce modèle global, il nous a été permis de plus précisément quantifier les effets de l'émissivité des parois, ainsi que de la masse de l'ergol utilisé, sur la décharge et la performance du propulseur.

Toutefois, des limitations sont présentes dans les simulations conduites au cours de ce travail. Si ces limitations ne permettent pas de modéliser réellement un propulseur à effet Hall, cet outil n'étant pas utilisé comme aide au design des propulseurs, elles n'empêchent pas l'étude des mécanismes physiques à l'oeuvre. Elles ouvrent au contraire un nouveau champ de possibles pour de futures études et simulations.

Abstract

Space technology applications are increasingly present and essential in our everyday lives. While satellite launch costs are currently falling sharply thanks to the development of low-cost reusable launchers, and new applications are emerging from the new space elan, the costs of using and operating satellites must be drastically reduced. This can be achieved, among other things, by using electric propulsion systems that are more efficient than their traditional chemical equivalents. Indeed, thanks to a higher gas exhaust speed, these thrusters offer a much better efficiency.

Although many electric space propulsion systems exist, the present work concentrates on one type of thruster: the Hall effect thruster, also known as Hall current thruster or stationary plasma thruster. This type of thruster is one of the most popular and successful thrusters available today. However, these propulsion systems remain complex and relatively little understood. Indeed, some key questions remain open, whether about anomalous electron transport or plasma-wall interactions.

The answers to these two questions are based on kinetic mechanisms, and therefore cannot be studied through fluid simulation codes. Moreover, the characteristic time and space scales of these mechanisms make them difficult to experimentally and exhaustively study. Thus, in order to answer these questions and complete the experimental work carried out so far, a two-dimensional kinetic simulation code has been developed from scratch.

The development of this simulation code has been characterized by a particular attention given to the reliability of the results thanks to the use of well documented test cases. In addition, this simulation tool has been designed to make efficient use of the computational powers available today. This effort has led to a massively parallelized architecture of the IT tool, allowing numerous parametric studies.

Thanks to the use of a simplified Hall effect thruster model, we were able to study the different physical phenomena taking place in the plasma discharge of a thruster. Based on the recent results of a kinetic theory developed specifically to describe the plasma discharge of Hall effect thrusters and

the abnormal transport of electrons, it has been possible to highlight the importance of the electron drift instability concerning the abnormal transport of electrons in the discharge channel.

Then, by refining the model used to simulate plasma discharge in a more realistic way, it was possible to quantify the contribution of the walls to the anomalous transport of electrons. The effect of the walls on the plasma discharge and its behavior could be confirmed, and its intrication with the electron drift instability was highlighted. Thanks to an exhaustive parametric study, the impact of the emissivity from the walls on the plasma discharge has been quantified, allowing the identification of three distinct discharge regimes.

Finally, numerous parametric studies have been carried out on the impact of dielectric walls, secondary emission models, and alternative propellants. These parametric studies were made possible by the flexibility and performance of the simulation tool developed during this work. Thanks to realistic models (autonomously and coherently modeled electrical models, collision processes derived from experimental measurements), these studies confirmed the previous results.

In addition, the various parametric studies conducted have led to the development of a global model allowing for a better understanding of the operation of plasma discharge in a Hall effect thruster. Thanks to this global model, we have been able to quantify more precisely the effects of the emissivity of the walls, as well as the mass of the propellant used, on the discharge and the performance of the thruster.

However, limitations are present in the simulations conducted during this work. While these limitations do not allow for the actual modeling of a Hall effect thruster, since this tool is not used as an aid to the design of thrusters, they do not prevent the study of physical mechanisms at work. On the contrary, they open up a new field of possibilities for future studies and simulations.

Acknowledgements

I would first like to thank my advisors, Anne Bourdon and Pascal Chabert, for having guided and supported my work. They made these three years of research the most fruitful experience. Next, I would like to thank Trevor Lafleur, whose mentoring and contributions to this work are invaluable. Not having the possibility to ask him questions will be one of the most difficult aspects of the years to come. Finally, I would like to acknowledge Stephan Zurbach for his support and trust. The freedom he granted me with was the strongest sign of trust.

I also want to acknowledge all those involved in the present work. Zdeněk Bonaventura for his help and friendship in the darkest moments of the informatics development. Abdoul Wahid Mainassara for his commitment in developing this code with me. I am sure his future projects will be characterized by quality and efficiency, and I can only wish him properly commented and indented codes. Antoine Tavant and Romain Lucken for their help and motivation during the last year of my Ph.D. I wish them bug-free developments, successful publications, and thrilling LPPintes. François Péchereau for all his experience and his kind help. Benjamin Khiar and Loic Nicolas for their friendly and helpful discussions all along the development of LPPic2D.

I would like to thank all the members of the jury, and in particular the two chairmen: Francesco Taccogna and Miles Turner, for their numerous advices. It is an honor as well as a pleasure to present my work to them.

On a more personal note, I would like to acknowledge my family: my sister, Cassandre-Gabrielle Dupuis, and my parents Dominique Bouffange, Jean-François Dupuis, and Éric Croes. Without their unfailing longterm support and trust, none of this would have been possible. I would like to thank as well my grand-mother Irène Dupuis, for having followed me along the years. Finally, I would like to thank my partner in crime and life, Marie Mouries, for having supported me through all the highs and lows that I went through. This has not been the easiest nor the most restful experience. But I know her support will never weaken towards our future adventures.

X

Contents

List of Figures

List of Tables

List of Code samples

List of Acronyms

Ar	= argon
Al_2O_3	= alumina
BN	= boron nitride
BN-SiO_3	= borosil
CCP	= capacitively coupled plasma
CFL	= *Courant-Friedrichs-Lewy* condition (Equation 2.2)
CIC	= cloud-in-cell
CPU	= computational power unit
EP	= electric propulsion
GAFA	= *Google, Amazon, Facebook, Apple*
HET	= Hall effect thruster
HPC	= high performance computing
I_2	= iodine
Isp	= specific impulse (Equation 1.3)
Kr	= krypton
LEO	= low Earth orbit
MCC	= Monte Carlo collisions
MPI	= message passing interface
PIC	= particle-in-cell
PPT	= pulsed plasma thruster
PPU	= power processing unit
RO	= relaxation oscillations
RSO	= relaxation sheath oscillations
SCL	= space charge limited
SCS	= space charge saturated
SEE	= secondary electron emission
Xe	= xenon

Chapter 1

Introduction

Contents

1.1 Electric propulsion and the "New Space" peril

Space exploration has held an important place in literature and art. What was a dream for authors like *Cyrano de Bergerac*, *Jules Vernes*, or *Hergé* only became reality decades, or even centuries, after their utopian works. However, the first technological step of space conquest took place in the terrible

context of the Second World War. The *V2* missile, built by concentration camp prisoners of Peenemünde and Dora, demonstrated the military potential of suborbital flight, paving the way to modern rockets.

The technological heir of the *V2*, *Sputnik 1* from the USSR, launched on 4 October 1957 by a *R-7 Semyorka*, proved the feasibility of orbital flight. In the context of the Space Race, the USA launched their first satellite, *Explorer 1*, on 1 February 1958.

Finally the *Apollo* missions in the 70's, and later the multiple space stations (*Skylab*, *Mir*,...) illustrated the possibilities offered by human space flight.

Thus the space sector, and *a fortiori* the satellite sector, has been built in a context of state-driven research, development, and management. Every state eager to develop its space power has funded a space agency in order to trigger the necessary impetus to the development of space activities on its soil: *NASA* in the USA (1958), *Roscosmos* in Russia (1992), *CNES* in France (1961)...

However, the satellite sector has been early on a target for private funding and companies. After July 1962, when the American satellite *Telstar* demonstrated the possibility of direct transatlantic video transmission through space, the telecommunication capacities of satellites ignited private appetites. Hence in the Spring of 1965, the first privately owned telecommunication satellite, *Intelsat 1*, was launched. This success will be the cornerstone on which has been funded the private satellite operator *Intelsat ltd*, opening the way for further private satellite operators, and to the modern satellite value chain.

Since Sputnik and its famous "beep" in 1957, more than 7000 satellites have been launched [1], exploring and developing new applications. From Earth observation to localisation services, including telecommunications (TV, radio, Internet), military applications, space exploration, or human flight, satellites are more and more essential to our every-day lives. Our increased dependency on space systems is reflected in the good health of the satellite sector which is considered to meet a solid 12 %/year growth rate since 2010, representing an economic annual activity between $230bn and $314bn [2, 3].

Following the increase in bandwidth requirements, the satellite industry has been focused on the development of always larger satellite platforms. Launched by always more powerful rockets, like *Ariane 5* which is able to launch up to 21t in low Earth orbit (LEO), these heavy satellites (3t to 6t in "all-electric" propulsion configuration) represent 80 % of the market [2].

Nevertheless new entrants like the companies *Alphabet*, *Planet* or *SpaceX* are attempting to develop new applications, standards, and usages. Betting

Figure 1.1 – The Peenemünde test facility and factory for *V2* missiles. 250km North from Berlin. In the background: a *V2* missile. (Source: *Dominique Bouffange*, August 2016)

Figure 1.2 – Real size *Dove* satellite from *Planet*. A super-constellation of little less than a hundred of these satellites is capable of imaging the entire Earth every day. Coupled to machine learning algorithms and Big Data methods, this could lead to the development of new applications: Fire detection in remote places, automatic mapping, real-time monitoring of vulnerable places... Evolving on LEOs only for a short lifetime (couple of years), these satellites are opening, since 2010, the way to "agile aerospace" methods. (Source: *Planet Labs*, June 2016)

on very low cost ($<$ 500 k\$/unit), light ($<$ 500 kg), and easily replaceable satellites, as well as on the sharp decrease of launch prices, these companies try to set-up super-constellations of hundreds, if not thousands, of satellites in LEO. An example of one of those satellites is highlighted by Figure 1.2 with one of the *Dove* satellites used by *Planet* to picture the Earth.

Complimented by the latest numerical data processing methods (Big Data, Machine Learning), these projects are the first step in the satellite sector of processes inherited from the GAFA (*Google*, *Amazon*, *Facebook*, and *Apple*) and the digital industry.

Finally the new Mars Space Race, even though not as intense as the Moon Space Race from the 70's, led by state-owned agencies as well as private companies (*SpaceX, Blue Origins*), requires the development of highly efficient

high-thrust propulsion systems.

With an expected lifetime exceeding 10 years, the propulsion system propellant required when using chemical thrusters can be a major part of the satellite total mass (up to 50 % for heavy satellites requiring numerous maneuvers) [4]. Thus, these three main trends in the satellite sector are challenges addressed to the electric propulsion (EP) sector, since EP technologies are a way to drastically lower the needed propellant mass.

Hence the need for highly reliable, highly efficient, and adaptable electric propulsion systems has become particularly important since the 2010's. Coupled with the drastic decrease of development time in the space sector, due to the introduction of new methods from the digital industry, the EP sector is now facing an acceleration in both the development needs and the production capabilities.

Consequently, the EP manufacturers need to better understand the systems they are developing. The era of decades long development cycles is now over, and manufacturers need to be able to develop new models using shorter try/error cycles.

While heavier telecommunication satellites as well as space exploration spacecraft require the development of high thrust and very reliable thrusters, microsatellite constellations are in need of an adaptable, low thrust, fully integrated, and low cost propulsion system. To match both of those objectives, development needs to be shortened and made more reliable by being able to validate upstream key technological choices. This can be obtained by developing reliable, fast, and adaptative simulation tools.

EP technologies mostly rely on plasma discharges in order to ionize the propellant, and thus generate thrust. Consequently these simulation tools need to properly model the wide range of mechanisms and kinetic effects governing the plasma discharge behavior, which is at the root of thruster performance.

1.2 What are Hall effect thrusters (HETs)?

Electric propulsion (EP) consists of methods and systems designed to thrust a satellite in space using electric or magnetic fields as the main accelerator for the propellant. The thrust is most commonly obtained through the acceleration of a previously ionized gas. Numerous devices exist with different ways of ionizing the propellant, and sustaining the plasma discharge, but the present work will concentrate on Hall effect thrusters (HETs).

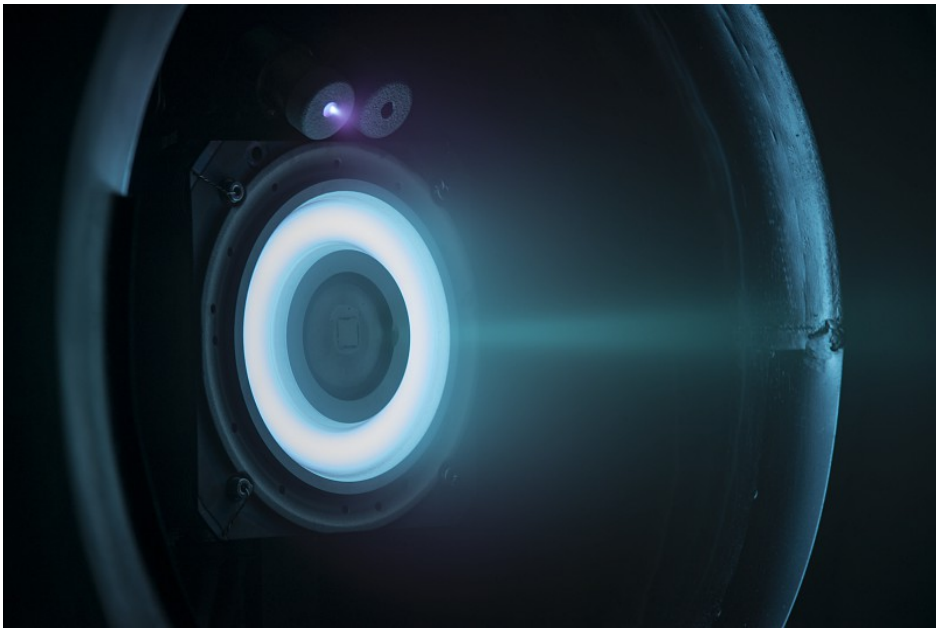

Figure 1.3 – Example of EP: HET built by *Safran Aircraft Engines*, the *PPS-1350G* is being tested in a vacuum chamber. (Source: *CNES*, February 2015)

1.2.1 A short history of electric propulsion (EP)

Hall effect thrusters (HETs) are one of the most successful technologies used to electrically generate thrust for satellites. The first in-space demonstration of EP was made by a concurrent technology, an ion engine, in 1964 aboard the *SERT-1* spacecraft [5]. It was followed by the first HET in 1974 aboard the USSR *Meteor* satellite [6]. Since then, numerous satellites have been successfully operated using HETs as primary or secondary propulsion systems, for commercial, military, or exploration purposes [7]. For instance, from 2003 to 2006, *SMART-1*, a satellite propelled by a solar-powered HET built by *Safran Aircraft Engines* reached the Moon orbit, demonstrating the feasibility of so-called "all-electric" satellites [4], using EP technologies as the only propulsion systems.

However the full potential of EP, and in particular HETs, has only started to be realized in the last few years with the appearance of all-electric heavy telecommunication satellites, and small-satellite super-constellation projects as discussed in Section 1.1.

HETs are also known as stationary plasma thrusters or Hall current thrusters. All these names designate the same propulsive systems. For the sake of clarity, these systems will only be referred to as Hall effect thrusters (HETs) in the following work.

1.2.2 Comparison of EP technologies

Since HETs are in competition with other systems (electric or chemical) to thrust satellites, it is important to rapidly sum up the pros and cons of those systems.

Nonetheless we firstly need to rapidly define the concepts used to characterize and compare thruster performances. Without burdening the present work with unnecessary equations, it appears useful to follow [7], and clearly define some of the most useful concepts. Thus the thrust, T, produced by a given propulsion system, can be defined from Newton's second law [8], as given in Equation 1.1.

$$T = M\frac{dv}{dt} \tag{1.1}$$

With M the spacecraft mass, and v its velocity. Yet the thrust on the spacecraft can be as well expressed as the opposite of the time rate of change of the momentum of the propellant, as given by Equation 1.2 [7].

$$T = -v_{ex}\frac{dm_p}{dt} \tag{1.2}$$

Where m_p is the propellant mass stored in the spacecraft, and v_{ex} its exhaust velocity as seen from the spacecraft reference frame.

Furthermore another key concept is the specific impulse (Isp). The value of the Isp is a measure of the thruster performance, and is defined as given in Equation 1.3, in the simplified case where all the propellant is ionized and there is no beam divergence.

$$\mathrm{Isp} = \frac{v_{\mathrm{ex}}}{g} \tag{1.3}$$

Where g is the acceleration by gravity, with $g = 9.807\,\mathrm{m}\cdot\mathrm{s}^{-2}$. Equation 1.3 leads to the unusual unit of seconds to quantify Isp.

Nevertheless this specific impulse, as defined by Equation 1.3, makes sense when defining the change in velocity of the spacecraft needed for the mission, Δv. Indeed, the Tsiolkovsky's "rocket equation" or "ideal rocket equation" [9] shows us that Δv can be expressed as:

$$\Delta v = (\mathrm{Isp}\cdot g) ln\left(\frac{m_d + m_p}{m_d}\right) \tag{1.4}$$

Where m_d is the delivered mass, thus $m_d + m_p = M$ corresponds to the total mass of the spacecraft at the start of the mission. By rewriting Equation 1.4 in order to obtain the required propellant mass for a given Δv, as done in Equation 1.5, we observe that a thruster providing a large Isp compared to the mission Δv will require only a small amount of propellant in comparison to the spacecraft total mass $M = m_d + m_p$.

$$m_p = m_d\left(e^{\Delta v/\mathrm{Isp}\cdot g} - 1\right) \tag{1.5}$$

Finally following [7], the efficiency, η, of an EP thruster is given by Equation 1.6.

$$\eta = \frac{\mathrm{T}_{\mathrm{final}}^2}{2\dot{m}_{\mathrm{p}}\mathrm{P}_{\mathrm{in}}} \tag{1.6}$$

Where $\mathrm{T}_{\mathrm{final}}$ is the effective thrust, $\dot{m}_{\mathrm{p}}$ the mass flow rate of propellant, and P_{in} the total electrical power into the thruster.

While chemical thrusters can be a major part of a satellite mass (up to 50 % for heavy satellites), they can deliver thrusts of up to 500N. In comparison, electrical thrusters, for 2kW of power available on the satellite, can only deliver 100mN. But the propellant mass consumed for the same total impulse is divided by a factor of 5 since its Isp is much higher [4, 7].

Consequently, due to a lower thrust, the use of EP leads to longer thrust runs requiring different and longer transfer orbits. However the significantly

Table 1.1 – Typical operating parameters for thrusters with flight heritage [7, 10] (PPT stands for "pulsed plasma thruster").

Thruster	Specific impulse [s] (Equation 1.3)	Input power [kW]	Efficiency range [%] (Equation 1.6)	Propellant
Cold gas	$50 - 75$	-	-	Various
Chemical (monoprop.)	$150 - 225$	-	-	N_2H_4 H_2O_2
Chemical (biprop.)	$300 - 450$	-	-	Various
Resistojet	300	$0.5 - 1$	$65 - 90$	N_2H_4
Arcjet	$500 - 600$	$0.9 - 2.2$	$25 - 45$	N_2H_4
Ion thruster	$2500 - 3600$	$0.4 - 4.3$	$40 - 80$	Xe
HET	$1500 - 2000$	$1.5 - 4.5$	$35 - 60$	Xe
PPT	$850 - 1200$	< 0.2	$7 - 13$	Teflon

higher Isp allows EP technologies to drastically reduce the propellant mass needed to obtain a given Δv. Thus, the optimal implementation of an EP system on a satellite should allow the saving of a lot of payload, but without leading to an excessive penalty in maneuver duration.

Furthermore, multiple EP technologies have been developed in the past decades. Those technologies have reached very different maturation levels. Summed up in Table 1.1 are the operating parameters for thrusters with flight heritage [7, 10].

1.2.3 HETs description

To ionize the propellant and sustain the plasma discharge, an intake of energy is needed. In the HETs this intake of energy is obtained through a cross field discharge: an electric field is established perpendicular to an applied magnetic field, this electro-statically accelerates ions to high exhaust velocities, while an imposed transverse magnetic field inhibits electron motion that would tend to short out the electric field. This so-called $\mathbf{E}_0 \times \mathbf{B}_0$ discharge is the fundamental principle on which HETs are based.

Typical HETs consist of three main parts detailed in Figure 1.4 [7, 12]:

1. An annular ceramic channel where the propellant gas is injected (through

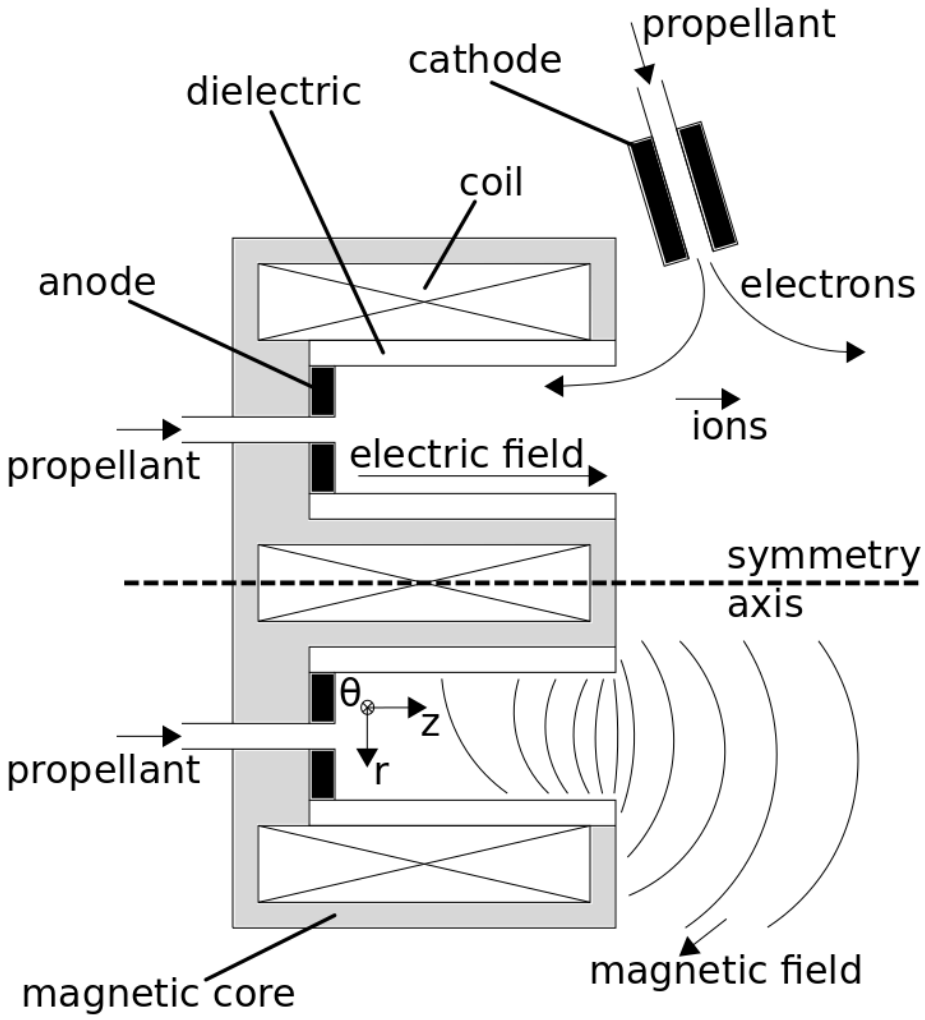

Figure 1.4 – Schematic cut of a Hall thruster showing the radial magnetic field imposed by the coils. The accelerating electric field is imposed through the porous anode and the hollow cathode. Propellant is injected through the porous anode to be ionized and accelerated, and through the hollow cathode to generate electrons [11].

a porous anode), ionized, accelerated, and ejected through one end. This channel usually has a length of the order of centimeters [4]. In addition, densities in the channel are typically in the range between 10^{17} to $10^{18}\,\mathrm{m}^{-3}$ for the plasma, and 10^{18} to $10^{20}\,\mathrm{m}^{-3}$ for the neutral gas [13].

2. An external hollow cathode (asymmetrically located near one side of the channel, or along its central axis), providing electrons to sustain the plasma discharge inside the channel, as well as neutralizing the exiting ion beam. A large potential difference (100's of Volts) is applied between the anode and cathode, which accelerates the ions to high velocities to generate thrust. This potential difference also causes some electrons from the cathode to travel upstream inside the channel towards the anode. The physics governing the hollow cathode is a subject of interest to better understand the HET operation, however it will not be treated in this work.
3. A specially designed magnetic circuit, used to impose a predominantly radial magnetic field (10's of mT) in the channel region. This magnetic field acts to impede electrons and increases their residence time in the channel so as to allow a higher probability of ionization, and thus ensure maximal use of the injected propellant gas [7]. HETs are electrostatic devices since the external magnetic field imposed by the coils is much more important than the magnetic field produced by any fluctuations generated by electrons and ions motion.

These three main components are fixed through a metallic structure allowing electrostatic as well as thermal control of the system. Once fixed on the spacecraft (most often through an extensible sliding arm system), it is connected to a power processing unit (PPU) in order to provide power, and a propellant tank. Despite their importance in the operation of the thruster, both of these systems are not studied in this work.

1.2.4 Basic concepts

After this brief description of the HET components and a first glimpse of their general functioning, we now discuss and detail some key characteristics of the plasma discharge in a HET, defining some key concepts used in this work.

Larmor radii

The Larmor radius, r_g, is the gyration length of electrons (or ions) around the magnetic field. An illustration of the gyration trajectory is shown in

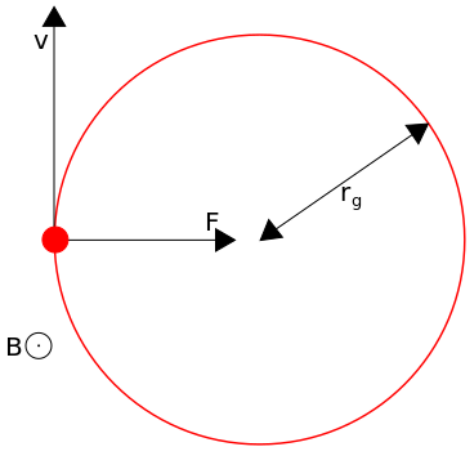

Figure 1.5 – Example of a positively charged (ion) particle trajectory (red) in an uniform vertical magnetic field. Here v is the particle velocity perpendicular to the magnetic field, which is noted B, and F the force induced by the magnetic field. The Larmor radius, r_g, is the the radius of the movement projected on a plane orthogonal to the magnetic field.

Figure 1.5, while the Larmor radius of an electron is given in Equation 1.7.

$$r_{\mathrm{g}}^{\mathrm{electron}} = \frac{m_e\, v_\perp}{eB} \tag{1.7}$$

Where $v_\perp$ is the electron's velocity component perpendicular to the magnetic field, m_e the electron mass, e the elementary charge, and B the magnetic field norm. Consequently the heavier the particle, the larger the Larmor radius. This property will be used in the following to trap specifically electrons, while ions can exit the system.

Electrons not neutralizing the plume have to be kept inside the channel in order to sustain the plasma discharge. This is only possible if the electronic Larmor radius, r_g^{electron}, is much less than the characteristic scale length of the discharge channel, L_{system}.

$$r_g^{\mathrm{electron}} = \frac{m_e v_\perp}{eB} << L_{\mathrm{system}} \tag{1.8}$$

In a similar manner the ions have to be accelerated out of the channel to obtain thrust. This is achieved if the ionic Larmor radius, r_g^{ion}, is much greater than the characteristic channel length, L_{system}.

$$r_g^{\mathrm{ion}} = \frac{m_i v_\perp}{eB} >> L_{\mathrm{system}} \tag{1.9}$$

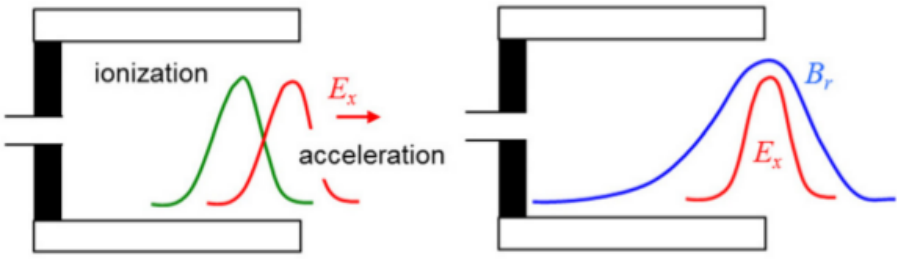

Figure 1.6 – Schematic representation of the acceleration and ionization regions in a cut of a HET: (red) the axial electric field, noted E_x, (green) the ionization rate, and (blue) the radial magnetic field, B_r [14].

With m_i the ion mass.

In a typical HET, L_{system} is of the order of some centimeters, while r_g^{electron} is of the order of a μm [4]. On the other hand with xenon as propellant, r_g^{ion} is of the order of the meter, satisfying the requirements defined above.

The magnetic field is imposed radially so that electrons are trapped on magnetic field lines going from one wall to another. Furthermore the magnetic field intensity is at its highest value in the exhaust region, and in the range of $15 - 20$mT for a typical HET like the SPT100 [14]. This intensity value decreases until a near zero value outside of the thruster and at the anode, as it shown in Figure 1.6.

Electron drift

Charged particles are rotating around magnetic field lines as illustrated by Figure 1.5. Thus a frequency, ω_c, describing the individual ion or electron movement around the magnetic field is defined. This cyclotron frequency is described for an electron in Equation 1.10:

$$\omega_{c,e} = \frac{eB}{m_e} \tag{1.10}$$

Since the applied discharge voltage gives an axial electric field, and the applied magnetic field is predominantly in the radial direction, this causes an $\mathbf{E} \times \mathbf{B}$ drift of electrons in the azimuthal direction. For typical electric and magnetic field values, such as those to be used in the subsequent simulations, the electron drift velocity can reach values as high as $10^6\,\text{ms}^{-1}$. Fluid description of these instabilities will be discussed in Section 1.4.2.

Moreover, for every collision of an electron with a heavier particle, a drift of the electron toward the anode occurs. This means the electron gets closer

and closer to the anode, where it will finally be absorbed. Thus, in order to have a sufficiently high residence time of electrons in the channel, the magnetized electrons have to realize many orbits around a field line before colliding with a neutral or an ion. This can be stated by saying that the square of the electron Hall parameter, Ω_e^2, must be large compared to unity. This is expressed in the following Equation 1.11:

$$\Omega_e^2 = \left(\frac{\omega_{c,e}}{\nu}\right)^2 >> 1 \tag{1.11}$$

Where ν is the total collision frequency of electrons.

Fluid theory about the electron mobility and drift in HETs is briefly detailed in Section 1.4.2, and in the sections following this.

Beam neutralization

Electrons produced by the hollow cathode are partly trapped inside the channel discharge. Indeed some fraction of the electrons emitted from the hollow cathode also leaves the thruster with the ion beam to neutralize the exiting charge. This is illustrated on Figure 1.7 and happens in order to respect the quasi-neutrality condition defined in Section 1.4.1 below.

The plasma physics in the plume is a key topic concerning HET performance, however it will not be treated in this thesis.

Ionization rates

Since ions are the ones producing the thrust, the ionization rate of the neutrals going through the discharge channel has to be significant. In practice it is around 95 % of the neutrals injected in the channel that are ionized after the exit plane [16]. Given that the electron density is the highest upstream of the exit plane, this region is characterized by a double role: firstly the ionization of neutrals, and secondly the acceleration of the produced ions due to the electric field from the applied discharge voltage.

This double role of the exhaust region is illustrated in Figure 1.6, where we can observe schematically the respective intensities of the magnetic field and the ionization rate. Yet we can more precisely detail the key physical values in the exhaust region. This is illustrated in Figure 1.8, where we can observe that the exhaust region's double role of propellant ionization and acceleration is directly observed in the charged particles' densities. Indeed, the axial distribution of the ionization source term and the potential highlights the overlapping of the ionization and acceleration regions. Moreover this double role is observed in the charged particles' densities, where the

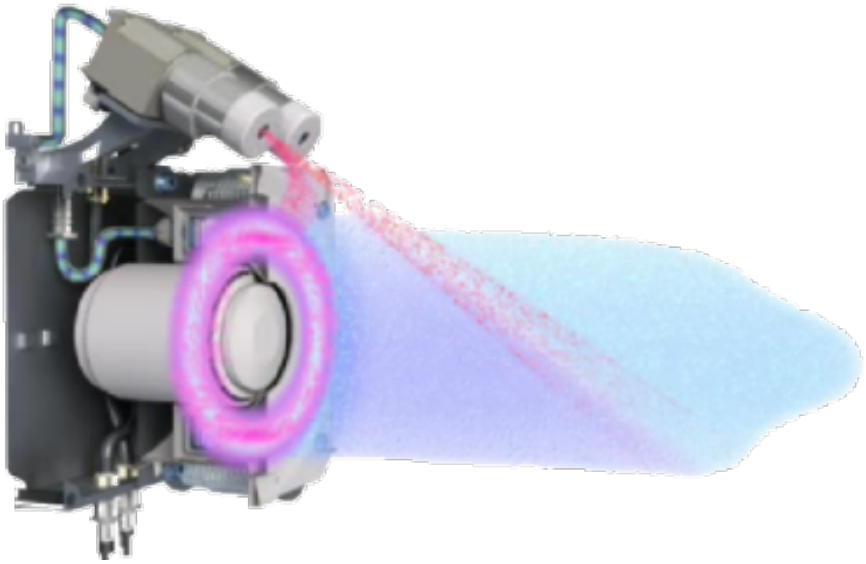

Figure 1.7 – Artist view of a standard HET operation with a side hollow cathode [15]: (dark blue) the xenon ions, (light blue) the neutral xenon, and (pink) the electrons, which are either trapped by the magnetic field inside the channel or neutralizing the expelled xenon ions.

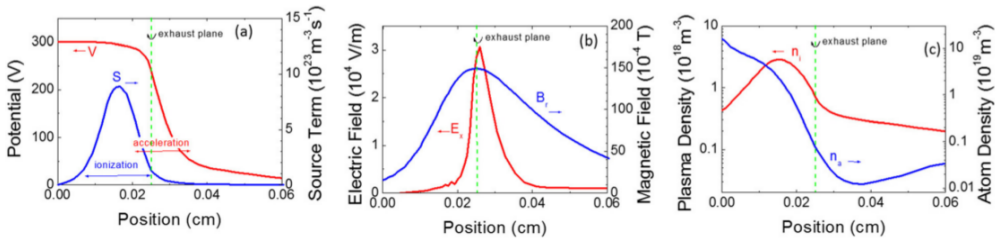

Figure 1.8 – Axial distributions of time averaged (a) plasma potential and ionization rate, (b) external radial magnetic field and axial electric field, (c) plasma density and xenon atom density, from a 2D hybrid model of a Hall thruster (SPT100 type, xenon mass flow rate 5 mg/s, applied voltage 300 V) [14, 13].

trapped electrons are at a maximum density in the ionization region, while the neutral gas density reaches a minimum right after the exhaust region, where they have been accelerated.

In HETs operating at high power levels, which means high mass flow rate and high discharge voltage (typically > 300V), a significant number of multiply charged ions can be generated. Creation of a significant amount of multiply charged ions can lead to a noticeable effect on the thruster performance [7]. Furthermore the recombination rate measured shows low levels. This is as expected in order to maximize the thruster efficiency.

In order to physically separate the propellant ionization and the acceleration of the produced ions, double stage HETs have been proposed. However they have not been observed to outperform classical HETs [17, 18, 19], and will not be investigated further in this work.

Channel walls and propellants

The channel walls are typically manufactured from dielectric materials such as boron nitride (BN), or borosil (BN-SiO_3) for flight models, alumina (Al_2O_3) in some laboratory models [7]. These dielectric materials have a low sputtering yield and relatively low secondary electron emission coefficients. They have good thermal and mechanical properties as well. The shape and material of the discharge region channel, and the details of the magnetic field configuration determine the performance, efficiency, and life of the thruster [7].

The propellant usually used on flight models is xenon (Xe), but some other propellants are tested in laboratories such as argon (Ar), krypton (Kr), or

iodine (I_2) [7]. Challenges related to the use of alternative propellants are further detailed in Section 1.3 below.

Magnetic topology and beam divergence

Furthermore, the radial magnetic field gradient in the channel also forms what is called an "ion lens", which has a double purpose: it tends to deflect the ions away from the channel walls, and it focuses the ions out of the channel into the beam [7]. The divergence of the beam directly impacts the efficiency of the thruster, as shown in Equation 1.12, since it impacts the propellant exhaust velocity, v_{ex}, along the thrust axis. Consequently the quality of the magnetic topology, which is governing the beam divergence, is found to directly influence the thruster efficiency.

$$v_{\text{ex}} = \sum_{i=0}^{i_{max}} (v_i \cos(\theta_i))^2 < \sum_{i=0}^{i_{max}} v_i^2 \tag{1.12}$$

Where i_{max} is the total number of particles ejected by the thruster, v_i and θ_i are respectively the velocity and the divergence of the ith particle to the thrust axis.

An example of these magnetic field lines can be found in Figure 1.9, where the so-called "magnetic lens" or "ion lens" is visible.

Due to the beam divergence from the channel, a high density region is formed at the center of the plume, along the thruster symmetry axis. Indeed if we use the same schematic cut as in Figure 1.4, we can easily understand that the superposition of the beams from each side of the channel leads to this effect. This is illustrated in Figure 1.10 for the plume near the exit plane. Nevertheless the plume behavior in a real environment, with satellite solar panels and instruments, is a complex topic which has been studied in the past, numerically [20, 21, 22] and experimentally [7, 23]. Thus the plume behavior will not be treated in the present work.

1.3 Key issues to develop new HETs

As detailed in the previous section, HETs are complex devices, and their operation is still poorly understood. However, as detailed in Section 1.1, new designs (higher thrust or miniaturization) of HETs need to be developed in order to match industrial needs. Development of these new designs encounters numerous key challenges that are treated in this section.

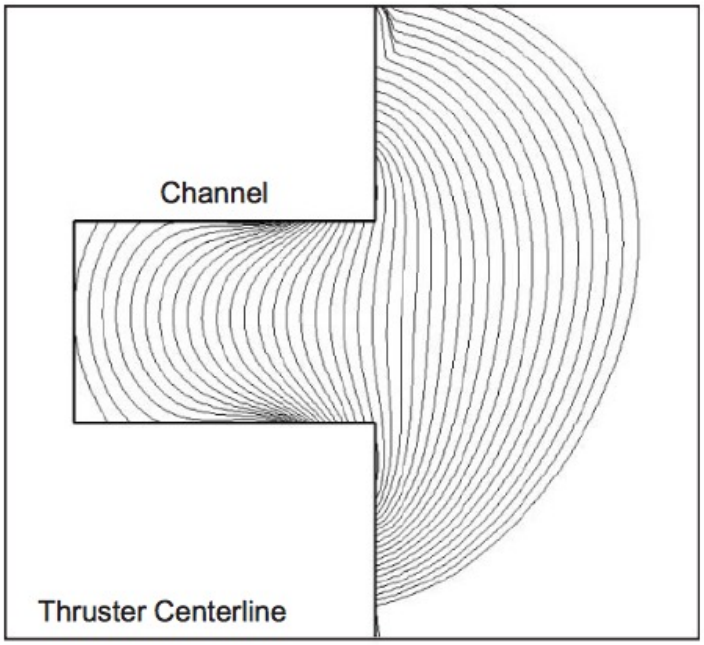

Figure 1.9 – Magnetic field lines of the NASA-173Mv Hall thruster [7].

1.3.1 Plasma/wall interactions

As described in Section 1.2.4, the plasma/wall interactions are determined by the magnetic field topology, the wall materials, and the velocity distribution functions of charged particles. These interactions impact the HET operation behavior by two mechanisms:

Channel erosion The lifetime of HETs is limited due to a large erosion of the walls through ion sputtering [19]. Indeed $30 - 40$ % of the total ion production in the channel is estimated to be absorbed by the walls because of the mild electrostatic confinement near the walls [24]. This erosion leads to a poorly understood striation of the ceramics [25] imaged in Figure 1.11 and to a widening of the channel. This erosion modifies the thruster performance, eventually leading onto the thruster failure.

Secondary electron emission (SEE) leads to the exchange of hot electrons from the plasma by cold electron from the walls. This implies large energy losses. Thus the tail of energetic electrons that are collected by the walls is likely to be highly depleted [26, 27].

A better understanding of these mechanisms is one of the key issues to

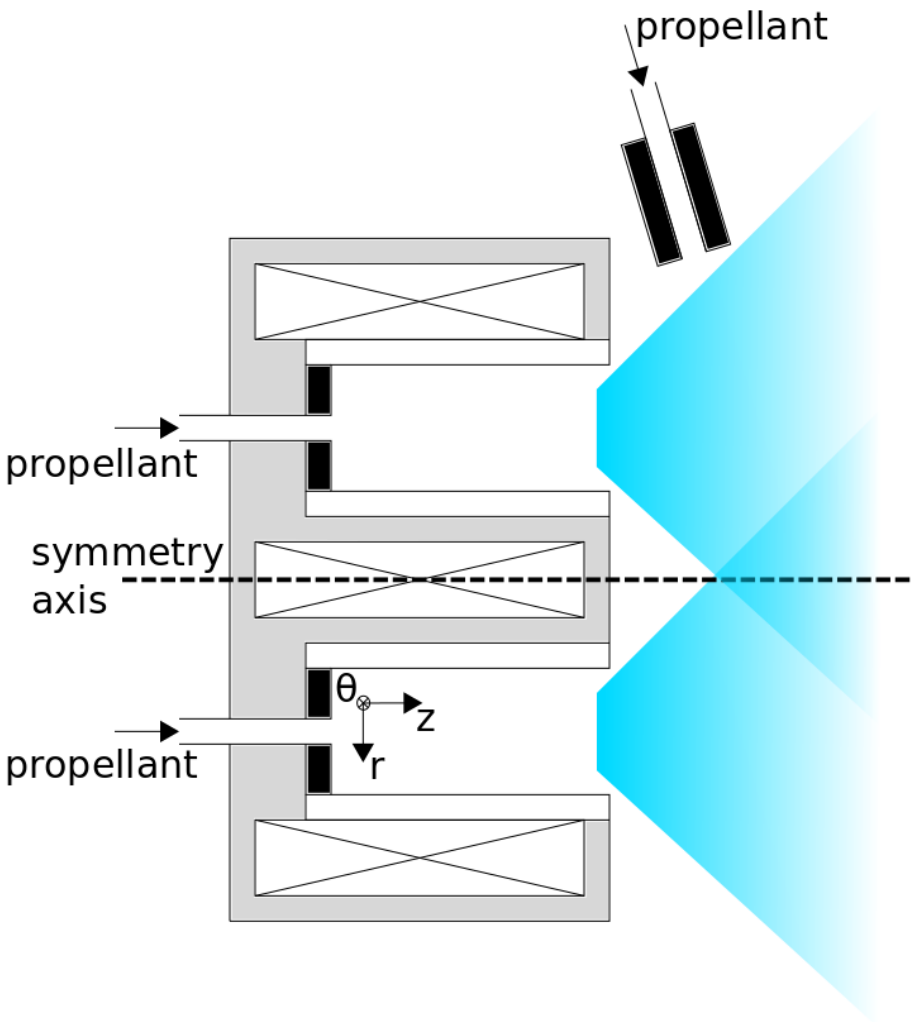

Figure 1.10 – Schematic cut of a HET and its associated plume near the exit plane.

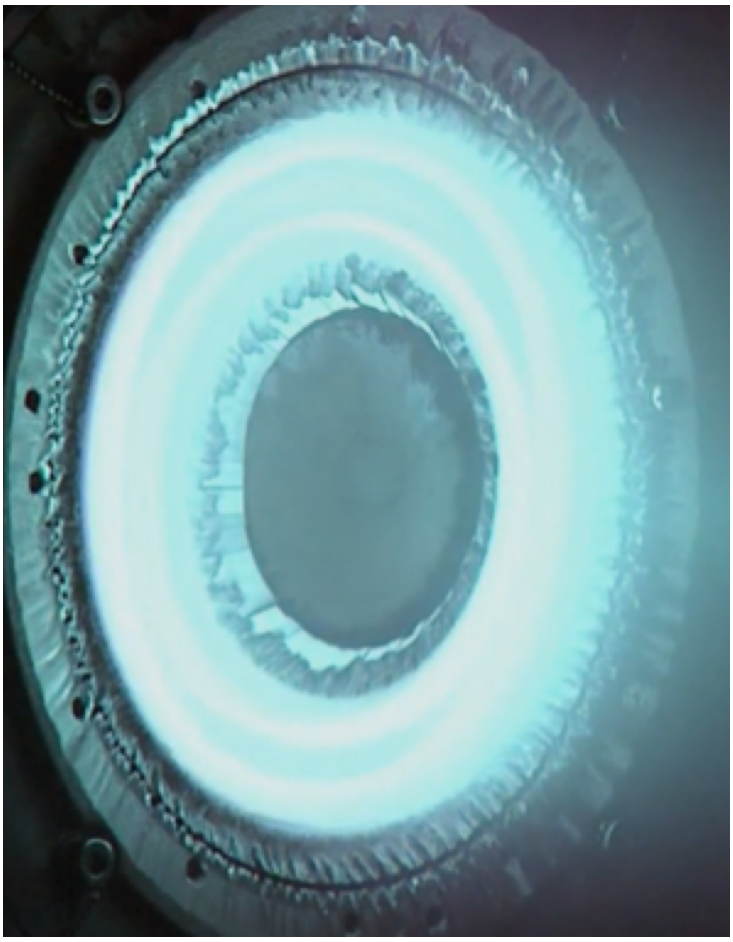

Figure 1.11 – Erosion of the ceramic walls in a *PPS1350* built by *Safran Aircraft Engines* as observed during an endurance test. The slimming of the ceramic walls can lead to the exposure of the magnetic circuit to the hot plasma, inducing a thruster failure. The poorly understood striation is clearly visible at the channel wall edges.

the design of more efficient and more reliable HETs.

1.3.2 Instabilities and anomalous transport

HETs are characterized by the presence of many oscillation modes propagating azimuthally or longitudinally, with frequencies from a few kHz to tens of MHz [28]. Some longitudinal oscillations are well understood like ion-transit time oscillations in the $100 - 500$kHz range [29, 30], or the breathing mode in the $10 - 30$kHz range [31]. However in contrast to longitudinal modes, our understanding of azimuthal modes is poorer.

Numerous studies have shown that the electron mobility across the magnetic field tends to be anomalously high in comparison to the mobility predicted by classical diffusion theories based on standard electron-neutral or electron-ion collisions [32, 7, 33, 13, 34], particularly near the thruster exit and in the near-plume region [33, 13, 35, 36]. Historically four main mechanisms have been proposed to explain this anomaly, including:

1. Intense secondary electron emission arising from electron-wall collisions enhancing the electron mobility near the channel walls [32, 27, 37]
2. sheath instabilities in the radial direction due to intense secondary electron emission [37, 38]
3. Large electron drift velocities in the azimuthal direction leading to the formation of strong instabilities [39, 40, 41, 42]
4. gradient driven fluid instabilities [43, 44, 45, 46].

The role of thruster wall materials on this anomalous transport has been experimentally highlighted in numerous studies [7, 27, 37, 47], however evidence suggests that electron-wall collisions and secondary electron emission are not sufficient to explain the observed cross-field electron transport [39, 48, 49, 50, 51, 52].

Thus the most plausible explanation seems to be the formation of instabilities in the azimuthal direction, as highlighted by both experimental and numerical studies [53, 54, 55, 56]. The large electron drift velocity in the azimuthal direction appears to be the main driving force for these instabilities [40, 41, 57], which give large amplitude fluctuations in both the plasma density and azimuthal electric field.

The importance of these instabilities on electron transport was highlighted in [40], which modeled a HET in a 2D $z - \theta$ plane using PIC simulations. These simulations were able to reproduce self-consistently numerous experimental observations, without requiring the addition of any empirical

parameters to increase the electron collisionality. Although the channel walls or secondary electron emission were not explicitly modeled, these simulations observed a strong electron drift instability in the azimuthal direction, suggesting this as the main phenomenon causing the anomalous electron transport [13]. These instabilities have frequencies in the MHz range, wavelengths of the order of the mm, and electric field amplitudes almost as large as the axial accelerating field itself [13]. Moreover some of these results were independently confirmed by similar 2D simulations [58].

1.3.3 Alternative propellants

As already discussed in Section 1.2.4, HETs use quite exclusively xenon as propellant. Indeed thanks to its large mass, relatively low ionization threshold, and its chemical inertness, xenon appears as the perfect propellant. However xenon being a rare gas, its production is expensive, subject to supply fluctuations, and supply limitations as shown in Figure 1.12.

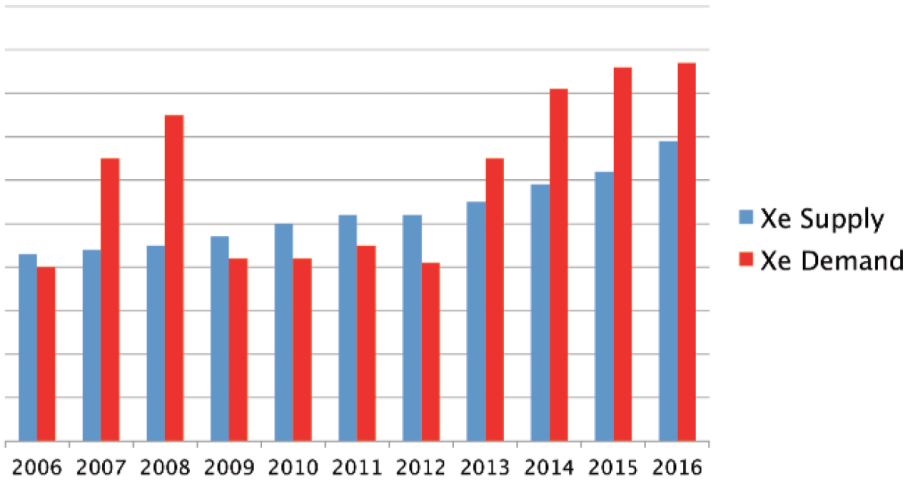

Figure 1.12 – World demand for xenon gas between 2006 and 2016 [59].

Hence alternative propellants are studied in laboratories. The gases considered to replace xenon are listed below.

Argon would be the most cost effective solution. However the changes in ionization threshold imply completely new scaling and magnetic topologies. Double stage thrusters were proposed to overcome those limitations, but with limited success [19, 18, 17].

Krypton has also been tested as it does not require too many modifications in the HET, and generates a high Isp (but it has a lower efficiency than xenon) [60].

Bismuth could also be a potential candidate, however its operation requires heating the propellant to 271°C, and bismuth is likely to deposit on satellite surfaces.

Iodine is also considered nowadays [61, 62] and *Busek Co. Inc.* is proposing both HETs and gridded thrusters operating with iodine. Studies are lead to better understand the operation of EP systems using iodine [63].

Atmospheric propellants could also be a solution, mostly used for very low orbiting systems, that could use the atmosphere residuals as propellant. A *PPS1350-TSD* from *Safran Aircraft Engines* was tested using pure nitrogen as well as a nitrogen/oxygen mixture after an ignition with xenon. Both cases showed a lower propellant efficiency and a higher anode erosion compared to operations using xenon [64].

Not being strictly speaking a limitation of the HET technology, the need for alternative propellants is an economic demand if HET technology is to be more widely used. Thus adaptation of the HET technology to other propellants than xenon is a key topic.

1.4 Main properties and characteristics of plasmas in HETs

The plasma is a state of matter *per se*, thus its properties and characteristics do differ from the other states of matter. Since EP in general, and HETs in particular, are based on physical plasma properties, main aspects of plasma physics have to be detailed.

1.4.1 Dominant physical effects in plasmas

Collisional or non-collisional plasmas

In a fully ionized plasma, interactions are mostly governed by electromagnetic forces. This is in contrast to a neutral gas where collisions are the main driver of the global behavior. However since these forces are long ranged, decreasing in $1/r^2$, a field is created by each particle, and can interact with charged particles in a whole region around the charged particle. Thus we have a "collective" interaction where each particle is interacting with a field created

by all the particles around it (and sometimes superposing to an imposed field due to external conditions). We obtain a significant electromagnetic coupling particle/field.

On the one side, the effect of the fields on the particles can be estimated using the Lorentz force, and knowing the fields $\mathbf{E}$ and $\mathbf{B}$ at the particle position. On the other side, knowing the positions $\mathbf{x}$ and velocities $\mathbf{v}$ of every particles, the density ρ and the current $\mathbf{j}$ can be obtained, leading us to the Maxwell equations to estimate the variations of $\mathbf{E}$ and $\mathbf{B}$.

In a partly ionized plasma, the mechanical coupling due to collisions and the electromagnetic field coupling described previously are overlapping. Both are governing the dynamics of the particles. To describe the importance of collisions (with neutrals or charged particles) the notion of mean free path is used.

The mean free path is defined in any gas, ionized or not, as the average distance traveled by a moving particle (such as a neutral atom, an ion, or an electron) between successive collisions, which modify its properties (direction, energy,...). This is illustrated in Figure 1.13.

The comparison of the mean free path with the distance between the particles and the geometrical properties of the system is essential to determine whether or not collisions have a significant effect on the plasma behavior. The different types of collisions (neutral/neutral, ion/neutral, electron/neutral,...) can be described at the microscopic level through typical frequencies (the collisions frequencies) or typical lengths (different mean free paths for each collision type).

In the case of HETs, which feature a partly ionized plasma as detailed in Section 1.2.4, a mean free path analysis shows the relative importance of ion/neutral, neutral/neutral as well as electron/neutral collisions since they are comparable to the system characteristic length [66].

The mean free path can be compared to other typical lengths such as the Landau length, r_0, or the mean distance between particles, d, to characterize the plasma behavior. The Landau length represents in some way the size of the particle viewed by the electrostatic interaction. Indeed the Landau length corresponds to the distance between two particles for which the interaction energy is equal to their mean kinetic energy. This length, r_0, is expressed in Equation 1.13 below:

$$r_0 = \frac{e^2}{4\pi\,\epsilon_0\,k_\mathrm{B}T_\mathrm{n}} \tag{1.13}$$

Where e is the elementary charge, ϵ_0 the vacuum permittivity, k_B the Boltzmann constant, and T_n the neutral gas temperature. As in most plasmas,

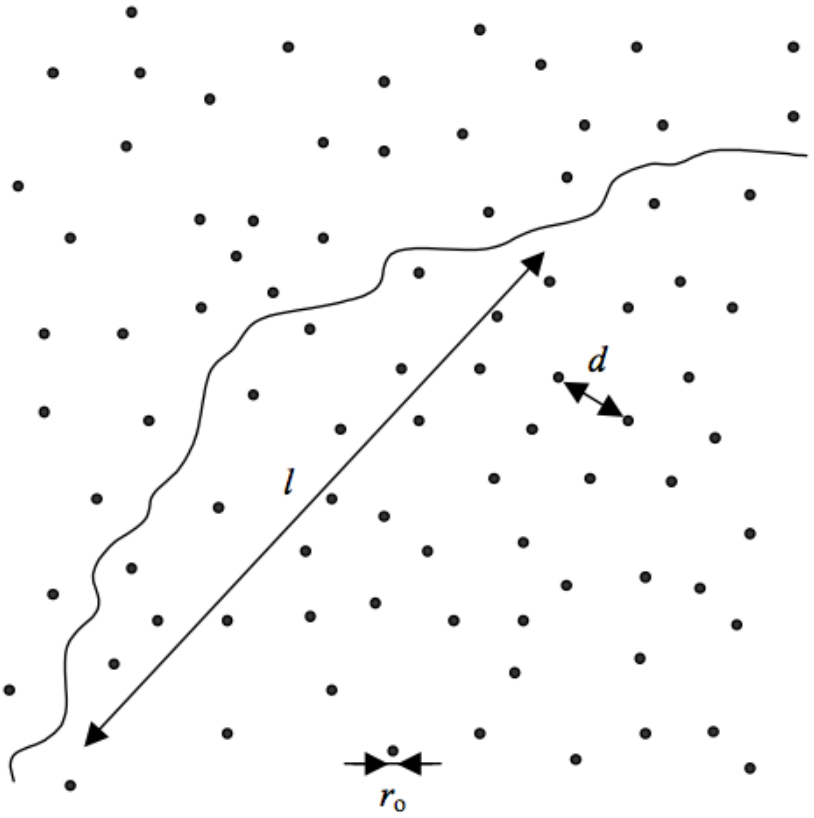

Figure 1.13 – Example of an electron (or ion) trajectory in a plasma [65]. Typical distances are represented: l is the mean free path, d the mean distance between particles, and r_0 is the Landau length, or size of a particle.

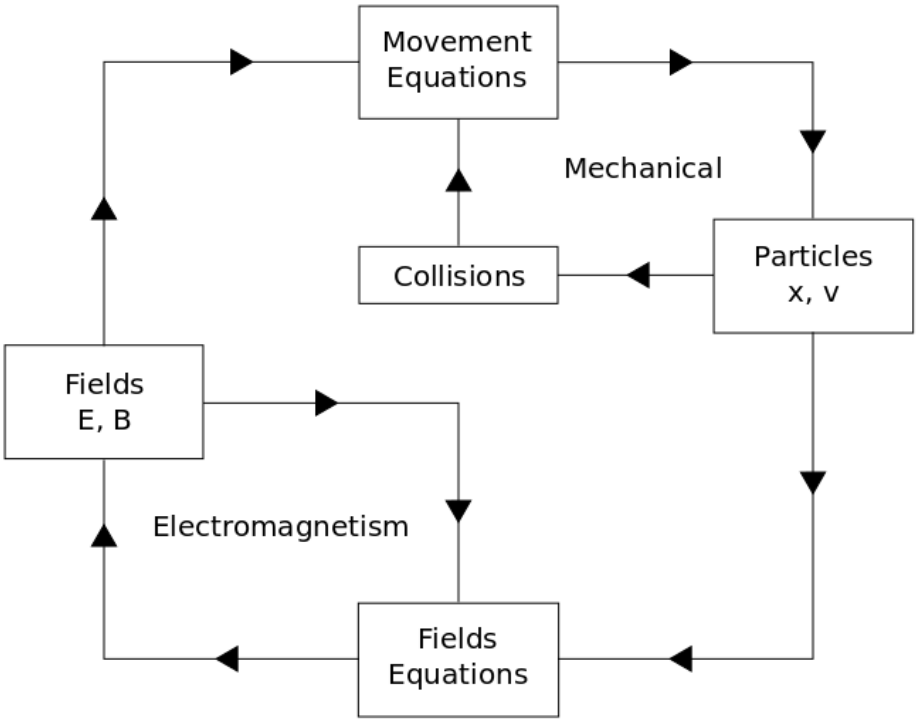

Figure 1.14 – Coupling between particle movement and electromagnetic field fluctuations in a general plasma case.

and in particular in HETs plasma discharges, d is greater than r_0, the probability of a binary close collision between two charged particle is considered negligible in comparison to collisions with a neutral particle.

Field/particles coupling

The overlapping of these two couplings, electromagnetic and mechanical, creates a complex system where the particle positions, as well as the forces acting on them, are determined through three main loops, as illustrated in Figure 1.14. One loop corresponding to the electromagnetic coupling, through particle/field interactions, another for the mechanical coupling, through collisions, and finally one loop linking those two couplings.

Quasi-neutrality condition and Debye length

An important plasma property is the quasi-neutrality condition. This means that the densities of negative and positive charges are (almost) equal.

In the case of a plasma containing only singly charged ions, this means we have an equality between the two charged particle densities: $n_i = n_e$, with n_i the singly charged ion density, and n_e the electron density. Nevertheless ions can bear more than a single charge, and the previous expression then has to take into account the presence of z-times charged ions (of density n_z). Consequently the quasi-neutrality condition is expressed as:

$$n_e = \Sigma_z z \cdot n_z \tag{1.14}$$

In usual cases, and in particular in HETs operating at moderate power levels, multiply charged ion densities are negligible in comparison to singly charged ion density. However as mentioned in Section 1.2.4, at high power levels, a significant number of multiply charged ions can be generated.

By estimating what amount of deviation to the quasi-neutrality, Δn, is possible over a given length, L, we obtain:

$$\frac{1}{2} k_{\mathrm{B}} T_e \approx \frac{1}{2} \frac{e^2}{\epsilon_0} \cdot \Delta n \cdot L \tag{1.15}$$

Since only thermal energy can fuel such a deviation. With k_{B} the Boltzmann constant and ϵ_0 the vacuum permittivity. The Debye-Hückel length, λ_{De}, is defined as:

$$\lambda_{De} = \sqrt{\frac{\epsilon_0 k_{\mathrm{B}} T_e}{n_e e^2}} \tag{1.16}$$

Thus when substituting $k_{\mathrm{B}} T_e$ from Equation 1.15 by λ_{De} from Equation 1.16, we obtain:

$$\frac{\Delta n}{n} \approx \left(\frac{De}{L} \right)^2 \tag{1.17}$$

According to Equation 1.17, the condition of quasi-neutrality, which can be expressed as $\Delta n << n_e, n_i$, is equivalent to $L >> \lambda_{De}$. Thus the Debye length is the length scale over which significant deviations from quasi-neutrality can occur. It describes the equilibrium between electrostatic and electronic pressure when ions are immobile.

From the definition of the Debye length, we can easily understand that being able to model this length is a condition for simulations trying to capture kinetic effects deviating from the quasi-neutrality condition. This is detailed in Section 2.1.1.

Plasma oscillations

An estimation of the electric field, E, created through charge separation gives us Equation 1.18.

$$E = \frac{e}{\epsilon_0} nx \tag{1.18}$$

Where n is the density of the corresponding charged particle, and x the separation length. Considering an electron separated from immobile ions, we obtain the following movement equation:

$$eE = \frac{e^2}{\epsilon_0} nx = m_e \frac{d^2x}{dt^2} \tag{1.19}$$

As easily observed, Equation 1.19 describes a harmonic oscillator with an eigenfrequency, $\omega_{\mathrm{p,e}}$, defined as:

$$\omega_{p,e} = \sqrt{\frac{ne^2}{m_e \epsilon_0}} \tag{1.20}$$

This so-called (electron) plasma frequency characterizes the plasma fluctuations when the dominant force is the electrostatic force due to the density fluctuations of the charged particles (electrons and ions). In most cases the important inertia of the ions leads to the domination of the electrostatic fluctuations by the electrons' movement.

As the plasma frequency characterizes the plasma fluctuations, it is as well as the Debye length, an important condition for simulations. As for the Debye length, these conditions on the simulation set-up are summarized in Section 2.1.1.

Closed plasmas

In the case of a HET, the plasma is not infinite in space, but bounded by walls. These walls are in most HETs composed of dielectrics, and thus have a floating potential. While the potential at the walls is not the topic of the present section, the potential evolution at the edge of the bounded plasma is an important subject. Indeed at the edge of a bounded plasma, a potential exists to contain the more mobile charged species. Thanks to this potential, the flow of positive and negative charged particles to the walls are balanced.

In the classical case of a HET, where an equal number of singly-charged ions and electrons constitute the plasma, electrons are, due to their mass, far more mobile than ions. Therefore the plasma is positively charged with

respect to a grounded wall. The non-neutral potential region near the wall is then usually called a *sheath*. As detailed in [67], the electron density in the sheath decays on the order of a Debye length, λ_{De}, defined above, in order to shield the electrons from the wall.

In addition to this sheath, a transition region, called the *pre-sheath* exists between the plasma bulk and the sheath. The transition between the pre-sheath and the sheath, as well as the continuity of ion flux, gives an ion velocity at the plasma sheath, u_s, higher than a given velocity known as the *Bohm velocity*, noted u_B. In order to estimate the Bohm velocity and describe the sheath, some significant assumptions are made:

1. Electrons are Maxwellian at a temperature T_e,
2. Ions are cold in comparison to electrons, so that $T_i = 0$,
3. At the plasma sheath interface, an arbitrary zero is imposed so that, $x = 0$ and $\Phi(x = 0) = 0$. This region is characterized by $n_i(x = 0) = n_e(x = 0) = n_s$,
4. The plasma is considered as collisionless.

Following these assumptions, the Bohm velocity can be estimated, and the condition on the ion velocity at the sheath edge is given by:

$$u_s \geq u_B = \left(\frac{qT_e}{m_i}\right)^{1/2} \tag{1.21}$$

The result presented in Equation 1.21 is known as the *Bohm sheath criterion*. Quantitative behavior of the sheath and pre-sheath in contact with a wall is shown in Figure 1.15.

The potential drop across a collisionless plasma pre-sheath, $\Delta\Phi_{\text{p-s}}$, which accelerates the ions to the Bohm velocity, is obtained by:

$$\frac{1}{2}m_i u_B^2 = q\Delta\Phi_{\text{p-s}} \tag{1.22}$$

Where $\Delta\Phi_{\text{p-s}}$ is the plasma potential with respect to the sheath/pre-sheath edge, where we considered $\Phi(x = 0) = 0$. By substituting Equation 1.21 into Equation 1.22, we obtain a simple expression of the potential drop in the pre-sheath:

$$\Delta\Phi_{\text{p-s}} = \frac{T_e}{2} \tag{1.23}$$

In order to estimate the potential drop in the sheath, $\Delta\Phi_{\text{s}}$, with respect to the sheath/pre-sheath edge, we equate the ion flux at the wall, Γ_i, to the electron flux at the wall, Γ_e:

$$n_s u_B = \Gamma_i = \Gamma_e = \frac{1}{4}n_s \bar{v}_e e^{\Delta\Phi_{\text{s}}/T_e} \tag{1.24}$$

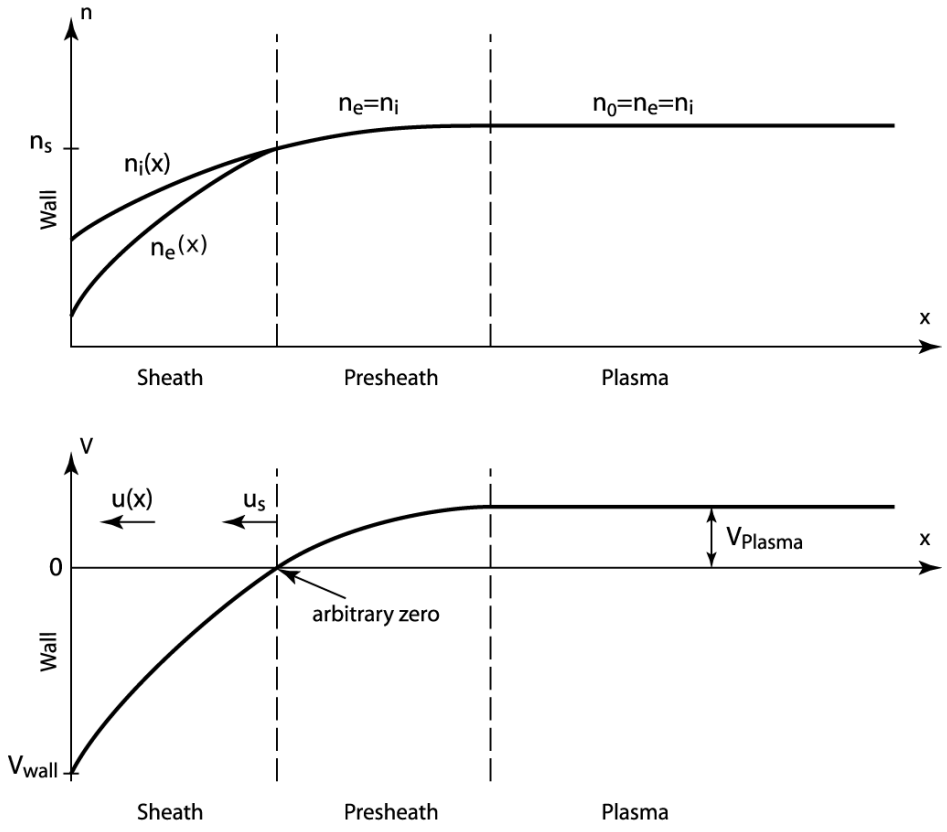

Figure 1.15 – Schematic of a plasma sheath near a wall [67].

Where $\bar{v}_e = \sqrt{8qT_e/\pi m_e}$ is the mean electron speed.

Solving Equation 1.24 for $\Delta\Phi_s$, we obtain:

$$\Delta\Phi_s = -T_e \ln\left(\frac{m_i}{2\pi m_e}\right)^{1/2} \tag{1.25}$$

However this expression does not take into account the presence of an electron flux coming from the wall due to secondary electron emission. Indeed, as detailed in Sections 1.2.4 and 1.3, secondary electron emission from the walls plays a significant role in the HET operation, as well as on the electron anomalous transport. Thus this electron flux has to be taken into account in the estimate of the sheath potential drop. This will be done in Section 5.1.

1.4.2 Fluid description of a magnetized plasma in HETs

The precedent properties are general plasma properties, yet relevant to correctly set-up simulations and models of HET plasma discharges. However the present Section is focused on the fluid description of some of the plasma properties in the typical HET set-up. Firstly the classical diffusion theory proposed to quantify the cross-field electron transport observed in HETs, and expressed in Section 1.3, is discussed. Secondly the fluid description of instabilities in HETs, in particular the fluid description of high frequency and short wavelength instabilities expected to enhance the electron transport is presented.

Definition of mobility in a magnetized plasma

We consider the plasma in the HET discharge channel. Positioning our system in the channel center, the static magnetic field, $\mathbf{B}$, is set along the (Oy) axis, the applied electric field, $\mathbf{E}$, is defined in the (Oz) direction, while the plasma is assumed to be infinite in the azimuthal direction, noted x. In such a system, the momentum conservation equation, obtained by taking the first moment of the Boltzmann equation, is given, for any charged particle population, by:

$$nm\left[\frac{d\mathbf{v}}{dt} + (\mathbf{v}\cdot\nabla)\mathbf{v}\right] = nq(\mathbf{E} + \mathbf{v}\times\mathbf{B}) - \nabla p - m\mathbf{v}[n\nu_m + Q_s] \tag{1.26}$$

Where n is the density of the considered charged particles, m the particle mass, $\mathbf{v}$ its velocity vector, $\mathbf{E}$ the electric field, p pressure force on the given charged particle population, ν_m the collision frequency, and Q_s the arithmetic

source and loss term. Since our goal is to study the plasma bulk in the center of the plasma discharge at steady state, the left hand side of Equation 1.26 can be considered negligible.

The present study concentrates on the electron mobility, indeed an anomaly of electron transport along (Oz) has been observed in HETs, as detailed in Section 1.3.

As the pression contribution can be expressed through a thermodynamical equation of state, since electrons are considered isothermal, we obtain $\nabla p = k_{\mathrm{B}} T \nabla n$. Thus Equation 1.26 written for electrons, and projected respectively on (Oy) (Equation 1.27) and (Oz) (Equation 1.28), gives:

$$-n_e e v_{e,z} B_x - m_e n_e v_{e,y} \nu_m = 0 \tag{1.27}$$

$$-n_e e (E_z - v_{e,y} B_x) - k_{\mathrm{B}} T_e \frac{\mathrm{d}n_e}{\mathrm{d}z} - m_e n_e v_{e,z} \nu_m = 0 \tag{1.28}$$

Where $\nu_{e/n}$ is the electron/neutral collision frequency. An important note is that, in the (Oy) direction, the gradients as well as the electric field are considered as null. From Equation 1.27, we obtain:

$$v_{e,y} = -\frac{e B_x v_{e,z}}{m_e \nu_m} \tag{1.29}$$

Substituting Equation 1.29 in Equation 1.28, we finally obtain:

$$-n_e e E_z - k_{\mathrm{B}} T_e \frac{\mathrm{d}n_e}{\mathrm{d}z} - n_e v_{e,z} m_e \nu_m \left[1 + \frac{\omega_{\mathrm{c,e}}^2}{\nu_m^2}\right] = 0 \tag{1.30}$$

Where $\omega_{\mathrm{c,e}}$ is the electron cyclotron frequency as defined in Section 1.2.4. Moreover since the axial density gradients are considered negligible in the HET case, Equation 1.30 simplifies to:

$$-e E_z - v_{e,z} m_e \nu_m \left(1 + \frac{\omega_{\mathrm{c,e}}^2}{\nu_m^2}\right) = 0 \tag{1.31}$$

Where Equation 1.31 can easily be rewritten as:

$$\frac{v_{e,z}}{E_z} = \frac{\frac{e}{m_e \nu_m}}{1 + \frac{\omega_{\mathrm{c,e}}^2}{\nu_m^2}} = \mu_{\mathrm{classical}} \tag{1.32}$$

Where $\mu_{\mathrm{classical}}$ is considered as the classical mobility from diffusion. As detailed in Section 1.2.4, the electron mobility measured in HETs channel is shown to be much larger than this, particularly near the thruster exit. Chapter 4 focuses on both highlighting this anomaly through simplified HET simulations, as well as confirming and complimenting a kinetic theory proposed by [68, 69] in our bi-dimensional simulation set-up.

Fluid description of plasma instabilities

As expressed in Section 1.3, instabilities play a significant role in HETs. Numerous instabilities and oscillations are observed in HET plasma discharges, propagating longitudinally and azimuthally, with frequencies from a few kHz to tens of MHz [28]. While some longitudinal oscillations are well understood, like the ion-transit time oscillations in the $100 - 500$kHz range [29, 30], or the breathing mode in the $10 - 30$kHz range [31], our understanding of azimuthal modes is poorer.

Since azimuthally propagating oscillations are the most plausible explanation to electron anomalous transport as already highlighted [53, 54, 55, 56], the present work tends to describe these azimuthally propagating modes. Moreover the large electron drift velocity in the azimuthal direction appears to be the main driving force for these instabilities [40, 41, 57], which give large amplitude fluctuations in both the plasma density and azimuthal electric field. Consequently the present study focuses on the electron drift instability, thus the frequencies of interest are in the 1 - 10 MHz range.

In the same set-up as for Equation 1.26, the continuity equation can also be obtained from the Boltzmann equation by taking its zeroth moment. This is given for any charged particles by:

$$\frac{dn}{dt} + \nabla \cdot (n\mathbf{v}) = Q_s \tag{1.33}$$

Using Equations 1.26 and 1.33 for both singly charged ions and electrons, we obtain a set of four equations:

$$\frac{dn_e}{dt} + \nabla \cdot (n_e \mathbf{v_e}) = 0 \tag{1.34}$$

$$m_e n_e \frac{d\mathbf{v_e}}{dt} + m_e n_e \mathbf{v_e} \cdot \nabla \mathbf{v_e} = -en_e(\mathbf{E} + \mathbf{v_e} \times \mathbf{B}) - \nabla(n_e T_e) - m_e \nu_e n_e \mathbf{v_e} \tag{1.35}$$

$$\frac{dn_i}{dt} + \nabla \cdot (n_i \mathbf{v_i}) = 0 \tag{1.36}$$

$$m_i n_i \frac{d\mathbf{v_i}}{dt} + m_i n_i \mathbf{v_i} \cdot \nabla \mathbf{v_i} = -en_i \mathbf{E} - \nabla(n_i T_i) - m_i \nu_i n_i \mathbf{v_i} \tag{1.37}$$

These four equations are coupled via Poisson's equation:

$$\nabla^2 \Phi = -\frac{e}{\epsilon_0}(n_i - n_e) \tag{1.38}$$

Where:

$$\mathbf{E} = -\nabla \Phi \tag{1.39}$$

Indeed our plasma is considered to be only composed of singly charged ions, neutrals, and electrons. Furthermore the source term in Equations 1.26 and 1.33 is considered negligible at steady state.

In order to study the possible presence of instability in this system, a perturbation analysis is performed. Consequently Equations 1.26 and 1.33 are linearized considering perturbations of the form:

$$A = A_0 + \delta A \exp^{i(\mathbf{k}\cdot\mathbf{x}-\omega t)} \tag{1.40}$$

Where A represents any physical value encountered in our set of equations, outside of the magnetic field that is externally imposed, and the temperatures since both ions and electrons are considered isothermal. Consequently $\delta T_e = \delta T_i = \delta B = 0$. Since $\delta A \exp^{i(\mathbf{k}\cdot\mathbf{x}-\omega t)}$ is a perturbation, we have $\delta A << A_0$, while $\mathbf{k}$ is the perturbation wave-vector, and ω its frequency. In the following, the subscript 0 will refer to the equilibrium value.

In further developing, only instabilities satisfying $k << \nabla$, and $\omega >> \frac{d}{dt}$ are considered. This means only high-frequency and short wave-length instabilities are here considered. Although gradients of the equilibrium plasma properties being assumed as second order, and thus not considered, an equilibrium electric field is allowed, and hence the gradient of the equilibrium potential is not zero. Following these assumptions, Equation 1.33 disappears, while Equations 1.26 for ions and electrons, as well as Equations 1.38 and 1.39 become at equilibrium:

$$-e(\mathbf{E_0} + \mathbf{v_{e,0}} \times \mathbf{B}) - m_e \nu_e \mathbf{v_{e,0}} = 0 \tag{1.41}$$

$$e\mathbf{E_0} - m_i \nu_i \mathbf{v_{i,0}} = 0 \tag{1.42}$$

$$\nabla^2 \Phi_0 = -\frac{e}{\epsilon_0}(n_{i,0} - n_{e,0}) \tag{1.43}$$

$$\mathbf{E_0} = -\nabla \Phi_0 \tag{1.44}$$

Where ν_i and ν_e correspond respectively to the ion/neutral and electron/neutral collision frequencies.

The applied magnetic field is along (Oy), while the applied electric field is in the (Oz) direction. Now we can, through substitution, obtain the non-equilibrium equations corresponding to Equation 1.33, for both electrons and ions:

$$-i\omega\delta n_e + i(\mathbf{k}\cdot\mathbf{v_{e,0}})\delta n_e + i n_{e,0}(\mathbf{k}\cdot\delta\mathbf{v_e}) = 0 \tag{1.45}$$

$$-i\omega\delta n_i + i(\mathbf{k}\cdot\mathbf{v_{i,0}})\delta n_i + i n_{i,0}(\mathbf{k}\cdot\delta\mathbf{v_i}) = 0 \tag{1.46}$$

Applying the same method to Equation 1.26, for both electrons and ions, we

can write:

$$m_e n_{e,0}\left[-i\omega\delta\mathbf{v_e} + i(\mathbf{k}\cdot\mathbf{v_{e,0}})\delta\mathbf{v_e}\right] = -en_{e,0}(-i\mathbf{k}\delta\Phi + \delta\mathbf{v_e}\times\mathbf{B}) \\ -i\mathbf{k}k_{\mathrm{B}}T_e\delta n_e - m_e\nu_e(n_{e,0}\delta\mathbf{v_e} + \delta n_e\mathbf{v_{e,0}}) \tag{1.47}$$

$$m_i n_{i,0}\left[-i\omega\delta\mathbf{v_i} + i(\mathbf{k}\cdot\mathbf{v_{i,0}})\delta\mathbf{v_i}\right] = +en_{i,0}\mathbf{k}\delta\Phi \\ -i\mathbf{k}k_{\mathrm{B}}T_i\delta n_i - m_i\nu_i(n_{i,0}\delta\mathbf{v_i} + \delta n_i\mathbf{v_{i,0}})w \tag{1.48}$$

Finally the perturbed Poisson equation is obtained the same way, giving:

$$k^2\delta\Phi = \frac{e}{\epsilon_0}(\delta n_i - \delta n_e) \tag{1.49}$$

In the sake of clarity and convenience we define thermal velocities, respectively for electrons and ions, $v_{th,e} = \sqrt{k_{\mathrm{B}}T_e/m_e}$ and $v_{th,i} = \sqrt{k_{\mathrm{B}}T_i/m_i}$. In the same way we can use $\omega_{p,e}$ and $\omega_{p,i}$, respectively electron and ion plasma frequency, as defined in Section 1.2.4. Furthermore we are interested in modes propagating azimuthally, corresponding to the $\mathbf{E}_0\times\mathbf{B}_0$ direction (in the (Ox) direction in the present coordinate system). By re-arranging Equations 1.45 to 1.49, we obtain the following dispersion relation:

$$1 - \frac{\omega_{p,e}^2\left(\alpha^2 - \frac{k_z^2}{k^2}\omega_{\mathrm{c,e}}^2\right)}{\alpha(\alpha-\omega_{\mathrm{c,e}}^2)(\omega-\mathbf{k}\cdot\mathbf{v_{e,0}}) - k^2v_{th,e}^2\left(\alpha^2 - \frac{k_z^2}{k^2}\omega_{\mathrm{c,e}}^2\right)} \\ - \frac{\omega_{p,i}^2}{(\omega-\mathbf{k}\cdot\mathbf{v_{i,0}})(\omega-\mathbf{k}\cdot\mathbf{v_{i,0}}+i\nu_i) + i\nu_i\omega - k^2v_{th,i}^2} = 0 \tag{1.50}$$

Where we defined $\alpha = \omega - \mathbf{k}\cdot\mathbf{v}_{\mathrm{e},0} + i\nu_e$ for convenience.

We assume ions as collision-less ($\nu_i = 0$) and at a low temperature ($v_{th,i} = 0$). Moreover electrons are also assumed collision-less ($\nu_e = 0$, consequently $\alpha = \omega - \mathbf{k}\cdot\mathbf{v}_{\mathrm{e},0}$). Thus, assuming the instability as mainly azimuthal, so that $k_z = 0$, Equation 1.50 becomes:

$$1 - \frac{1}{k^2\lambda_{De}^2}\frac{1}{\frac{(\alpha^2-\omega_{\mathrm{c,e}}^2)}{k^2v_{th,e}^2} - 1} - \frac{\omega_{p,i}^2}{(\omega-\mathbf{k}\cdot\mathbf{v_{i,0}})^2} = 0 \tag{1.51}$$

Equation 1.51 is a dispersion relation, for which solutions depend on the frequency domain. Since the instabilities of interest are in the 1 - 10 MHz range, whereas the typical electron cyclotron frequency is in the 100 - 500 MHz range, as detailed above, we have $\alpha^2 << \omega_{\mathrm{c,e}}^2$. Thus Equation 1.51 simplifies to:

$$1 - \frac{1}{k^2\lambda_{De}^2} - \frac{\omega_{p,i}^2}{(\omega-\mathbf{k}\cdot\mathbf{v_{i,0}})^2} = 0 \tag{1.52}$$

Consequently the obtained dispersion relation does allow an instability, with the following frequency:

$$\omega = \mathbf{k} \cdot \mathbf{v_{i,0}} \pm \frac{k\, c_s}{\sqrt{1 + k^2 \lambda_{De}^2}} \tag{1.53}$$

Nonetheless this dispersion relation does not show any imaginary part. Thus the growth rate of the instability is observed to be null. This means the investigated instability can be present in a fluid model, but its ignition cannot come from the model itself. Consequently the investigation of these instabilities needs kinetic simulation models to properly observe and investigate these instabilities and their effects. The development of such a simulation tool has been the core of this work, and is presented in the following chapters.

1.5 Scope and outline of the thesis

1.5.1 Scope

A simulation tool, LPPic2D, was developed *ex nihilo* and independently in order to model the complex systems that are HETs. Since these systems feature a rich variety of physical mechanisms, for which only kinetic models can appreciate and model their complexity, LPPic2D has been designed as a fully kinetic collisional model.

On the one hand, while 1D fully kinetic models have very low computational needs, their geometrical limitations do not allow them to model all the intricacy of the plasma discharge. On the other hand, 3D models bear the promise of fully covering the range of physical mechanisms [70], yet they are strongly limited by their gigantic computational needs. Thus, the plasma discharge characteristics in plasma thrusters lead fully kinetic 3D models to use a geometrical scaling [71]. Yet, despite being an elegant way to decrease the computational time needed, geometrical scaling seems to impact some of the plasma discharge characteristics [69]. If not using any scaling, modeling a slice of a real HET geometry with 3D models features heavy calculation times, that can only be partially decreased through long and complicated developments. Thus 3D models, if they can represent a solution to study realistic geometries and behaviors, are at present still not suitable for parametric studies. Nonetheless, thanks to recent computational developments [72], there can be hope in significative improvements in the long run.

Consequently a compromise between computational costs and physical modeling was made: it was chosen to develop a 2D fully kinetic simulation tool without any geometrical scaling. This tool allowed us, thanks to our

attention to preserve the code's efficiency, to investigate kinetic effects and mechanisms in HETs through various parametric studies.

However plasma thrusters have been historically studied both empirically and numerically, leading to a better understanding of the thrusters characteristics and operation. These studies have led to highlight the importance of plasma/wall interactions [7, 27, 37, 47], as well as the significant deviation of anomalous electron transport, in particular near the thruster exit [32, 7, 33, 13, 34, 33, 13, 35, 36].

As already detailed in Section 1.3, while the role of the electron drift instabilities on the anomalous transport has been highlighted [53, 54, 55, 56], the role of plasma/wall interactions has been experimentally observed [7, 27, 37, 47], but is shown to be insufficient [39, 48, 49, 50, 51, 52]. Thus the present work focuses on both mechanisms, and their effects on the anomalous transport, as they are expected to lead to a significant deviation of the electron cross-field mobility in comparison to classical and Bohm electron mobility estimates [32, 7, 33, 13, 34, 33, 13, 35, 36].

The electron drift instability has been observed to feature high frequency (of the order of the MHz) and short wavelength (of the order of the mm) oscillations [13]. Fully kinetic simulations can self-consistently capture this instability. In particular, 2D fully kinetic simulations in the $z - \theta$ plane already self-consistently highlighted this instability as the main phenomenon for anomalous transport [40, 58]. However, due to the chosen simulation geometry, neither the channel walls nor the secondary electron emission were explicitly modeled. In the same way, 2D $r - z$ simulations [36] were able to correctly model some of the features of HETs such as the magnetic field curvature, and the plasma/wall interactions. Yet the geometry prevented a self-consistent modeling of the electron drift instability.

Therefore in order to correctly address both the plasma/wall interaction and the electron drift instability, a 2D $r-\theta$ or a 3D geometry has to be used. Since the 3D model [70] is expected to be too computationally intensive, or needing geometrical scaling, the solution appears to be a 2D $r - \theta$ geometry. This allows us to self-consistently capture the electron drift instability propagating along the θ direction, as well as to study the effects from the walls. Furthermore, the $r - \theta$ cut axial location is positioned at the acceleration region of the thruster, near the exit plane. Indeed this part of the HET is characterized by both a large electron drift instability, and a strong secondary electron emission.

Investigations using fully kinetic 2D $r - \theta$ simulations have been previously realized [73, 42]. These simulations self-consistently modeled both the electron drift instability, the floating dielectric channel walls, and the secondary electron emission process. They gave a first description of the

relative importance and coupling of the secondary electron emission and the electron drift instability.

Nevertheless by generalizing a method developed by 1D simulations [74, 68], simulations presented in this work were able to coherently model the input from the (Oz) direction. Thanks to this method, it is possible to "mimic" the third dimension, without computationally burdening the simulation. Despite not being a self-consistent solution, as it is in a 3D model, and thus to be properly studied in term of numerical errors and impact on the plasma behavior, this method allowed our simulation set-up to draw nearer to a real HET geometry.

Finally the development, thanks to insights from 1D kinetic simulations along θ mimicking the (Oz) direction [68, 74], of a kinetic theory detailing the electron drift instability in HETs [69], gave us inputs to properly describe this instability. Results from our 2D fully kinetic $r-\theta$ simulations, allowed us to put this theory in question, and test its reliability on a more geometrically accurate set-up. However this kinetic theory [69], allowed us to properly quantify the relative effects of the electron drift instability and the secondary electron emission on anomalous transport.

1.5.2 Outline of the thesis

In the following work, we firstly detail the development of the 2D fully kinetic $r-\theta$ simulation code, called LPPic2D, then various studies are conducted in order to investigate the impacts of the electron drift instability, as well as of the secondary electron emission, on the electron anomalous transport. Inputs and details from the kinetic are presented along this work as they are needed in the interpretation of the simulation results. From these simulation results, a global model is developed in order to better understand the behavior of the plasma discharge.

Therefore, in Chapter 2, we firstly describe the development of LPPic2D, as a generic 2D fully kinetic collisional code. From scratch to a flexible simulation tool, the successive steps of the development are highlighted and detailed. Along the way, we describe both the PIC/MCC methods and the numerous verifications that were accomplished, in order to ensure the code's quality and reliability.

Secondly, as limitations of the generic simulation tool are highlighted, specific models are developed, implemented, and verified. These features are detailed in Chapter 3, and allow the model to get closer to a realistic simulation of a HET discharge channel.

Once the model has been presented in the two first chapters, Chapter 4 focuses on a simplified model in order to highlight the impacts of the

electron drift instability on the anomalous transport. In this case, neither secondary electron emission or floating dielectric walls are modeled. This allows a useful verification of the general set-up introduced in Chapter 3, as well as an appropriate questioning of the kinetic theory [69] in a 2D geometry.

Adding secondary electron emission models, Chapter 5 studies, through parametric studies, the impact of the plasma/wall interactions on the plasma discharge behavior. This set-up allows a correct study of the convoluted effects and mechanisms of plasma/wall interactions and electron drift instability on the anomalous transport.

In Chapter 6, floating dielectric walls were added to the system, investigating the impact of the dielectric width and permittivity on the plasma discharge behavior. The correct fit of the dielectric walls and the secondary electron emission models for boron-nitride walls allows us for a realistic simulation of the plasma discharge in the HET channel.

Finally Chapter 7 is devoted to a parametric study in order to estimate the impacts of alternative propellants on the plasma discharge behavior and its characteristics.

The informatics aspects of LPPic2D development and operation are detailed in the appendices, such as its structure or the way it is using modern distributed clusters. Complete details about the benchmark used to verify LPPic2D reliability [75] are exposed in the Appendix as well.

Chapter 2

Code development and verification: From scratch to a bi-dimensional Particle-In-Cell/Monte Carlo collision (PIC/MCC) simulation program

Contents

2.1 MiniPIC development: 1D-1V PIC

The first step was to develop a simple version of a PIC simulation code. This version, one-dimensional in space and velocity is called *MiniPIC*.

2.1.1 Generalities about the PIC method

MiniPIC is the first attempt to develop, and thus test, the particle-in-cell (PIC) methods described in [76]. In this method the particles are moved inside a defined simulation domain, where the field values are estimated on a defined grid.

In order to keep these first simulations simple, only electrons and singly charged ions are modeled. Neutrals are considered to be a constant and homogeneous background.

Following these choices, MiniPIC models the movement of "macro-particles" on a fixed grid. While the grid is defined with Cartesian coordinates, noting Δx the distance between two grid-points, each macro-particle models the behavior of more than one physical particle. Estimating the weight coefficient, q_f, of the macro-particles is easy knowing the initial plasma density, n, the length of the system, L, and the number of macro-particles modeled (ions plus electrons), i_{max}.

$$q_f = \frac{2nL}{i_{max}} \tag{2.1}$$

In the following, for sake of clarity and briefness, the macro-particles will be referred to as particles. However it should not be forgotten that they represent q_f physical particles.

Furthermore since these macro-particles are modeled on a grid, it is important to keep a minimal number of particle per grid-cell. Indeed it has been shown that an insufficient number of particles in a cell leads to numerical artifacts preventing a correct simulation [77]. Consequently in the following work, the number of particle per grid-cell is never lower than 50.

The PIC method

The PIC method in such a configuration is quite simple, based on a temporal loop, where the same steps are repeated to model the time evolution of the system. At each step of the loop, the system progresses through one time-step, Δt. The steps are presented in Figure 2.1.

These steps are carried out once the initialization step is done, at $t = 0$, and are repeated every loop.

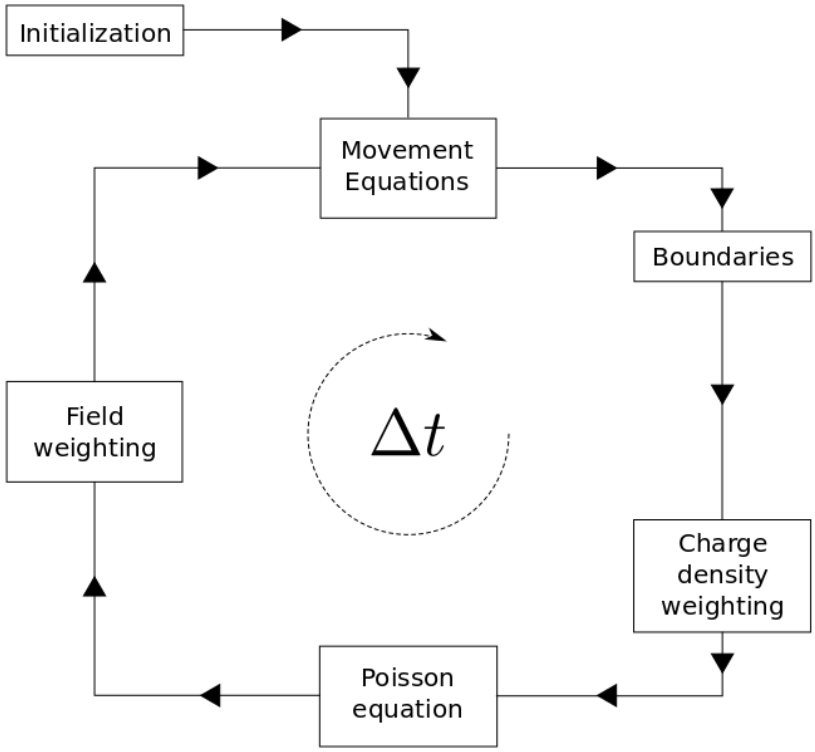

Figure 2.1 – The PIC method temporal loop [76].

— An *initialization step* where the simulation environment is defined: Allocation of arrays and vectors used for the simulation, initialization of the particle positions and velocities. This step is passed only once at the beginning of the simulation.
— An *integration of the equations of motion* where the particles are moved thanks to the equations of movement. Each particle (electron or ion) is moved for one time-step, Δt, obtaining its new position and velocity.
— A *boundaries* step where the particles are kept in the system. This can be by absorbing the particle when it reaches the system boundaries, re-injecting it periodically or after a bounce on the boundary.
— A *density weighting* where the charge density on each grid-point is obtained from the particle position.
— A step where the *Poisson equation* is solved, allowing the system to obtain the plasma potential, and thus the electric field at each grid-point, from the charge density.
— A step of *electric field weighting* where the electric field at the particle position is obtained from the value of the electric field on the grid.

As can be seen in the previous listing, the PIC method corresponds to a back and forth movement between the particles and the grid. A detailed description of each step for MiniPIC can be found in Section 2.1.3.

Operating conditions

Obviously as for every simulation model, the PIC method does have operating conditions. These operating conditions are based on PIC method characteristics as well as on properties of the modeled system. These conditions are listed below.

A first condition is on the value of q_f. Obviously this value cannot be too low for a dense plasma discharge in order to keep the computational time in a reasonable range, since a low value of q_f would mean a high number of particles modeled in the system. However in order to prevent any numerical effects, this value should stay low enough. As detailed above, it is chosen to set q_f so that the number of particles per grid-cell is never lower than 50.

The *Courant-Friedrichs-Lewy* condition, or CFL condition. which fixes the time-step, Δt, as a function of the spacing between grid-points, Δx and the maximum velocity attained by a particle during the simulation, $\max_i(V)$. The CFL condition is expressed by:

$$\Delta x < \Delta t \cdot \max_i(v) \tag{2.2}$$

This condition ensures an accurate following of the particle on the grid.

However in the simulations presented in this thesis, we only ensure the CFL condition for electron at the thermal velocity. Some electrons do travel faster than the CFL condition inside the system. Nonetheless their number is considered low in comparison to the electron population, and the time-step would be too small, increasing the computational time.

Another condition applies on the cell size. This is given by:

$$\Delta x \approx \lambda_{\mathrm{De}} \tag{2.3}$$

Where the Debye length, λ_{De}, has been defined in Section 1.4.1 by Equation 1.16. This is needed in order to properly model the plasma discharge behavior and its kinetic mechanisms, specially in a bounded plasma featuring sheaths. Indeed the Debye length being the scale over which significant deviations from quasi-neutrality can occur, the grid spacing has to be lower than this in order to capture these deviations.

Finally a condition applies on the time-step as a function of the electron plasma frequency (as defined in Section 1.4.1) and is given by:

$$\Delta t < \frac{0.2}{\omega_{\mathrm{p}}} \tag{2.4}$$

Indeed in order to properly model electron motion, the time-step has to be small enough to be able to capture the plasma oscillations. This is traditionally achieved by taking a factor 0.2 [76].

2.1.2 In-code normalization of physical values

In order to minimize the computational time needed to complete each time-step, the physical values are normalized. Thus the position (of grid-points as well as particles) and velocities are given by Equations 2.5 and 2.6.

$$x_{\mathrm{normalized}} = x_{\mathrm{physical}} \frac{1}{\Delta x} \tag{2.5}$$

$$v_{\mathrm{normalized}} = v_{\mathrm{physical}} \frac{\Delta t}{\Delta x} \tag{2.6}$$

Thus, this normalization naturally propagates to the normalization of the other physical values used in the model: Electric field, E, plasma potential, Φ, charge density, ρ, and the magnetic field, B. These normalizations are

given in Equations 2.7 to 2.10.

$$E_{\text{normalized}} = E_{\text{physical}} \frac{q\Delta t^2}{m_i \Delta x} \tag{2.7}$$

$$\Phi_{\text{normalized}} = \Phi_{\text{physical}} \frac{q\Delta t^2}{m_i \Delta x^2} \tag{2.8}$$

$$\rho_{\text{normalized}} = \rho_{\text{physical}} \frac{q\Delta t^2}{m_i \epsilon_0} \tag{2.9}$$

$$B_{\text{normalized}} = B_{\text{physical}} \frac{q}{m_i} \tag{2.10}$$

Where q is the elementary charge, m_i the ion mass, and ϵ_0 the vacuum permittivity. It is important to note that in this normalization scheme, it has been chosen to use the ion mass in order to normalize physical values.

This normalization allows a lower computational cost, as well as less rounding errors, through the simplification of the movement equations. Indeed these equations described in Section 2.1.3 are, thanks to the normalization, eased from unnecessary and computational costly multiplications.

2.1.3 Description of main subroutines

As described in Section 2.1.1 and Figure 2.1, the PIC method is based on temporal loops where at each time-step the same subroutines are called. As for the PIC method, operating conditions and normalization were described previously, now each step called in the PIC temporal loop are detailed.

In order to simplify the notations the values presented in the following are assumed to be normalized as described in Section 2.1.2 if not stated otherwise. Moreover the positions corresponding to the jth grid-point will be noted X_j, while the ith particle position will be noted x_i.

Density weighting

This step is used in order to obtain the charge density at each grid-point from the particle positions. This is done thanks to a linear interpolation. This cloud-in-cell (CIC) method is described in Figure 2.2 as well as in Equations 2.11 and 2.12.

$$\rho(X_j) = sign(q)(X_{j+1} - x_i) \tag{2.11}$$

$$\rho(X_{j+1}) = sign(q)(x_i - X_j) \tag{2.12}$$

Where sign(q) is dependent on the particle charge: positive if it is an ion, and negative if it is an electron. This density weighting is expressed using the normalized values defined previously in Section 2.1.2.

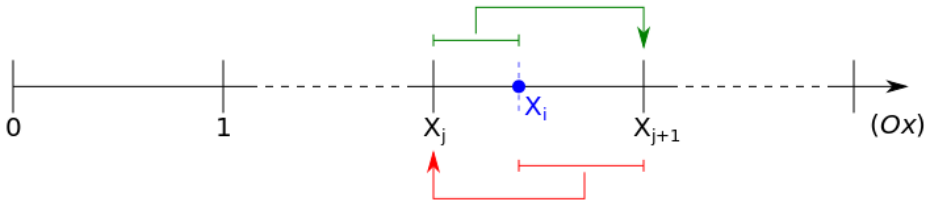

Figure 2.2 – The charge density linear weighting method, also called the Cloud-In-Cell (CIC) method [76], in one dimension.

Poisson equation

As described in Section 1.4.1, HETs are electrostatic devices. Thus the simulation tool MiniPIC is created to solve the Poisson equation, given in 2.13 in its unnormalized form. However this equation needs to be discretized thanks to a three points stencil and normalized as described in 2.14.

$$\nabla^2 \Phi_{\text{physical}} = -\frac{\rho_{\text{physical}}}{\epsilon_0} \tag{2.13}$$

$$\Phi(j-1) - 2\Phi(j) + \Phi(j+1) = \rho(j) \tag{2.14}$$

Where the values are expressed using the normalized expressions defined previously in Section 2.1.2.

In MiniPIC, the boundary conditions can be set as periodic or closed. The way in which this equation is set depends on the chosen boundary condition.

Periodic conditions means the cell $j = 0$ is equivalent to the cell $j = x_{\max}$. Thus $\Phi(0) = \Phi(x_{\max})$, but such a periodic system needs a reference potential. The needed value is the electric field on the grid, which is obtained from the potential gradient. Consequently any point of the grid can be considered as a potential reference. In MiniPIC it is chosen to follow [76] and use $\Phi(0) = \Phi(x_{\max}) = 0\text{V}$.

Closed boundaries corresponds to the case of metallic walls in MiniPIC. In this case, the potentials at $x = 0$ and $x = x_{\max}$ are those corresponding to the values on the electrode. In MiniPIC it has been chosen to keep the electrode placed at $x = 0$ grounded, while only

the electrode placed at $x = x_{\max}$ sees its potential varying. This variation is set-up as a sinusoidal variation so that at each time-step t, $\Phi(x_{\max}) = V_0 sin(\Omega t)$.

Knowing that the system is made of grid-points equally spaced from 0 to $x_{\max}$, and that $\Phi(0) = 0$V, the matrix form of this equation can then easily be obtained as detailed in Equation 2.15.

$$\begin{pmatrix} 2 & -1 & & & 0 \\ -1 & \ddots & \ddots & & \\ & -1 & 2 & -1 & \\ & & \ddots & \ddots & -1 \\ 0 & & & -1 & 2 \end{pmatrix} \begin{pmatrix} \Phi(1) \\ \vdots \\ \Phi(j) \\ \vdots \\ \Phi(x_{\max}-1) \end{pmatrix} = \begin{pmatrix} \rho(1) \\ \vdots \\ \rho(j) \\ \vdots \\ \rho(x_{\max}-1) - \Phi(x_{\max}) \end{pmatrix} \tag{2.15}$$

This matrix equation is solved using the well-known tridiagonal algorithm (or Thomas algorithm). Electric field is then obtained directly through a finite difference scheme. Normalization of the potential and electric field gives us the simplified Equation 2.17.

$$E_{\text{physical}} = -\nabla \Phi_{\text{physical}} \tag{2.16}$$

$$E(j) = \frac{\Phi(j-1) - \Phi(j+1)}{2} \tag{2.17}$$

Concerning the electric field estimation at the boundary, it depends on which boundary set-up has been chosen. In the case of a periodicity set-up, the periodicity of the system is used. Thus to obtain, for instance $E(x = 0)$ normalized, we have:

$$E(0) = \frac{\Phi(-1) - \Phi(1)}{2} = \frac{\Phi(x_{\max}-1) - \Phi(1)}{2} \tag{2.18}$$

Since $\Phi(-1) = \Phi(x_{\max} - 1)$ due to the system periodicity.

However in the case of a closed system, the electric field at the boundary is estimated thanks to a linear extrapolation. Thus to obtain the normalized value of $E(0)$, we have: $E(0) = 2E(1) - E(2)$, which is a coarse estimate, not taking into account the space charges present in the half cell centered in $x = 0$. This linear extrapolation method is a strong approximation, nevertheless it has been observed to offer a satisfying result in the case of a wall not emitting any secondary electron. The case of an emitting wall will be treated in Section 3.2.6.

Electric field interpolation

Once the electric field, E, is known at the grid-points, it is needed at the particle position. Thus for each particle the electric field value is linearly interpolated thanks to the same CIC method as for the charge density weighting, described in Section 2.1.3.

Integration of the equations of movement

The movement equations are summed up in Equations 2.19 to 2.21. The normalization plays its full role here. Indeed thanks to the normalization described in Section 2.1.2, these equations now limit the number of operations, rounding errors, and the computational time.

$$v_{\text{new}}^{\text{ion}} = v_{\text{old}}^{\text{ion}} + sign(q)E \tag{2.19}$$

$$v_{\text{new}}^{\text{electron}} = v_{\text{old}}^{\text{electron}} + sign(q)ME \tag{2.20}$$

$$x_{\text{new}} = x_{\text{old}} + v_{\text{new}}(i) \tag{2.21}$$

Where M is the mass ratio, so that $M = m_i/m_e$, sign(q) is the sign of the particle charge, and E is the electric field at the particle position.

It is important to note that the integration scheme is the leapfrog scheme described in [76]. This scheme introduces a shift of $\Delta t/2$ between the velocity and the position in order to reduce numerical noise. This is described in Figure 2.3.

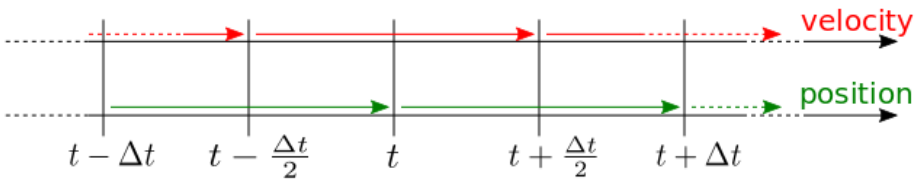

Figure 2.3 – The Leapfrog method [76]. Estimations of velocity and position are shifted in time by half a time step, i.e. $\Delta t/2$, in order to reduce numerical errors.

Boundary conditions

Finally once the particles have been moved to their new position, the boundary conditions of the system have to be applied. In MiniPIC, the

boundary conditions are periodic or closed. The boundary is placed at the cell center so that particles are modeled in a space defined from $x = 0$ to $x = x_{\max}$. Thus two methods are implemented as a function of the chosen boundary:

Periodic condition Particle positions are estimated Modulo $x_{\max}$. This is a consequence of the equivalence between the points $x = 0$ and $x = x_{\max}$ as defined in Section 2.1.3. Consequently a given particle positioned in $x = x_{\max} + a$ will be placed, thanks to the boundary condition, in $x = a$, with $a \in \mathbb{R}$.

Closed condition Every particle leaving the system (i.e. $x \leq 0$ or $x \geq x_{\max}$) is absorbed and removed from the model.

In the final 2D version of the simulation tool, LPPic2D, secondary electron emission processes are implemented. These physical effects correspond in the simulation tool to a certain boundary condition, where particles hitting the system are re-injected under certain conditions. These models are discussed in Section 3.2.

2.1.4 Unitary test cases

Some unitary tests were conducted, each testing one step of the temporal loop. Each of these unitary tests evaluated one functionality of the code, and most of them are taken from [78]. Those tests are used in any further development and implementation. In order to test the Poisson solver, a given density is imposed and the result is compared to the analytical solution. The boundary step as well as the integration of movement equations are tested by running a case with a single particle flying through the whole system. Finally both weightings are tested the same way: by initializing particles to a specific position and comparing the obtained potential with analytical expressions.

Once unitary tests are conducted for each step, a global test has to be run. Since the modeled system at this stage is simple and well-known test cases to verify the code's quality were easily identifiable. In order to check the code's reliability it was chosen to run a case where a two-stream instability was present. This two streams instability is highlighted in Figure 2.4, where a phase space vortex is present. This transitional episode is followed by the thermalisation of the plasma.

As a further verification, the temporal evolution of the system energies are plotted, including the kinetic, electrostatic, and total system energy. This is illustrated in Figure 2.5 where we can observe the temporal plots of the three energies. As expected the kinetic energy is at its maximum at the beginning

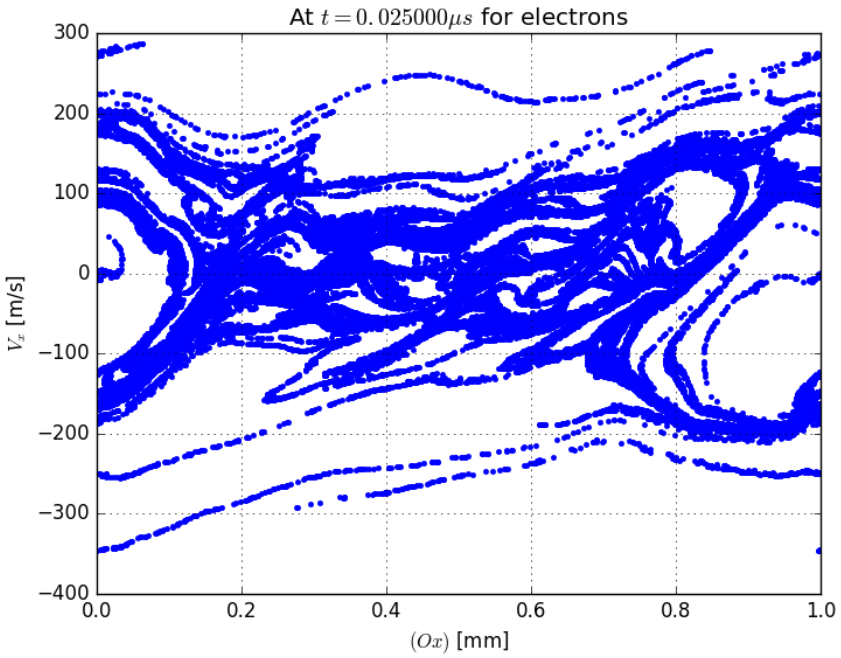

Figure 2.4 – Phase space ($v_x = f(x)$) for electrons inside the system at $t = 0.025\mu$s. As expected the typical form of a two-stream instability is observed.

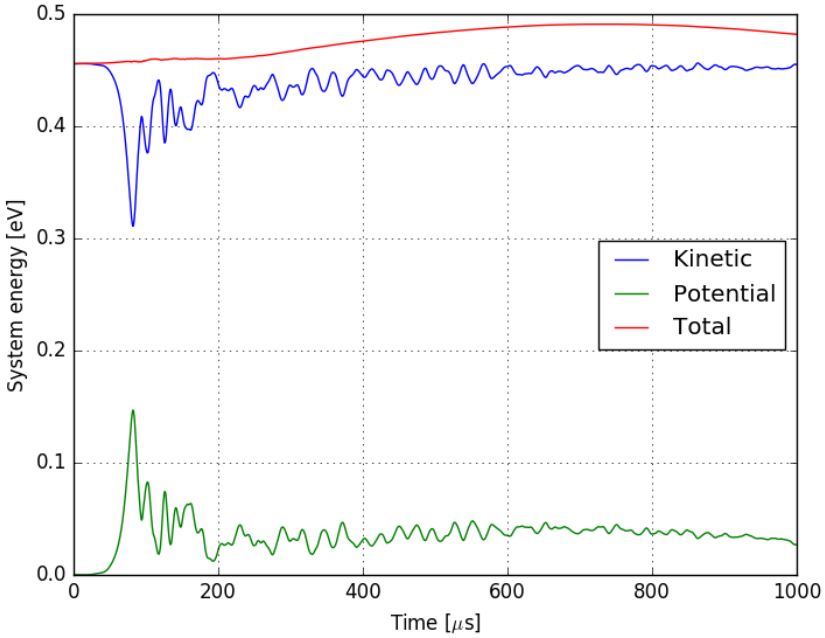

Figure 2.5 – Temporal evolution of energies in the system: (green) kinetic energy, (blue) potential energy, and (red) total system energy. The total energy is not perfectly conserved since velocities, needed to obtain the kinetic energy, and charge densities, needed to obtain the potential energy, are not estimated at the same time but are shifted of half a time-step due to the leapfrog method.

of the simulation, while the potential energy is null. This is followed by a transition phase where the kinetic energy of particles reaches its lowest level, corresponding to the highest level of potential energy. Finally the system reaches a stable state.

As detailed in Figure 2.5, the total energy is not perfectly conserved. Indeed a variation is observed while the system reaches a thermalized steady state. This is due to the fact that the potential energy is obtained from the electric field, while the kinetic energy is obtained from the particles velocity. Yet, as expressed in Section 2.1.3, the estimates of electric field and velocity are shifted in time by Δt. Consequently, while the potential energy is estimated at t, the kinetic energy is estimated in $t + \Delta t$, leading to a numerical error. By taking the average between v^{new} and v^{old}, as defined in Equation 2.19, this numerical error is lowered, and the total energy is then conserved.

However, it was chosen to highlight this specificity of the leapfrog method through Figure 2.5 in order to keep this in mind for later results in this work.

2.2 MiniPIC development: 1D-3V PIC/MCC

2.2.1 From 1D-1V to 1D-3V

Once MiniPIC had been verified in the previous Section 2.1, the particle velocities are changed to take into account the three dimensions. This means the particles are still only mobile along the (Ox) axis, but their velocities are expressed along the three dimensions. Thus, the particle energy is now allocated between the three velocity components.

This implementation is effected by changing the data structure of MiniPIC as detailed in Appendix A.

2.2.2 Monte Carlo collision (MCC) model

The Monte Carlo collision (MCC) module has to be inserted in the PIC temporal loop. This is done by inserting the model of collision events after the system boundaries check as illustrated in Figure 2.6.

The MCC module is used in order to model collisions between the neutral atoms, considered as a background, and the charged particles. Neither the collisions between charged particles nor recombination collisions are modeled in MiniPIC. This is chosen from the physical properties of HETs, as well as the CCP benchmark [75].

The "null collision" method

In order to keep the calculation time in a reasonable range, the MCC method used is the "null collision" method developed by [79] for isotropic collisions, and by [80] for anisotropic ones. In our case, anisotropic collisions are considered, and thus the method presented by [80] is used. In this method, only particles eligible to have a collision process during the time-step are followed, instead of the entire charged particle population. This allows for a significant gain in computational time for cases where a low fraction of particles have a collision, such as in the capacitive discharge modeled in [75], or the HET plasma discharge.

This is done by adding an artificial collision process, the so-called "null collision", to the other physical processes so that the sum of collision frequencies, ν' is constant as a function of the incident particle energy, ϵ_i. This is

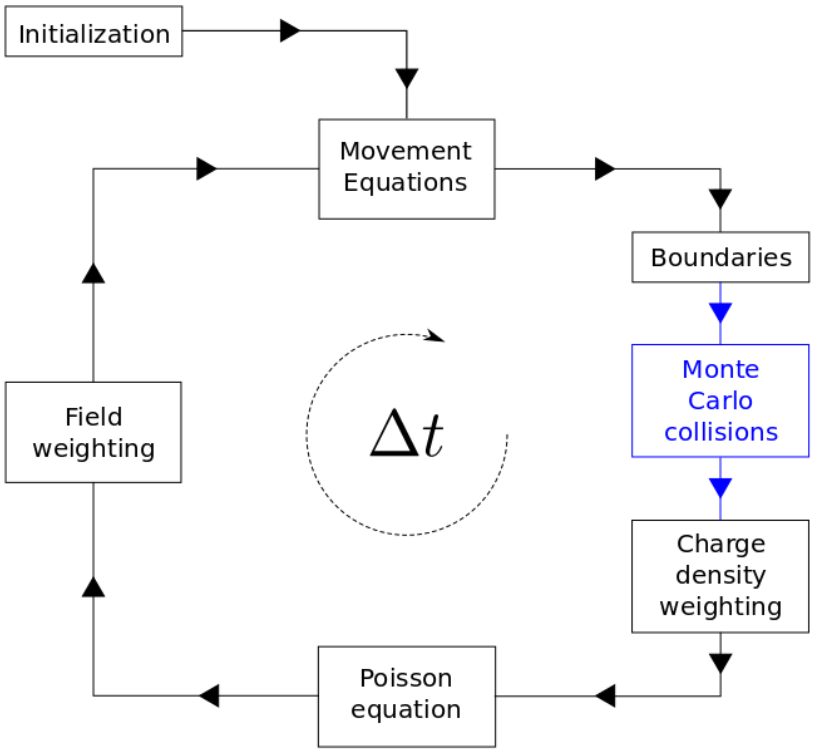

Figure 2.6 – Insertion of the MCC module (blue) in the PIC temporal loop.

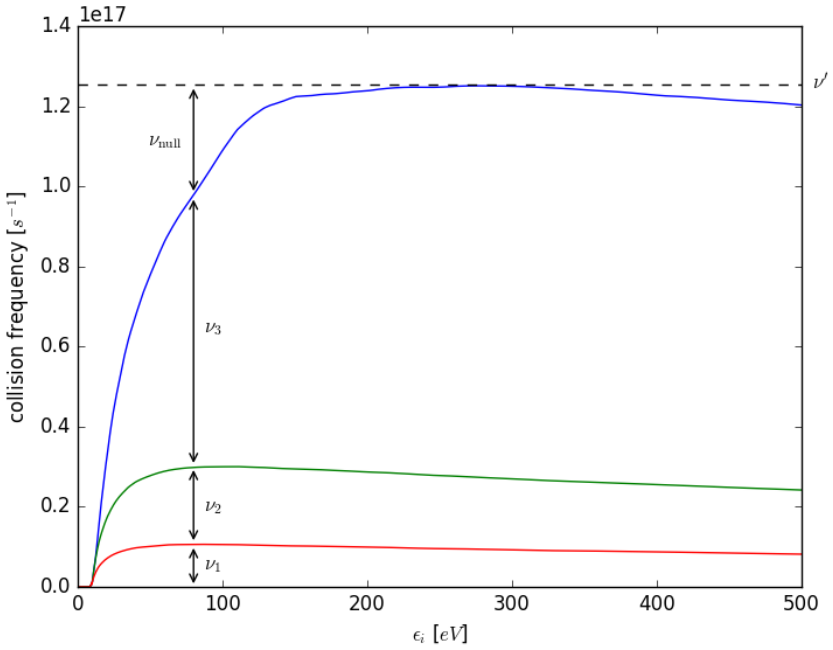

Figure 2.7 – Construction of the "null" collision as described in [80] for an imaginary gas.

mathematically summed up in Equation 2.22 and in Figure 2.7.

$$\nu' = max_{x,\epsilon}(n_g(x)\sigma_T(\epsilon)v_i) = n_g max_\epsilon(\sigma_T(\epsilon)v_i) \tag{2.22}$$

Where v_i is the relative speed between the target and the incident particles, and σ_T is the sum of the cross-sections from every collision process modeled. Since the neutral gas density is homogeneous and constant, this value can be removed from the max, and so the "null collision" consists of creating an artificial cross-section so that $max_\epsilon(\sigma_T(\epsilon)v_i) =$ constant.

Once the total collision frequency is constant by construction, the fraction of particles colliding during the time-step, Δt, can be estimated directly by:

$$P_{\text{null}} = 1 - exp(-\nu'\Delta t) \tag{2.23}$$

Noting $i_{\max}$ the total number of particles from one species, $P_{\text{null}} \cdot i_{\max}$ particles have to be chosen randomly in the system. This allows a gain in computation time since only a fraction of the particles are considered as eligible to have a collision event.

Once these particles are picked from the charged particle population, an integer, R, is randomly chosen from a uniform distribution defined between $[0, 1]$. Then the collision type is chosen as a function of R value, as detailed in Equations 2.24 to 2.26.

$$R \leq \nu_1(\epsilon_i)/\nu' \tag{2.24}$$

$$\nu_1(\epsilon_i)/\nu' < R \leq (\nu_1(\epsilon_i) + \nu_2(\epsilon_i))/\nu' \tag{2.25}$$

$$\vdots$$

$$(\nu_1(\epsilon_i) + ... + \nu_{\text{null}}(\epsilon_i))/\nu' < R \tag{2.26}$$

Where ν_{null} corresponds to the null collision frequency, and ν_k to the *kth* collision type frequency. Then if the particle is chosen to have a null collision, nothing happens.

Scattering velocity vector

Scattered velocity after the collision is defined using three angles: Θ, χ and Φ, as presented in Figure 2.8. Noting v_{inc} and v_{scat} respectively for the incident velocity and the scattered, these angles are defined by:

$$\cos\theta = v_{\text{inc,x}}/\sqrt{v_{\text{inc,x}}^2 + v_{\text{inc,y}}^2 + v_{\text{inc,z}}^2} \tag{2.27}$$

$$\sin\theta = \sqrt{1 - \cos^2(\theta)} \tag{2.28}$$

$$\cos\Phi = \cos(2\pi R_1) \tag{2.29}$$

$$\sin\Phi = \sin(2\pi R_1) \tag{2.30}$$

$$\cos\chi = 1 - 2R_2 \tag{2.31}$$

$$\sin\chi = \sin(\arccos(1 - 2R_2)) \tag{2.32}$$

Where R_1 and R_2 are random numbers taken from a uniform distribution defined on $[0, 1]$.

Following these angle definitions, the scattering velocity vector can be obtained from the incident velocity vector with:

$$v_{\text{scat}} = v_{\text{inc}}\ \cos\chi + v_{inc} \times \mathbf{i}\frac{\sin\chi\ \sin\Phi}{\sin\theta} + (\mathbf{i} \times v_{\text{inc}}) \times v_{\text{inc}}\frac{\sin\chi\ \cos\Phi}{\sin\theta} \tag{2.33}$$

In the case of an electron/neutral collision, the electron is considered to have a sufficiently high velocity compared to the neutral, and to be sufficiently light compared to the neutral, in order to consider the neutral as

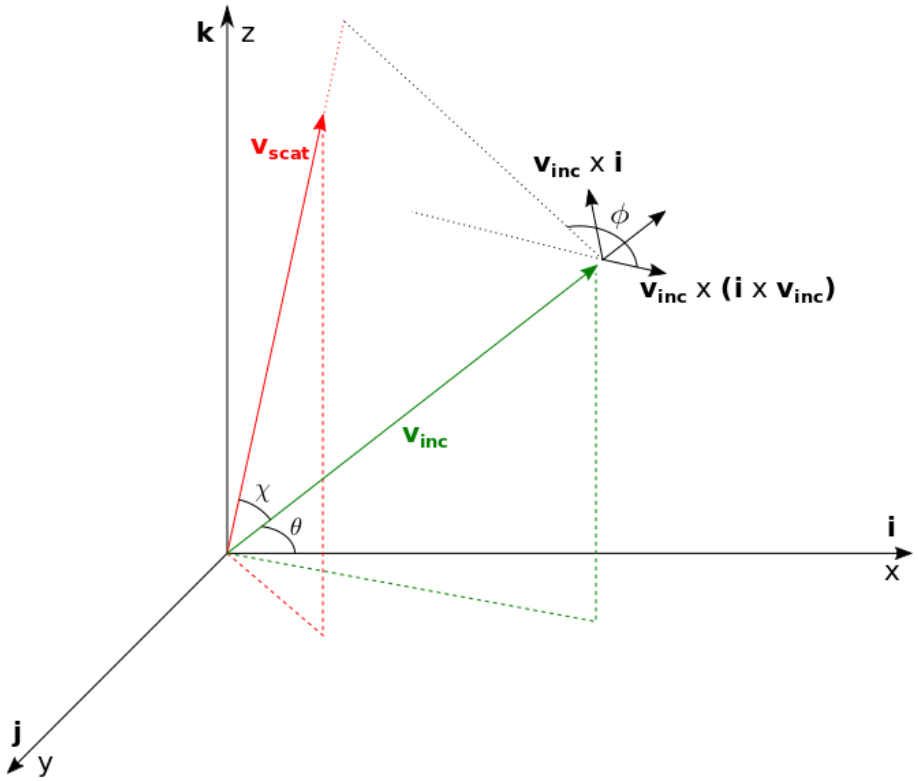

Figure 2.8 – Vector diagram for scattering collisions as described in [80]

immobile. Thus, the incident velocity of the electron is the electron speed in the laboratory frame. However, in the case of ion/neutral collision, the two colliding particles have comparable mass and velocities. Thus, a neutral particle is created from the homogeneous background, at the collision position. The ion/neutral collision is then considered in the neutral reference frame.

Moreover, during the collisional process an energy loss, $\Delta\epsilon$, has to be taken into account. In case of an elastic electron/neutral collision, it is dependent on the incident particle kinetic energy as given in:

$$\Delta\epsilon = \frac{2m_e}{m_i}(1 - \cos\chi)\epsilon_i \tag{2.34}$$

Similarly in the case of an elastic ion/neutral collision, the energy of the scattered ion, ϵ_{scat}, is obtained from the incident ion kinetic energy, ϵ_{inc} as detailed by Equation 2.35.

$$\epsilon_{\text{scat}} = \epsilon_{\text{inc}} \cos^2\chi \tag{2.35}$$

Where ion and neutral have the same mass, and χ is defined as the scattering angle in the laboratory frame.

For other electron/neutral processes, a fixed amount of energy, $\Delta\epsilon$, is retained from the incident electron in order to obtain the scattering electron kinetic energy. The value of $\Delta\epsilon$ is given by the chemistry of the given process (excitation or ionization).

Lastly, in case of an ion/neutral charge exchange process, the ion is given the velocity vector from the neutral created for the collision process.

2.2.3 Implementation and benchmarking in MiniPIC

The helium collision processes modeled in MiniPIC

The implementation of the MCC module in MiniPIC allowed us to benchmark it with a well-known capacitively coupled plasma (CCP) discharge, documented in [75]. This benchmark is not to be compared to the operating conditions of a HET. However the quality of its documentation make it suitable to test MiniPIC reliability on a global test.

This benchmark is designed to be run with helium. Thus a first set of reactions were implemented into MiniPIC using cross-sections from [75].

These reactions are:

$$e^- + He \rightarrow e^- + He \quad \text{(Elastic scattering)} \quad (2.36)$$
$$e^- + He \rightarrow e^- + He^* \quad (\epsilon = 20.61\text{eV, Singlet excitation}) \quad (2.37)$$
$$e^- + He \rightarrow e^- + He^{**} \quad (\epsilon = 19.82\text{eV, Triplet excitation}) \quad (2.38)$$
$$e^- + He \rightarrow e^- + He^+ + e^- \quad (\epsilon = 24.587\text{eV, Ionization}) \quad (2.39)$$

$$He^+ + He \rightarrow He + He^+ \quad \text{(Charge exchange)} \quad (2.40)$$
$$He^+ + He \rightarrow He^+ + He \quad \text{(Elastic scattering)} \quad (2.41)$$

Complementing this set of reactions, significant assumptions are made. First of all, the neutral gas, considered with a constant and homogeneous density, n_g, from the beginning, is stated to be kept at the same temperature, T_g. This means no heating of the neutral gas through collisions is modeled.

Secondly the meta-stable states are not followed in this model. Indeed the de-excitation processes are thought to have a much shorter temporal scale than the ones observed in the model.

Finally in the case of an electron/neutral collision, the neutral is considered to have a velocity more than one order of magnitude lower than the electron. Thus the neutral is considered immobile during the collision, an assumption reinforced by the mass ratio. This assumption cannot be made for ion/neutral collisions since neutrals and ions have comparable velocities and masses. Thus in the case of an ion/neutral collision a neutral is artificially "created" at the ion position. This neutral is initialized with velocities taken from a Maxwellian distribution at the neutral gas temperature, T_g. The algorithm used to generate Maxwellian distributions at a given temperature in order to initialize particles' velocities is detailed in Appendix A.3.

First verification of the MCC module quality

A first verification in order to check the MCC module quality consists of comparing the collision frequencies between analytical values and measurements from MiniPIC. Indeed the rate, $K_k(T)$, of the kth collisional process can be analytically estimated if we consider the incident particle distribution to be an isotropic Maxwellian at temperature T. Following [67], we obtain an analytical value of $K_k(T)$:

$$K_k(T) = \left(\frac{m}{2\pi k_\mathrm{B} T}\right)^{\frac{3}{2}} \int_0^\infty \sigma_k(v) v \exp\left(-\frac{mv^2}{2k_\mathrm{B}T}\right) 4\pi v^2 dv \quad (2.42)$$

Where m, v, and T are the mass, speed, and temperature of the incident particle (ion or electron). $\sigma_k(v)$ is the cross-section value of the kth process

for an incident particle having the speed v. Consequently we can obtain from the corresponding collisional cross-sections, the constant rates of each collisional process as a function of temperature.

Moreover the discretization of Equation 2.42 allows for us to write:

$$K_k(T) = \left(\frac{m}{2\pi k_b T}\right)^{\frac{3}{2}} \sum_{v=0}^{v_{\max}} \sigma_k(v) v \exp\left(-\frac{mv^2}{2k_b T}\right) 4\pi v^2 \Delta v \tag{2.43}$$

Where Δv is the discretization step, and $v_{\max}$ is the maximum velocity considered in the discretization. This $v_{\max}$ value has to be considered sufficiently high in order to properly solve the integral from Equation 2.42. Thus by covering a large range in T, we obtain an analytical value of $K_k(T)$

Since the constant rate is directly related to the collision frequency through:

$$K_k(T) = \frac{\nu_k(T)}{n_g} \tag{2.44}$$

It is possible to directly compare the collision frequencies since the neutral density, n_g, is a parameter in our model.

Thus we compare the results obtained analytically from Equation 2.43 to measurements from MiniPIC. Indeed, by loading in MiniPIC a significative amount of immobile particles (electrons or ions), and observing how many collisions from each collision type they encounter during one time-step, we can directly measure $\nu_k(T)$. Nonetheless the number of particles has to be sufficient in order to ensure reliable statistics. Moreover by changing the temperature of the Maxwellian, $\nu_k(T)$ can be obtained for a given range of T.

This method has been used for each gas used in MiniPIC, and later LP-Pic2D. For instance the comparison between measured collision frequencies and their analytical counterparts can be found in Figure 2.9 for xenon. A good agreement is observed from 5 to 300eV, validating the MCC module developed. Whereas at low frequencies, statistical noise is observed, at high energies (higher than 300 eV) a mismatch is observed in every cases. This is due to the fact that the cross-sections used are truncated for high energies. Thus, when integrating Equation 2.43, the contribution of high energetic electrons is neglected. While this is acceptable for low energy cases, in the case of high energies this neglecting is impacting the result.

Global benchmarking and verification of MiniPIC

Once the MCC module has been tested as detailed above, the global 1D CCP helium case [75] has been used to globally benchmark and verify

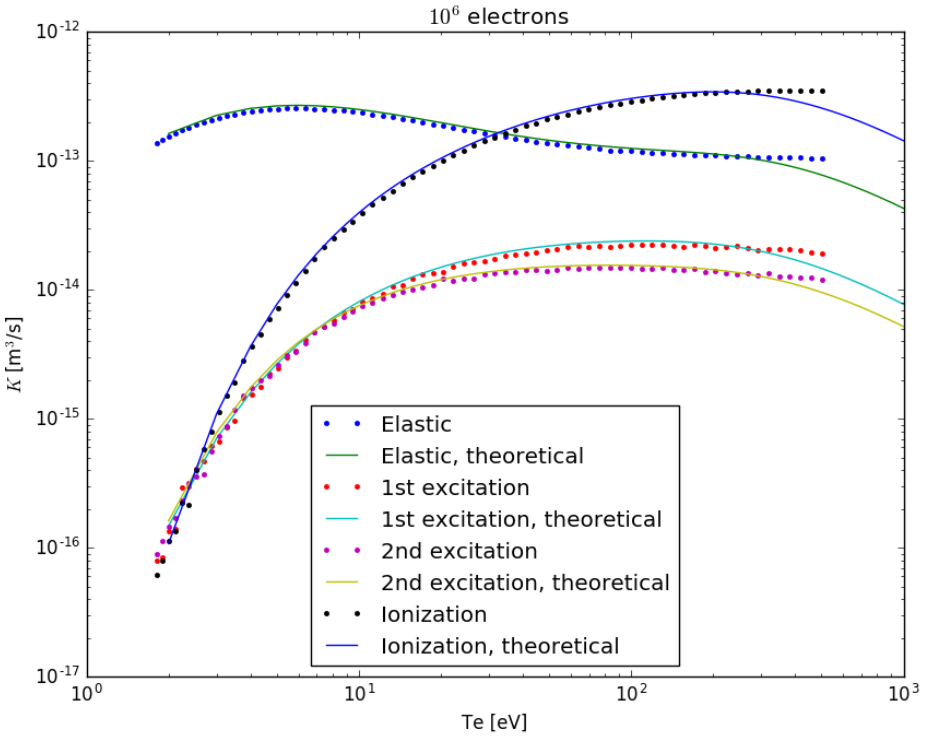

Figure 2.9 – Comparison between theoretical analytical frequencies (lines) [67] and frequencies calculated with MiniPIC MCC module ones (points) for electrons hitting Xenon neutrals. 10^6 electrons were used to count the collisions.

Table 2.1 – Simulation environment used for the first case of the CCP benchmark [75]

Physical Parameters		
Electrode separation	$L\,[cm]$	6.7
Neutral density	$n_{\mathrm{g}}\,[10^{20}m^{-3}]$	9.64
Neutral temperature	$T_g\,[K]$	300
Frequency	$f\,[MHz]$	13.56
Voltage	$V_0\,[V]$	450
Simulation time	$t_s\,[s]$	$1280/f$
Averaging time	$t_A\,[s]$	$32/f$
Physical constants		
Electron mass	$m_e\,[kg]$	9.109
Helium ionic mass	$m_i\,[kg]$	6.67
Initial conditions		
Plasma density	$n_0\,[10^{14}m^{-3}]$	2.56
Electron temperature	$T_e\,[K]$	30.000
Ion temperature	$T_i\,[K]$	300
Particles per cell	$N_{/C}$	512
Numerical parameters		
Cell size	$\Delta x\,[m]$	$L/128$
Time step	$\Delta t\,[s]$	$(400f)^{-1}$
Steps to execute	N_S	512.000
Steps to average	N_A	12.800

MiniPIC. In this system, MiniPIC has to model a one-dimensional plasma closed between two absorbing electrodes. One grounded, the other at a fixed sinusoidally varying potential, so that $\Phi(x = 0) = 0\mathrm{V}$ and $\Phi(x = x_{\max}) = V_0 \sin(\Omega_0 t)$. The other simulation parameters are summed up in Table 2.1.

In this benchmark, the simulation runs for some time-steps, N_S in total, and during the last N_A time-steps the output values are averaged and compared to the benchmark values. An example of such a comparison is presented in Figure 2.10.

Here only the parameters and results for the first case given in the CCP helium benchmark of [75] are presented. However this benchmark is comprised of four cases. Parameters and results of MiniPIC for the three other

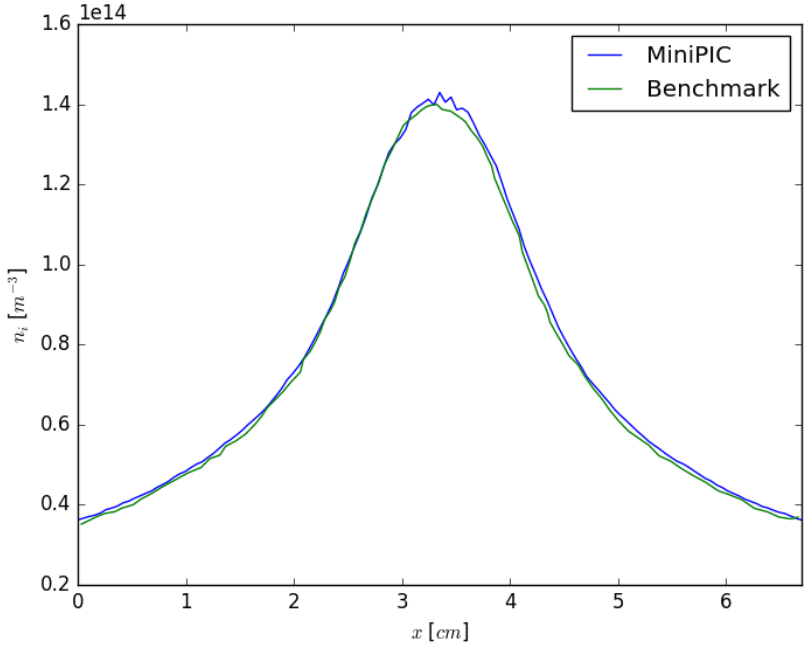

Figure 2.10 – Comparison between the results obtained with MiniPIC (blue) and the first test case of the benchmarks described in [75] (green). The ionic density, n_i, is represented as a function of the position, x, in the system.

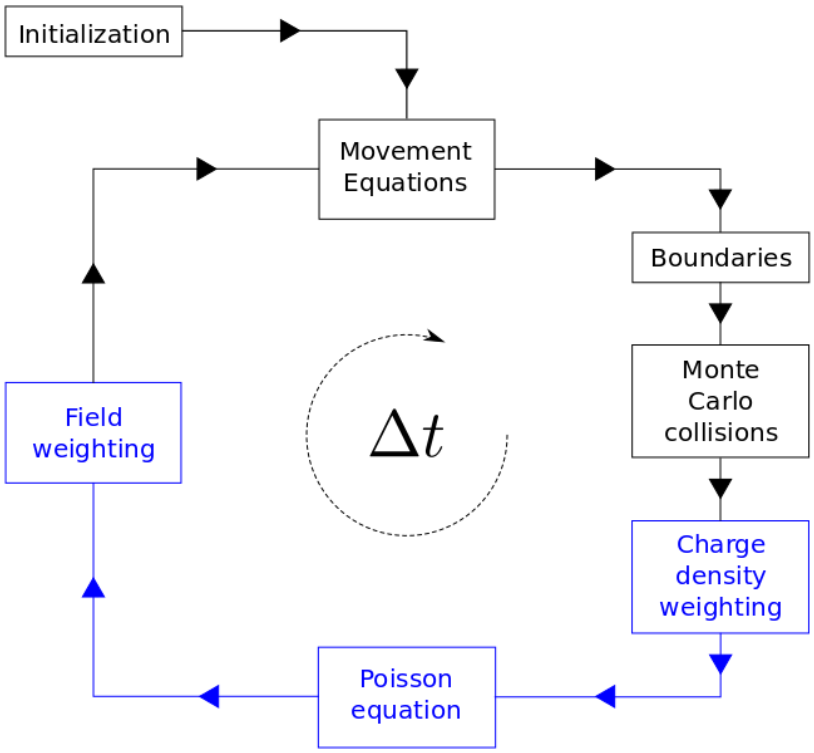

Figure 2.11 – The PIC method temporal loop [76]. In blue the subroutines that are significantly impacted by the 2D code extension.

cases are given in Appendix E.

2.3 LPPic2D Development: 2D-3V PIC/MCC

2.3.1 2D simulation model

Once MiniPIC has been developed and benchmarked, this simulation tool is extended in order to model a bi-dimensional system. This leads to changes in the data structure as well as in the algorithms used by the now named LPPic2D program. Indeed since particle positions are now represented by a couple of scalars and are evolving on a bi-dimensional grid, subroutines are changed. Subroutines impacted by the bi-dimensional extension of LPPic2D are marked in Figure 2.11.

First of all the Cartesian grid on which the particles are evolving is de-

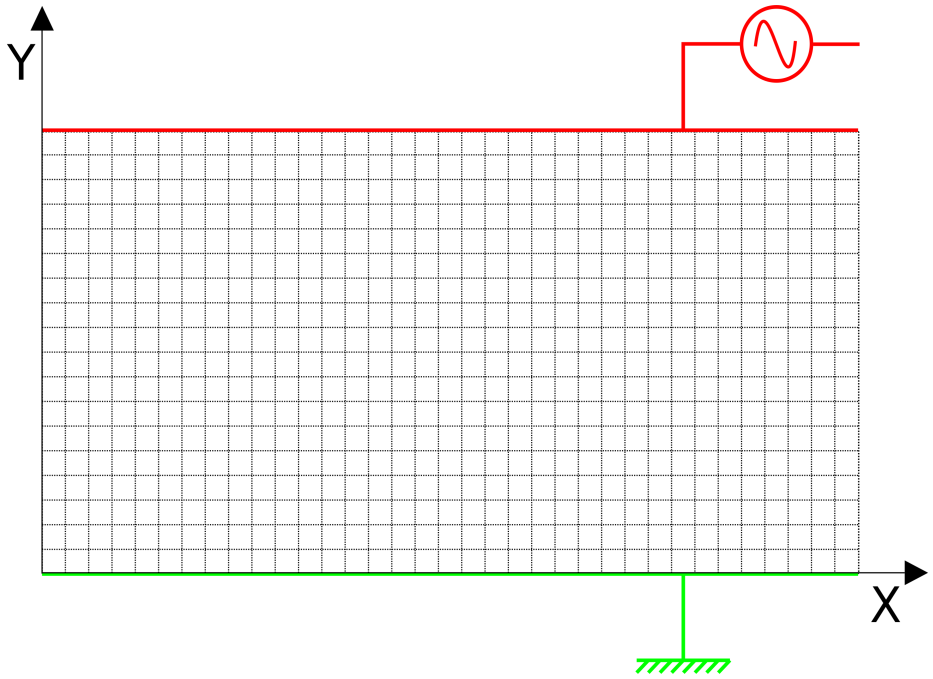

Figure 2.12 – The bi-dimensional system modeled by LPPic2D with its square Cartesian mesh. Periodic conditions are closing the system in the (Ox) direction, while absorbing metallic walls at fixed potentials are closing it in the (Oy) direction. One wall has a grounded potential (green) while the other sees its potential varying sinusoidally with time (red).

signed so that $\Delta x = \Delta y$. The mesh in LPPic2D is thus Cartesian, uniform and square. This will be conserved in the further developments of LPPic2D.

Furthermore in order to benchmark LPPic2D, the geometry modeled is chosen so that the given results can be compared to the one-dimensional CCP benchmark [75]. Thus periodic conditions are applied in the (Ox) direction, while absorbing metallic walls at fixed potentials ($\Phi(x = 0) =$ 0V and $\Phi(x = x_{\max}) = V_0 \sin(\Omega_0 t)$) close the (Oy) direction. The system geometry is detailed in Figure 2.12.

2.3.2 Modified subroutines

Minor changes

Some subroutines implemented in the LPPic2D tool needed a number of minor changes. First of all the equations of motion have now to be integrated

on the (Ox) axis as well as the (Oy) axis. Secondly, the boundaries are now to be taken in two directions since periodic boundaries close the system in the (Ox) direction, while absorbing walls close the system in the (Oy) direction.

Field interpolation and charge density weighting

For the interpolation of the electric field as well as for the charge density weighting, the algorithm now has to take rectangles into account instead of line segments. Since $\Delta x = \Delta y$ the charge weighting can easily be done as detailed in Equation 2.45 and Figure 2.13.

$$\rho(X_{j+1}, Y_j) = sign(q)\frac{(x_i - X_j)(Y_{j+1} - y_i)}{\Delta x^2} \tag{2.45}$$

The same algorithm for the charge weighting is used for field interpolation.

Solving Poisson's equation

The bi-dimensional Poisson equation has to be normalized thanks to the normalization detailed in Section 2.1.2, then discretized using a five point stencil. This leads to Equation 2.46. Then the electric field components can be obtained through a finite difference scheme as described in Equations 2.47 to 2.48.

$$\rho_{i,j} = \Phi_{i+1,j} + \Phi_{i-1,j} - 4\Phi_{i,j} + \Phi_{i,j+1} + \Phi_{i,j-1} \tag{2.46}$$

$$E_x(i,j) = \frac{\Phi_{i-1,j} - \Phi_{i+1,j}}{2\Delta X} \tag{2.47}$$

$$E_y(i,j) = \frac{\Phi_{i,j-1} - \Phi_{i,j+1}}{2\Delta X} \tag{2.48}$$

Where E_x and E_y represent the electric field in the (Ox) and (Oy) directions, and all values are normalized using the normalization scheme presented in Section 2.1.2.

In order to solve the Poisson's equation in the domain, the grid has to be labeled using the natural order. However, since the potential at the walls is fixed, the Poisson equation does not need to be solved at $y = 0$ and $y = y_{\max}$. Following the natural order we transform the matrix description

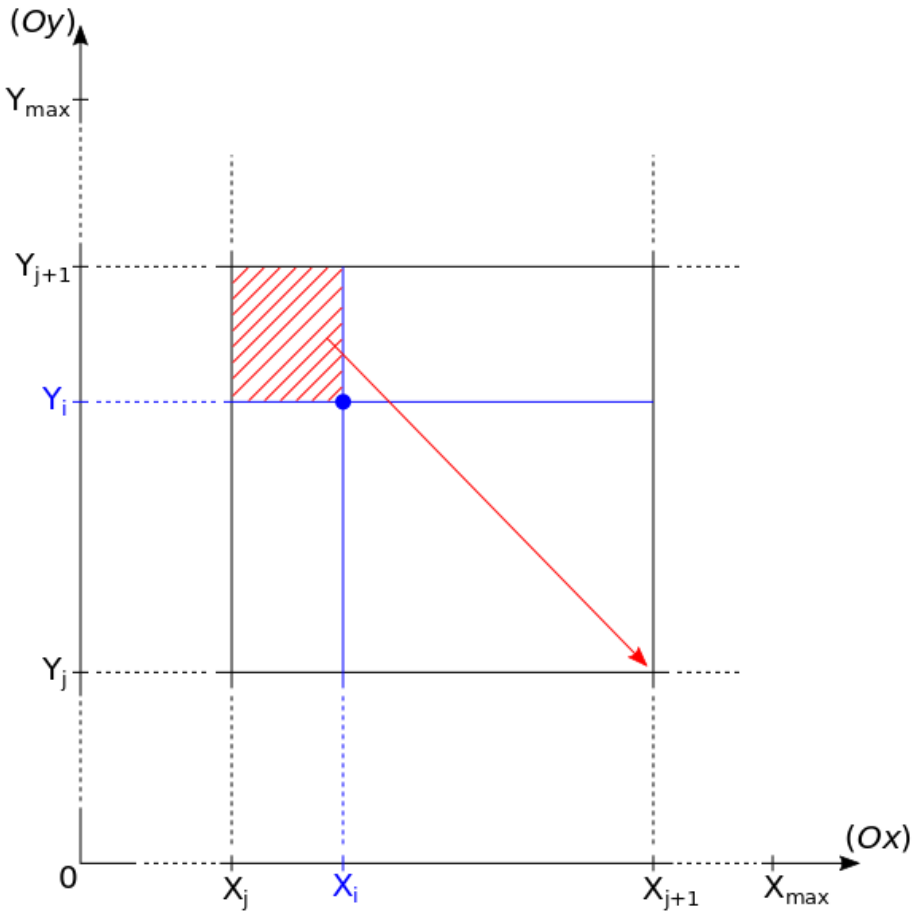

Figure 2.13 – Bi-dimensional CIC algorithm used in charge density weighting as well as field interpolation. The particle (blue) sees its charge allocated to each grid-point of the cell, proportionally to the opposing surface (red stripes).

of the potential on the grid, detailed in Equation 2.49:

$$\begin{pmatrix} \Phi(0, y_{\max}-1) & \cdots & \Phi(x_{\max}-1, y_{\max}-1) \\ & \ddots & \\ \vdots & \Phi(i,j) & \vdots \\ & \ddots & \\ \Phi(0,1) & \cdots & \Phi(x_{\max}, y_{\max}) \end{pmatrix} \tag{2.49}$$

in a vector, described in Equation 2.50:

$$\begin{pmatrix} \Phi(0) \\ \vdots \\ \Phi(m = i + 1 + (j-1)x_{\max}) \\ \vdots \\ \Phi(y_{\max}-1, y_{\max}-1) \end{pmatrix} \tag{2.50}$$

The same transformation is applied on the electric field matrix as well as on the coefficient matrix. This coefficient matrix is then constructed following the boundary conditions summarized in Equations 2.51 to 2.53.

$$\forall i, \Phi_{\text{new}}(i, y_{\max}-1) = \Phi_{\text{old}}(i, y_{\max}) - V_0 \sin(\Omega_0 t) \tag{2.51}$$

$$\forall j, \Phi(x_{\max}, j) = \Phi(-1, j) \tag{2.52}$$

$$\forall j, \Phi(x_{\max}+1, j) = \Phi(0, j) \tag{2.53}$$

Once these equations are posed, a library is called in order to solve it. In the sequential version of LPPic2D, the sequential library *MUMPS* [81] is used. In the later parallelized version of LPPic2D, *PetSc* [82] or *HYPRE* [83] are used. Comparisons in terms of performance between these libraries can be found in Appendix D.1, while their implementation is detailed in Appendix B.2.

2.3.3 High Performance Computing considerations

Because LPPic2D is a bi-dimensional PIC/MCC simulation tool, sequential architecture, working only on one single computational power unit (CPU), is not a viable solution anymore. In order to keep the computational time coherent with an operational functioning, LPPic2D needs to be structured and designed according to the latest standards.

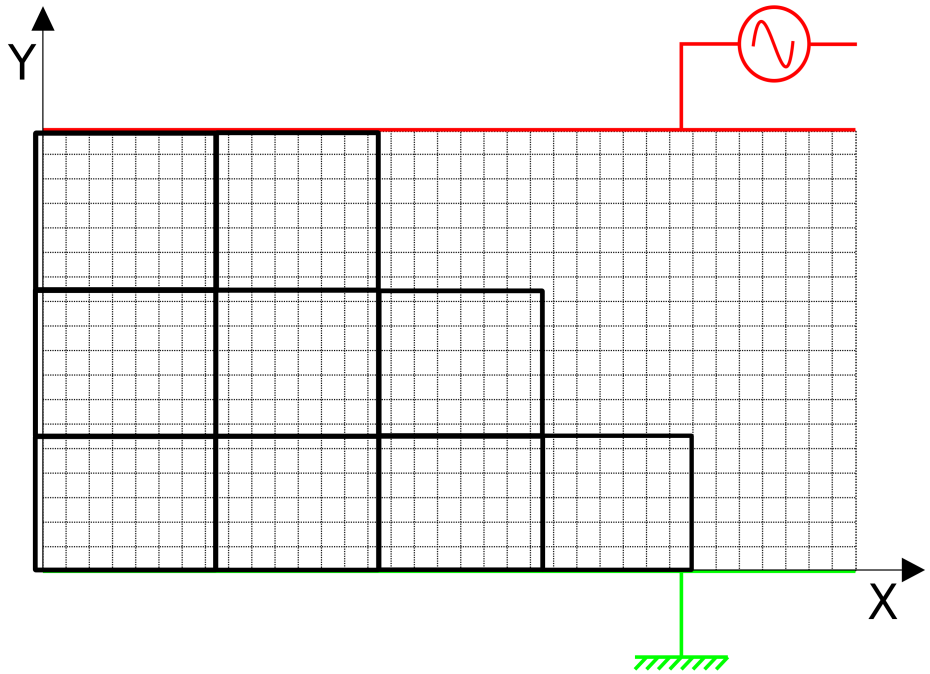

Figure 2.14 – Domain decomposition of the LPPic2D system in the CCP benchmark case [75]. Each CPU is responsible for the time evolution of its spatial domain (bold black line) [84].

These solutions used on LPPic2D are detailed in Appendix B. However the main principles have to be given here to understand the simulation environment related to the parallel version of LPPic2D.

Thus LPPic2D is parallelized using a "spatial domain decomposition" method [84] with a distributed memory scheme. Using the *MPI* library, each CPU models the evolution of one domain in the system as described in Figure 2.14.

In such a spatial decomposition, each CPU deals with its own memory space and communications between CPUs need to be explicit. In its memory we can find the particles that are in the domain at this moment, as well as grid values (plasma potential, charge densities,...) in the domain.

This spatial decomposition is one of the most intuitive parallelization available for PIC codes (to be compared to "particle decomposition methods" where each CPU deals with all the geometrical system but only with a given fraction of particles). However exchanges between CPUs need to be efficiently designed. These exchanges concern two types of data:

Particles that are exchanged between CPUs when, due to their movement, particles move from one domain to another. All the information concerning the particle needs to be transferred from one CPU to another efficiently. Thus a particle exchanger is designed and implemented in the integration of motion equations subroutine. Details about this particle exchanger are given in Appendix B.3.

Grid data that are exchanged in order to fill the so-called "ghost-cells" at the domain boundary. Indeed, in order to compute the electric field at the domain boundary, the CPU needs to know the value of the plasma potential in the neighbor cells. This is detailed in Figure 2.15 as well as in Appendix B.4.

Moreover, the parallelization of LPPic2D impacts the solving of the Poisson equation since the libraries chosen need to be able to efficiently use the parallel environment available. Multiple parallel libraries exist and two were successfully interfaced with LPPic2D: *PetSc* [82] and *HYPRE* [83]. Performance comparisons can be found in Appendix D.1.

Finally the parallelization required the implementation of output compatible with the parallel structure of the code. Indeed to obtain diagnostics about the system modeled by LPPic2D, a set of diagnostics was implemented as detailed in [85]:

Global values These are used to follow in time some global values about the behavior of the modeled system: number of macro-particles, number of collisions,...

Grid values These are bi-dimensional arrays used in order to follow in time the physical values at each grid-point: charge density, electron density, collision density,...

Individual particles This diagnostic is used in order to follow in time a set of individual particles and thus trace individual trajectories.

Collective particles A certain number of particles from every CPU is output from the code. This allows post-processes like energy distribution functions, phase spaces,...

Every N_A time-steps these diagnostics are called, and output files are created. The combination of those files allow us to follow the system behavior in time. In order to create efficiently, and in a parallel way these output files, the *HDF5* library [86] is used. Concerning the three first diagnostics, the output values are not "snapshots" from the simulation at a given time-step. Indeed, in order to lower the noise level due to the PIC simulation, the diagnostics output every N_A time-steps are averaging all the physical values output over

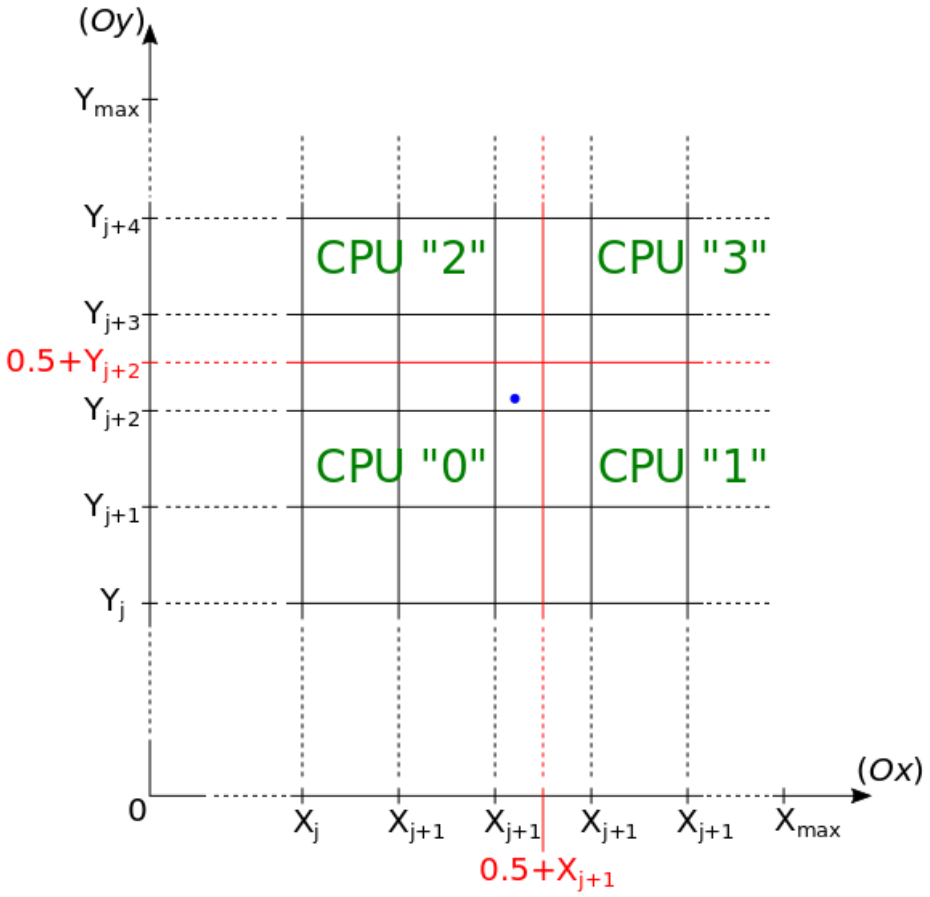

Figure 2.15 – Interface (red) between four CPU domains (green). The interface is placed at the cell interface (at $x_j + 0.5$ in normalized values), thus particle (blue) near the interface needs the electric field value in the neighbor domain to integrate the equations of motion.

the past N_A time-steps. Obviously this averaging is not applied to collective particle diagnostics.

Although this spatial decomposition choice seems one of the most intuitive to implement, some important limitations are present:

— In the presence of some load unbalance (due to a certain domain in the simulation having too many macro-particles to model in comparison with the other ones) the global performance of the code is impacted. In order to overcome this limitation, multiple methods are possible: Merging/splitting algorithms [87, 88], or an *OpenMP/MPI* hybridation [89]. However, due to the complexity of these solutions, they were not implemented on the final version of LPPic2D.

— The scalability limitation to solve the Poisson's equation leads to a limitation in the number of CPUs that can be efficiently used. Scalability studies of LPPic2D can be found in Appendix D.2.

2.3.4 Benchmarking and verification of LPPic2D

The extension of LPPic2D to a 2D-3V geometry does not impact significantly the model. Indeed, only the solving of the Poisson equation is substantially modified, while the linear CIC scheme is expanded in a natural way. However, the algorithmic foundations are deeply impacted by this extension. As a matter of fact, the extension of 1D-3V MiniPIC into a performant 2D-3V LPPic2D simulation tool can only happens thanks to the implementation of high performance computing (HPC) methods. Otherwise the calculation time needed for simulations would prevent us from a flexible and efficient use of LPPic2D.

HPC considerations can be found in Section 2.3.3, as well as in Appendix A.1, B, C, and D. Despite a performant and flexible use of available computational power, these methods drastically increase the complexity of the code. Consequently it is more than ever needed to test each implementation in LPPic2D, to ensure sufficient reliability and quality.

This has been done thanks to unitary tests from [78]. Yet, if these unitary tests allow a proper testing of precise subroutines and functions inside the code, a global benchmark is needed to ensure the correct operation of the simulation tool. This has been done using the geometry given in Section 2.3.1 as well as the CCP helium benchmark from [75]. Indeed, the use of periodic boundaries allow us to model in a 2D geometry this 1D benchmark.

As for MiniPIC, LPPic2D gave correct answers for the Helium benchmarks [75], and was consequently considered as reliable for further development.

2.4 Conclusion

This Chapter is devoted to the development description of a generic 2D-3V PIC/MCC simulation tool. Starting from scratch, a simplified periodic 1D-1V set-up, called MiniPIC, allowed us to verify the code reliability through the modeling of a two stream instability. This provided us a sound basis for the further development of a collisional 1D-3V version of MiniPIC. We were able to verify this latter collisional version thanks to a well-documented helium CCP discharge benchmark [75], allowing us to further secure the code reliability and quality.

Once MiniPIC has been developed and tested, this simulation tool is extended into a 2D-3V PIC/MCC simulation tool, called LPPic2D. As for MiniPIC, the set-up of an adapted geometry has allowed the verification of LPPic2D through a generalized version of the 1D-3V CCP discharge benchmark [75], as well as through numerous unitary tests [78]. Nevertheless, the geometrical extension of MiniPIC to 2D has come with a significant increase of the code complexity. Indeed, the computational burden related to 2D simulations is significant, if used for geometries comparable to a HET channel. Therefore deep developments were made in order to overcome this computational load through the use of modern HPC clusters. These clusters are efficiently used thanks to heavy parallelization and third party libraries.

The development of LPPic2D from scratch to a 2D-3V PIC/MCC simulation tool able to model a helium CCP discharge case has provided us with a healthy, reliable, and efficient code, that now needs to be adapted to the specificities of modeling the HETs exit plane along the $r - \theta$ directions.

Chapter 3

Specific model development: From a generic 2D-3V PIC/MCC model to simulations of Hall effect thrusters (HETs)

Contents

3.1 The 2D HET model development

3.1.1 The "infinite radius" HET model

As described in Section 1.2, wall materials play an important role in HET behavior and performances [19, 25, 32, 27, 37]. However, the formation of a strong instability in the azimuthal direction seems to play an important role that has been highlighted both empirically and numerically [53, 90, 54, 55, 56]. Although the respective roles and mechanisms of those two processes will be discussed later on in Chapters 4 and 5, it is decided to model the $r-\theta$ plane of the HET in order to be able to observe and study both the wall effects and the azimuthal instability.

As the modeling of the totality of the $r-\theta$ plane seems out of reach for a non-scaled PIC simulation tool, it is decided as well to only observe a "camembert slice" of the thruster as detailed in Figure 3.1.

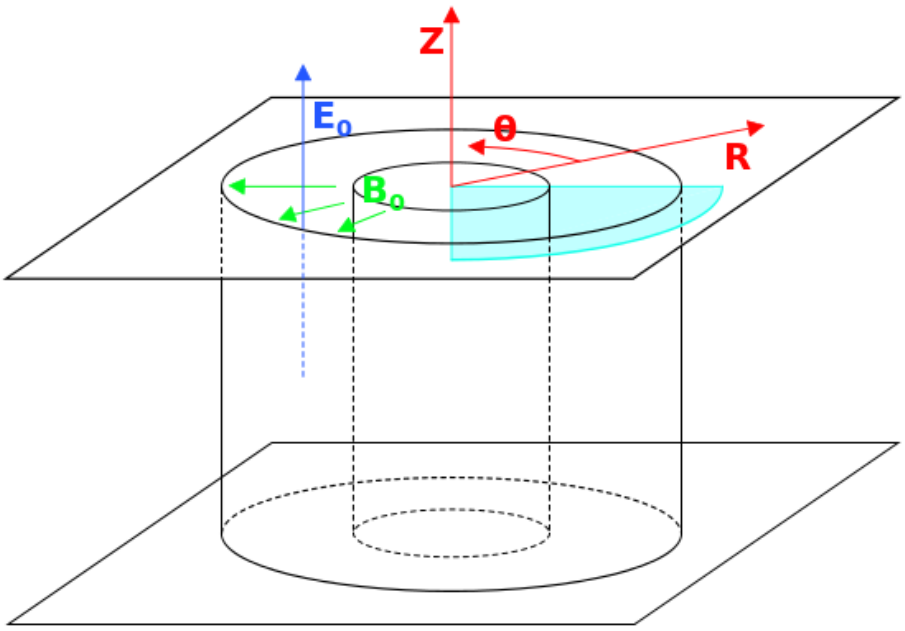

Figure 3.1 – Simplified scheme representing a HET discharge channel: (light blue) the modeled domain is a slice in the $r-\theta$ plane, (dark blue) the constant axial electric field, (light green) the constant magnetic field, and (red) the cylindrical coordinates.

Since the electron drift instability features a wavelength of the order of

mm [13, 73, 42], the assumption is made that the curvature of the discharge channel can be neglected. As the simulation code developed in this work does not attempt to model simulations predicting the thruster performance and behavior, but try to have a glance at the physics governing the thruster. Furthermore, numerical studies [42] have shown that the curvature effect does not play an important role for channel radii usually used in large to very large HETs (typically in the order of tens of centimeters).

Thus, the considered HET is then defined as having an infinite radius. The simulation domain becomes a rectangle, closed in the r direction by dielectric walls, and periodic in the θ direction. This allows us to directly use the LPPic2D tool with the geometry detailed in the previous sections.

Moreover the Cartesian coordinates system can be kept, with (Oy, Ox, Oz) corresponding to the cylindrical coordinates (r, θ, Oz). In order to keep the notation system clear and avoid confusion, if not stated otherwise, Cartesian coordinates will be used from now on in the following sections and chapters.

To sum up, the infinite radius HET model, or so-called "infinite HET" model corresponds to:

— A Cartesian mesh with squared cells ($\Delta x = \Delta y$)
— Closed walls in $y = 0$ and $y = y_{\max}$
— Periodic boundaries in $x = 0$ and $x = x_{\max}$
— A constant and uniform magnetic field, B_0, along the Oy axis
— A constant and uniform electric field, E_0, along the Oz axis

To this model, characteristics features and processes will be added to correspond to the HET behavior.

3.1.2 Modeling a magnetized plasma

The first modification of LPPic2D consist to implement the possibility to model a fixed magnetic field imposed on the electrons. This is firstly done by adding the magnetic field in the field interpolation, in order to obtain the value of the magnetic field at the particle position, in the case where the magnetic field is not uniform. Secondly the integration of the equations of motion has to be changed for the electrons in order to take into account the magnetic force on their trajectory. Since the magnetic field is considered constant and only along the (Oy) axis, the Boris scheme is used to integrate the equations of movement for the electrons [91].

This scheme does a decomposition of the integration of the equations of motion into three separate steps. First a half acceleration phase, described

in Equation 3.1

$$v_k(t') = v_k(t - \frac{\Delta t}{2}) + sign(q)\frac{E_k(t)}{2} \tag{3.1}$$

Where the values are normalized according to Section 2.1.2 and $k = x, y$. Then as a second step a rotation detailed in Equation 3.2.

$$\begin{bmatrix} v_x(t'') \\ v_z(t'') \end{bmatrix} = \begin{bmatrix} \cos(\omega_c \Delta t) & \sin(\omega_c \Delta t) \\ -\sin(\omega_c \Delta t) & \cos(\omega_c \Delta t) \end{bmatrix} \begin{bmatrix} v_x(t') \\ v_z(t') \end{bmatrix} \tag{3.2}$$

With $\omega_c = \frac{qB_0}{m_e}$ (B_0 and q being arithmetical values). And finally a last half acceleration given by Equation 3.3.

$$v_k(t + \frac{\Delta t}{2}) = v_k(t'') + sign(q)\frac{E_k(t)}{2} \tag{3.3}$$

With $k = x, y$, and $t - \frac{\Delta t}{2} < t^{'} < t^{''} < t + \frac{\Delta t}{2}$.

Ions not being magnetized, as detailed in Section 1.2, no modification is needed on their side. Finally, this implementation is tested by following in time the trajectory of a single electron in a constant and uniform magnetic field, allowing a simple measurement of its Larmor radius, defined in Section 1.2.4. This is illustrated by Figure 3.2.

3.1.3 The "fake" Oz length

The orthogonal electric field

Starting from the model described in the Section 3.1, in order to model properly a HET, a magnetic field, B_0, along the (Oy) axis, must be imposed, as well as an electric field, E_0, along the (Oz) direction. While the magnetic field, B_0, acts inside the simulation plane, $(Ox - Oy)$, the electric field imposed along the (Oz) axis is orthogonal to it.

In order to take into account the effect of this orthogonal electric field, E_0, particle positions and velocities are tracked in all three dimensions: (Ox), (Oy), and (Oz). Whereas the applied electric field in the (Oz) direction is arbitrarily imposed in the system (constant in space and time), the electric field in the simulation plane is obtained self-consistently by solving Poisson's equation. Consequently, in order to get the charge densities needed to solve Poisson's equation, the particles are all weighted to the same 2D $(Ox - Oy)$ grid using the CIC scheme described in Section 2.1.3 regardless of their position along (Oz). This means densities are estimated using the projections of the particles along (Oz) on the $(Ox - Oy)$ simulation plane. Moreover, as

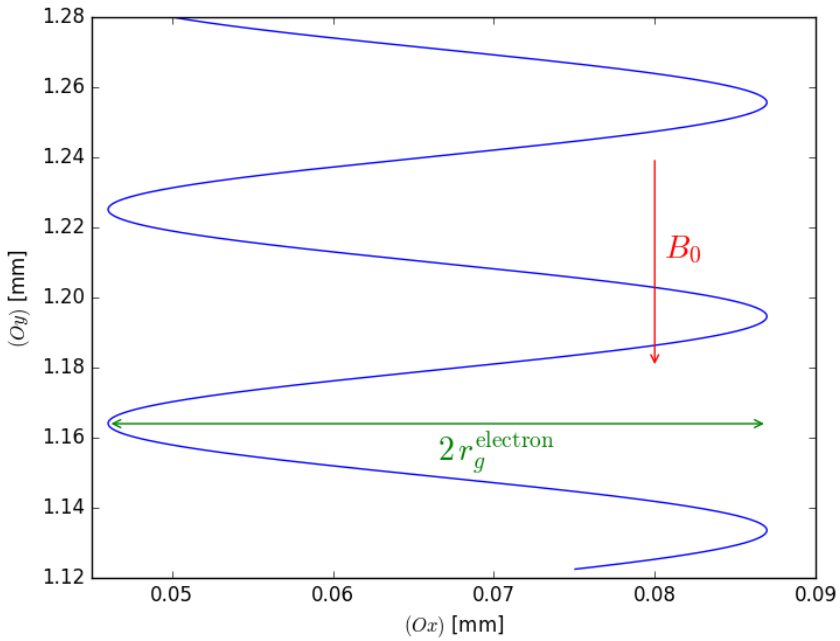

Figure 3.2 – Trajectory of a single electron (blue) in a constant and uniform magnetic field (red), $\mathbf{B}_0$, along (Oy) as observed in the $(Ox - Oy)$ plane in LPPic2D. The Larmor radius (green), r_g^{electron}, is observed, and its comparison to analytical value allows us to verify the reliability of the particle pusher for magnetized electrons.

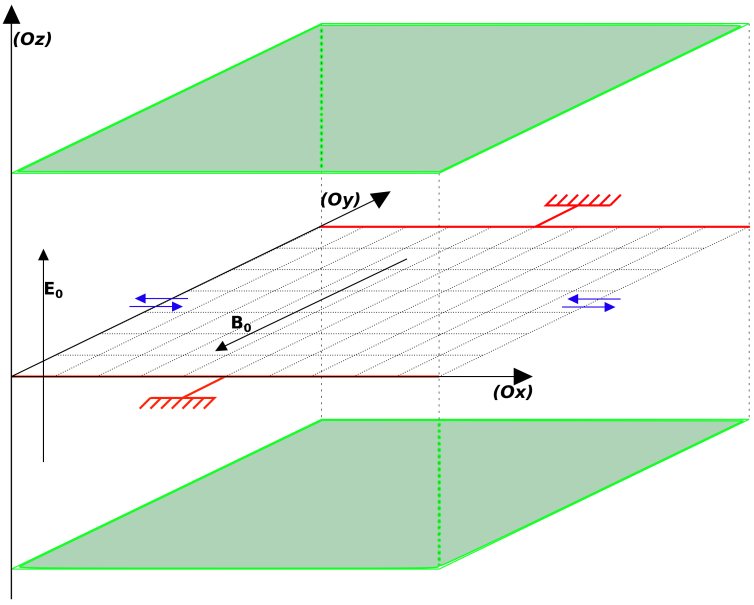

Figure 3.3 – System modeled by LPPic2D in order to simulate the plasma discharge in a HET without dielectrics: (red) the two grounded walls, (blue) the periodicity along the (Ox) axis, and (green) the closed planes at $z = 0$ and $z = z_{\max}$. The closed planes in (Oz) can be removed, leading to the modeling of a case with $L_z \mapsto \infty$.

the Poisson equation is only solved inside the 2D $(Ox - Oy)$ plane, the PIC operating conditions, such as the *CFL* condition, detailed in Section 2.1.1, do not need to be met along the (Oz) direction.

In order to solve Poisson's equation in the $(Ox - Oy)$ simulation plane, periodic conditions are used in the (Ox) direction, while grounded metallic walls are used in the (Oy) direction. (Oz) direction can be either infinite or finite, with closed boundaries at $z = 0$ and $z = z_{\max}$. The obtained geometry is described in Figure 3.3.

The diverging $L_z \mapsto \infty$ case

Closing the (Oz) direction is needed because an infinitely long system along (Oz) $(L_z \mapsto \infty)$ would lead the charged particles to be constantly accelerated by the applied electric field, E_0. Indeed, the modeled system would not reach a steady state due to a constant input of energy. Figure 3.4 confirms that, for $L_z \mapsto \infty$, the mean energy diverges rapidly to non-physically high values (not respecting the CFL condition detailed in Section

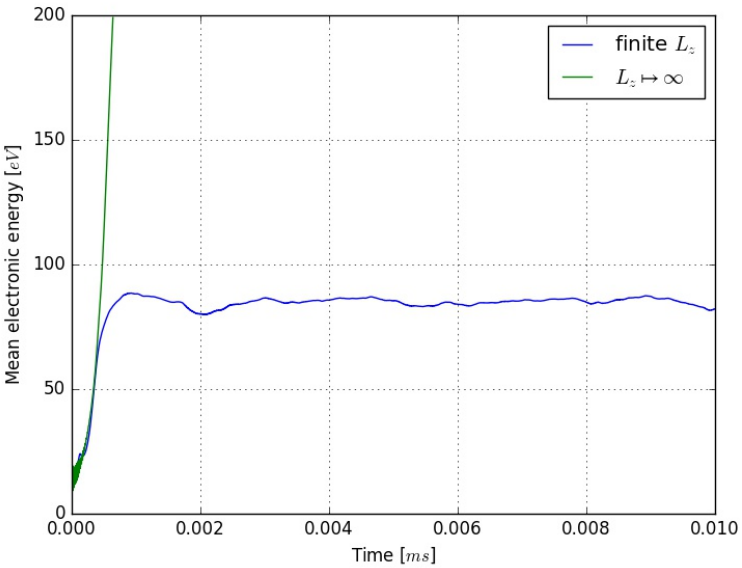

Figure 3.4 – Time plot of the electron energy averaged over the entire electron population in the system for: (green) $L_z \mapsto \infty$, (blue) $L_z = 1\,cm$. No collisions are modeled, and the system lengths used are: $L_x = 0.5$cm and $L_y = 2$cm.

2.1.1) within less than $1\,\mu$s.

Such set-up was used by [42], and while it allowed for a first insight into the electron drift instability, it could not model the system on long timescales due to this divergence of the mean electron energy. Consequently, the instability could not be studied for more than a few oscillation periods.

The stable finite L_z case

Generalizing a solution proposed for 1D simulations [74, 68], L_z is set to a finite value in order to allow the modeled system to reach a steady-state. The value for the axial length is chosen to be $L_z = 1$ cm in order to repeat the conditions used in the previous 1D simulations in [68] and [74]. This distance is also representative of the length of the acceleration zone in a HET [4].

In this case, ions which cross the (Oz) boundaries are replaced by new ions (with the initial ion temperature of $T_i = 0.1$ eV) injected at the entrance ($z = 0$). Whilst electrons which are lost the same way are replaced by new electrons (at the initial electron temperature of $T_e = 5$ eV) injected at the exit plane ($z = z_{\max}$). In this way the number of particles followed by the

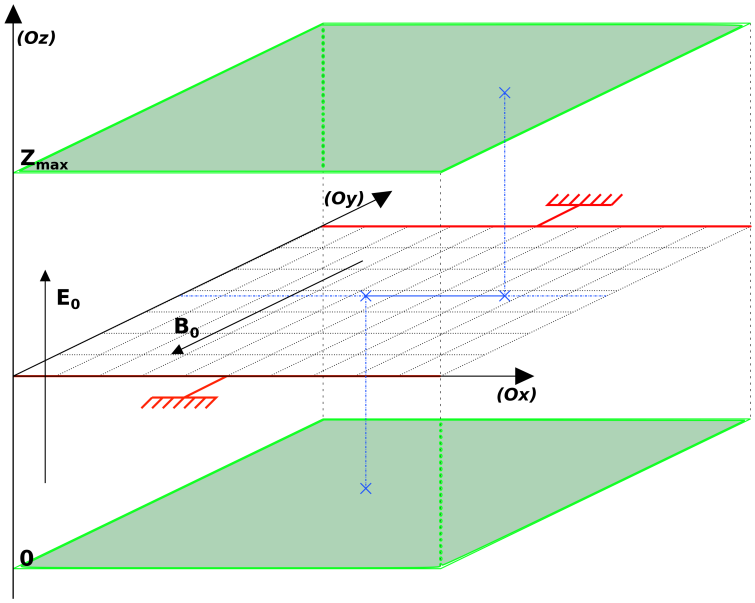

Figure 3.5 – Injection process in LPPic2D when L_z is set to a finite value: (blue) particles are injected with a random position along (Ox) but keep the same (Oy) position

simulation remains constant if losses at the walls are neglected. Still particles injected in this manner are injected with a random position along (Ox) but keeping the same (Oy) position, otherwise the sheaths are prevented from correctly forming (since new "thermalized" particles could be loaded in the sheath). This injection process is detailed in Figure 3.5.

For the same conditions as the simulation using $L_z \mapsto \infty$, but with $L_z = 1.0\,\text{cm}$, Figure 3.4 shows that the simulation reaches a steady-state within about $1 - 2\,\mu\text{s}$.

Indeed this 2.5D-3V simulation set-up mimics the real thruster geometry, with electrons being injected at the exit plane and ions being injected from the anode at the bottom. Furthermore it allows a loss of energy through the re-injection of particles having been accelerated by $\mathbf{E}_0$ before leaving the system from the (Oz) boundary, and then re-injected with their initial temperature. It is this loss of energy which allows the system to reach a steady state.

Ion transit time oscillations

In some cases with a finite L_z, a low frequency oscillation can be observed during the steady state. This fluctuation has a frequency of approximately 0.5 MHz and seems to be related to the finite length in the (Oz) direction. Indeed, when collisions are turned off, ions injected at $z = 0$ need a certain transit time to reach $z = z_{\max}$. Since the mean ion velocity along (Oz) is approximately $10^4\,\mathrm{ms}^{-1}$ and $L_z = 1.0$ cm, we can estimate a transit time of 10^{-6} s. This means that most of the ion population is "renewed" with a frequency of 1 MHz, which is close to the low frequency fluctuation observed.

In order to confirm this observation, we have replaced the constant acceleration of ions by the applied E_0 field, by a constant ion velocity along (Oz) (i.e. the electric field for the ions has been turned off and they have been given a constant drift along (Oz)). We have checked that, with a constant value of $v^z_{ions} = 10^4\,\mathrm{ms}^{-1}$, results are similar to those obtained before. With a much higher initial velocity of $v^z_{ions} = 10^5\,\mathrm{ms}^{-1}$, we have observed that the frequency of the low-frequency oscillation is now increased (due to the reduced ion transit time across the axial simulation dimension). These results are not presented for the sake of clarity and brevity.

As this oscillation is related to the ion transit time along L_z, it can be attenuated by initializing the particles (ions+electrons) with a velocity along (Oz), taking into account the acceleration due to the constant electric field along (Oz), E_0. Indeed, instead of initializing all the ions at the same temperature from a Maxwellian distribution, the velocity along (Oz) of each ion is obtained from a Maxwellian distribution, but the acceleration corresponding to its z position is added. This is what has been done in Figure 3.4 where the oscillation is particularly attenuated.

Numerical artifacts and self-consistency

As detailed in one-dimensional similar simulations [68], the value of L_z has a significant impact on the plasma discharge behavior. This can be highlighted by varying the value of L_z or L_x. While the unstable modes propagating along (Oy), that are allowed to develop in the system, are set by the L_x length, varying the value of L_z tends to affect the temporal evolutions of these modes. Thus for some combinations of lengths, $L_x - L_z$, it is observed that, after the simulation has reached an equilibrium, a transition occurs, changing the frequency and wavelength of the dominant azimuthal mode of the simulation. The importance of the $L_x - L_z$ combination on the plasma discharge behavior is illustrated in Figures 3.6 and 3.7, where only L_x is varied between 0.5 cm and 1 cm, while L_z is kept constant with $L_z = 1.0$ cm.

When $L_z \mapsto \infty$, before the system diverges, as already detailed by Figure 3.4, oscillations of the plasma potential are observed to grow and saturate as already highlighted [42]. In Figure 3.6, where for $L_x = 0.5$ cm and $L_z = 1.0$ cm, the oscillations grow and saturate, showing a behavior similar in frequency and wavelength to the $L_z \mapsto \infty$ case (before it diverges) presented in [42]. This behavior features a propagating mode, already observed in numerous numerical studies modeling HETs along the $r - \theta$ [73, 42] or the $z - \theta$ [40], and corresponding to the electron drift instability (EDI), which is detailed in Chapter 4.

In contrast, Figure 3.7 shows, for $L_x = 1.0$ cm and $L_z = 1.0$ cm, a turbulent transition between two oscillation regimes, with a first behavior characterizing the first microsecond, followed by a turbulent transition to a slower mode. We believe this turbulent transition to be a numerical artifact due to the too small value of L_z, and to the fact that the electric field along (Oz) is not self-consistently obtained from the particle positions, but is imposed and fixed. Indeed, the convection mechanisms of particles along the (Oz) direction are not properly modeled in our simulation set-up.

For a given L_x, by comparing the case with $L_z \mapsto \infty$ (before it diverges) and the case with a finite L_z, it is possible to prevent the appearance of what we consider as an artifact of the model. Thus the choice of the combination of $L_x - L_z$ is an empirical process, where for each L_x chosen, L_z has to be chosen in order to obtain instability characteristics comparable to the case where $L_z \mapsto \infty$ (before it diverges).

Moreover, in order to better understand the way the plasma discharge behavior is impacted by the choice of the $(L_x - L_z)$ couple, various simulations were conducted with different values for L_x and L_z ($L_x \in [0.25, 0.5, 1.0, 2.0]$ and $L_z \in [0.25, 0.5, 1.0]$). This is summed up in Figure 3.8 where we observe that when L_z is too small in comparison to L_x the slow, artificial mode is observed, while for a large enough L_z the EDI mode is featured. Thus, for each L_x, a minimal L_z exists, L_z^{min}, for which, if $L_z < L_z^{min}$, the artifact mode is observed. Indeed, as already exposed, as the convection along (Oz) is not self-consistently solved but imposed by the simulation parameters, for a too small L_z the convection mechanism is observed to be stronger than the wave propagation, thus disabling the fast modes and enabling numerical modes, as observed in the simulations. Nevertheless, further studies should be required in order to better quantify the value of L_z^{min} as function of the simulation parameters, and in particular its relation to L_x.

The limitations of the 2.5D-3V set-up described in this section are inherent to the model. However this method allows the plasma discharge to reach a steady state, mimicking a third dimension. Only real 3D-3V simulations with a self-consistently solved electric field along (Oz) could properly

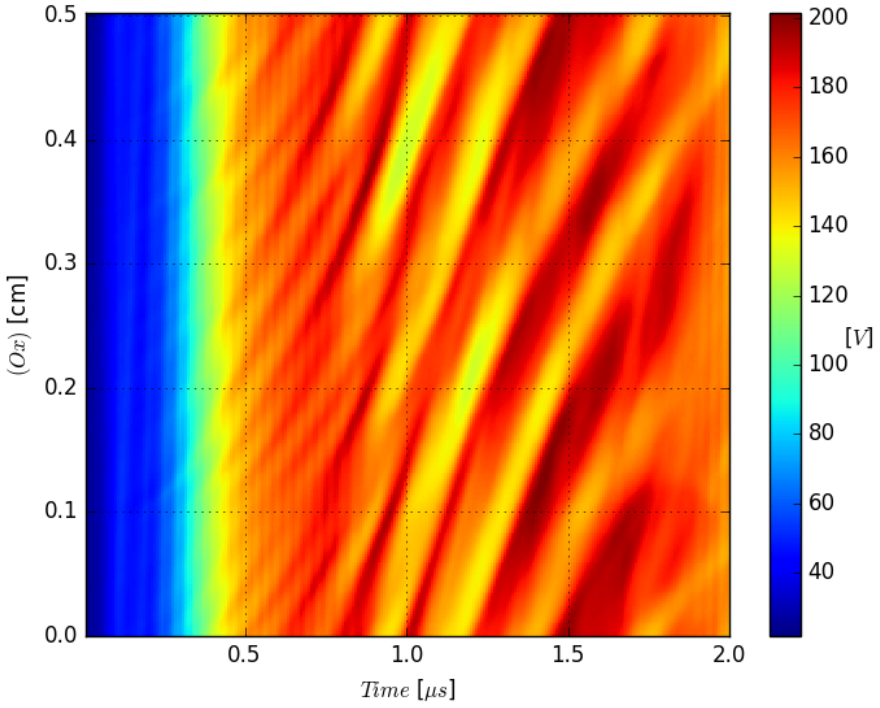

Figure 3.6 – Temporal evolution of the plasma potential taken along (Ox) at $y = L_y/2$, with $L_y = 2$ cm and $L_z = 1$ cm, and $L_x = 0.5$ cm, without any collision process. We observe a stable grow ans saturation of the instability, comparable to the beginning of the case where $L_z \mapsto \infty$ (before it diverges) and to other simulations of the EDI.

model the instability convection. However, as highlighted in Section 1.5, fully kinetic 3D models of HETs are nowadays complex to achieve and operate.

This "fake" (Oz) length is a feature, detailed in [92], added to LPPic2D in order to be a parameter that can be set to different values. However, in the following cases L_z will be fixed at the value identified as properly modeling the electron drift instability. Consequently, in the following work, and if not stated otherwise, we use the values of $L_x = 0.5$ cm, $L_y = 2.0$ cm, and $L_z = 1.0$ cm, as summed up in Table 3.3, in Section 3.4.

3.1.4 Compensating losses at the walls

The $(Ox - Oy)$ simulation plane is closed by grounded walls in the (Oy) direction. Particles are absorbed by these walls if no secondary electron

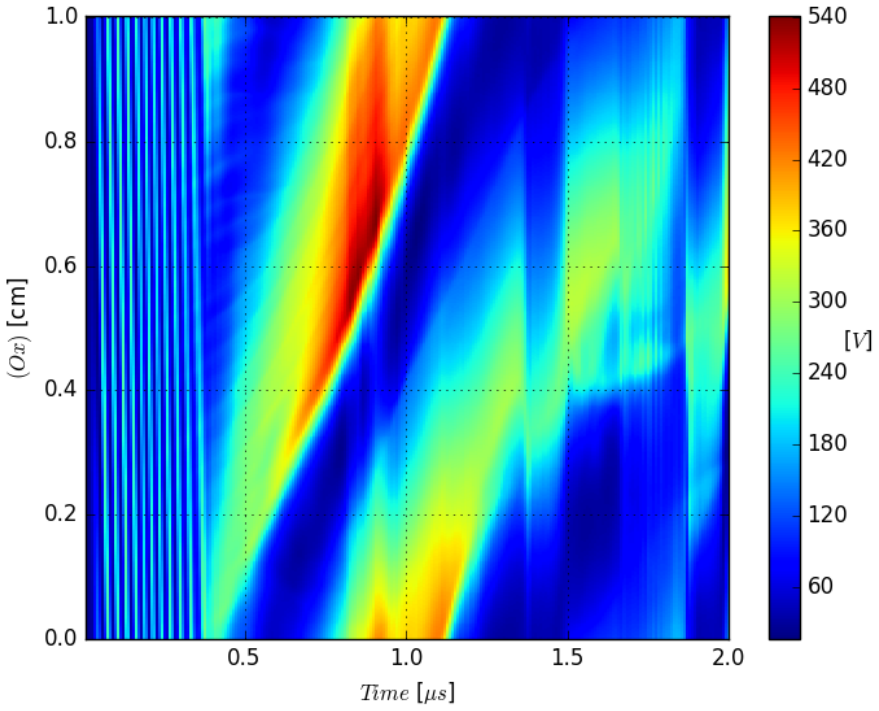

Figure 3.7 – Temporal evolution of the plasma potential taken along (Ox) at $y = L_y/2$ with $L_y = 2$ cm and $L_z = 1$ cm, and $L_x = 1$ cm, without any collision process. We observe a turbulent transition not comparable to the $L_z \mapsto \infty$ case before its divergence.

emission process is modeled. However, in order to keep the number of macro-particles in the system relatively constant at steady state, some of these absorbed particles have to be re-injected. This is needed since the axial electric field and the axial boundary conditions (porous anode at $z = 0$ and hollow cathode at the exit plane, at $z = z_{\max}$) are not self-consistently solved.

This is done by tracking the number of ions and electrons having hit the walls during the preceding time-steps, represented as $\mathscr{N}_{ions}^{absorbed}(t)$ and $\mathscr{N}_{electrons}^{absorbed}(t)$. At the end of the time-step, the number of particles to be re-injected, $\mathscr{N}_{couples}(t)$, is estimated as:

$$\mathscr{N}_{couples}(t) = \min(\mathscr{N}_{ions}^{absorbed}(t), \mathscr{N}_{electrons}^{absorbed}(t)) \tag{3.4}$$

These couples are then uniformly re-injected back into the system. New couples are loaded at the same position uniformly in the system with the

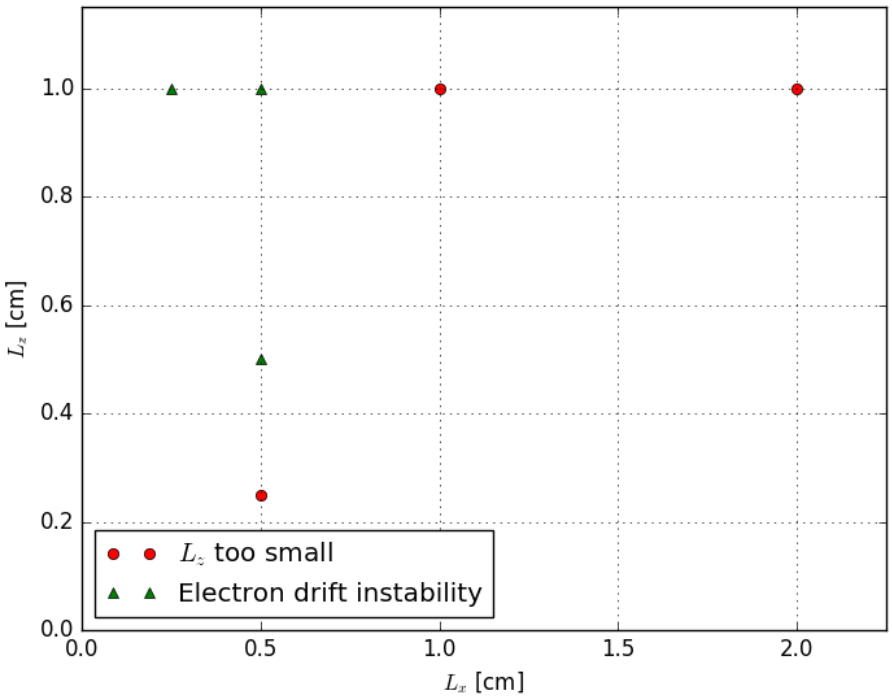

Figure 3.8 – Simulations conducted with various L_x and L_z: (red circle) simulations with a too small L_z, (green triangle) simulations featuring an EDI.

initial temperatures ($T_e = 5\,\text{eV}$ and $T_i = 0.1\,\text{eV}$). In order to take into account unpaired particles that have been absorbed by the walls, we have:

$$\mathscr{N}_{ions}^{absorbed}(t+\Delta t) = \mathscr{N}_{ions}^{absorbed}(t) - \mathscr{N}_{couples}(t) + \mathscr{N}^{absorbed}(t, t+\Delta t) \quad (3.5)$$

where $\mathscr{N}^{absorbed}(t, t+\Delta t)$ is the number of ions having hit the walls between t and $t+\Delta t$. The same process is done with the electrons.

These unpaired partners thus allow a charge imbalance to exist in the simulation, and hence for sheaths at the walls to form. This procedure is similar to that used in the 2D PIC simulations in [40], despite our simulation code uses indifferently grounded metallic walls or floating dielectrics. As a test, by setting $E_0 = B_0 = 0$ and grounded metallic walls, a sheath forms with a plasma potential of about $5-6\,T_e$, as expected from standard floating sheath theory [93].

The counting of particles is done globally on every cell of both walls, based on the assumption that the walls are metallic. Thus, it allows for the

possibility of internal wall currents. This assumption is not valid if floating dielectric walls are modeled. This will be treated in Section 3.3. In the same way, the counting has to be changed if secondary electron emission (SEE) processes are implemented in the model, as described in Section 3.2.

3.1.5 Electron temperature

The electron temperature, T_e, measured in the simulation, is obtained from the mean electron energy, ϵ_e, since $\epsilon_e = 3/2kT_e$. A plot of the temporal evolution of ϵ_e in the case of $L_z \mapsto \infty$, and in the case of $L_z = 1$cm, is given in Figure 3.4. As already detailed, the use of a finite L_z value allows the instability to saturate, thus enabling modeling of the plasma discharge on longer time-scale.

The value at which the electron energy stabilizes after some micro-seconds is obtained self-consistently from the simulation parameters. However, since the electric field along the (Oz) axis is not obtained from the charge density along (Oz), but arbitrarily imposed, the value of T_e is not resulting from the energy flux in the (Oz) direction.

Moreover the temperature is not observed to be isotropic. Indeed by observing the values of the electron energy in all three directions, as in Figure 3.9, we observe that they stabilizes at sensibly different levels. Thus the electron temperature is observed to be anisotropic.

This difference between the electron temperature, or energy, parallel to the magnetic field, $T_{e_{//}}$, and the one perpendicular to it, $T_{e_\perp}$, has already been highlighted in numerous studies [73, 42, 11].

Nonetheless this steady-state value of T_e needs to be estimated from the simulation parameters, at least grossly. This can be done considering the power balance in the (Oz) direction, and making some simplifying assumptions. First we make the hypothesis that $T_{e_{//}} = T_{e_\perp}$. Secondly we consider the electrons to have a Maxwellian distribution, although some previous works have shown that it is not the case in HETs [42]. Finally the energy losses by collisions are considered to be negligible in comparison to other losses in the system, as it will be highlighted through simulation results in Section 4.2.1.

Using these assumptions, the electron flux at the walls, $\Gamma_{e,w}$, is obtained from:

$$\Gamma_{e,w} = \int_{-\infty}^{\infty} v_x f(\mathbf{v}) d^3\mathbf{v} \tag{3.6}$$

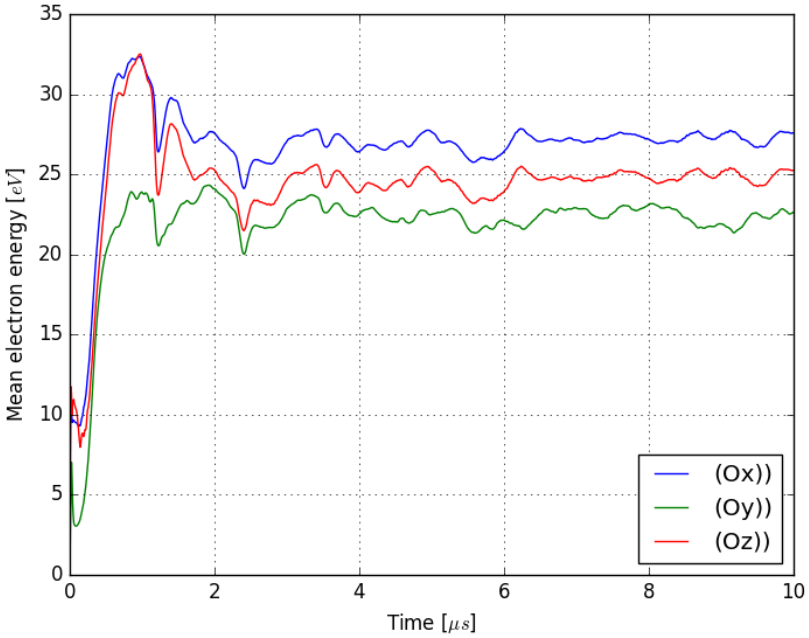

Figure 3.9 – Temporal evolution of the mean electron energy in all three directions: (blue) along (Ox), (green) along (Oy), and (red) along (Oz).

which at the walls simplifies as:

$$\Gamma_{e,w} = \int_0^\infty v_x f(\mathbf{v}) d^3\mathbf{v} \tag{3.7}$$

with f a Maxwellian distribution, v_x the electron velocity along (Ox), and $\mathbf{v}$ the electron velocity vector. Integration of Equation 3.7 gives us:

$$\Gamma_{e,w} = \frac{1}{4} n_e v_{th} \tag{3.8}$$

With n_e the electron density at the walls, and $v_t h = \sqrt{8qT_e/\pi m_e}$, the electron mean thermal velocity.

The electron energy flux at the walls, noted $W_{e,w}$, is similarly obtained from:

$$W_{e,w} = \int_0^\infty \frac{1}{2} m_e v^2 v_x f(\mathbf{v}) d\mathbf{v} \tag{3.9}$$

which gives us after integration:

$$W_{e,w} = \frac{1}{4} n_e v_{th}\, 2T_e \tag{3.10}$$

Thus by dividing Equation 3.8 by Equation 3.10, we obtain the average electron energy:

$$< \epsilon >= \frac{W_{e,w}}{\Gamma_{e,w}} = 2T_e \tag{3.11}$$

Then, since no sheaths are modeled at the (Oz) boundaries, in $z = 0$ and $z = z_{\max}$, due to the imposed electric field, E_0, following [93] and Equation 3.11, the power loss at the axial walls can be given by:

$$P_{\text{loss}} = J_{ez} \ < \epsilon > \ L_x L_y = J_{ez}\, 2T_e\, L_x L_y \tag{3.12}$$

Moreover the absorbed power for electrons in the (Oz) direction, P_{abs}, is given by:

$$P_{\text{abs}} = J_{ez}\, E_0\, L_x L_y L_z \tag{3.13}$$

where J_{ez} is the mean electron current along (Oz) at steady state.

By writing the simplified power balance for electrons along the (Oz) direction, and equalizing P_{loss} and P_{abs}, Equations 3.13 and 3.12 give us:

$$J_{ez}\, E_0\, L_x L_y L_z = J_{ez}\, 2T_e\, L_x L_y \tag{3.14}$$

By simplifying and rewriting Equation 3.14, we obtain:

$$T_e = \frac{E_0\, L_z}{2} = \frac{2 \cdot 10^4 \times 1 \cdot 10^{-2}}{4} = 100\,\text{eV} \tag{3.15}$$

where the values used for E_0 and L_z are given in Table 3.3.

The estimate given by Equation 3.15 is a correct approximate of the electron temperature measured in the simulation. Indeed, Figure 3.4 shows a mean electron energy $\epsilon_e = 85 \pm 5$ eV, which gives us an electron temperature $T_e = 57 \pm 5$ eV. Moreover, the estimate given by Equation 3.15 confirms the fact that T_e is determined by the simulation set-up and the parameters used.

This can be further confirmed by varying L_z for a given simulation set-up. In this case, the electron temperature is observed to increase, as expected from Equation 3.15. This can be easily understood as the charged particles can be accelerated by the electric field, $\mathbf{E}_0$, along a longer distance along L_z. As the particles are accelerated for a longer time and less thermalized, it is expected that the ion and electron temperatures are higher for a higher L_z.

This model is significantly simplified, and considered a first attempt to estimate the electron temperature from the simulation parameters. Thus an extended model, taking into account the secondary electron emission from the walls will be presented and discussed in Section 5.4.

3.1.6 MCC module to model HET plasma discharges

As detailed in Sections 2.2.2 and 2.2.3, LPPic2D is implemented with a MCC module to model electron/neutral and ion/neutral collisions. In order to model a HET the MCC module has to be adapted in order to use the Xenon cross-sections. The collision processes were chosen following previous studies [73, 42], and are:

$$e^- + Xe \rightarrow e^- + Xe \qquad \text{(Elastic scattering)} \tag{3.16}$$

$$e^- + Xe \rightarrow e^- + Xe^* \qquad (\epsilon = 8.315\text{eV, Excitation}) \tag{3.17}$$
$$e^- + Xe \rightarrow e^- + Xe^* \qquad (\epsilon = 9.447\text{eV, Excitation}) \tag{3.18}$$
$$e^- + Xe \rightarrow e^- + Xe^* \qquad (\epsilon = 9.917\text{eV, Excitation}) \tag{3.19}$$
$$e^- + Xe \rightarrow e^- + Xe^* \qquad (\epsilon = 11.7\text{eV, Excitation}) \tag{3.20}$$

$$e^- + Xe \rightarrow e^- + Xe^+ + e^- \qquad (\epsilon = 12.13\text{eV, Ionization}) \tag{3.21}$$

$$Xe^+ + Xe \rightarrow Xe + Xe^+ \quad \text{(Charge exchange)} \quad (3.22)$$
$$Xe^+ + Xe \rightarrow Xe^+ + Xe \quad \text{(Elastic scattering)} \quad (3.23)$$

The corresponding cross-sections are obtained from [94].

3.2 Model development: Secondary electron emission (SEE) models

Secondary electron emission (SEE) at the walls play a crucial role in the plasma discharge behavior. Thus SEE have been implemented in LPPic2D. Different models were implemented and tested, allowing for parametric studies as well as comparisons between models.

3.2.1 Constant yield model

In a first attempt to model the SEE process, a constant re-emission rate, $0 < \sigma_{\text{constant}} < 1$, is implemented. In this case, for each electron hitting the walls, a random number is picked; if this random number is greater than σ_{constant}, the electron is absorbed, if it is lower the electron is re-emitted. Thus, for a sufficiently large number of electrons hitting the walls, the mean fraction of electrons re-emitted, $\bar{\sigma}$, is approximately equal to σ_{constant}.

An illustration is given by Figure 3.10.

Re-emitted electrons are injected in the plasma thanks to an injection flux distribution described in Appendix A.3 at a given temperature, typically $T_{\text{see}} = 1\text{eV}$. Moreover, since the incident electrons hit the walls during the time-step, the re-emission has been done before the time-step ends. Consequently the injected electron, produced from SEE processes, has to be moved by a time-step fraction. This is done by picking a random number, R and moving the injected particle by $vR\Delta t$. Thanks to this, the injected particles are not all placed exactly at the plasma/wall interface when being re-injected, preventing some numerical effects due to boundary conditions. This method is kept in further SEE models.

3.2.2 Linear yield model

A second model has been introduced by [95] and later used in [42, 96, 97]. In this model the incident electron energy, ϵ, is used to estimate the

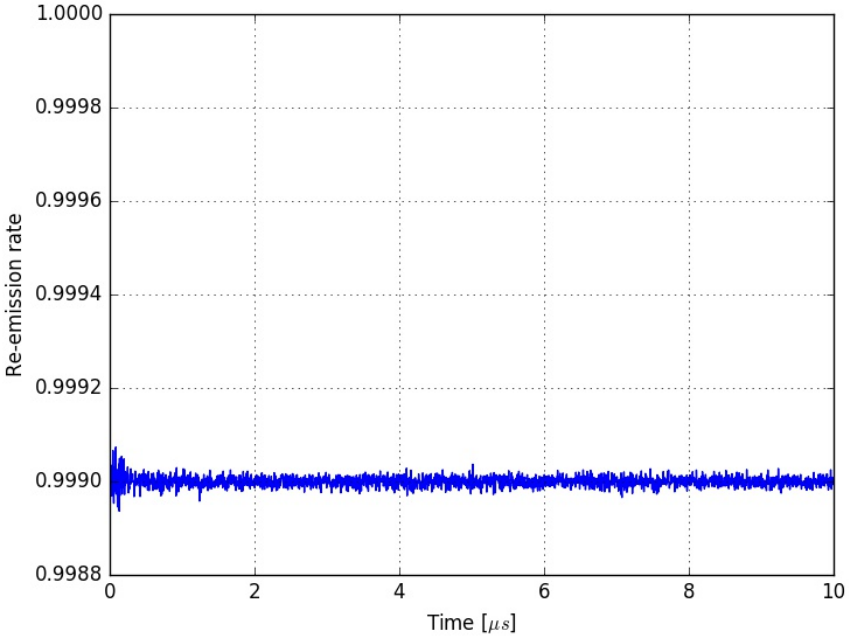

Figure 3.10 – SEE rate measured as a function of time for a case $\sigma_{\text{constant}} = 0.999$. As expected the mean SEE rate, $\bar{\sigma}$, does not deviate much from the $\sigma_{\text{constant}} = 0.999$ value.

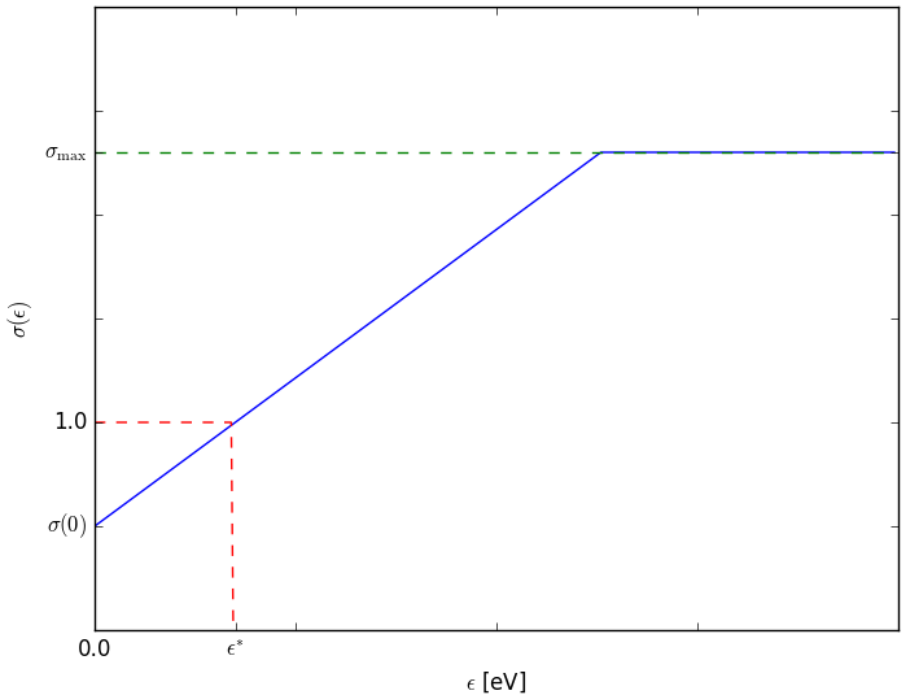

Figure 3.11 – Linear function used in order to model SEE probability when an electron hits the wall, as given in Equation 3.24, using the parameters ϵ^*, σ_0 and σ_{max}.

re-emission probability, $\sigma(\epsilon)$. A linear function describes this relation as expressed in Equation 3.24.

$$\sigma(\epsilon) = \sigma_0 + \frac{\epsilon}{\epsilon^*}[1 - \sigma_0] \tag{3.24}$$

Where ϵ^* is the crossover energy, and σ_0 the probability of attachment.

This function shows that $\sigma(\epsilon > \epsilon^*) > 1$, or even $\sigma(\epsilon > n\epsilon^*) > n$, with n an integer. In such a case, n electrons are re-emitted, until $\sigma(\epsilon) < 1$, then a random number, R, is picked, and if $\sigma(\epsilon) - n > R$ another electron is emitted. However $\sigma(\epsilon)$ cannot exceed a certain value σ_{max} defined by the walls material properties. This is shown in Figure 3.11.

The values of ϵ^* and σ_0 are parameters that can be varied in order to model different wall materials. However since HETs mostly use BN ceramics as dielectrics for the channel walls, these parameters were obtained in [96] by fitting experimental data from multiple datasets about BN ceramics. This fit led to $\epsilon^* = 35.04$ eV and $\sigma_0 = 0.578$. In the same way, measurements

done in [98] gave a value $\sigma_{\max} = 2.9$ for BN walls. These parameters for BN dielectric walls are summed up in Table 3.1.

3.2.3 Vaughan yield model

In order to refine the SEE model by taking into account the electron incidence angle, θ, as well as its energy, ϵ, another model was also implemented into LPPic2D. This model was developed in [99] with the parameters corresponding to dielectric walls. In this model the re-emission probability, $\sigma(\epsilon, \theta)$, is obtained as:

$$\sigma(\epsilon, \theta) = \gamma_{\max}(\theta)\Big(v(\epsilon, \theta)\exp[1 - v(\epsilon, \theta)]\Big)^k \tag{3.25}$$

Where

$$v(\epsilon, \theta) = \frac{\epsilon - w_0}{w_{\max}(\theta) - w_0} \tag{3.26}$$

$$w_{\max} = w_{\max,0}\Big(1 + \frac{k_s}{\pi}\theta^2\Big) \tag{3.27}$$

$$\gamma_{\max}(\theta) = \gamma_{\max,0}\Big(1 + \frac{k_s}{\pi}\theta^2\Big) \tag{3.28}$$

$$k = \begin{cases} 0.62 & \text{if } \epsilon < w_{\max}(\theta) \\ 0.25 & \text{if } \epsilon > w_{\max}(\theta) \end{cases} \tag{3.29}$$

With w_0 the emission threshold energy, k_s the smoothness factor of the surface (the lower the rougher), and $w_{\max}$ and $\gamma_{\max}$ are the primary electron energy and the emission coefficient at the maximum of emission for normal incidence.

This relation is plotted for a normal angle of incidence in Figure 3.12.

Note that the parameter $\gamma_{\max,0}$ is equivalent in this model to the parameter $\sigma_{\max}$ used in the linear yield model. Thus we have chosen to keep the empirical value taken from [98] and not that given in [99]. Other parameters are summed up in Table 3.1.

The implementation of various SEE models allows for the parameters to be changed in order to estimate the impacts of the wall material on the plasma discharge, as well as to compare the different models with each other. Nevertheless the SEE processes can be easily "turned on" and "off" in the simulation set-up.

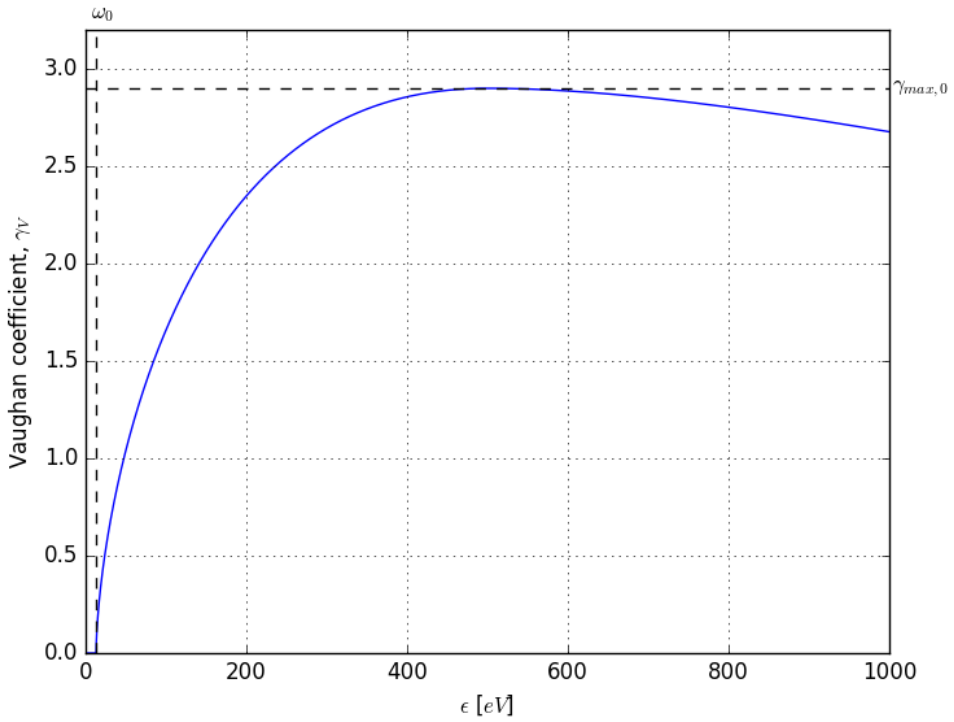

Figure 3.12 – Vaughan function used in order to model SEE probability when an electron hits the wall, as given in Equation 3.25, with a normal incidence angle.

Table 3.1 – Parameters used to configure the SEE models described in Section 3.2 for BN ceramic dielectrics [96, 98, 99].

Model	Parameter	Unit	Value
Linear			
	ϵ^*	[eV]	35.04
	σ_0		0.578
	$\sigma_{\max}$		2.9
Vaughan			
	k_s		1.0
	w_0	[eV]	13.0
	$w_{\max,0}$	[eV]	500.0
	$\gamma_{\max,0}$		2.9

3.2.4 Monte Carlo based SEE models

More complex SEE models have been used in the past in PIC simulations for HETs. If it is difficult to exhaustively detail every model proposed, however let us quickly mention two important models that have been used:

— A Monte Carlo probabilistic model used in [73], based on [100, 101, 102, 103, 104].

— A similar Monte Carlo probabilistic model proposed in [105] and based on a Monte Carlo adaptation of the Vaughan model [99] detailed in Section 3.2.3.

Both models are characterized by their ability to differentiate between three mechanisms leading to a re-emission of the incident electron:

Elastic reflection where the electron is reflected in the system with its incident energy.

Inelastic backscattering where a loss occurred, considered to be uniformly distributed between zero and the energy of the incident electron.

True secondary electron where one or more electrons are injected through a Maxwellian injection flux at a given temperature, usually $T_{\text{see}} = 1\text{eV}$.

While the respective yields for each of the three mechanisms are different in the two models, the two models agree well on the mechanisms at the root of the re-emission. Nonetheless an important difference between the two models has to be noted for very low energy electrons ($\epsilon_e < 10\text{eV}$), where the first model proposes an increase of the SEE yield, while the second proposes a decrease.

As a test it was chosen to implement the second model inside LPPic2D. Using the parameters given in Table 3.2, we were able to reproduce the curves given by [105] for each mechanism for a normal incidence angle. This is illustrated by Figure 3.13.

These Monte Carlo probabilistic models are expected to provide a more accurate model of SEE processes. However, as already highlighted, these models show a significant discrepancy at very low energies. Yet comparisons with experimental values, in both [105] and [73], show that values are missing for low energy electrons. Furthermore, as it will be shown in Section 5.5.2, the yield angle dependence is observed to be non-significant in HET case, where all the electrons hit the walls with an approximately normal angle. Thus, the precision obtained from these models seems difficult to compare to experiments, and not needed in the HET case.

Finally, these Monte Carlo probabilistic models are unduly computationally costly, since a large number of calculations need to be done to determine

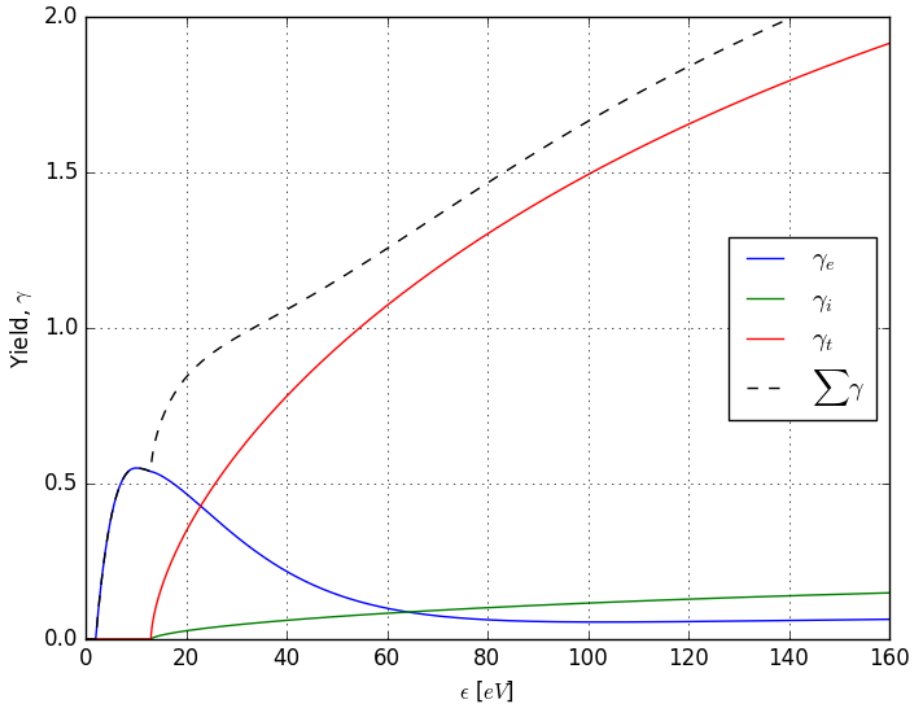

Figure 3.13 – Emission coefficients as a function of the incident electron energy for a normal angle of incidence: (blue) elastic reflection, (red) inelastic backscattering, (green) true secondary electron emission, and (dashed black) total yield. The model used is the one proposed in [105], and set-up with parameters from Table 3.2.

Table 3.2 – Parameters used to set-up the SEE model proposed in [105].

Parameter	Unit	Value
ω_0	[eV]	13
k_s		1
$\gamma_{max,0}$		3
$w_{max,0}$	[eV]	500
r_e		0.03
$w_{e,0}$		2
$\gamma_{e,max}$		0.55
$w_{e,max}$	[eV]	10
r_i		0.07
Δe		12
T_{see}	[eV]	1

the relevant emission mechanism for each incident electron. Consequently these models were not used in the following.

3.2.5 Ion-induced secondary electron emission

Previous sections have described models corresponding to SEE due to electron impact on the wall, or so-called electron-induced secondary electron emission. Nevertheless SEE from the wall can also result from ion impact on the wall. The so-called ion-induced secondary electron emission. This ion-induced SEE for ceramics are characterized by a secondary electron yield, σ_{ion}, nearly independent from the incident ion energy [106]. Thus, a constant yield model similar to the one described in Section 3.2.1 could be applied. However for singly charged Xenon ions, $\sigma_{\text{ion}} \approx 0.02$ [106] and is consequently insignificant compared to electron-induced SEE.

It is important to note that ion-induced SEE for multiply charged Xenon ion, Xe^{2+}, has a yield varying between 0.3 and 0.2 [106], which is comparable to electron-induced SEE. Since only Xe^{+} ions are modeled in our set-up, ion-induced SEE is chosen to be ignored. In further studies modeling multiply charged ions, ion-induced SEE could easily be taken into account through a constant SEE model.

3.2.6 Impact on electric field extrapolation

As detailed in Section 2.1.3, the electric field at the boundary, namely at the cell center where the grounded metallic wall is placed, is obtained by a linear extrapolation. Although being a valid solution in the case of a non-emitting wall, in the case of a strongly emitting wall, this approximation appears limited. Indeed, in this case, a so-called space charge limited regime (regime exhaustively detailed in Chapter 5) can take place.

The complete detail of this regime and its physical roots will be exhaustively detailed in Chapter 5, while the present section will only focus on its consequences on the way the electric field at the boundary is computed in *LPPic2D*. Indeed, since one of the features of this regime is the presence of "trapped" electrons near the wall, the plasma potential is observed to reach negative values near the walls. In this case, the electric field is also observed to increase drastically approaching the wall. These features are illustrated by Figure 3.14, which is a typical case studied in Section 5.3.1.

In order to quantify the impact of this extrapolation, simulations were conducted with a refined mesh under the same conditions. The standard mesh used in Figure 3.14 is detailed in Table 3.3 and uses $NG = 255 \times 1000$ grid-cells. Additionally, and despite computational cost, simulations were done with $NG = 512 \times 2000$ grid-cells, and $NG = 1024 \times 4000$ grid-cells, allowing comparison of the behavior near the wall, in the same case than the one illustrated by Figure 3.14.

The first result from this comparison is that the complex and turbulent behavior identified with the standard mesh, as exhaustively detailed in Section 5.3.1, is observed with the exact same features with the refined meshes. Furthermore, the near-wall values are conserved as illustrated by Figure 3.15. Yet some difference is observed concerning the radial electric field, E_y, between Figure 3.14 and Figure 3.15.

However, these results are only concerning cases modeling a grounded metallic wall. In the contrary, the modeling of floating dielectric walls, emitting or not secondary electron emission, does not encounter this difficulty, since the electric field at the plasma/wall is self-consistently obtained as detailed in Section 3.3.

3.3 Model development: Floating dielectric walls model

Since HETs have floating dielectric walls closing the discharge channel, LPPic2D needs to model these walls when solving the Poisson equation.

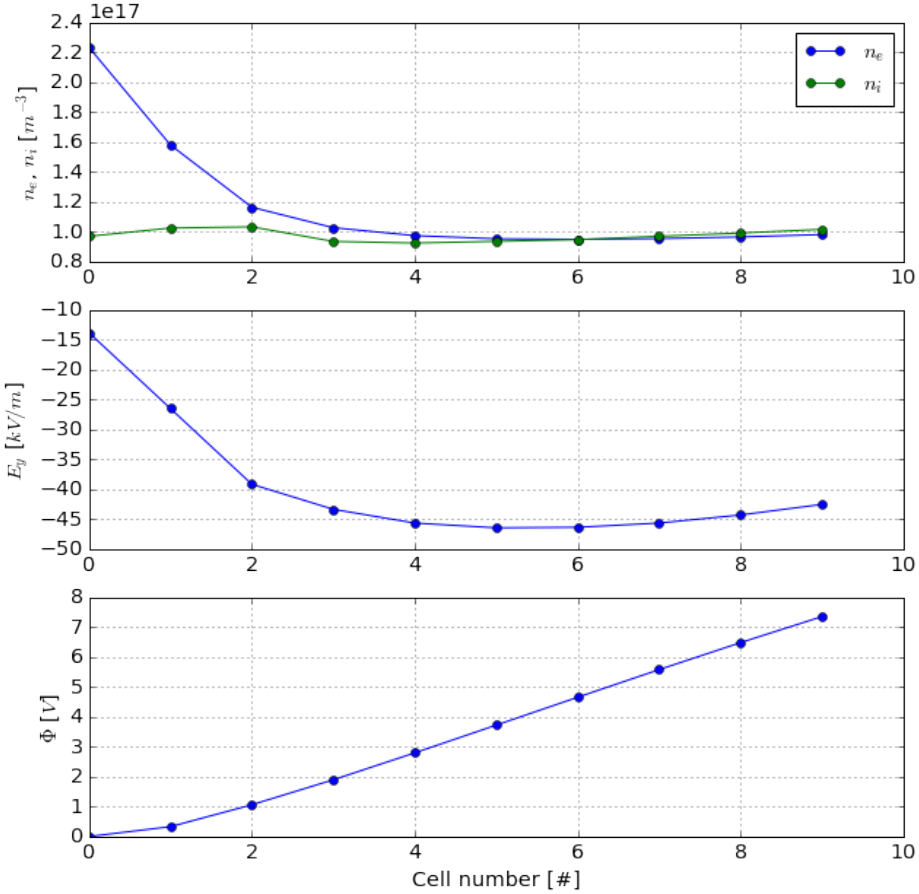

Figure 3.14 – Near wall values averaged between $1.2\,\mu s$ and $1.3\,\mu s$ (when the SEE yield is higher than σ_{cr}) in a case with strong emitting grounded walls ($\epsilon^* = 45$eV and $\sigma_0 = 0.5$ as detailed in Section 5.3) with the wall placed at cell number 0: (top) charged particles densities, (middle) radial electric field, and (bottom) plasma potential. The trapped electrons near the wall and the corresponding potential inversion is easily observed in this figure, which is using the "classical" $NG = 255 \times 1000$ grid-cells mesh.

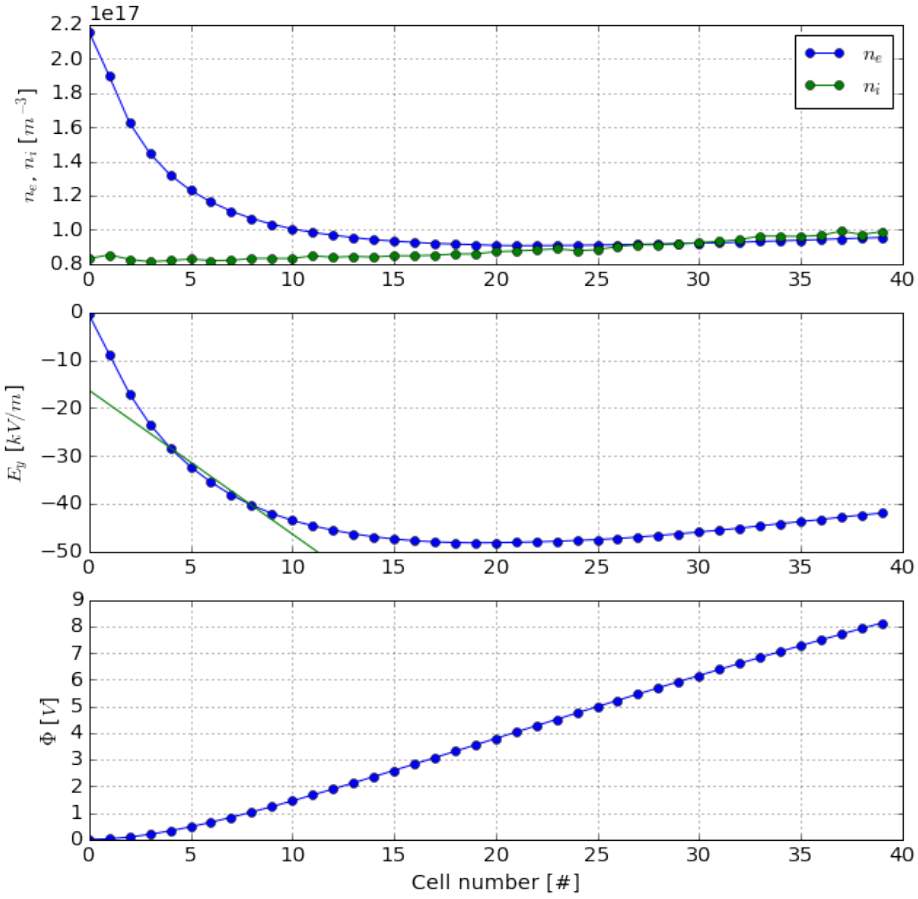

Figure 3.15 – Near wall values averaged between $1.2\,\mu s$ and $1.3\,\mu s$ (when the SEE yield is higher than σ_{cr}) in a case with strong emitting grounded walls ($\epsilon^* = 45$eV and $\sigma_0 = 0.5$ as detailed in Section 5.3) with the wall placed at cell number 0: (top) charged particles densities, (middle) radial electric field, and (bottom) plasma potential. The trapped electrons near the wall and the corresponding potential inversion is easily observed in this figure, despite the refined $NG = 1024 \times 4000$ grid-cells mesh. Concerning the radial electric field, E_y, the extrapolation corresponding to the "standard" mesh (middle, green line) shows similar result as the one illustrated in Figure 3.14.

Further description and testing of this feature is detailed in [92]. Diverse methods have been proposed and used to model the floating potential at the walls in PIC/MCC simulations of HET. As done in [73, 42], a Neumann condition can be used at the wall interface for the potential:

$$\frac{d\Phi}{dy}(y = y_{\text{wall}}) = E_{\text{y,wall}} = -\frac{\sigma(y = y_{\text{wall}})}{\epsilon_0} \tag{3.30}$$

Where the wall is situated at $y = y_{\text{wall}}$, $E_{\text{y,wall}}$ is the electric field at the wall interface orthogonal to the wall surface, and $\sigma(y = y_{\text{wall}})$ is the accumulated surface charge on the corresponding wall. This allows to estimate the electric field according to Gauss' law. However this kind of condition means that the imposed value of the electric field on one boundary automatically yields the correct value on the other boundary [42].

Another approach from [66] is to consider the capacitance of the wall in the estimation of the potential at the wall interface. In an electrostatic approach, where the charges re-arrange themselves at each time-step, we can consider the potential in the ith grid-cell near the wall, $\Phi_{i,y=y_{\text{wall}}}(t)$, from the accumulated charges held by the grid-cell, and the capacitance of the wall, C. This gives us:

$$\Phi_{i,y=y_{\text{wall}}}(t) = \frac{\sigma(y = y_{\text{wall}})}{C} \tag{3.31}$$

Where we can obtain $\sigma(y = y_{\text{wall}})$ the same way as in the previous model: by counting the accumulated charge at the wall from the beginning of the simulation.

In LPPic2D, it is chosen to solve the Poisson equation in the dielectric separating the plasma from the grounded metallic walls. While being a simplification of the actual 3D industrial geometry, this reflects quite effectively the actual HET geometry [12, 4]. This geometry is detailed in Figure 3.16. This is done in order to properly solve the potential inside the dielectric, and thus obtain the possible fluctuations of the azimuthal electric field, E_x, inside the dielectrics.

In order to add this dielectric layer, grid cells are added to the geometry as described in Figure 3.16. However, particles cannot move in these cells, and plasma/wall processes (absorption of particles and SEE processes) take place at the boundary between the dielectrics and the plasma. Moreover the permittivity, ϵ_r, in those cells is changed in order to model diverse ceramics, as well as the thickness of the dielectric layer on each side, L_{diel} (the dielectric has the same thickness on both sides).

Since no volumetric charges are taken into account inside the dielectric, the potential computed in this region is varying linearly. Thus, the size of

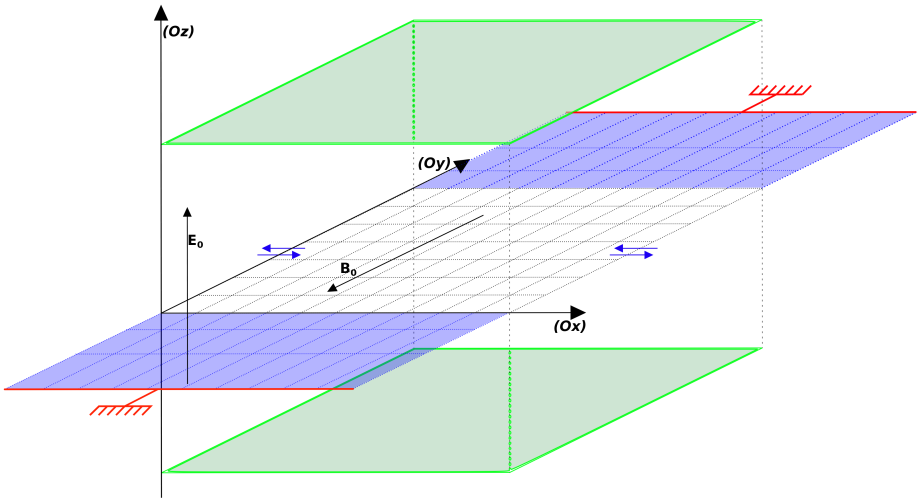

Figure 3.16 – Geometry used to model the HET with dielectric walls (purple) separating the plasma from the grounded metallic walls (red).

the cells inside the dielectric can vary. Varying the grid-cell size allow us to save on computational time. Coefficients describing the cell size variation along (Ox) and (Ox) are noted respectively $c_i = d_i/\Delta x$ and $c_j = d_j/\Delta x$.

Charges at the dielectric surface have to be taken into account in the solving of Poisson equation described in Section 2.3.2. Thus the number of particles absorbed by the walls are counted as well as the number of electrons extracted from the walls by SEE processes (in the case where $\sigma > 1$). The number of particles "left" in the walls is then used to calculate the surface charge.

We note in the following $S^{\mathrm{E}}_{i,j} = S^{\mathrm{W}}_{i,j} = d_i d_z$ and $S^{\mathrm{N}}_{i,j} = S^{\mathrm{S}}_{i,j} = d_j d_z$ the cell surface in the four directions. In the same way, the cell volume is noted $\Omega_{i,j} = d_j d_i d_z$. The interface between the dielectric wall and the plasma is placed at the cell center as shown in the Figure 3.17. Thus the integration of the Poisson equation in one cell of volume $\Omega_{i,j}$ is given by:

$$\int_{\Omega_{i,j}} \rho dv = \Omega_{i,j}\bar{\rho} + S^N_{i,j}\sigma_{i,j} \tag{3.32}$$

With $\bar{\rho}$ the mean charge density in the cell, and $\sigma_{i,j}$ the surface charge at the interface, i.e. at the cell center.

Since the interface is placed at the cell center, the permittivity in the cell has to be decomposed into two different values: one value "North", $\epsilon^N_{i,j}$, and one value "South", $\epsilon^S_{i,j}$. Using this notation, the Poisson equation is

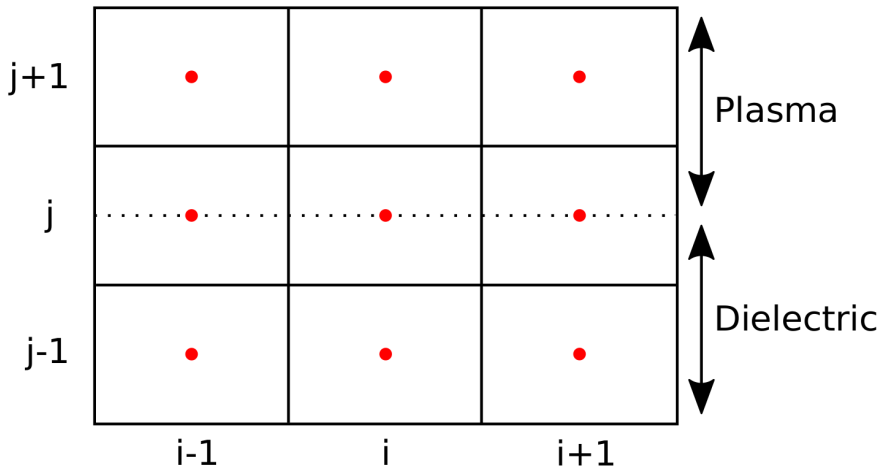

Figure 3.17 – Discretization method used for the interface between the plasma and the dielectric. The plasma/dielectric interface (dashed lines) is placed at the cell center (red).

discretized using the finite volume scheme, which gives:

$$S^E_{i,j}Q^E_{i,j}\phi_{i+1,j} + S^W_{i,j}Q^W_{i,j}\phi_{i-1,j} + S^N_{i,j}Q^N_{i,j}\phi_{i,j+1} + S^S_{i,j}Q^S_{i,j}\phi_{i,j-1} - Q^C_{i,j}\phi_{i,j} = -\Omega\bar{\rho}_{i,j} + S^N_{i,j}\sigma_{i,j} \tag{3.33}$$

With

$$Q^E_{i,j} = 2\frac{\epsilon_{i,j}\epsilon_{i+1,j}}{\epsilon_{i,j}d_{i+1} + \epsilon_{i+1,j}d_i} \tag{3.34}$$

$$Q^W_{i,j} = Q^E_{i-1,j} \tag{3.35}$$

$$Q^N_{i,j} = 2\frac{\epsilon^N_{i,j}\epsilon^S_{i,j+1}}{\epsilon^N_{i,j}d_{j+1} + \epsilon^S_{i,j+1}d_j} \tag{3.36}$$

$$Q^S_{i,j} = 2\frac{\epsilon^S_{i,j}\epsilon^N_{i,j-1}}{\epsilon^S_{i,j}d_{j+1} + \epsilon^N_{i,j-1}d_j} \tag{3.37}$$

$$Q^C_{i,j} = Q^E_{i,j}S^E_{i,j} + Q^W_{i,j}S^W_{i,j} + Q^N_{i,j}S^N_{i,j} + Q^S_{i,j}S^S_{i,j} \tag{3.38}$$

Since the interface is placed at the cell center, we have $\epsilon^S_{i,j} = \epsilon^N_{i,j-1}$. Thus the system remains symmetric. Equation 3.33 is given with physical values for the sake of clarity, however the equations solved in LPPic2D are normalized as expressed in Section 2.1.2.

Furthermore, in the system described in Figure 3.17, we have $d_z = d_x = \Delta x$ (i.e. $c_i = 1$). The cell width in the dielectric is varying with a polynomial law. The polynomial law is set so that the dielectric cells in contact with the plasma have the same width, Δy, as the cells inside the plasma. Cells deeper in the dielectric have a wider Δy in order to reduce the calculation time.

3.4 Summary of the physical set-up to model HETs

Complimenting the values used in Table 3.1, the physical parameters used to set up the simulations of HETs are summed up in Table 3.3. These values can be changed to perform parametric studies or explore different behaviors. However if not stated otherwise, it is implied that the physical parameters used are the ones detailed in Table 3.3. Moreover this set up is designed in order to respect the operating conditions described in Section 2.1.1. Furthermore the $r - \theta/(Ox - Oy)$ cut axial location is positioned at the acceleration region of the thruster, near the exit plane, where both a large electron drift instability and a strong secondary electron emission are observed. These two mechanisms lead to a significant deviation of the electron mobility in comparison to classical and Bohm values [34]. Note that N_A is the number of time-steps used to average the results. Thus, results are output from the simulation each N_A time-steps.

3.5 Conclusion

From a generic 2D-3V PIC/MCC code able to model a CCP helium discharge, LPPic2D has been extended and completed in order to realistically model a HET discharge channel. As the choice has been made in Section 1.5, LPPic2D is meant to model the HET exit plane along a $r - \theta$ cut. However, Cartesian coordinates were kept as the curvature is neglected, thus (Oy, Ox, Oz) correspond to the cylindrical coordinates (r, θ, Oz). In order to keep the notation system clear and avoid confusion, if not stated otherwise, Cartesian coordinates will be used from now on in the following sections and chapters.

Since a 2D-3V PIC/MCC model presents numerous limitations in order to realistically model a HET exit plane, diverse methods in order to overcome the multiple limitations inherent to this simulation set-up were developed and implemented. However, if modeling magnetized electrons is an easily verifiable implementation, dielectric walls, SEE processes, as well as a finite

Table 3.3 – Standard operating and numerical parameters used in the 2D PIC simulations for a HET.

Parameter	Unit	Value
Gas		Xenon
L_x	[cm]	0.5
L_y	[cm]	2.0
L_z	[cm]	1.0
B_0	[G]	200
E_0	[Vm^{-1}]	2×10^4
n_0	[m^{-3}]	3×10^{17}
Δt	[s]	4×10^{-12}
$\Delta x = \Delta y = \Delta z$	[m]	2×10^{-5}
T_e	[eV]	5.0
T_i	[eV]	0.1
T_{see}	[eV]	1.0
N	[particles]	25×10^6
NG	[gridpoints]	256×1000
N/NG	[part/cell]	≈ 100
N_A	[time-step]	2000
P_n	[mTorr]	1.0
T_n	[K]	300
n_g	[m^{-3}]	3.22×10^{19}

(Oz) extension of the simulation domain are unusual implementations, and thus difficult to verify.

However significant effort was put into checking and testing these implementations in order to preserve the code quality and reliability. At each new implementation, unitary tests from [78] were conducted to lower the risk of "bugs". Moreover, retro-compatibility was ensured, and by modeling the benchmarks from [75] it was possible to globally test parts of the code. Despite not testing all the features newly implemented in LPPic2D, this retro-compatibility testing ensured that LPPic2D's reliability at least did not decrease.

Now that the LPPic2D simulation tool is developed, and the used models are detailed, the further chapters will concentrate on the studies that were conducted using it.

Chapter 4

Electron drift instability and electron anomalous transport

Contents

4.1 The electron drift instability

The present simulation set-up models a plasma with an imposed $E \times B$ field. As expected, and already detailed in Sections 1.3 and 1.4.2, such a set-up features an electron drift instability under certain conditions.

Before presenting the results from the PIC simulations, we briefly revise the classical theory of electron cross-field transport, as presented in Section 1.4.2, and extend it with the kinetic description proposed in [68, 69]. This kinetic theory proposes to describe the electron drift instability observed in

the PIC/MCC simulations as detailed in Section 1.3. While demonstration of this theory is not the goal of this work, and thus is not detailed in the following, results relevant for the present study are highlighted in this section.

4.1.1 Electron drift instability characteristics

The first significant result from [69] is the expression of the instability growth rate, γ_{max}. As shown in Section 1.4.2, γ_{max} is expected to be zero in the fluid theory, while in [69], it is given by:

$$\gamma_{max} = \sqrt{\frac{\pi m_e}{54 m_i}} \frac{v_{de}}{\lambda_{De}} \tag{4.1}$$

From which we obtain the growth time, τ_g, as:

$$\tau_g = \frac{1}{2\gamma_{max}} \tag{4.2}$$

where m_e is the electron mass, and v_{de} is the azimuthal electron drift velocity. While the growth time, τ_g is difficult to precisely quantify in PIC/MCC simulations, a proper evolution can be observed, as highlighted in Section 4.3.2.

Then, as described by the kinetic theory [69], the instability wavelength, λ, is given by:

$$\lambda = 2\pi\lambda_{De}\sqrt{2} \tag{4.3}$$

where the Debye length, λ_{De}, has been defined as $\lambda_{De} = \sqrt{(\epsilon_0 T_e)/(|q|n)}$ in Section 1.4.1.

Furthermore the frequency, f, of the instability is estimated using Equation 1.53 by considering the instability to be azimuthal. Thus, we obtain the frequency by:

$$f = \frac{k c_s}{2\pi\sqrt{1 + k^2\lambda_{De}^2}} \tag{4.4}$$

Yet, at maximal growth we have $k_{max} = 1/(\sqrt{2}\lambda_{De})$, thus by replacing k by k_{max} in Equation 4.4, we obtain:

$$f = \frac{\omega_{pi}}{2\pi\sqrt{3}} \tag{4.5}$$

with the ion plasma frequency that was given as $\omega_{pi} = \sqrt{(nq^2)/(\epsilon_0 m_i)}$ in Section 1.4.1.

Finally the phase velocity, v_{ph}, is given by:

$$v_{ph} = f\lambda = \sqrt{2/3}\, c_s \tag{4.6}$$

Where $c_s = \sqrt{|q|T_e/m_i}$ is the ion sound speed.

These instability features can be compared to the ones obtained from the classical diffusion theory detailed in Section 1.4.2, and shows a good agreement. However, as expressed in Section 1.4.2, the classical expression is not properly describing the electron drift instability characteristics as its growth rate is null, in contrast to the kinetic theory from [69].

Analytical expressions of f, v_{ph}, and λ allow a comparison between measurements from the PIC/MCC simulations where the electron drift instability is present, and the kinetic theory.

Finally the kinetic theory developed in [69] gives analytical expressions to describe the amplitude of the oscillations of the instability at saturation. Indeed the theory predicts a value of $|\delta\widetilde{n}_e|/n_e \approx |\delta\widetilde{\Phi}|/T_e = 1/3$. This value can be easily compared to measurements from the PIC/MCC simulations.

4.1.2 Anomalous electron cross-field transport

Since the present work focuses on the electron cross-field transport, the different definitions and estimates of the electron mobility have to be detailed. These estimates are then measured during the simulations in order to be compared between each other or with analytical expressions given in [68, 69].

As demonstrated in Section 1.4.2, and expressed in Equation 1.32, the electron cross-field mobility classically obtained from diffusion theory, $\mu_{\text{classical}}$, is given by:

$$\mu_{\text{classical}} = \frac{\frac{|q|}{m_e\nu_m}}{1 + \frac{\omega_{ce}^2}{\nu_m^2}} \tag{4.7}$$

This classical estimate can easily be obtained from the simulations by measuring ν_m, while the other values are parameters. This value of the electron mobility will be referred to as $\mu_{\text{classical}}$, μ_{cla}, or "classical mobility".

The value of ν_m is monitored in the simulation using:

$$\nu_m(t') = \int_{t'}^{t'+T} \frac{dt}{T} \frac{\mathscr{N}_{collisions}(t)}{\mathscr{N}_{electrons}(t)} \tag{4.8}$$

Where $\mathscr{N}_{collisions}(t)$ is the number of electron-neutral collisions at each time-step, $\mathscr{N}_{electrons}(t)$ is the number of electrons in the system at each time-step,

and $T = 2 \times 10^3 \Delta t = 8\text{ns} = N_A \Delta t$ an averaging period used in order to minimize the statistical noise levels due to the PIC model.

Although Equation 4.8 is strictly speaking the total collision frequency, and not the momentum transfer collision frequency, in the MCC routine we have used isotropic electron scattering, for which it is appropriate to use the momentum transfer scattering cross-sections. Thus in this case, Equation 4.8 correctly yields the momentum transfer collision frequency [107].

Once the classical electron mobility can be estimated it has to be compared to a value of the mobility directly measured from the simulation. This is done by:

$$\mu_{\text{pic}} = \frac{\sum_{j=1}^{\mathscr{N}_{e^-}} v_{jz}}{\mathscr{N}_{e^-} E_0} \tag{4.9}$$

Where the summation is over all electrons in the whole system (including electrons in the sheaths), $\mathscr{N}_{e^-}$. Indeed, as for Equation 1.32, Equation 4.9 corresponds to $v_{e,z}/E_z$ averaged over the whole population of electrons. This value of the mobility, directly obtained from the PIC/MCC simulation, will be referred to as μ_{pic}, or "measured mobility".

As described in [68], the electric field along the $\mathbf{E_0} \times \mathbf{B_0}$ direction, E_x, should not be considered as null. Thus, the cross-field electron mobility is given by:

$$\mu_{\text{eff}} = \frac{\frac{|q|}{m_e \nu_m}}{1 + \frac{\omega_{ce}^2}{\nu_m^2}} \left[1 - \frac{\omega_{ce}}{\nu_m} \frac{\langle n_e E_x \rangle}{n_e E_0} \right] \tag{4.10}$$

Where n_e is the electron density, E_0 the norm of the axial electric field, and E_x is the electric field in the (Ox) direction. As we will see, the correlation term is generally negative so that $\langle n_e E_x \rangle < 0$, and thus fluctuations enhance the electron mobility. This mobility estimate is referred to in the following as the "predicted mobility", or μ_{eff}.

We follow in time the correlation term $\langle n_e E_x \rangle$ using:

$$\langle n_e E_x \rangle (t') = \int_0^{L_x} \frac{dx}{L_x} \int_0^{L_y} \frac{dy}{L_y} \int_{t'}^{t'+T} \frac{dt}{T} n_e(x,y,t) E_x(x,y,t) \tag{4.11}$$

Where the integrals are evaluated numerically by using the electron density, $n_e(x,y,t)$, and electric field along (Ox), $E_x(x,y,t)$, given by the simulation at each spatial grid point and at each time-step. The value is then averaged over N_A time-steps, corresponding to the T period in Equation 4.11.

The theory in [69] demonstrated that the electron drift instability leads to an enhanced electron-ion friction force, $\mathbf{R}_{ei}$. This force is predominantly

in the azimuthal direction, and opposes the electron drift motion with a magnitude given by:

$$|\mathbf{R}_{ei}| = \frac{|q|}{4\sqrt{6}}\frac{1}{c_s}|\nabla \cdot (\mathbf{v}_{di} n_e T_e)| \tag{4.12}$$

Where $c_s = \sqrt{|q|T_e/m_i}$ is the ion sound speed, $\mathbf{v}_{di}$ is the ion drift velocity, and the derivative, ∇, is over length scales larger than the instability wavelength.

In the present PIC/MCC simulations, ions enter the simulation domain with a very low velocity before being accelerated by the applied axial electric field, E_0. Also, there are no large-scale gradients in the radial (except within the thin sheath regions) or azimuthal directions. Thus we can approximate the derivative in Equation 4.12 as: $\nabla \cdot (\mathbf{v}_{di} n_e T_e) \approx \frac{d}{dz}(v_{zi} n_e T_e) \approx v_{zi} n_e T_e / L_z$, where v_{zi} is now the final velocity which ions leave the simulation domain with, and L_z is the simulation length in the (Oz) direction. The final ion velocity, v_{zi}, can be analytically estimated by making the assumption that ions are continuously accelerated along L_z by the vertical electric field without any effects of collisions.

Thus Equation 4.12 simplifies to:

$$|\mathbf{R}_{ei}| \approx \frac{|q|}{4\sqrt{6}}\frac{v_{zi} n_e T_e}{c_s L_z} \tag{4.13}$$

This electron-ion friction force results from the correlation between oscillations in the electron density and electric field, and can more generally be written as $|R_{ei}| = |q\langle n_e E_x\rangle|$. As shown in Equation 4.10 however, this correlation term leads to an enhanced electron cross-field mobility at instability saturation, which in the presence of electron-neutral collisions, reduces to:

$$\mu_{\text{eff}}^{sat} = \frac{\frac{1}{m_e \nu_m}}{1 + \frac{\omega_{ce}^2}{\nu_m^2}}\left[|q| + \frac{\omega_{ce}}{\nu_m}\frac{|\mathbf{R}_{ei}|}{n_e E_0}\right] \tag{4.14}$$

Substituting Equation 4.13 into Equation 4.14, and simplifying then yields:

$$\mu_{\text{eff}}^{sat} = \frac{\frac{|q|}{m_e \nu_m}}{1 + \frac{\omega_{ce}^2}{\nu_m^2}}\left[1 + \frac{|q|}{m_e \nu_m}\frac{B_0}{E_0}\frac{v_{zi} T_e}{4\sqrt{6} c_s L_z}\right] \tag{4.15}$$

By then using the known electron temperature and ion exit velocity in the simulations, Equation 4.15 can be used to predict the enhanced electron cross-field mobility.

Interestingly, for the present simulation geometry, Equation 4.15 is independent of the plasma density, and depends only on the applied simulation

conditions, electron-neutral collision frequency, and the electron temperature. Also, for $\nu_m \mapsto 0$, Equation 4.15 reduces to Equation 4.16.

$$\mu_{\text{eff}}^{sat}(\nu_m \mapsto 0) \approx \frac{1}{4\sqrt{6}} \frac{v_{zi} T_e}{c_s B_0 E_0 L_z} \tag{4.16}$$

Using the different estimates given for the electron cross-field mobility, in Equations 4.9, 4.7, 4.10, and 4.15, it is possible to study the reliability of the different models. Thus simulations were done in order to observe the electron drift instability in a simplified model, using parameters and operating conditions similar to those presented in the 1D simulations in [68, 74].

Since it has been properly shown in [13] through empirical studies, a Bohm-like electron mobility model (e.g. proportional to the inverse of the magnetic field, B_0, or squared magnetic field) is not appropriate to model electron cross-field transport in a HET channel, this model is not taken into account in this study.

4.2 Observations from the simulations

4.2.1 Observations of instability characteristics

As detailed in Section 1.5, observations were realized though 1D [68, 74], 2D $r - \theta$ PIC/MCC simulations [42, 73], and even 3D scaled PIC/MCC simulations [70].

Using the model described in Chapter 3 with grounded metallic walls, no SEE processes, and the parameters summarized in Table 3.3, the simulations set-up are configured to reproduce and compliment the 1D PIC/MCC simulations [68]. As expected an instability forms in the system.

As shown in Figure 3.4, the discharge requires about $1 - 2\,\mu$s before the instability saturates, and a quasi steady-state is reached, which is characterized by large amplitude fluctuations in the charged particles densities, electric field, plasma potential, and electron energy. In order to visualize the instability formation, saturation, and propagation, the time evolution of plasma properties taken along (Ox) (respectively (Oy)) at position $y = L_y/2$ (respectively $x = L_x/2$) are plotted. Since the instability is propagating along (Ox), cuts along (Oy) allow us to study the sheaths and any tilt in the instability propagation, while cuts along (Ox) allow the study of the propagation velocity. Such examples can be seen in Figure 4.1 for the electron density along (Oy), and Figure 4.2 for the plasma potential taken along (Ox).

The plot of the electron density in Figure 4.1 shows that it takes about $1\,\mu s$ before the sheaths at the radial walls fully develop from the initially

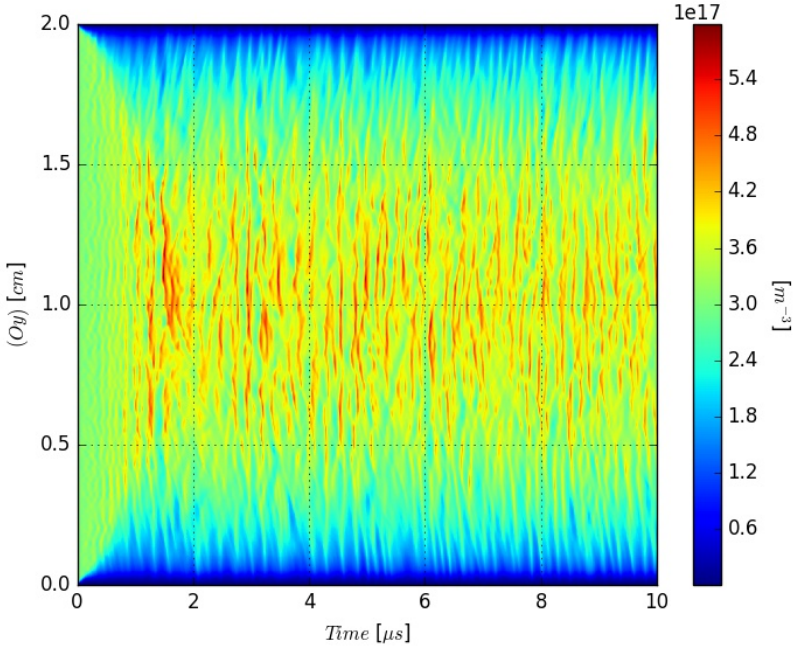

Figure 4.1 – Plots of the time evolution taken from 1D cuts in the 2D ($Ox - Oy$) domain in a non-collisional simulation with parameters from Table 3.3. Time evolution of the electron density taken along (Oy), at $x = L_x/2$.

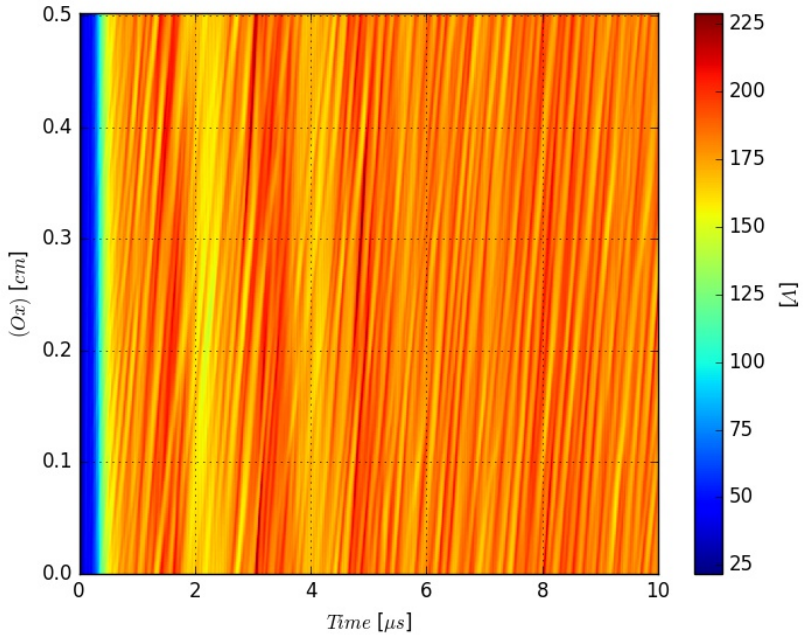

Figure 4.2 – Plots of the time evolution taken from 1D cuts in the 2D ($Ox - Oy$) domain in a non-collisional simulation with parameters from Table 3.3. Time evolution of the plasma potential profile taken along (Ox), at $y = L_y/2$.

uniform state. The fluctuations observed in the electron density are around $20-30\%$ of the equilibrium value, and there is also a clearly visible spatially and temporally periodic structure that can be seen in both Figures 4.1 and 4.2, which gives a wavelength of about 1.7 mm, and a frequency around 5 MHz. These values are close to those observed in [40, 41, 42, 58].

Turning on ion-neutral collisions as well as electron-neutral collisions confirms the ion transit time hypothesis described in Section 3.1.3. Indeed in a collisional simulation, the low frequency oscillations are damped, as seen in Figures 4.3 and 4.4, in comparison to the non-collisional case. An additional test with only electron-neutral collisions (i.e. with ion-neutral collisions "switched off") shows that the low frequency oscillation is seen again. Thus it is stated that the effect of ion-neutral collisions is to damp the low-frequency oscillation by causing a more uniform loss of ions through the (Oz) boundaries as a function of time. Figures 4.3 and 4.4 show that the instability is only slightly affected by the presence of collisions, with the main change being that the plasma potential is slightly higher with collisions.

As described in the 1D simulations in [41, 68], changes of L_z and/or L_y directly impact the instability behavior, thus L_z and L_y have to be chosen carefully. More detailed discussion about this is to be found in [68] and in Section 3.1.3.

4.2.2 Ion trapping and ion drift velocity

As described in Section 4.2.1, the instability needs $\approx 1-2\,\mu$s to saturate and reach a steady-state. After a few μs, nonlinear effects begin to set in, and limit subsequent growth. This saturation often occurs due to particle-wave trapping [108]. After observation of the electron and ion phase space plots, it is found that the electrons show no obvious signs of trapping. The ions however show strong signs of trapping, as is illustrated in Figure 4.5, which presents a case where collisions were "switched off", and with simulation parameters equal to those from Table 3.3. Similar ion trapping was observed in all other simulations where the instability formed, even with more complicated simulation set-ups such as those with SEE or dielectric walls.

These results confirm those highlighted previously by the 1D PIC simulations [68]. Furthermore it highlights two important characteristics of the ion drift velocity in the (Ox) direction:

1. $\langle v^x_{ions} \rangle \neq 0$,
2. and $\langle v^x_{ions} \rangle \approx v^{thermal}_{ions}$.

These two points can be confirmed by measuring from the simulation the

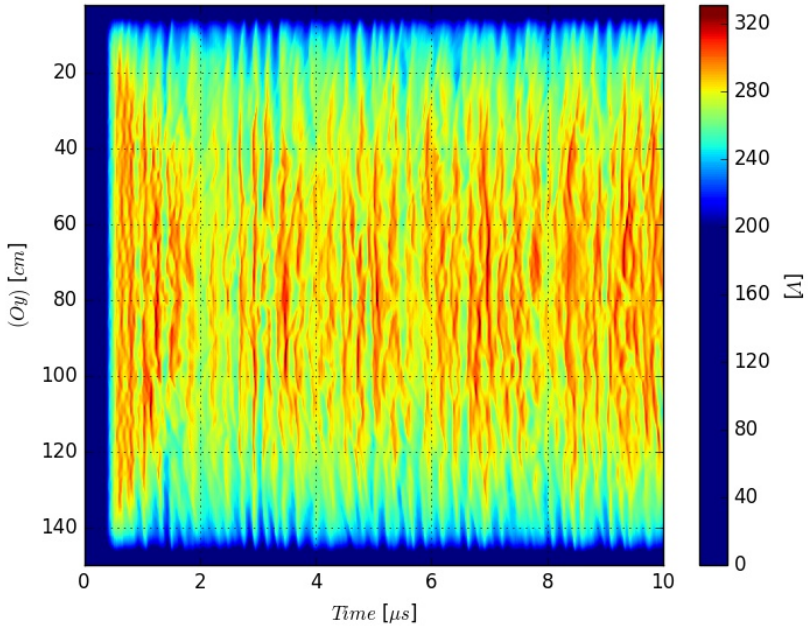

Figure 4.3 – Time evolution of the plasma potential profile taken from 1D cuts of the 2D $(Ox - Oy)$ simulation domain taken along (Oy), at $x = L_x/2$. Collisions are "turned on" with parameters from Table 3.3. The color-bar has been rescaled in order to highlight the instability behavior.

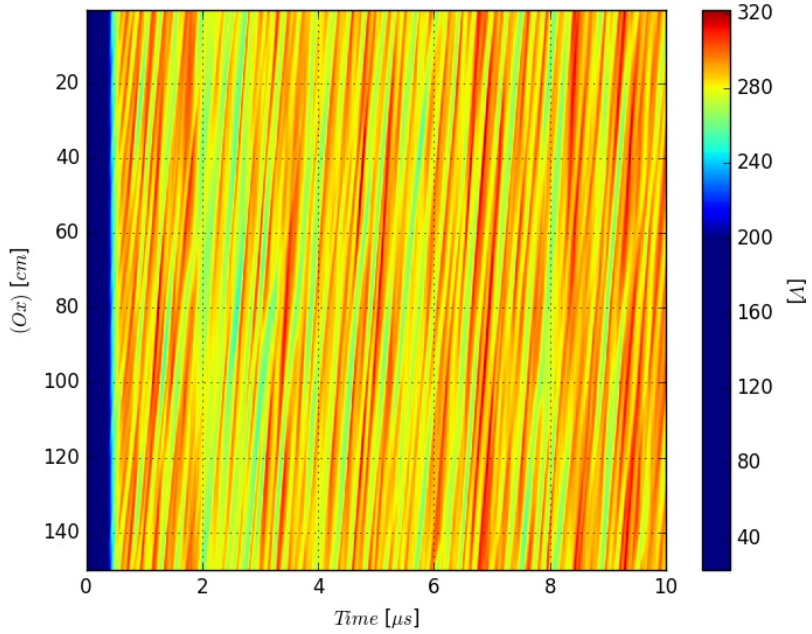

Figure 4.4 – Time evolution of the plasma potential profile taken from 1D cuts of the 2D $(Ox - Oy)$ simulation domain taken along (Ox), at $y = L_y/2$. Collisions are "turned on" with parameters from Table 3.3. The color-bar has been rescaled in order to highlight the instability behavior.

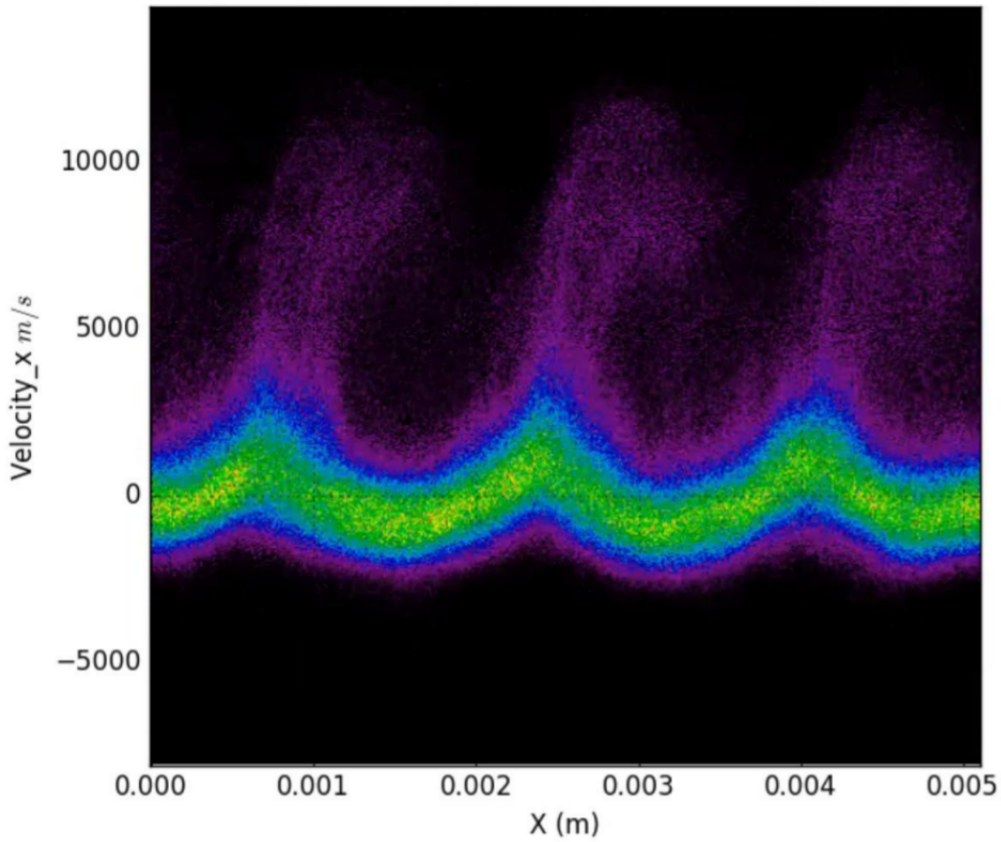

Figure 4.5 – Ion phase space at $t = 1.2\,\mu s$ in the (Ox) direction showing the characteristics "loops" indicative of ion-wave trapping.

average ion velocity in the (Ox) direction:

$$\langle v^x_{ions} \rangle = \frac{\sum_{i=1}^{i=\mathcal{N}_{ions}} v^x_i}{\mathcal{N}_{ions}} \tag{4.17}$$

where drift velocities of the order of $0.5 - 1\,\mathrm{kms}^{-1}$ are found. These values are similar to those measured experimentally in [109].

In [110] it is shown that the electron drift instability not only leads to an enhanced electron transport, but also to an enhanced ion rotation in the azimuthal direction with a value given by:

$$\langle v^x_{ions} \rangle \approx \sqrt{\frac{|q|T_e}{96 m_i}} \tag{4.18}$$

Where m_i is the ion mass, and $T_e = 2/3\langle \epsilon_e \rangle$ is the electron temperature taken from the mean electron energy $\langle \epsilon_e \rangle$. For typical electron temperatures observed in our 2D PIC simulations, Equation 4.18 predicts ion drift velocities of about 0.65 kms^{-1}. This is consistent with the ion drift velocities measured directly from the PIC simulations with Equation 4.17.

4.2.3 Enhanced transport verification

Before investigating electron transport in the case where an instability is present, we firstly confirm that we recover the classical cross-field electron mobility, $\mu_{\text{classical}}$, given above and demonstrated in Section 1.4.2, when no instability is present. As described by Equation 4.7, if $\nu_m \mapsto 0$, then $\mu_{\text{classical}} \mapsto 0$.

This verification can be obtained by setting the macro-particle weight in the PIC simulations, q_f, to a very small number (giving a very low plasma density), no instability forms and the electric field in the (Ox) direction is near zero. With all other simulation parameters corresponding to those listed in Table 3.3 (except collisions, that are "switched off"), we obtain a simulation where the instability is not present, and the resulting cross-field electron mobility is, as expected, zero.

The results corresponding to the collisional case (collision processes "switched on") are shown in Figure 4.6. This figure shows us that:

— Firstly despite the presence of strong oscillations, the cross-field electron mobility tends to a non-zero value (of about $6.5 \pm 2\,\mathrm{m}^2\mathrm{V}^{-1}\mathrm{s}^{-1}$), as predicted by Equation 4.10, and confirming the 1D PIC results [68].

— Secondly, except for the first $0.2\,\mu$s where the sheaths are forming, μ_{eff} seems to be consistent with the measured values of the electron

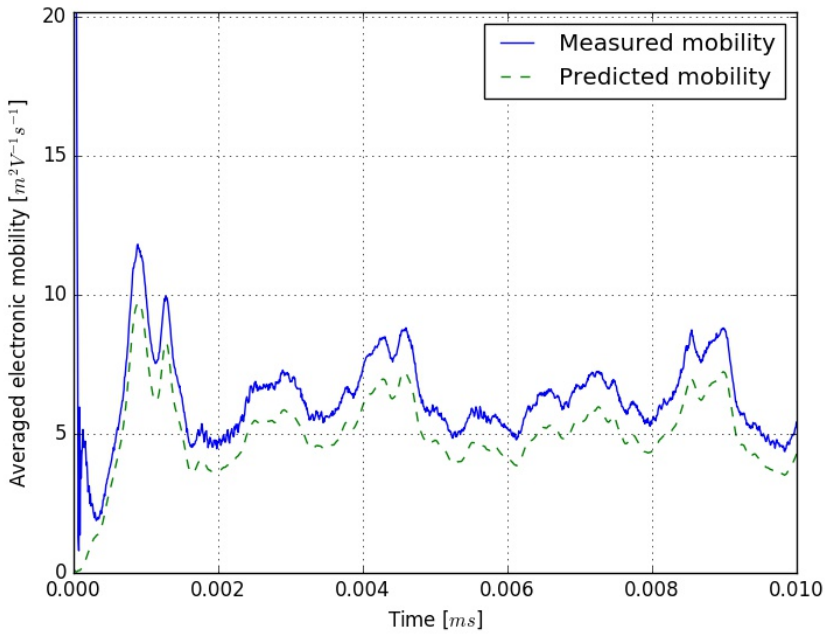

Figure 4.6 – Time plot of the measured average electron mobility in the system, μ_{pic} (blue), and the "predicted mobility", μ_{eff} (green), estimated from the correlation term, $\langle n_e E_x \rangle$ with collision processes turned on (electron/neutral as well as ion/neutral collisions).

mobility in the system. The very slight difference between the directly computed electron mobility, μ_{pic}, and the "predicted mobility", μ_{eff}, is most likely due to the neglect of the inertial and pressure terms in the electron momentum conservation equation used in the derivation leading to Equation 4.10.

— Finally we observe in Figure 4.6 that the low frequency oscillation ($\approx 0.5\,\text{MHz}$), related to the ion transit time along the (Oz) direction, has an influence on the electron cross-field mobility.

Another simulation is done without any collision processes modeled, two main observations were done:

— This allows us for another verification using an important property of Equation 4.10: if $\nu_m \mapsto 0$, then $\mu_{\text{eff}} \mapsto -\langle n_e E_x \rangle / n_e E_0 B_0$, where this term is in general not equal to zero, while following Equation 4.7 $\mu_{\text{classical}} \mapsto 0$. Comparison between the mobilities obtained from the PIC/MCC simulation confirms this property.

— Results from the simulation show the same agreement between the "effective mobility", μ_{eff}, and the measured mobility, μ_{pic}. Moreover it shows mobility levels comparable to the case with collisions processes modeled. This confirms an important result from the 1D PIC simulations [68]: The enhanced electron transport is essentially independent of electron/neutral collisions at the pressures typically present in HETs.

4.3 Comparison with kinetic theory

Starting from the observations of Section 4.2, diverse cases were modeled in order to investigate the relevance of the kinetic theory developed in [69], and Section 4.1.

4.3.1 Parametric study

In order to study the impact of the plasma density on the instability behavior and electron transport, two further simulations were made using modified plasma densities of: $n = n_0/4 = 0.75 \times 10^{17}\,\text{m}^{-3}$ and $n = 4n_0 = 12\times10^{17}\,\text{m}^{-3}$ (for which the time-step was lowered in order to respect the PIC conditions). These two simulations, together with the original one realized at a density of $n_0 = 3.0\times10^{17}\,\text{m}^3$, will be referred to as "n_0", "$4n_0$" and "$n_0/4$" in the following. Finally, all three simulations were done with electron/neutral collision as well as ion/neutral collision processes "turned on".

The results concerning the n_0 run can already be observed in Figures 4.3, 4.4, and 4.6. The time evolution of the plasma potential along (Oy) and (Ox) for the "$4n_0$" case are shown in Figures 4.7 and 4.8, while Figures 4.9 and 4.10 show the same results for the "$n_0/4$" case.

4.3.2 Comparison of instability characteristics

The first observation from these figures is the shorter growth time of the instability for the higher density case (with $n = 4n_0$). By contrast, the growth time is longer for the lower density case. This is consistent with the kinetic theory in [69], where the growth time, τ_g, can be expressed by Equation 4.2. Indeed if n increases, λ_{De} decreases, leading to a higher growth rate γ_{max}, and thus a longer growth time.

If the frequency and wavelength of the instability depend on the plasma density, we can observe that the phase velocity is almost constant. These measurements are again consistent with the kinetic theory from [69] presented

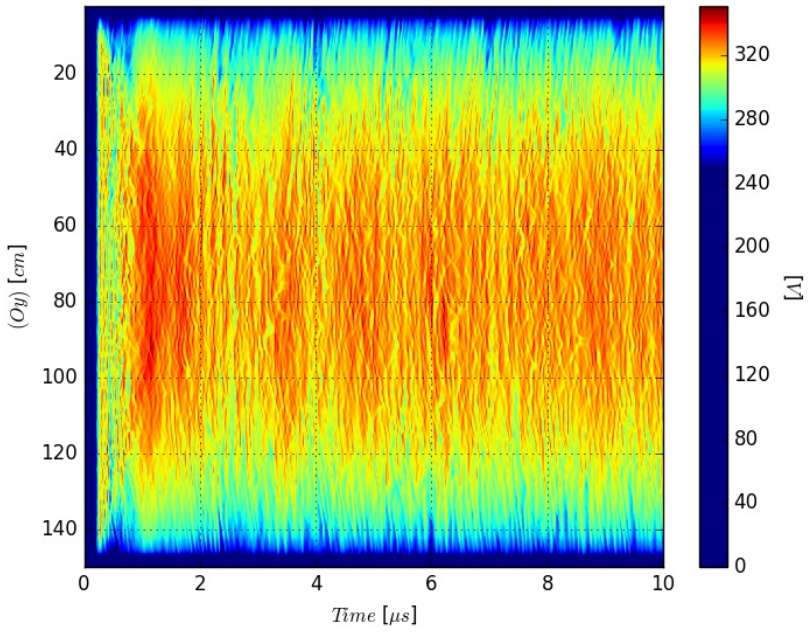

Figure 4.7 – Time evolution plots of the plasma potential taken from 1D cuts of the 2D $(Ox - Oy)$ domain taken along (Oy) at $x = L_x/2$. Collisions are enabled with parameters from Table 3.3, but the plasma density is increased to $4n_0 = 12 \times 10^{17}\,\mathrm{m}^{-3}$. The color-bar is rescaled in order to highlight the instability behavior.

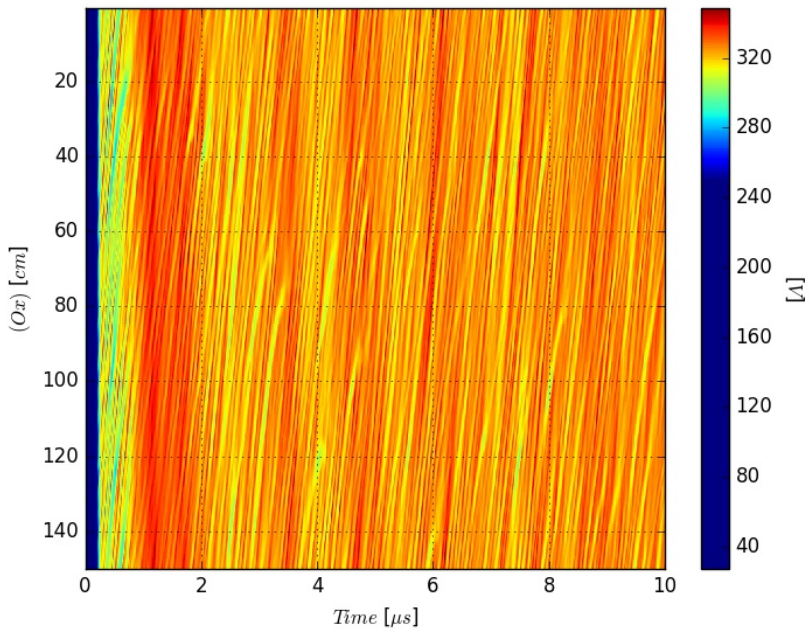

Figure 4.8 – Time evolution plots of the plasma potential taken from 1D cuts of the 2D $(Ox - Oy)$ domain taken along (Ox) at $y = L_y/2$ $(r = L_r/2)$. Collisions are enabled with parameters from Table 3.3, but the plasma density is increased to $4n_0 = 12 \times 10^{17}\,\mathrm{m}^{-3}$. The color-bar is rescaled in order to highlight the instability behavior.

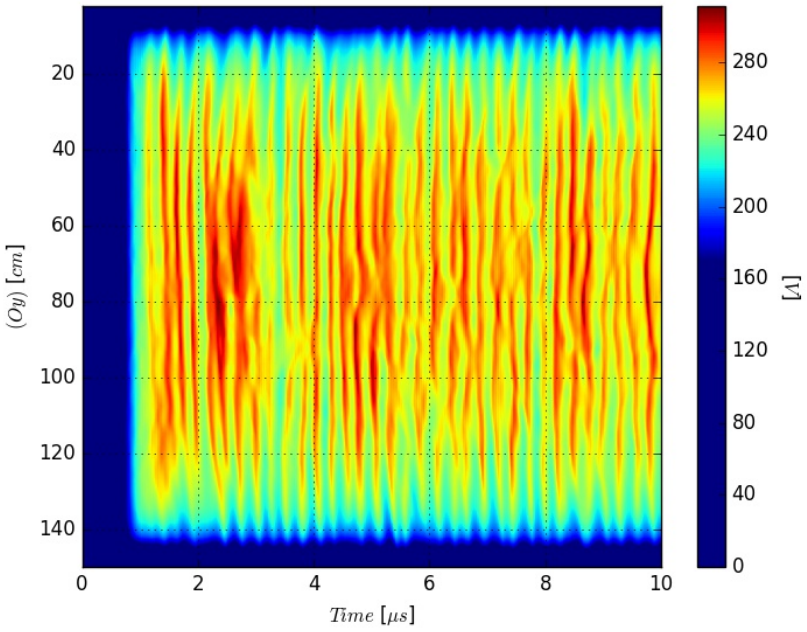

Figure 4.9 – Time evolution plots of the plasma potential taken from 1D cuts of the 2D $(Ox - Oy)$ domain taken along (Oy) at $x = L_x/2$. Collisions are enabled with parameters from Table 3.3, but the plasma density is reduced to $n_0/4 = 0.75 \times 10^{17}\ \mathrm{m}^{-3}$. The color-bar is rescaled in order to highlight the instability behavior.

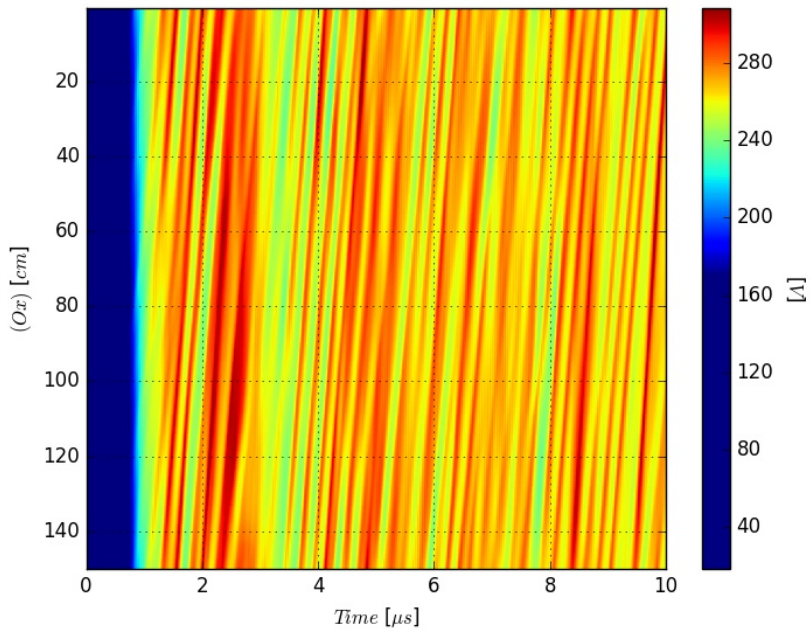

Figure 4.10 – Time evolution plots of the plasma potential taken from 1D cuts of the 2D $(Ox - Oy)$ domain taken along (Ox) at $y = L_y/2$. Collisions are enabled with parameters from Table 3.3, but the plasma density is reduced to $n_0/4 = 0.75 \times 10^{17}\,\mathrm{m}^{-3}$. The color-bar is rescaled in order to highlight the instability behavior.

in Section 4.1.1 through Equations 4.3 to 4.6. Comparisons between the results from the PIC/MCC simulations and the theoretical predictions are summarized for all three cases in Table 4.1. The analytical estimates of the instability wavelength, frequency, and phase velocity are in quite good agreement with the values obtained by the 2D PIC/MCC simulations.

As already expressed in Section 4.1.1, oscillations are predicted by the kinetic theory developed in [68]. Thus measurements are done in order to obtain comparable simulation values. Simulation values are measured by calculating the standard deviation at saturation of the oscillations, multiplied by $\sqrt{2}$ (since the theory looks at the peak amplitude, and not the standard deviation values). As can be seen in Table 4.1, where $|\delta\widetilde{n}_e|/n_e \approx 0.12 - 0.2$, and $|\delta\widetilde{\Phi}|/T_e \approx 0.155 - 0.32$, the predicted values are in reasonable agreement, but tend to over-predict the instability amplitude.

Observation of the electron drift instability, frequency, and phase velocity confirms an observation already made by 1D PIC/MCC simulations [68], that $\lambda f \approx v_{ph}$.

Measurements presented in Table 4.1 were done using the measured value of $T_e = 53\,[\text{eV}]$. This value is taken from the mean value of the electron energy, ϵ_e, by using the relation: $T_e = 2/3\,\epsilon_e$. Since this value is measured from the temporal plots of the energy, for which an example is given in Figure 3.4, the uncertainty can be estimated from the plots to be $\approx \pm 5\,[\text{eV}]$. This uncertainty is then echoed in T_e, and therefore in the subsequent instability estimates.

The oscillation amplitudes are measured directly from the time evolution plots from 1D cuts in the 2D domain. Examples of such plots are shown in Figures 4.4, 4.8, and 4.10. Consequently, the error margin is ≈ 10 %. In further chapters the measurement method concerning the oscillation amplitude has been systematized, leading to a gap between the present measurements and the ones in the following sections.

In the same way, the phase velocity is obtained by measuring the slope in Figures 4.4, 4.8, and 4.10, leading to an uncertainty of $\approx \pm 1.0[10^3\,\text{ms}^{-1}]$. In the following chapters a more systematized method will be detailed and used, leading, once more, to a gap with the present results.

These figures are used as well to measure the wavelength of the instability. Given the measurement method, uncertainty is $\approx \pm 0.1$ [mm].

Finally concerning the frequency, a Fourier analysis of the plasma potential temporal evolution is conducted, with an uncertainty in the range of $\approx \pm 0.5$ [MHz]. This is illustrated in Figure 4.11. Moreover, Figure 4.11 allows us to further compare the results obtained to the kinetic theory [69]. Indeed, as expressed in the kinetic theory, the relation obtained from the

Table 4.1 – Comparison between physical values measured in the simulation and predictions from the kinetic theory about the instability characteristics for several plasma densities.

PIC values			
Case	λ [mm]	f [MHz]	v_{ph} [10^3ms^{-1}]
$n_0/4$	2.0	2.5	5.0
n_0	1.0	5.0	5.0
$4n_0$	0.7	10.0	5.0
Case	$\lvert\delta\widetilde{n}_e\rvert/n_e$ [%]	$\lvert\delta\widetilde{\Phi}\rvert/T_e$ [%]	
$n_0/4$	20	32	
n_0	17	25	
$4n_0$	12	15.5	
Analytical values			
Case	λ [mm] (Equation 4.3)	f [MHz] (Equation 4.5)	v_{ph} [10^3ms^{-1}] (Equation 4.6)
$n_0/4$	1.7	2.9	5.0
n_0	0.8	5.8	5.0
$4n_0$	0.4	11.6	5.0
Case	$\lvert\delta\widetilde{n}_e\rvert/n_e$ [%]	$\lvert\delta\widetilde{\Phi}\rvert/T_e$ [%]	
$n_0/4$	33	33	
n_0	33	33	
$4n_0$	33	33	
$n_0 = 3.0 \times 10^{17}\,\mathrm{m}^{-3}$			

dispersion relation given in Equation 1.53 is given as:

$$\frac{\omega_r}{\omega_{pi}} = \frac{k\lambda_{De}}{\sqrt{1+(k\lambda_{De})^2}} \tag{4.19}$$

As observed in Figure 4.11, the agreement is quite respected for low values of ω_r/ω_{pi}.

4.3.3 Comparison of mobility estimates

As shown in Equation 4.15, for the present geometry, the electron cross-field mobility when the instability is saturated is independent of the plasma

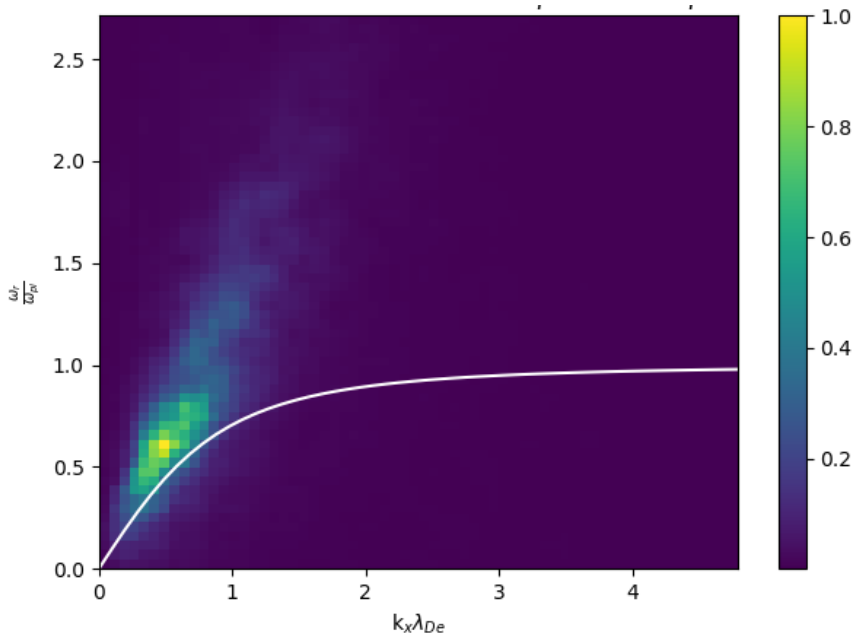

Figure 4.11 – Fast Fourier transform used to analyse the instability characteristics. This image is obtained by averaging the data between 5.00 μs and 6.90 μs. The colorbar used in normalized to the maximum of intensity. The white curve represents the expected result from the kinetic theory [69].

density. This allows us to predict the mobility from the simulation parameters, using the calculated values of ν_m and T_e. Thus, in order to compare the different mobility estimates, for each case μ_{pic} from Equation 4.9, μ_{eff} from Equation 4.15, μ_{eff}^{sat} from Equation 4.16, and $\mu_{\text{classical}}$ from Equation 4.7 are estimated and averaged spatially and temporally. These results are presented in Table 4.2 and in Figure 4.12.

Measurements are done by temporally averaging μ_{pic} as well as μ_{eff} from $t = 5.0\,\mu$s to $t = 10.0\,\mu$s. This allows us to ignore the initial transient that occurs at the beginning of the simulation. Moreover the values are averaged over the whole electron population concerning μ_{pic}, and over the whole simulation domain concerning μ_{eff}. Thus both estimates are including the sheaths in the average. As observed in Table 4.2, the two values show good agreement, confirming the kinetic theory from [69], as a correct estimation of the electron cross-field mobility with this simulation set-up.

In order to compare these results with the classical mobility definition, as given by Equation 4.7, $\mu_{\text{classical}}$ is estimated in the same conditions. As expected the result is about 25 times lower than that found in the PIC, μ_{pic}, and that predicted from the kinetic theory, μ_{eff}.

Table 4.2 – Comparison between physical values measured from the simulation and predictions from the kinetic theory for the electron cross-field mobility.

Case	PIC values		Analytical values	
$[\text{m}^2\text{V}^{-1}\text{s}^{-1}]$	μ_{pic}	μ_{eff}	μ_{eff}^{sat}	$\mu_{\text{classical}}$
(Equation)	(4.9)	(4.10)	(4.15)	(4.7)
$n_0/4$	6.0	5.9	3.2	0.2
n_0	5.8	5.6	3.2	0.2
$4n_0$	6.1	6.0	3.2	0.2
$n_0 = 3.0 \times 10^{17}\,\text{m}^{-3}$				

Finally μ_{eff}^{sat}, despite being a less precise estimate of the electron mobility than μ_{eff}, shows a better estimation than $\mu_{\text{classical}}$, thus being a good candidate for implementation in fluid simulations.

Values detailed in Table 4.2 and Figure 4.12 are based on measurements from the PIC/MCC simulations, and by so are exposed to error margins. Indeed, the PIC/MCC variability, highlighted by Figure 4.6, implies an error margin of $\approx \pm 0.5\,[\text{m}^2\text{V}^{-1}\text{s}^{-1}]$ over μ_{pic} and μ_{eff}. Concerning the analytical values, μ_{eff}^{sat} and $\mu_{\text{classical}}$, respectively expressed in Equations 4.15 and 4.7,

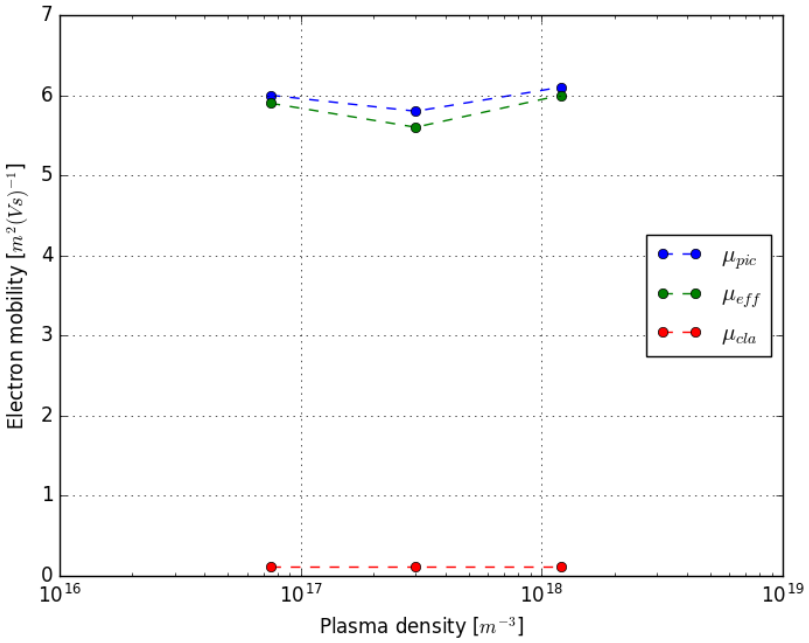

Figure 4.12 – Comparison of electron cross-field mobility estimates for the three studied cases as given by Table 4.2: (blue) μ_{pic} given by Equation 4.9, (green) μ_{eff} given by Equation 4.10, and (red) $\mu_{\text{classical}}$ given by Equation 4.7. Estimates of μ_{pic} and μ_{eff} are characterized by an error margin of $\approx \pm 0.5\,[\text{m}^2\text{V}^{-1}\text{s}^{-1}]$, while μ_{eff}^{sat} is exposed to a $\approx \pm 0.1\,[\text{m}^2\text{V}^{-1}\text{s}^{-1}]$ error margin.

they are obtained from values measured in the PIC simulations, such as T_e and ν_m, and consequently exposed to an error margin of $\approx \pm 0.1\,[\mathrm{m^2V^{-1}s^{-1}}]$.

4.4 Conclusion

In this chapter we have presented the results from a simplified $(Ox-Oy)$ PIC model, where enhanced electron cross-field transport has been observed, as well as a strong instability in the azimuthal direction. It has been seen that the instability and the enhanced electron transport are strongly associated, leading to an effective cross-field electron mobility many times larger than that from classical electron/neutral collisions.

This instability acts as an important momentum loss mechanism in addition to standard electron-neutral collisions. Although the instability, and consequently the momentum loss, occurs in the azimuthal direction, the presence of the magnetic field couples this with the axial direction.

Complementing previous 1D PIC results, these 2D PIC simulations highlight that this process is mostly independent of electron-neutral collisions, and does not require electron-wall collisions or secondary electron emission. Confirming the kinetic theory developed in [68] and [69], this study verifies that the enhanced cross-field electron mobility depends on an "electron density/electric field" correlation term, which represents an electron/ion friction force that is strongly enhanced by the instability.

However, since the focus of this Chapter 4 was to concentrate on the basic physics, a simplified model has been used, and it is important to highlight and discuss some limitations linked to this approach. Firstly, the obvious limitations are that:

— the walls are metallic and grounded

— no secondary electron emission is integrated in the model

Both of these points are in contradiction with the numerous studies that have highlighted the role of electron-wall collisions and secondary electron emission on the electron transport [7, 27, 37, 47]. However they are expected to alter the equilibrium values reached by the simulation (such as the plasma potential), but not necessarily the overall conclusions on electron transport. Adding in a model to account for secondary electron emission, as well as for dielectric walls, would let us more realistically simulate a real device. This will be done in the following chapters. Nevertheless, these simplified simulations still give useful insights on the basic physical mechanisms governing the instability formation and the associated electron transport.

A less obvious limitation of the present simulations is that Poisson's equation is only solved in the $(Ox-Oy)$ plane, but not along the (Oz) direction,

and so the wavenumber of any fluctuations along (Oz) is zero. This implies that convection of the instability away from the simulation plane is not correctly modeled. We have tried to account for this by using a finite axial length, and by removing particles which cross the boundaries in this direction. But this still only represents an approximation, where the (Oz) direction is mimicked by the model, since the wave propagation along (Oz) cannot be properly modeled without solving Poisson's equation along this axis. Unfortunately the solution to this limitation would be to fully kinetically model a 3D system.

Chapter 5

Effects of secondary electron emission (SEE)

Contents

5.1 Sheath model in the presence of SEE from the walls

As detailed in Section 1.4.1, the plasma in the presence of a closed boundary shows a potential drop near the wall, in two regions called the pre-sheath and the sheath. However, the estimates presented in Section 1.4.1 consider a plasma closed by non-emissive walls. As detailed in Sections 1.2.4 and 1.3, secondary electron emission from the walls play a significant role in HET operation. Consequently the sheath model used in the following section needs to be adapted in order to take into account the SEE flux from the walls. Consequently, Equation 1.24 becomes:

$$\Gamma_e(1-\bar{\sigma}) = \Gamma_i \tag{5.1}$$

Where $\bar{\sigma}$ is the effective total SEE yield.

As shown in [111], and later in [95, 7], the potential drop in the sheath, $\Delta\Phi_s$, can be expressed as:

$$\Delta\Phi_s = \frac{k_B T_{e_{//}}}{e} \cdot ln\left[(1-\bar{\sigma})\sqrt{\frac{m_i}{2\pi m_e}}\right] \tag{5.2}$$

With k_B Boltzmann constant, $T_{e_{//}}$ the mean electron temperature parallel to the magnetic field, B_0, thus along (Oy) axis, and m_e and m_i respectively the electron and xenon ion masses.

Equation 5.2 suggests that the plasma potential at the walls becomes zero for $(1-\bar{\sigma})\sqrt{\frac{m_i}{2\pi m_e}} = 1$, where the value of $\bar{\sigma}$ corresponds to a critical value σ_{cr}. By considering infinitely massive ions in comparison to electrons [111], we can obtain an estimate of σ_{cr}, as given by:

$$\sigma_{\text{cr}} = 1 - \sqrt{\frac{2\pi m_e}{m_i}} \approx 1 - 8.3\sqrt{\frac{m_e}{m_i}} \tag{5.3}$$

For xenon, this leads to $\sigma_{\text{cr}} \approx 0.985$ [95].

In the case of $\bar{\sigma} > \sigma_{\text{cr}}$, no monotonic solution exists for $\Delta\Phi_s$. This case is called a space-charge limited (SCL) or space-charge saturated (SCS) regime [111, 95, 97], and it will be studied in further detail in Section 5.3.1. This regime will be referred to as the SCL in the following.

Concerning the potential drop in the pre-sheath, $\Delta\Phi_{\text{p-s}}$, it is still expressed by the simple relation: $\Delta\Phi_{\text{p-s}} = T_{e_{//}}/2$, given by Equation 1.23.

The measurement of the plasma potential drop in the simulations, and its comparison to the analytical model previously described, is a way to verify the quality of the model, as it is used in the following Section 5.2.

5.2 Constant SEE yield: Model verification

In order to verify the reliability of LPPic2D's SEE module, as well as to explore the limit of the simulation, we firstly use the constant re-emission model, detailed in Section 3.2.1. Using different values of σ_{constant}, we can then observe different plasma discharge behaviors. In this case, the model set-up is comparable to the set-up from Chapter 4: metallic grounded walls are modeled, and the system is configured with values from Table 3.3. Only the presence of SEE differentiates these simulations from those from Chapter 4. This allows us to precisely identify the origin of the observed differences between the simulations.

5.2.1 Diverging case

The model detailed in Chapter 3 is configured to keep the number of particles modeled roughly constant: indeed as the (Ox) axis is closed by periodic conditions, particles are re-injected when hitting the (Oz) axis boundaries, and couples are re-injected when particles are absorbed by the walls closing the (Oy) axis. Thus setting the $\sigma_{\text{constant}} > 1$ (for instance 1.01), corresponds to a case where the walls are generating electrons, while absorbing ions. Indeed, since every electron hitting the wall is re-emitted from the wall through the SEE process, the number of couples re-injected, through the algorithm detailed in Section 3.1.4, is strictly zero.

An example for $\sigma_{\text{constant}} = 1.01$ is given in Figure 5.1, where the plasma potential from one wall to another (corresponding to the (Oy) direction) is plotted as a function of time. As expected, such a system does diverge rapidly.

5.2.2 Comparison with the sheath model

Another verification can be made by comparing the potential drop in the simulation at steady state, with the analytical value of the potential drop, $\Delta\Phi_{\text{tot}}$. Where $\Delta\Phi_{\text{tot}}$ is obtained by adding the pre-sheath potential drop, $\Delta\Phi_{\text{p-s}}$, and the sheath potential drop, $\Delta\Phi_{\text{s}}$.

Since in the case of a constant SEE yield, $\bar{\sigma} \approx \sigma_{\text{constant}}$, Equation 5.2

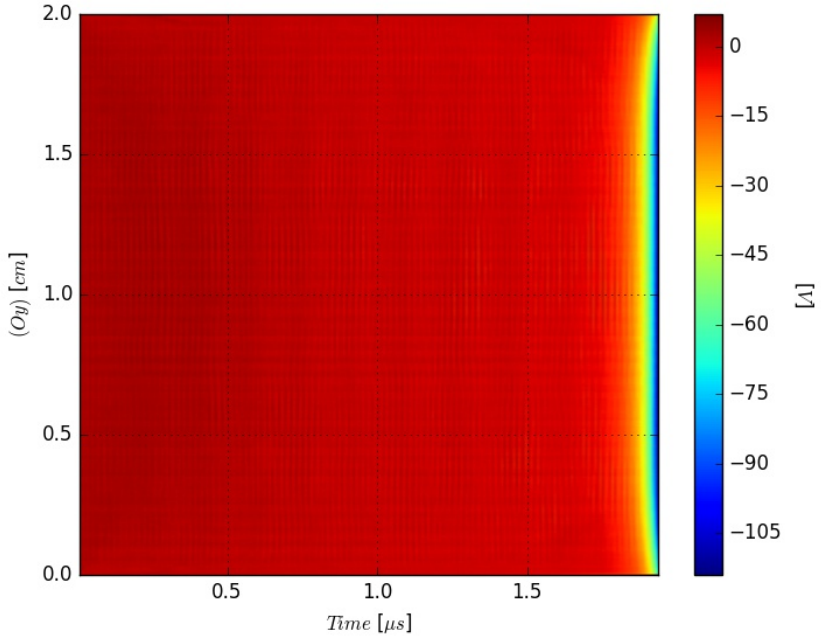

Figure 5.1 – Temporal evolution of the plasma cut along (Oy) at $x = L_x/2$ in the case $\sigma_{\text{constant}} = 1.01$. As expected, after an initialization time, the system diverges rapidly, leading electrons to not respect the CFL condition (Section 2.1.1) anymore.

Table 5.1 – Comparison between physical values obtained from the simulations, and predictions from the floating sheath theory including SEE.

Parameter	PIC values		
σ_{constant}	$T_{e_{//}}$ [eV]		$\Delta\Phi_{\text{tot}}$ [V]
0.5	2.5		12
0.92	42		125
0.99	40		60
Parameter	Analytical values		
σ_{constant}	$\Delta\Phi_{\text{p-s}}$ [V] (Equation 1.23)	$\Delta\Phi_s$ [V] (Equation 5.4)	$\Delta\Phi_{\text{tot}}$ [V]
0.5	1.25	11.5	12.75
0.92	21	116	137
0.99	20	26.9	46.9

becomes:

$$\Delta\Phi_s = \frac{k_B T_{e_{//}}}{e} \cdot ln\left[(1-\sigma_{\text{constant}})\sqrt{\frac{m_i}{2\pi m_e}}\right] \tag{5.4}$$

Thus, measurements of $\Delta\Phi_{\text{tot}}$ from the simulations can easily be compared to analytical values.

Results for three simulations with different values of σ_{constant} are shown in Table 5.1. The highest values chosen for σ_{constant} are close to the value estimated in [95] for the SCL, for which $\sigma_{\text{constant}} \approx 0.985$, which is expected to be present in HETs.

Furthermore results presented in Table 5.1 were done using the PIC-calculated value of $T_{e_{//}}$. This value is obtained from the mean value of the electron energy parallel to the magnetic field, $\epsilon_{e_{//}}$, by using the relation: $T_{e_{//}} = 2\epsilon_{e_{//}}$. Since this estimation is done from temporal plots of $\epsilon_{e_{//}}$ (as shown in Figure 3.4), the uncertainty can be estimated to be $\approx \pm 5$ [eV]. This uncertainty is then to be echoed in $T_{e_{//}}$, and also on the subsequent estimates.

The total sheath drop, $\Delta\Phi_{\text{tot}}$, is measured directly from the temporal evolution of the plasma potential, thus given the measurement method, the uncertainty on $\Delta\Phi_{\text{tot}}$ is in the range of ± 15 [V].

These simulations, using a constant re-emission yield, allowed us to validate the functioning of the SEE module in LPPic2D. Consequently, more precise models will be used below.

5.3 Linear SEE yield: Parametric study

Using the linear model described in Section 3.2.2, a parametric study over the crossover energy, ϵ^*, is conducted [112]. Indeed, changing the value of ϵ^* corresponds to a change in the material properties. Thus this parametric study allows us to investigate the effects of intensity of SEE processes on the plasma discharge behavior in HETs.

As for Section 5.2, the model set-up is comparable to the set-up from Chapter 4: metallic grounded walls are modeled, and the system is configured with values from Table 3.3. Only the more complex linear model for SEE processes differentiate these simulations from the ones from Section 4.

Moreover in comparison to the constant re-emission model of Section 5.2, the linear model allows for a dynamic equilibrium between the electron temperature in the system, T_e, and the re-emission rate, $\bar{\sigma}$.

5.3.1 Regime identification and characteristics

As described previously, the linear SEE yield model takes into account the incident electron energy, ϵ_e, in order to estimate the electron re-emission probability, $\sigma(\epsilon_e)$, thanks to a saturated linear function given in Equation 3.24, and illustrated in Figure 3.11. As stated, the crossover energy, ϵ^*, corresponds to the value for which $\sigma(\epsilon_e = \epsilon^*) = 1$. Thus the value of ϵ^* was changed in order to study the influence of the material on the plasma discharge. Indeed a low value of ϵ^* corresponds to a material easily emitting secondary electrons, and a high value corresponds to a material with less secondary electron emission.

Identification

Hence a parametric study could be performed over the ϵ^* parameter, with simulations done on a long time-scale, typically from 10μs to 40μs. This allowed us to identify three typical regimes corresponding to three different plasma discharge behaviors.

In an effort to avoid confusion, these three regimes will be referred in the following work as Regime I, Regime II and Regime III, corresponding to characteristic simulations obtained with the parameters from Table 5.2, but using respectively the values: $\epsilon^* = 38$eV, $\epsilon^* = 45$eV, and $\epsilon^* = 50$eV.

These values were chosen since they are featuring typical characteristics of the studied regimes, however the Regime I is observed for values of ϵ^* lower than ≈ 40eV, while the Regime III is observed for values higher than

Table 5.2 – Parameters used to configure the linear SEE yield model described in Section 3.2 for the three regimes identified in the parametric study.

Regime	ϵ^* [eV]	σ_0	$\sigma_{\max}$
I	38	0.5	2.9
II	45	0.5	2.9
III	50	0.5	2.9

≈ 47eV, and Regime II for $\epsilon^* \approx 40 - 47$eV. Details and a description about these three regimes are presented in the following.

General observations

The three regimes are characterized by the presence of "bursts", where the mean value of the SEE rate, $\bar{\sigma}$, is higher than 1 for a short period of time. These "bursts" generate different behaviors as a function of the value of ϵ^*, and the simulations do stabilize to a certain behavior and value of σ. A plot of these "bursts" of SEE rate can be seen in Figures 5.2 to 5.4 respectively for each of the three regimes.

While Regime I saturates at a high value of $\bar{\sigma} \approx 1$ (but $\bar{\sigma} < 1$ at saturation), Regime III saturates to a much lower value, with $\bar{\sigma} \approx 0.85$. Regime II on the contrary does not saturate but stabilizes with a pseudo-oscillation between these two saturation values.

Equation 5.3 gives us the value of σ_{cr} for which the sheath potential should be negative. Indeed, when $\bar{\sigma} > \sigma_{\text{cr}}$, the sheath potential is observed to reach negative values. We can observe in Figures 5.2, 5.3, and 5.4, that a "plateau" of SEE yield is present in all three Regimes. This "plateau" is characterized by the fact that $\sigma_{\text{cr}} < \bar{\sigma} < 1$.

Verifications

In order to verify the quality of these simulations, the analytical values obtained for the potential drop from Equation 5.4 were compared to the corresponding values from the simulations. As already done for the σ_{constant} case in the Section 3.2.1, these comparisons gave consistent results. These values are not given for the sake of brevity.

Moreover, since at steady state Regimes I and III reach a steady value of $\bar{\sigma}$, comparisons can be made between with simulations done with σ_{constant}. Thus, we can compare Regime I at steady state with a simulation using $\sigma_{\text{constant}} = 0.99$ as parameter, as well as Regime III and a simulation us-

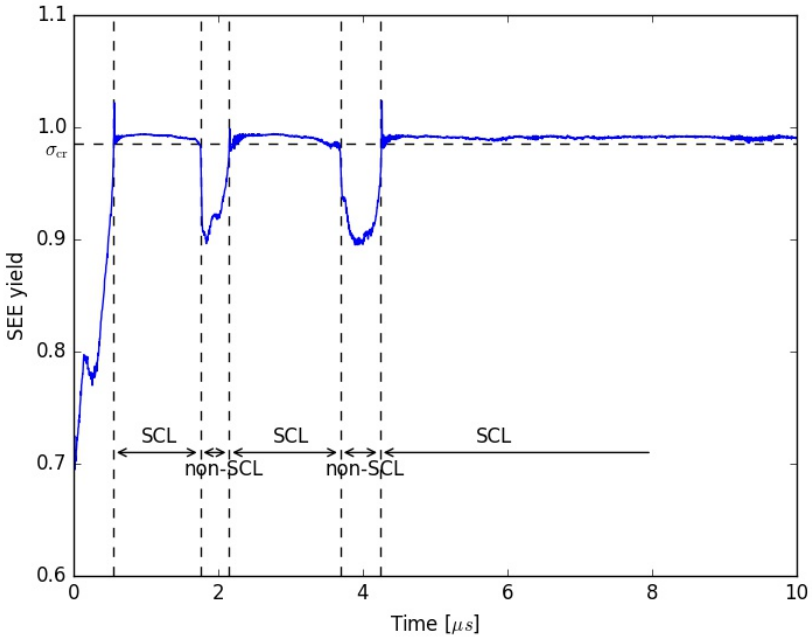

Figure 5.2 – Time evolution of the SEE yield, $\bar{\sigma}$, for Regime I. Are noted "SCL" the periods where $\sigma_{\mathrm{cr}} < \bar{\sigma}$, and "non-SCL" the periods where $\sigma_{\mathrm{cr}} > \bar{\sigma}$.

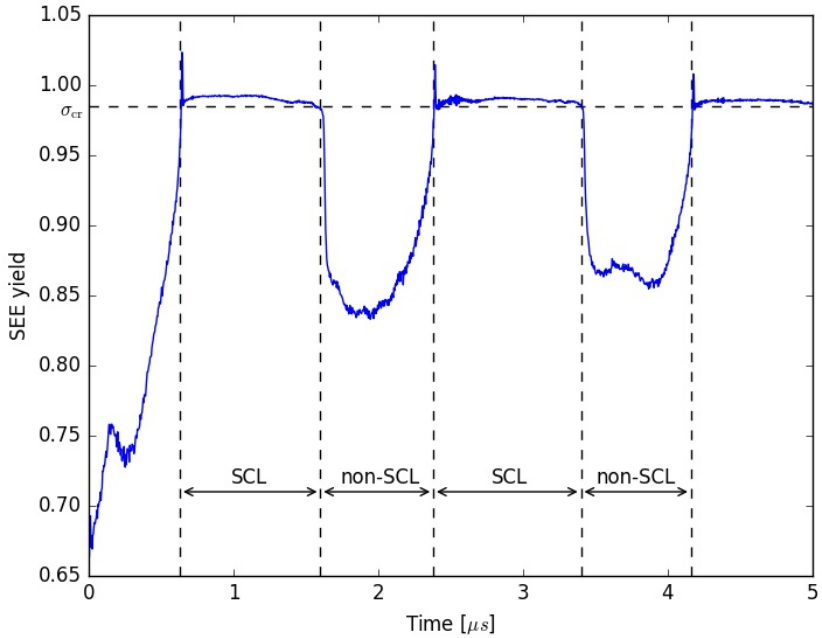

Figure 5.3 – Time evolution of the SEE yield, $\bar{\sigma}$, for Regime II. Are noted "SCL" the periods where $\sigma_{\mathrm{cr}} < \bar{\sigma}$, and "non-SCL" the periods where $\sigma_{\mathrm{cr}} > \bar{\sigma}$.

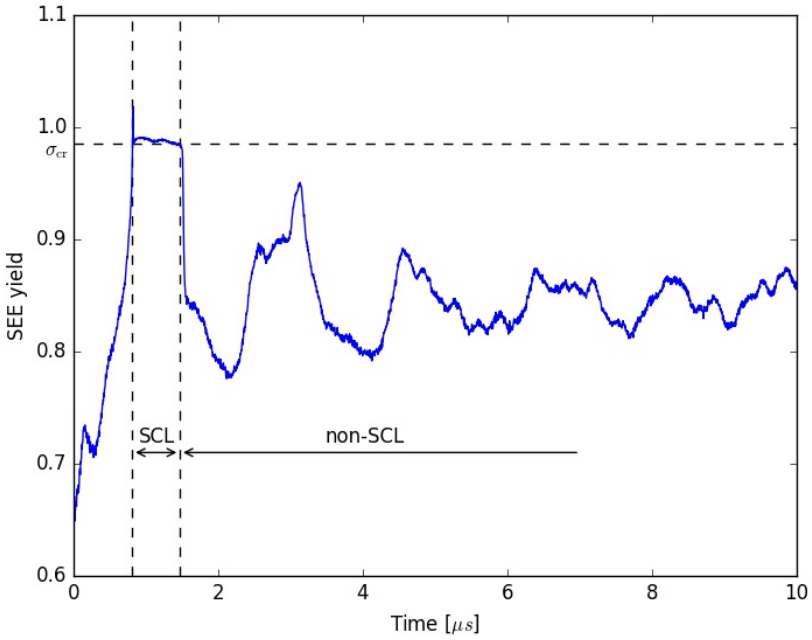

Figure 5.4 – Time evolution of the SEE yield, $\bar{\sigma}$, for Regime III. Are noted "SCL" the periods where $\sigma_{\mathrm{cr}} < \bar{\sigma}$, and "non-SCL" the periods where $\sigma_{\mathrm{cr}} > \bar{\sigma}$.

ing $\sigma_{\text{constant}} = 0.85$. Both comparisons showed good agreement in the way the plasma discharge is affected by the SEE processes. Results from these simulations are not shown in the present manuscript.

Regime I

Regime I is characterized at saturation by $\sigma_{\text{cr}} < \bar{\sigma} < 1$. Despite some initial oscillations of $\bar{\sigma}$ between 0.9 and 1.0, after a final "burst" with $\bar{\sigma} > 1$ for a short amount of time, the system stabilizes at $\sigma_{\text{cr}} < \bar{\sigma} < 1$. The SCL regime is stable from this last burst.

Using an even lower value of ϵ^* (for example $\epsilon^* = 25\text{eV}$) leads to the disappearance of the initial oscillations and to its stabilization after the first burst.

Regime III

Regime III is characterized by the inability of the SEE yield to reach σ_{cr} steadily. In the presented case with $\epsilon^* = 50\text{eV}$, the SEE yield reaches σ_{cr} at the beginning of the simulation after an initial "burst", but finally stabilizes at a lower value. By using an even higher value of ϵ^* (for example $\epsilon^* = 60\text{eV}$), the ignition burst and "plateau", where $\bar{\sigma} > \sigma_{\text{cr}}$, is not even observed.

Thus this Regime III is a case where the SEE yield stabilizes at values lower than σ_{cr}, typically $\bar{\sigma} \approx 0.85$ for $\epsilon^* = 50\text{eV}$. This stabilization value is observed to be lower for higher values of ϵ^*.

Regime II

Regime II is characterized by a pseudo-periodic oscillation between the two previously described regimes. Indeed, as shown by Figure 5.3, the SEE yield shows pseudo-periodic oscillations between "plateaus" where the SEE yield, $\bar{\sigma}$, is higher than σ_{cr}, and "valleys" where the yield has a value of approximately 0.8. Thus Regime II is considered as a low frequency oscillation between the two previous regimes at saturation: the "valleys" show the features corresponding to the Regime III at saturation, while the "plateaus" show the features corresponding to the Regime I at saturation.

In order to confirm the durability of the oscillations observed in this regime, a longer run ($40\mu s$ long) was done, showing the same pseudo-periodicity of the relaxation process. This is highlighted by Figure 5.5, where the effects of these SEE yield oscillations on the plasma potential can be observed.

These oscillations have a pseudo-periodicity of $\approx 2\mu s$, and are characterized by "plateaus" where SCL is featured. These plateaus are triggered by

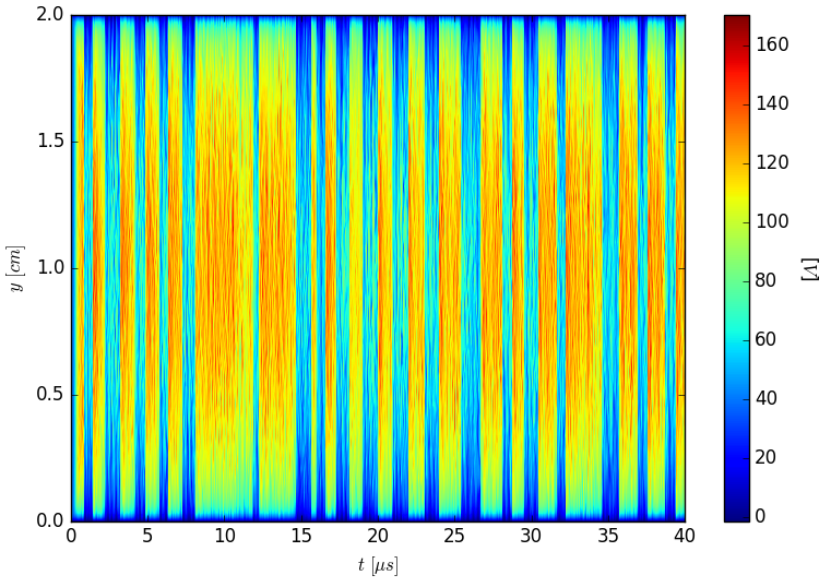

Figure 5.5 – Time evolution of the plasma potential from a 1D cut into the 2D domain. Cut taken along (Oy), at $x = L_x/2$. SEE processes as well as collisions are enabled, and the simulation is conducted on a longer time-scale in order to observe the pseudo-periodic oscillations' permanence.

a "burst", where the SEE yield is higher than 1 for a very short amount of time.

Nevertheless, as illustrated in Figure 5.6, the temporal evolution of the mean electron energy during the SCL regime does not feature the so-called "sawtooth" curve observed in 1D simulations [95, 97].

Since the Regime II is observed to be a pseudo-periodic oscillation between the Regimes I and II, it is chosen to call this behavior relaxation oscillations (RO) in the following.

Space charge limited (SCL)

Following Equation 5.4, and as already presented in Section 5.1, if $\bar{\sigma} > \sigma_{\text{cr}}$, the sheath potential is expected to be negative. This regime is called a space charge limited (SCL) [97] regime, and will be referred to as SCL in the following. Moreover as detailed in Section 5.1, in the case of a xenon plasma, we have $\sigma_{\text{cr}} \approx 0.985$ [95].

As observed in Figure 5.7, when $\bar{\sigma} > \sigma_{\text{cr}}$, the plasma potential profile near the wall features the typical "potential well". Moreover, as illustrated in Figure 5.8, the electron density profile is also changed when $\bar{\sigma} > \sigma_{\text{cr}}$, with

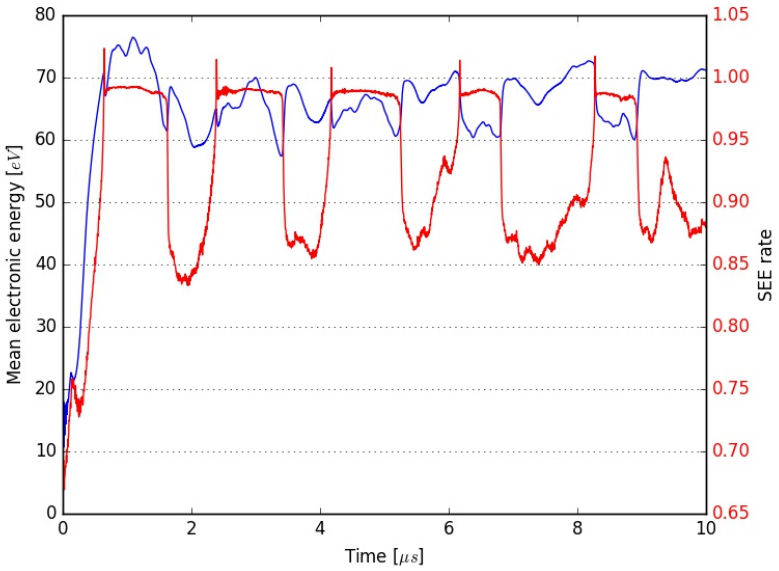

Figure 5.6 – Temporal evolution for Regime II of mean electron energy (blue) and SEE rate (red).

the expected trapped electrons near the wall [95, 97].

Nonetheless, the SCL is not observed to be a steady state as in comparable 1D simulations [95, 97]. Indeed during the SEE yield "plateau" (when $\bar{\sigma} > \sigma_{\mathrm{cr}}$), although the near-wall electron density shows only few changes, the "potential well" is not a stable state. The near-wall plasma potential oscillates during the RSO regime, between the "potential well" configuration and a configuration without sheath inversion. Thus, although the potential profile is significantly lower than in non-SCL, the plasma potential does not always show a sheath inversion when $\bar{\sigma} > \sigma_{\mathrm{cr}}$.

This perturbation can be further detailed, in the case of Regime II, by illustrating temporal evolution of near-wall values, as it is done in Figure 5.9. It is then possible to observe the fluctuations as a function of time. As already detailed, the plasma potential near the wall is periodically negative when $\bar{\sigma} > \sigma_{\mathrm{cr}}$, corresponding to the typical sheath inversion in SCL. However a perturbation periodically enhances the near-wall plasma potential.

At the same time, Figure 5.9 shows us, as Figure 5.8, that this perturbed SCL is characterized by a variation of the electron density near the wall. Although this variation is not as significant as for the plasma potential, it is still another observable characteristic.

Finally, fluctuations of the near-wall plasma potential as well as the elec-

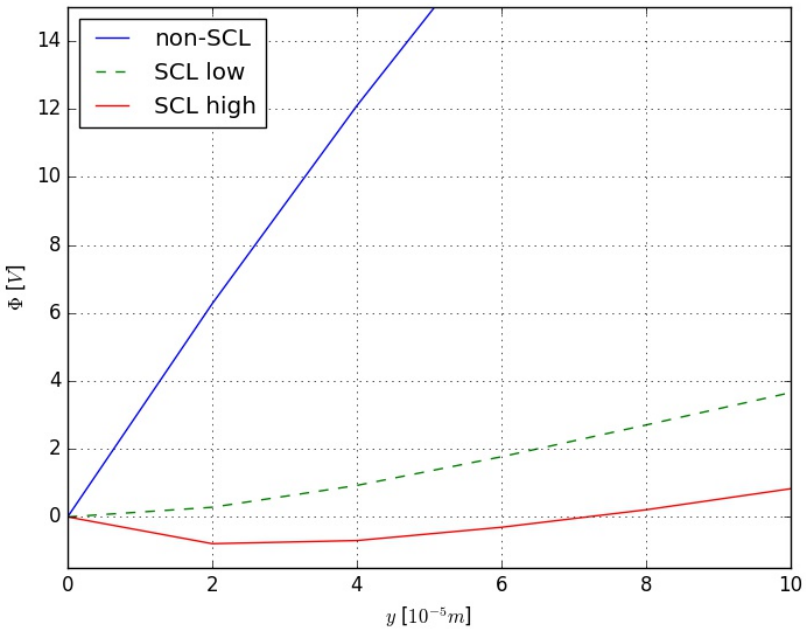

Figure 5.7 – Plasma potential profiles taken near the walls ($y = 0$) to compare between non-SCL (blue taken at $t = 2,4\,\mu$s) and SCL (green, taken at $t = 0,5\,\mu$s, and dashed red, taken at $t = 1,0\,\mu$s) measured from a Regime II simulation. SCL corresponds to $\bar{\sigma} > \sigma_{\mathrm{cr}}$, and non-SCL regime corresponds to $\bar{\sigma} < \sigma_{\mathrm{cr}}$. However, in the SCL, the plasma potential near the wall is not always negative, but oscillating between a "low" SCL where sheath inversion is observed (dashed red), and a "high" SCL (green).

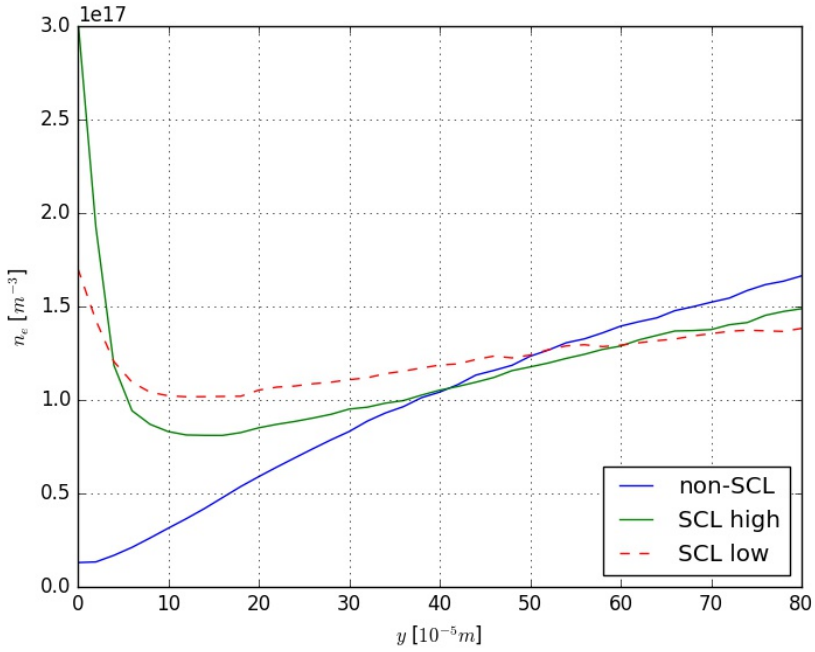

Figure 5.8 – Electron density profiles taken near the walls ($y = 0$) to compare between non-SCL (blue taken at $t = 2,4\,\mu$s) and SCL (green, taken at $t = 0,5\,\mu$s, and dashed red, taken at $t = 1,0\,\mu$s) measured from a Regime II simulation. SCL corresponds to $\bar{\sigma} > \sigma_{\mathrm{cr}}$, and non-SCL regime corresponds to $\bar{\sigma} < \sigma_{\mathrm{cr}}$. As highlighted here, both "low" SCL (dashed red) and "high" SCL (green) are characterized by trapped electrons near the walls.

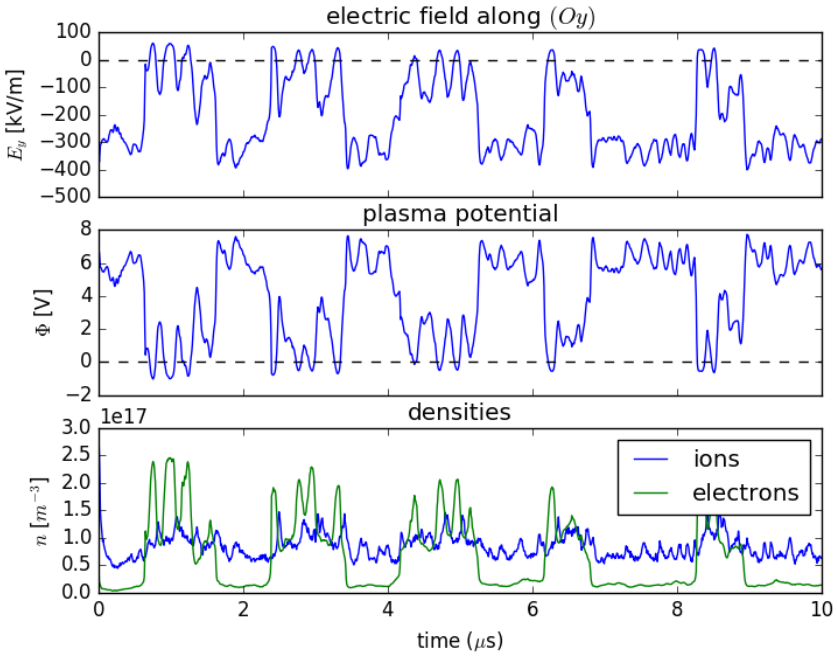

Figure 5.9 – Temporal evolution of near-wall values taken at $x = 0$ and $y < \lambda_{\mathrm{De}}$ for Regime II. Top: electric field along (Oy), center: plasma potential, bottom: charged particle densities (ions in blue, and electrons in green).

tron density during SCL feature a period of $\approx 0.2\mu$s. This period is corresponding to the 1D simulations from [95, 97] which observed a relaxation sheath oscillation (RSO), but is also coherent with a perturbation from the electron drift instability.

SEE yield oscillations and other physical properties

Figure 5.6 shows that when the characteristic SEE yield "bursts" occur, the electron energy significantly decreases. This can be explained by the injection of colder electrons from the walls due to SEE processes. Indeed as described in Section 3.2.1, the electrons injected in the plasma from the walls are thermalized at a given temperature, $T_{\text{see}} = 1$eV, that is significantly lower than the mean electron temperature in the plasma bulk. Another explanation could be the collapse of the sheath leading to a larger energy loss, and thus a decrease of T_e.

Most of the "bursts" are preceded by an increase in electron energy. This can be explained as an increase in the number of "hot" electrons, able to extract more than one electron, thus leading to a SEE yield higher than 1.

This is confirmed by Figure 5.10, where the electron flux at the walls is described. Indeed, it is highlighted that when a burst and, then, a "plateau" occur, a significant number of electrons hitting the walls extract more than one electron from the wall, leading to a SEE yield higher than 1.

Another observation can be made by comparing the mean plasma potential and the SEE yield. This is done in Figure 5.11. Highlighting observations made by comparing the Figure 5.3 and Figure 5.5, we can observe in Figure 5.11 that the plasma potential is evolving inversely to the SEE yield: indeed when the SEE yield is at a "plateau", the plasma potential is in its "valley", while when the SEE yield is in a "valley", the plasma potential is in a "plateau". This observation confirms results highlighted by 1D PIC/MCC simulations [97]. The plasma potential is expected to be lower when the SEE processes are stronger, as quantified in Equation 5.2.

5.3.2 Simulations without the electron drift instability

System definition

While Chapter 4 focused on a set-up with the electron drift instability without SEE, Section 5.3 concentrates on the investigation of a case with both SEE and the electron drift instability. Thus in order to complement the parametric study carried out in Section 5.3, it is necessary to be able to model a case where the SEE processes are present, while the electron drift instability

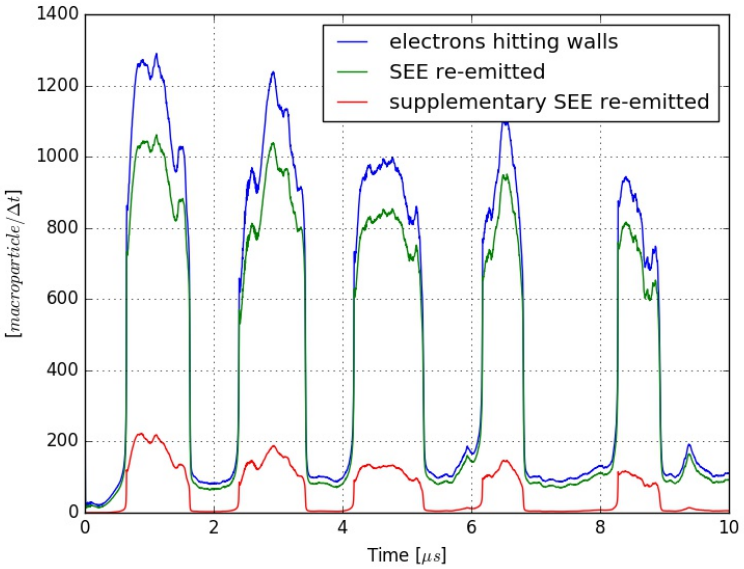

Figure 5.10 – Temporal evolution for Regime II of the number of macro-electrons hitting the walls (blue) at each time-step, and macro-electrons re-emitted as incident electron (green) and supplementary electrons extracted from the wall (red).

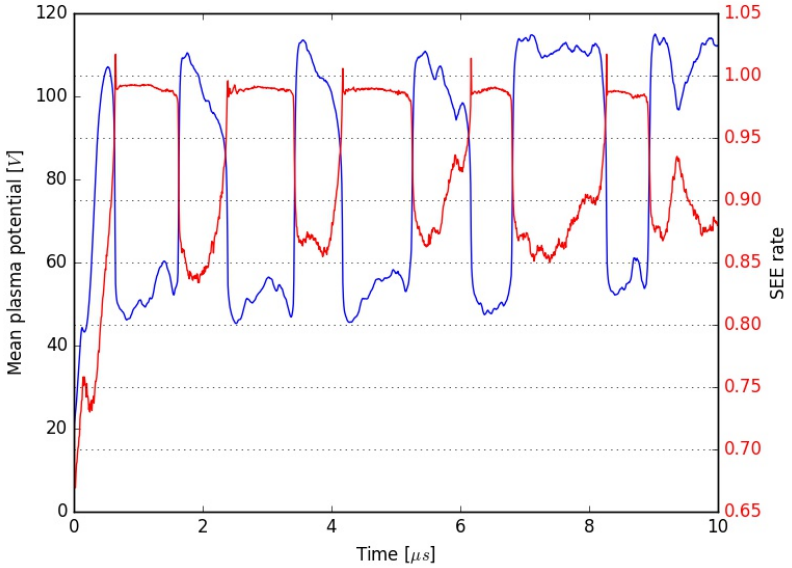

Figure 5.11 – Temporal evolution for Regime II of the SEE yield (red) and the mean plasma potential averaged over the plasma domain (blue).

is absent. This should allow us to reproduce results obtained by [97], and more properly detail the superposition of the electron drift instability and SEE effects.

In order to obtain a simulation set-up with SEE processes without any electron drift instability present, it is needed to downgrade the present simulation set-up to an approximately equivalent 1D model. Indeed, by preventing any unstable structure from forming in the (Ox) direction, it is possible to model a system without the electron drift instability.

This can be done by averaging at each time-step the value of the potential for each column of grid-cells in the (Oy) direction. This means that at each time-step the plasma profile along (Oy) (from one wall to another) is averaged along (Ox), and this value is used in order to estimate the electric field. By doing so no electric field along (Ox) can appear, since the electric field is obtained from the gradient of the potential. Thus, following the kinetic theory [69], and in particular Equation 4.10, no electron drift will form since $\langle n_e E_x \rangle = 0$ in the modeled system.

However a limitation of this model is the sensitivity of the simulation set-up to its initial conditions. Indeed, since the electric field along (Ox) is null, the particle velocities along (Ox) are only impacted through collisions with neutrals. Yet electron/neutral and ion/neutral collisions have been observed in Chapter 4 to play a minor role in the present simulation.

First simulation with $\epsilon^* = 45$eV

A first simulation can be done in this set-up using the same parameters as for Regime II from Section 5.3. In this case, we model grounded metallic walls, and use parameters from Table 3.3, with $\epsilon^* = 45$eV.

As expected, this simulation shows no presence of the electron drift instability. As illustrated in Figure 5.12, the plasma potential shows some perturbations at the simulation beginning, but once the system stabilizes, no electron drift instability is observed.

Now that the set-up is confirmed as valid, we can observe the SEE yield. This is illustrated in Figure 5.13. As observed, $\bar{\sigma}$ stabilizes at a very low value of approximately 0.69. This value is not comparable to the one observed with the same value of ϵ^* when the electron drift instability is present. Moreover no RSO are observed.

This can be easily understood since the electron drift instability is known to increase the electron temperature [42, 68]. Consequently the electron temperature in our system without the electron drift instability is much lower. The mean electron energies in all three directions are given in Figure 5.14. A quick comparison with Figure 3.4 shows that the averaged electron energy

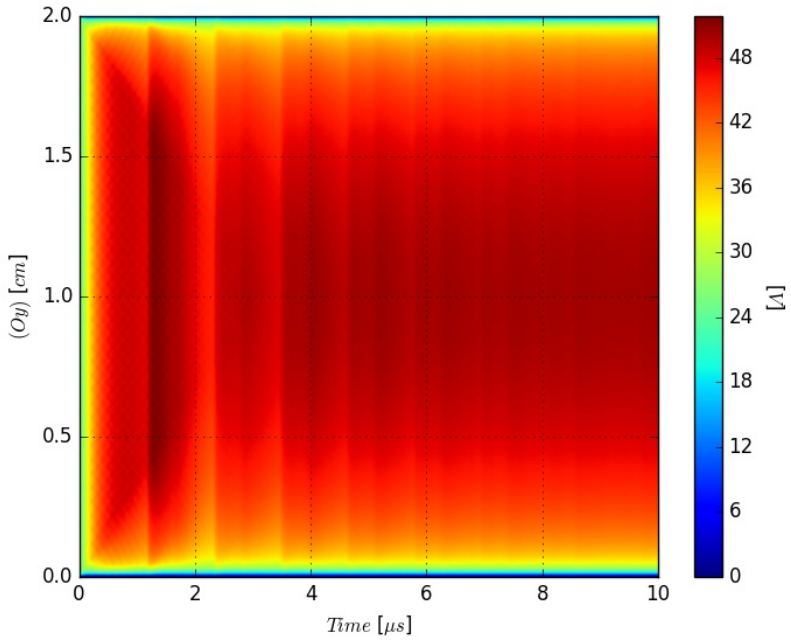

Figure 5.12 – Temporal evolution of the plasma potential taken along (Oy) at $x = L_x/2$. Despite initial perturbations the system does reach a steady state where no electron drift is observed, confirming the validity of the system set-up.

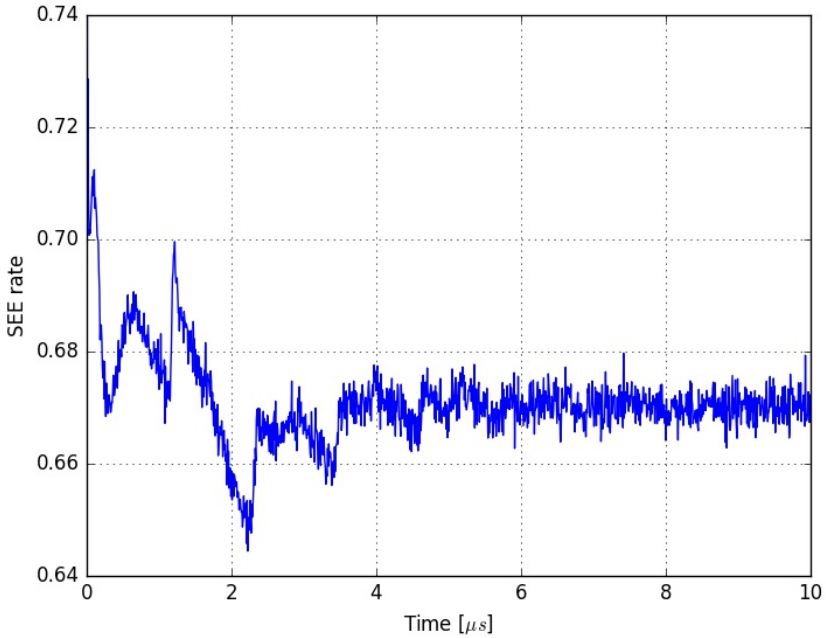

Figure 5.13 – Temporal evolution of the SEE yield, $\bar{\sigma}$, for a case without the electron drift instability but with linear SEE process ($\epsilon^* = 45$eV).

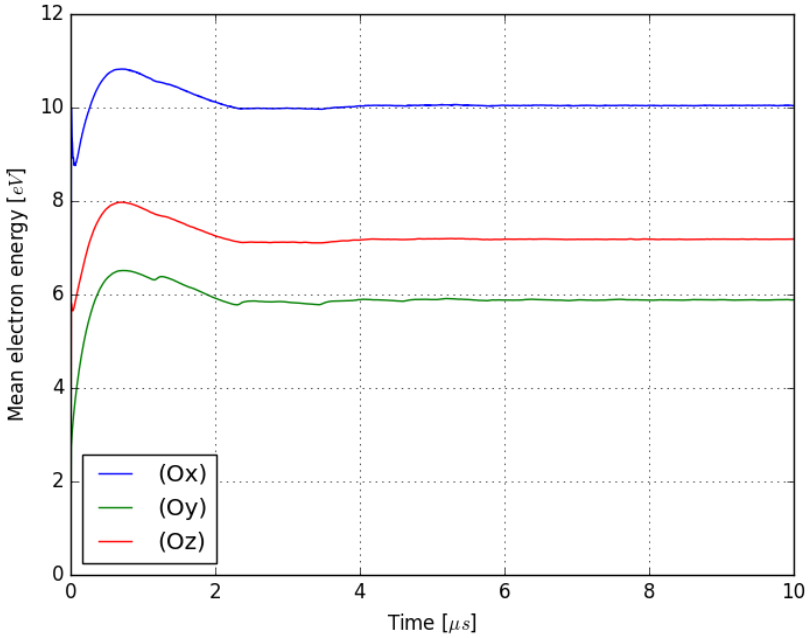

Figure 5.14 – Temporal evolution of the mean electron energies: (blue) along (Ox), (green) along (Oy), and (red) along (Oz). For a case without the electron drift instability but with linear SEE process ($\epsilon^* = 45$eV).

is indeed significantly lower in this set-up, where no electron drift instability is present.

Furthermore the absence of the electron drift instability in this model should set the electron cross-field mobility to a value coherent with the mobility obtained from the classical diffusion theory. Indeed in Figure 5.15, we can observe the radial profile (along (Oy)) of the electron mobility, averaged in time and along (Ox). As expected, in the plasma bulk, the measured mobility matches perfectly well with the classical mobility, while the effective mobility, estimated from the correlation term $\langle n_e E_x \rangle$, is null. Moreover Figure 5.15 highlights very explicitly the increased near-wall mobility due to the SEE processes. This increase of mobility is observed to be significant, with a mobility near the walls one order of magnitude larger than in the plasma bulk.

Since the electron mean energy is much lower than in the simulations from Section 5.3, where the electron drift instability is modeled, the value of ϵ^* needed to observe Regime II or III is much lower as well.

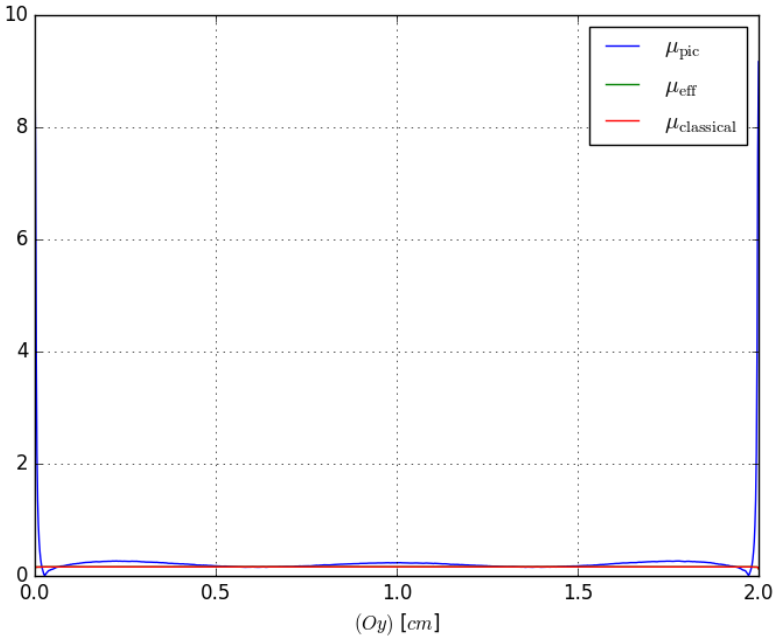

Figure 5.15 – Radial profile (along (Oy), from one wall to another) of the electron mobility, averaged in time and along (Ox): (blue) the mobility directly measured from the simulation, (red) the mobility obtained from the classical diffusion theory, and (green) the mobility estimated from the correlation term, which is, as expected, zero in this simulation set-up. For a case without the electron drift instability but with linear SEE process ($\epsilon^* = 45$eV).

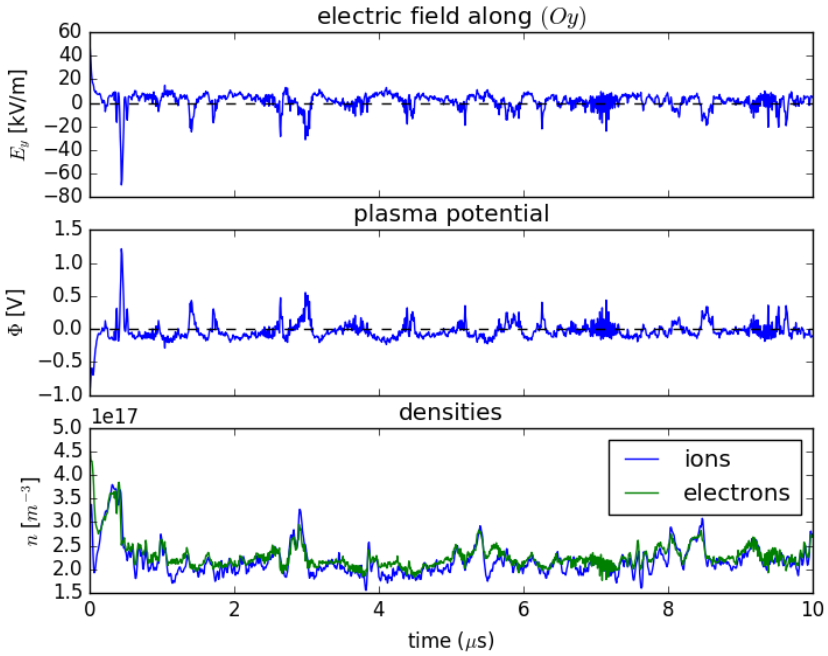

Figure 5.16 – Temporal evolution of near-wall values taken in $x = 0$ and $y < \lambda_{De}$ for Regime II. Top: Electric field along (Oy), center: Plasma potential, bottom: charged particle densities (ions in blue, and electrons in green). For a case without the electron drift instability but with linear SEE process ($\epsilon^* = 10$eV) featuring .

RO without the electron drift instability

In order to model the RO observed in Section 5.3, the value of ϵ^* is lowered until a SCL regime is observed. This is reached with $\epsilon^* = 10$eV. Indeed in this case we can observe a sheath inversion as well as trapped secondary electrons in the sheath. This can be highlighted by plotting the corresponding physical values near the walls (i.e. less than one Debye length from the wall). Figure 5.16 illustrates these observations.

Indeed it shows a negative potential inside the sheath corresponding to an electron density higher than the ion density. These features observed inside the sheath are characteristics of a SCL regime. Moreover the SCL regime is here characterized by its stability in contrast to the results observed in Section 5.3.1.

Finally, an oscillation is observed between SCL and non-SCL cases. However this oscillation does not show any clear pseudo-periodicity as for [97], and results from Section 5.3.1. These oscillations are observed as well in the

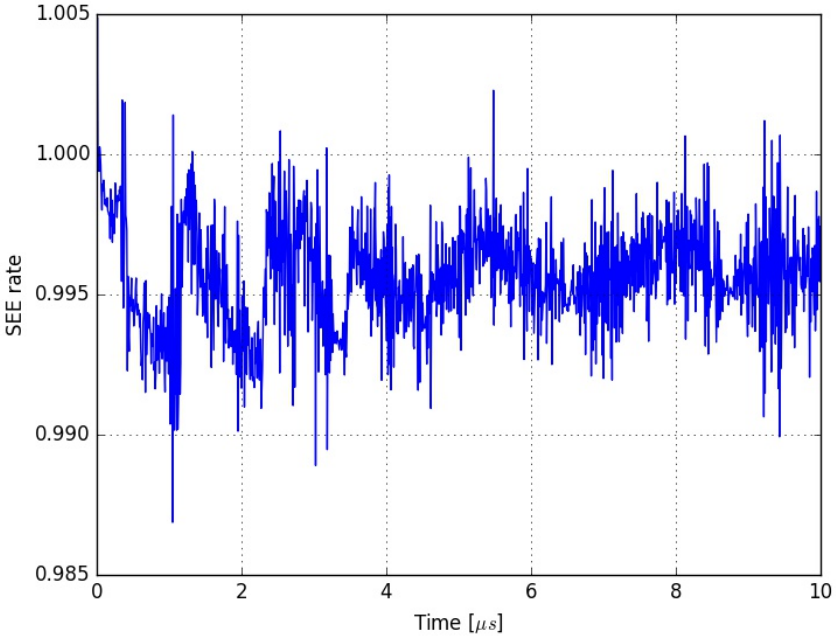

Figure 5.17 – Temporal evolution of the SEE yield in the case where oscillations are observed between a non-SCL and a SCL regime. No electron drift is here observed, since the system is changed in order to be 1D equivalent.

SEE yield, illustrated in Figure 5.17, despite a noisier behavior than in the case with the electron drift instability observed.

This result is quite different from the ones obtained in 1D by [97]. Another difference is observed with the electron energy temporal evolution. While 1D results observe a clear behavior, the present work does not observe any clear tendency. 1D results from [97], and the present 2D simulations do feature a common geometry and set-up, however an important point is that the results obtained in 1D used an imposed additional collision frequency to model the anomalous transport, while the present work does not, since we have artificially "turned off" the electron drift instability. Proper impact of this modeling should be investigated to correctly conclude on the observed differences.

Another observation is made by observing the temporal evolution of the plasma potential from one wall to another (i.e. along (Oy)). This is shown in Figure 5.18, and highlights, after some initialization time of 1μs, streams of secondary electrons being injected from the walls inside the plasma bulk. These streams are injected with a velocity of $\approx 2.5 \text{kms}^{-1}$, and are damped

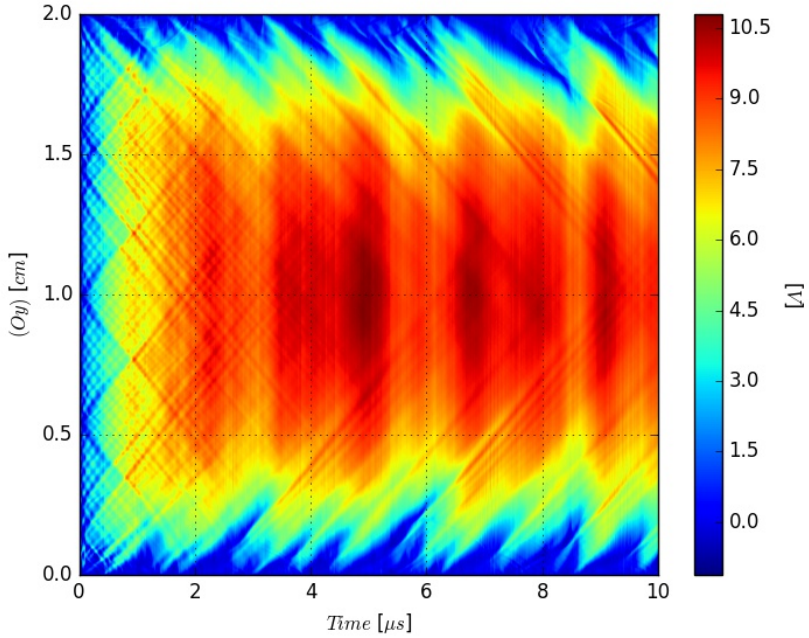

Figure 5.18 – Temporal evolution of the plasma potential taken along (Oy) in $x = L_x/2$. Case 1D equivalent, where ϵ^* is set-up in order to observe a RO regime.

in the plasma bulk.

The impact of these injected streams can also be observed on the electron mobility profile, as highlighted in Figure 5.19. Indeed the near wall enhanced mobility is not confined to the sheaths anymore, but oscillations from the walls are observed deeper in the plasma bulk.

Low ϵ^* values

The value of ϵ^* is further lowered, until the SEE yield saturates at values corresponding to $\bar{\sigma} \approx 1$, as illustrated in Figure 5.20. This is obtained by setting $\epsilon^* = 5$eV.

Moreover, the SCL regime is in this case steady, with a stable sheath inversion, as illustrated in Figure 5.21. Indeed we observe here that the plasma potential shows typical negative values near the walls. The very strong electron emission is responsible for the very low plasma potential in the bulk, as well as the negative potential in the very large sheaths.

Furthermore, this simulation featuring a particularly strong SEE, shows turbulent behavior, as highlighted by Figure 5.22. Streams observed in the

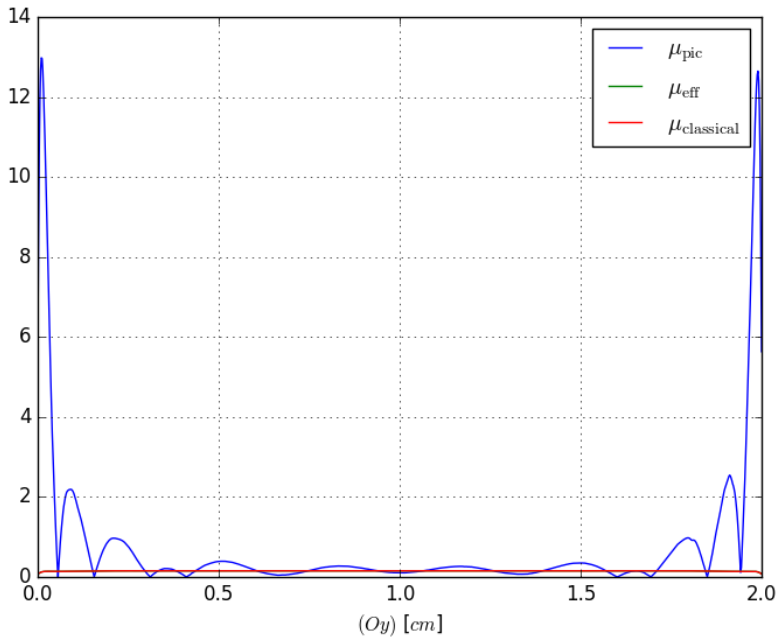

Figure 5.19 – Radial profile (along (Oy), from one wall to another) of the electron mobility, averaged in time and along (Ox): (blue) the mobility directly measured from the simulation, (red) the mobility obtained from the classical diffusion theory, and (green) the mobility estimated from the correlation term, which is, as expected, null in this simulation set-up.

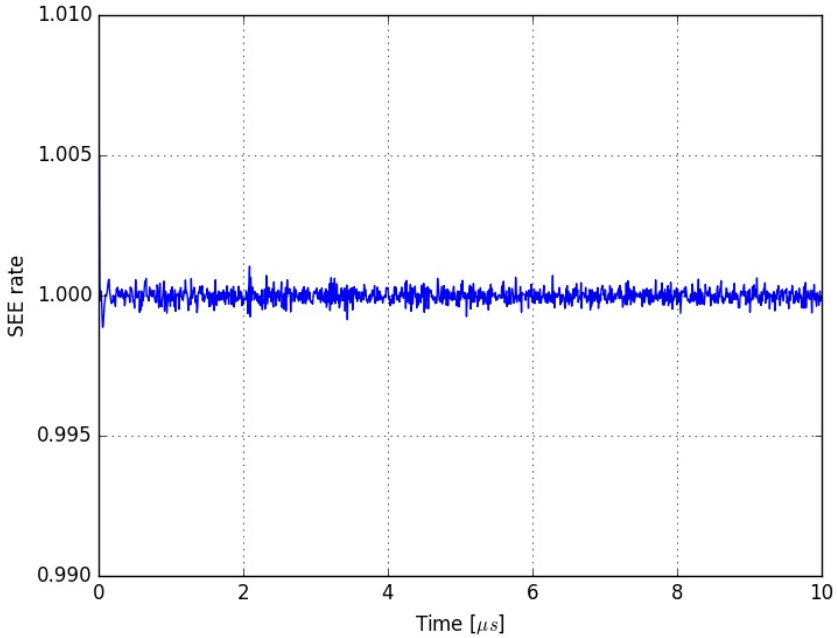

Figure 5.20 – Temporal evolution of the SEE yield for the case without the electron drift instability, and $\epsilon^* = 5$eV.

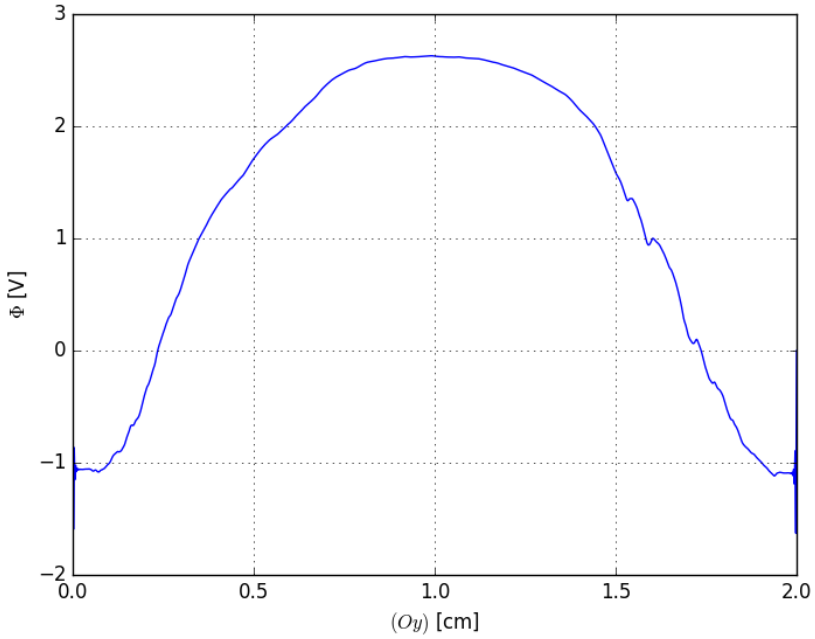

Figure 5.21 – Plasma potential profile along (Oy) averaged in time and along (Ox), for the case without the electron drift instability, and $\epsilon^* = 5\text{eV}$.

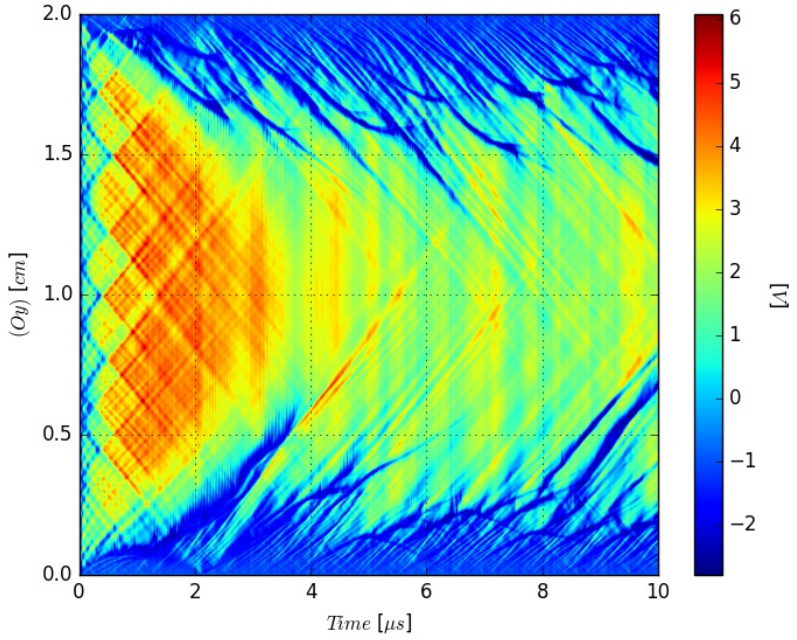

Figure 5.22 – Temporal evolution of the plasma potential taken along (Oy) at $x = L_x/2$.

previous case now sometimes show a velocity decrease when entering the plasma bulk.

This turbulence impacts directly the electron mobility. As observed in Figure 5.23, the near-wall enhanced mobility in the latest case is higher than in the oscillating case, which is expected since the SEE is stronger. But the effect of the SEE on the electron mobility inside the plasma bulk, observed in the previous oscillating case, is weaker here.

Now that the impact of SEE have been investigated in a case where no electron drift instability is present, the impact of the electron drift instability and SEE superposition have to be properly characterized. Indeed it has been shown that the electron drift instability has a significant impact on SEE features, such as an unstable SCL regime, but the effect of SEE on the electron drift instability, and on the electron anomalous transport have not been characterized, yet.

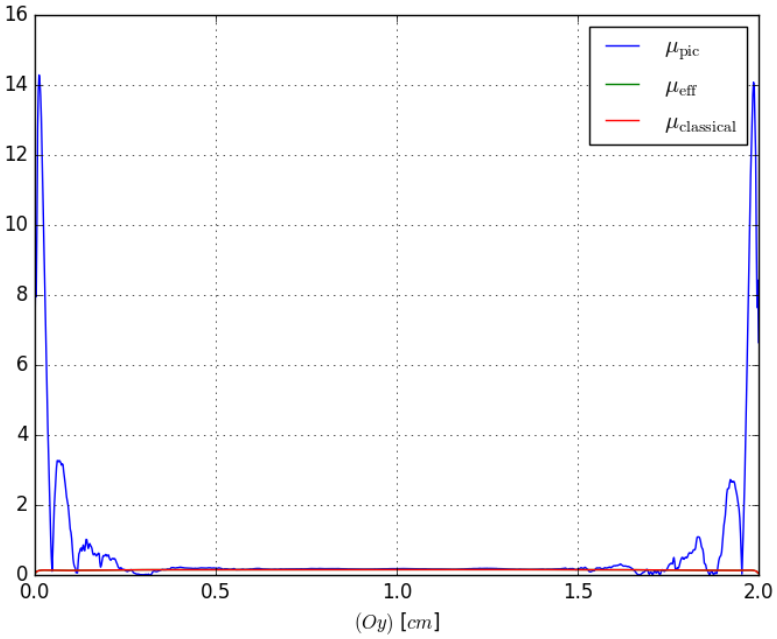

Figure 5.23 – Radial profile (along (Oy), from one wall to another) of the electron mobility, averaged in time and along (Ox): (blue) the mobility directly measured from the simulation, (red) the mobility obtained from the classical diffusion theory, and (green) the mobility estimated from the correlation term, which is, as expected, null in this simulation set-up.

5.3.3 SEE effects and the electron drift instability

Studying the simulations featuring a superposition of the SEE processes and the electron drift instability, detailed in Section 5.3.1, we now investigate the effect of this superposition on the electron drift instability characteristics.

To this end, these results have to be compared to the ones from Chapter 4 (Section 4.3.2, n_0 case), where no SEE process was present, as well as with the kinetic theory developed in [69].

Measurements of the electron drift instability features, in the cases described in Section 5.3.1, show that, through all three regimes studied in this work, the values measured to characterize the electron drift instability did not vary significantly. Thus the values obtained from the simulations of wavelength, frequency, phase velocity, as well as $|\delta\widetilde{n}_e|/n_e$ and $|\delta\widetilde{\Phi}|/T_e$, are perfectly coherent with the values obtained without SEE processes, and described in Chapter 4. These values are not shown here.

Furthermore, as observed for simulations without SEE processes in Chapter 4, and detailed in Section 4.2.2, ion trapping is observed in all cases with SEE processes, leading to the saturation of the electron drift instability.

Finally these values being equal to those without SEE, the measurements remain coherent with the kinetic theory developed in [69], as compared in Section 4.2.1.

It is then concluded that the electron drift instability is not affected by the presence of SEE processes. Indeed, in all three identified regimes, the expected instability characteristics are conserved, even despite the plasma potential being significantly lowered by SEE processes. As it was shown in Figure 5.5 for Regime II, the plasma potential varies due to the RSO with a $\approx 2\mu$s pseudo-period that is superimposed, without significant interference, on the plasma potential variations due to the electron drift instabilities.

5.3.4 SEE and anomalous transport

As shown previously the SEE does not affect the electron drift instability characteristics. However, SEE processes are shown to decrease the plasma potential, and thus increase the flux of electrons from plasma to the wall [113]. Consequently, as shown in Section 5.3.2, this process is expected to have an impact on the electron cross-field transport, since electron/wall non-absorbent collisions, and consequent electron scattering, are increasing the electron cross-field transport.

In order to compare the effect of SEE on the anomalous transport, the radial profile (profile along (Oy) in the Cartesian coordinates system used, direction in which the system is closed by the walls) of the mobility is mea-

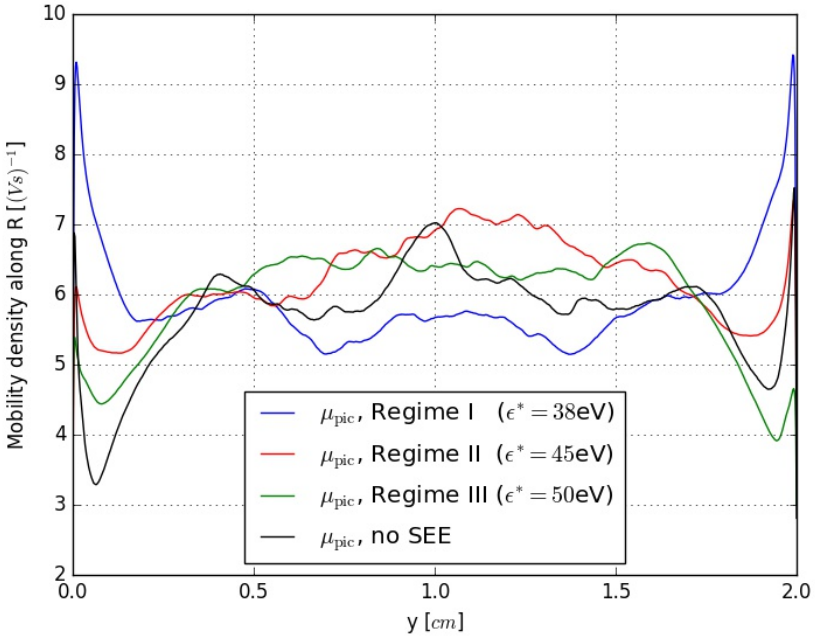

Figure 5.24 – Radial profile of the measured mobility, μ_{pic} (Equation 4.9), for all three regimes and the case without SEE.

sured for the three regimes, as well as for the n_0 case from Section 4.3.3, without any SEE process. This profile is obtained by averaging the cross-field electron mobility over the (Ox) direction, as well as over time.

The electron mobility measured from the simulation, μ_{pic} from Equation 4.9, is estimated by interpolating the mobility measured for each electron on the surrounding cells. This interpolation is done through a linear scheme, as detailed in Section 2.3.2 for the density weighting. Moreover by averaging the measured mobility over time and along both geometrical directions, we obtain a scalar mean mobility, noted μ_{pic}, corresponding to Equation 4.9 from Section 4.2.3.

The obtained profiles are shown in Figure 5.24, while the averaged scalars are summed up in Table 5.3. Temporal evolutions of the mobility averaged over the geometrical domain are not presented, but show comparable evolutions to Figure 4.6.

As observed in Figure 5.24, despite the fact that the radial profiles does not show any clear tendency in the system center, except for Regime I which is significantly lower, we can observe a clear change near the walls due to the SEE regime. Indeed the electron cross-field mobility seems to be higher

near the walls in the case of a Regime with a lower ϵ^*. This corresponds to a higher near wall mobility with stronger SEE, as already highlighted by [97] and Section 5.3.2.

However, this mobility increase near the walls, correlated with the strength of the SEE, does not deeply change the global value of the electron mobility. As expressed in Table 5.3, the mean value of μ_{pic} averaged along (Ox), (Oy), and in time does not vary significantly with the presence or strength of SEE.

Nonetheless, it is necessary to estimate the respective contributions of the SEE and the electron drift instability to the anomalous electron transport observed in the simulation. This can be done by estimating the effective mobility, μ_{eff} from Equation 4.10. Indeed Chapter 4 showed that the anomalous electron mobility due to the electron drift instability, as it is described in the kinetic theory developed in [69, 11], is well described by μ_{eff}. This allows us to highlight the role on electron anomalous transport of the so-called correlation term, $\langle n_e E_x \rangle$, where n_e is the electron density, and E_x the electric field along the (Ox) axis.

Following Equation 4.10, this value can be estimated directly from the simulations. Consequently, radial profiles can be plotted, as done for μ_{pic}, and the result is shown in Figure 5.25. The time and space averaged value is given in Table 5.3.

Following the kinetic theory expressed in Chapter 4, the effective mobility at saturation, $\mu_{\text{eff}}^{\text{sat}}$, can be analytically estimated following Equation 4.15. The obtained values for each regime are summarized in Table 5.3.

Values summarized in Table 5.3 are exposed to the same error margins as previous comparable estimates in this work. Indeed, T_e is measured from $< \epsilon_e >$, and is therefore exposed to an error margin of $\approx \pm 5\,[\text{eV}]$. Moreover, the PIC values of electron mobilities are directly measured from the PIC simulations, thus having an approximately $\pm 0.5\,[\text{m}^2\text{V}^{-1}\text{s}^{-1}]$ error margin, while the analytical values have an error margin of $\approx \pm 0.1\,[\text{m}^2\text{V}^{-1}\text{s}^{-1}]$, due to the measurements of T_e and ν_m.

The observation of Table 5.3 highlights the fact that the value of μ_{eff}, as well as μ_{eff}^{sat}, shows a decrease when the SEE processes get stronger (which corresponds to a lower ϵ^* in the linear model used). This can be explained as the mean electron temperature, $< T_e >$, which is derived from a direct measurement of the mean electron energy, $< \epsilon_e >$, decreases in the same time.

An illustration can be found in Figure 5.25, where a major difference between Regime I and the three other cases is observed. Indeed, in Regime I, where the SEE is the strongest, the effective mobility seems to be lower in the center of the system than for the three others, while near the wall, the effective mobility is greater. Moreover this regime shows a significantly lower

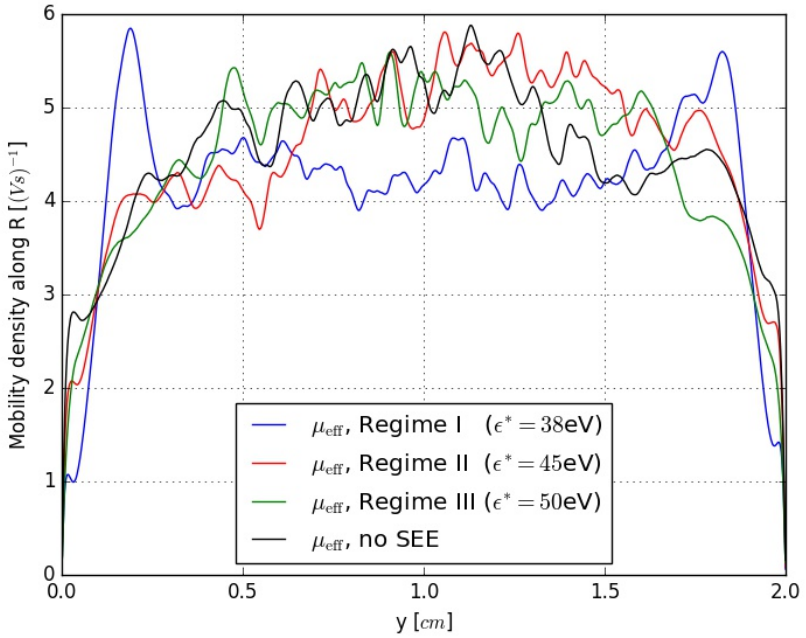

Figure 5.25 – Radial profile of the measured effective mobility, μ_{eff} (Equation 4.10), for all three regimes and the case without SEE.

mean electron temperature.

In these simulations, it appears that, despite a strong effect on the plasma potential, the SEE processes do not impact directly the electron anomalous transport in a global way. However, as highlighted by the evolution of μ_{eff} in Table 5.3, the contribution to the anomalous transport of the electron drift instability, despite not being impacted on its characteristics, is lower with a higher SEE emissions.

Indeed another impact of the SEE is the lowered electron temperature, T_e, already observed in 1D simulations [97], that directly affects the contribution of the electron drift instability to the anomalous transport. Consequently the SEE processes show an indirect effect on the anomalous electron transport. Nonetheless the reduced contribution of the electron drift instability is almost perfectly compensated by the added near-wall mobility generated by the strong SEE process. Thus SEE processes and electron-drift instability appear to be working in a coupled way [42], with the electron temperature as the key component for this coupling.

However, as highlighted in this study, the electron drift instability seems to bring the major contribution to the electron anomalous transport, while

Table 5.3 – Comparison of physical values associated with the anomalous transport for all three regimes and a case without any SEE.

Regime	PIC values		
	μ_{pic} (Eq. 4.9) $[\text{m}^2\text{V}^{-1}\text{s}^{-1}]$	μ_{eff} (Eq. 4.10) $[\text{m}^2\text{V}^{-1}\text{s}^{-1}]$	$< T_e >$ [eV]
I	5.6	4.1	40
II	5.8	4.6	44
III	5.6	5.4	48
no SEE	5.8	5.6	50
Regime	Analytical values		
	$\mu_{\text{eff}}^{\text{sat}}$ (Eq. 4.15) $[\text{m}^2\text{V}^{-1}\text{s}^{-1}]$	$\mu_{\text{classical}}$ (Eq. 4.7) $[\text{m}^2\text{V}^{-1}\text{s}^{-1}]$	
I	3.4	0.2	
II	3.6	0.2	
III	3.7	0.2	
no SEE	4.2	0.2	

SEE processes play only an auxiliary role. Indeed the effect of the SEE on the anomalous electron transport is weaker and spatially located near the walls. Thus, SEE processes could play a more significant role in a geometrically smaller thruster.

5.4 Power balance and global model

In Section 3.1.5, a first attempt was proposed to obtain the electron temperature from the simulation set-up and parameters by estimating the electron temperature at equilibrium using a power balance. This has been done in a case without any SEE processes modeled, and without taking the (Oy) direction into account. Thus this model has to be extended in order to take SEE, as well as geometrical effects, into account. Using the SEE model described in Section 3.2.2, we perform a parametric study over the value of ϵ^*, and compare results from the model to results from the PIC/MCC simulations.

Consequently, numerous PIC/MCC simulations were done to cover a wide range of ϵ^* values. All the simulations were done using $\sigma_{\max} = 2.9$ and $\sigma_0 = 0.5$. The ϵ^* values covered by the PIC simulations were: 3.0 eV, 8.0 eV,

15.0 eV, 30.0 eV, 38.0 eV, 40.0 eV, 45.0 eV, 50.0 eV, 55.0 eV, 60.0 eV, 100.0 eV, and 200.0 eV.

5.4.1 Global model presentation

In the model used, the system is volume-averaged, and the assumptions made in Section 3.1.5 are kept. Thus, for each value of ϵ^*, the value of the electron temperature at steady state is obtained by equalizing the power absorbed by the electrons, P_{abs}, with the power lost by the electrons in all three directions, P_{loss}, at steady state.

On the one hand, the power absorbed by the electrons in the system, P_{abs}, is obtained by:

$$P_{\text{abs}} = (J_{ez}E_0 + J_{ex}E_x + J_{ey}E_y)L_xL_yL_z \tag{5.5}$$

However, it has been measured in the PIC/MCC simulations that $J_{ex}E_x + J_{ey}E_y$ is negligible in comparison to $J_{ez}E_0$. Thus:

$$P_{\text{abs}} \approx J_{ez}E_0\, L_xL_yL_z \tag{5.6}$$

P_{abs} is obtained by Equation 5.6, where the electron cross-field mobility is given by:

$$\mu_{\text{eff}} = \frac{< v_z >}{E_0} = \frac{J_{ez}}{E_0\, n_e\, q} \tag{5.7}$$

with $< v_z >$ the mean electron velocity along the (Oz) axis at steady state, and J_{ez} the mean electron current along (Oz) at steady state.

By rewriting Equation 5.7 as $J_{ez} = qn_e\mu_{\text{eff}}E_0$, and substituting it into Equation 5.6, we obtain:

$$P_{\text{abs}} = q\, n_e\, \mu_{\text{eff}}^{sat}\, E_0^2\, L_xL_yL_z \tag{5.8}$$

where μ_{eff}^{sat} is the electron cross-field mobility at saturation obtained from the kinetic theory [69], and already expressed in Equation 4.15.

On the other hand, the lost power in the system is the sum of the power lost to the two walls closing the (Oy) direction, $P_{\text{loss,w}}$, and the power lost along the (Oz) axis, $P_{\text{loss,z}}$ (the (Ox) direction being closed by periodic boundaries, no power is lost along this axis). Which gives us: $P_{\text{loss}} = P_{\text{loss,w}} + P_{\text{loss,z}}$.

The power lost along (Oz) can be expressed from the value of the flux at the (Oz) boundary, where no sheaths are present (since E_0 is not self-consistently obtained from charge density along (Oz)), by substituting $J_{ez} = q\Gamma_{e,z}$ into Equation 3.12. This gives us:

$$P_{\text{loss,z}} = q\,\Gamma_{e,z}\, 2.3 \times 2T_e\, L_xL_y \tag{5.9}$$

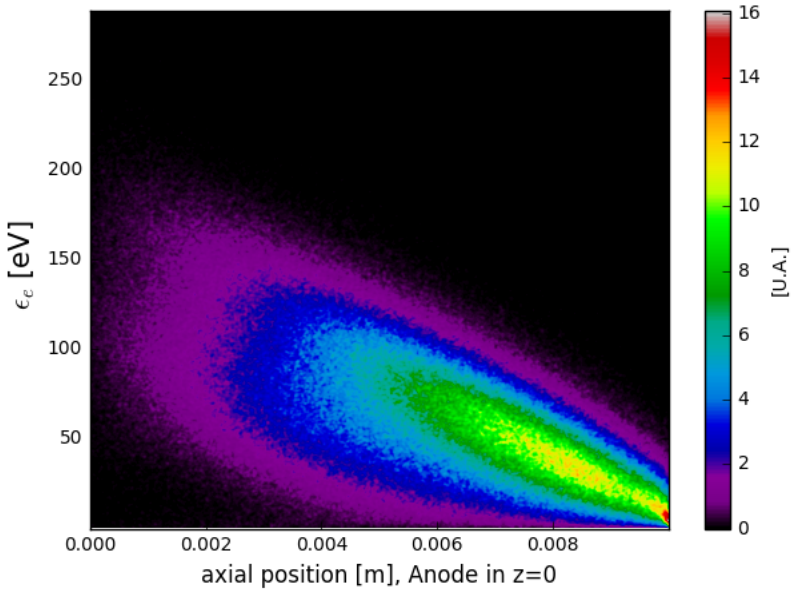

Figure 5.26 – Distribution along (Oz) of the electron energy distribution. "Cold" electrons are injected in $z = z_{max}$, accelerated by the imposed electric field, E_0, and reaches the anode $(z = 0)$ with a mean energy 2.3 times higher than the mean electron energy in the system.

where $\Gamma_{e,z}$ is the electron flux at the boundary. Then $\Gamma_{e,z}$ can be expressed as:

$$\Gamma_{e,z} = n_e \, v_z = n_e \, \mu_{\text{eff}}^{sat} \, E_0 \tag{5.10}$$

where, as already highlighted, μ_{eff}^{sat} is obtained from Equation 4.15. Furthermore the 2.3 coefficient inserted in Equation 5.9 in order to obtain the value of the electron energy at the wall, is measured from the simulation. Indeed the mean electron energy at the anode $(z = 0)$ is measured as 2.3 the mean electron energy measured in the whole system. This is illustrated in Figure 5.26.

In a similar manner, the lost power along (Oy) at steady state, $P_{\text{loss,w}}$, can be easily obtained from the electron energy flux at the walls, $Q_{e,w}$, by:

$$P_{\text{loss,w}} = Q_{e,w} \, 2L_x L_z \tag{5.11}$$

$Q_{e,w}$ takes into account the electrons hitting the walls after being accelerated by the sheath, as well as the electrons re-emitted from the walls at a temperature T_{see} (given in Table 3.3) and accelerated into the plasma bulk by the

sheath. Similarly to Section 3.1.5, integration of the electron fluxes at the sheath edge gives us:

$$< \epsilon >_w = \Delta\Phi_{\text{tot}} + 2T_e \tag{5.12}$$
$$< \epsilon >_{\text{see}} = \Delta\Phi_{\text{tot}} + 2T_{\text{see}} \tag{5.13}$$

With $< \epsilon >_w$ the mean energy of electrons hitting the walls, $< \epsilon >_{\text{see}}$ the mean energy of electron re-emitted from the walls by SEE, and $\Delta\Phi_{\text{tot}}$ the total potential drop in the sheath and pre-sheath. Thus we obtain the electron energy flux at the walls:

$$\begin{aligned} Q_{e,w} &= q\,\Gamma_{e,w} \ < \epsilon >_w \ - q\,\Gamma_{e,\text{see}} \ < \epsilon >_{\text{see}} \\ &= q\,\Gamma_{e,w}(\Delta\Phi_{\text{tot}} + 2T_e) - q\,\bar{\sigma}\,\Gamma_{e,w}(\Delta\Phi_{\text{tot}} + 2T_{\text{see}}) \end{aligned} \tag{5.14}$$

Where $\Gamma_{e,w}$ is the electron flux at the walls at steady state, $\Gamma_{e,\text{see}}$ is the electron flux emitted from the wall by SEE processes, and $\bar{\sigma}$ is the fraction of electron flux re-emitted by the walls through SEE processes at steady state, as already defined in Section 3.2.1. Following [93], $\Gamma_{e,w}$ can be expressed as:

$$\Gamma_{e,w} = \frac{1}{4} n_e\, v_{th}\, \exp\left[-\frac{\Delta\Phi_{\text{tot}}}{T_e}\right] \tag{5.15}$$

where $v_{th} = \sqrt{\frac{8q\,T_e}{\pi m_e}}$ is the electron thermal speed, defined in Section 3.1.5. Moreover the total potential drop $\Delta\Phi_{\text{tot}}$ is the sum of the sheath potential drop, $\Delta\Phi_s$, and the pre-sheath potential drop, $\Delta\Phi_{p-s}$, as respectively defined in Equations 5.2 and 1.23, thus:

$$\Delta\Phi_{\text{tot}} = \Delta\Phi_s + \Delta\Phi_{p-s} = \frac{k_B T_e}{e}\, ln\left[(1-\bar{\sigma})\sqrt{\frac{m_i}{2\pi m_e}}\right] + \frac{T_e}{2} \tag{5.16}$$

Finally $\bar{\sigma}$ is obtained as:

$$\bar{\sigma} = \frac{\Gamma_{e,\text{see}}}{\Gamma_{e,w}} = \frac{\int_\Omega \sigma(v_x) v_x f(\mathbf{v}) d^3\mathbf{v}}{\int_\Omega v_x f(\mathbf{v}) d^3\mathbf{v}} \tag{5.17}$$

where f is a Maxwellian distribution, v_x the electron velocity along (Ox), and σ the SEE linear model defined in Section 3.2.2. By integrating Equation 5.17, as detailed in Appendix F, we obtain:

$$\begin{aligned} \bar{\sigma} = \sigma_0 &+ \frac{2T_e}{\epsilon^*}(1-\sigma_0) \\ &+ (\sigma_{\max} - \sigma_0)\exp(-AR^2)(AR^2+1) \\ &+ \frac{(\sigma_0 - 1)T_e}{\epsilon^*}\exp(-AR^2)(AR^2(AR^2+2)+2) \end{aligned} \tag{5.18}$$

with:

$$A = \frac{m_e}{2T_e}$$
$$R = \epsilon_{\max} = \frac{\sigma_{\max} - \sigma_0}{1 - \sigma_0}\epsilon^*$$

where $\epsilon_{\max} = R$ is the minimum value of ϵ for which $\sigma(\epsilon) = \sigma_{\max}$.

In conclusion, both P_{abs} and P_{loss} at a given ϵ^* can be expressed as a function of the input parameters and T_e. Thus, for each ϵ^*, solving the power balance, $P_{\text{loss}} = P_{\text{abs}}$, gives us a certain T_e. Thus, T_e as well as P_{abs} and P_{loss} at equilibrium are function of ϵ^*.

However, an important point is that this value of T_e can only be obtained for values of ϵ^* higher than a certain value. Indeed for very low values of ϵ^*, the floating sheath model presented in Equation 5.16 collapse because $\Delta\Phi_s < 0$ since $\bar{\sigma} > \sigma_{\text{cr}}$.

5.4.2 First result

A first result of this global model is illustrated in Figure 5.27, where the $P_{\text{loss,w}}/P_{\text{loss}}$ ratio is plotted as a function of ϵ^*. This shows that the fraction of power losses to the walls is higher with a lower ϵ^*. This is consistent with the fact that the lower the value of ϵ^*, the stronger the SEE processes, leading to a lowered sheath potential.

As illustrated by Figure 5.27, $P_{\text{loss,w}}/P_{\text{loss}} \mapsto 0$ when $\epsilon^* \mapsto \infty$. Thus the assumption made in Section 3.1.5 to neglect the losses at the walls in the case where no SEE processes are modeled is coherent.

5.4.3 Comparisons with the PIC/MCC simulations

From the value of T_e at equilibrium of the power balance, we can then obtain estimates of both the SEE yield and the potential drop as a function of ϵ^*, using respectively Equations 5.18, and 5.16. These values obtained from the global model can then be compared to the results from PIC/MCC simulations.

The first comparison between the PIC/MCC results and the global model is the evolution of the electron temperature as a function of ϵ^*. This is illustrated in Figure 5.28, where the results from the PIC/MCC simulations and from the global model show good agreement. Two observations have to be made about Figure 5.28: first the electron temperature is observed to attain a lower limit in the case of PIC/MCC simulations, which is not the case in the global model, and second, the electron temperature is observed

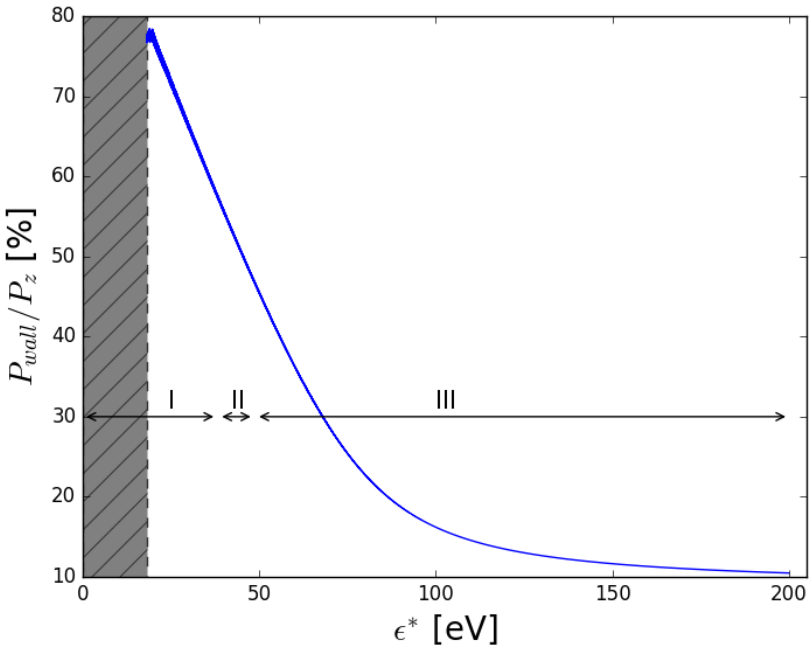

Figure 5.27 – Evolution of $P_{\mathrm{loss,w}}/P_{\mathrm{loss}}$ as a function of ϵ^* obtained from the global model detailed in Section 5.4.1. In gray, the area where the global model does not reach an equilibrium. The three arrows represent the ϵ^* ranges for each of the three Regimes identified in Section 5.3.1.

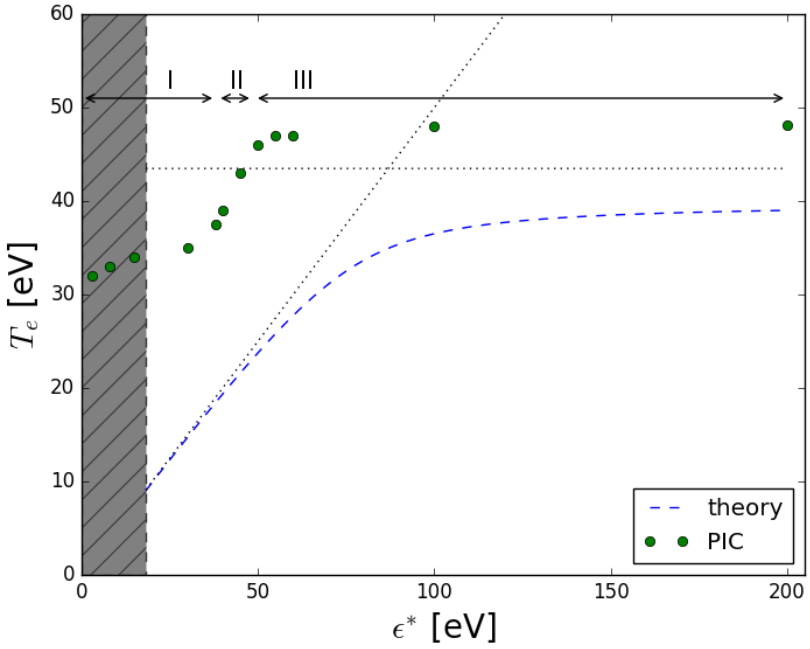

Figure 5.28 – Evolution of the electron temperature at steady state as a function of ϵ^*: (dashed blue) theoretical results from the global model, (green dots) PIC/MCC results. In gray, the area where the global model does not reach an equilibrium. The three arrows represent the ϵ^* ranges for each of the three Regimes identified in Section 5.3.1.

to saturate at a value of ≈ 45 eV for high values of ϵ^* for both PIC/MCC simulations and global model results.

A second result is the comparison concerning the SEE yield as a function of ϵ^*, illustrated in Figure 5.29. As for the electron temperature, this shows a good agreement between the PIC/MCC simulations and the global model. Figure 5.29 shows that the SEE yield is expected to have a high value at saturation, even for high values of ϵ^*, corresponding to materials with a low SEE yield.

Finally, the plasma potential drop from PIC/MCC simulations and from the global model are compared. Results are illustrated in Figure 5.30. While results from PIC/MCC simulations and global model show a good agreement for values of $\epsilon^* = 30 - 70$ eV, a difference is observed for lower and higher values of ϵ^*. Indeed, in the case of low ϵ^*, the global model underestimates the value of the potential drop, while in the case of high ϵ^* it overestimates it.

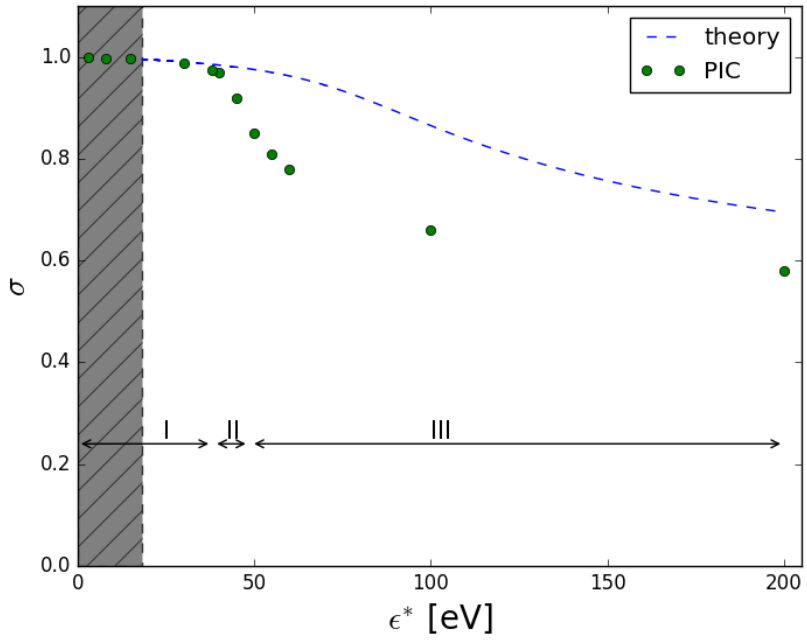

Figure 5.29 – Evolution of the SEE yield at steady state as a function of ϵ^*: (dashed blue) theoretical results from the global model, (green dots) PIC/MCC results. In gray, the area where the global model does not reach an equilibrium. The three arrows represent the ϵ^* ranges for each of the three Regimes identified in Section 5.3.1.

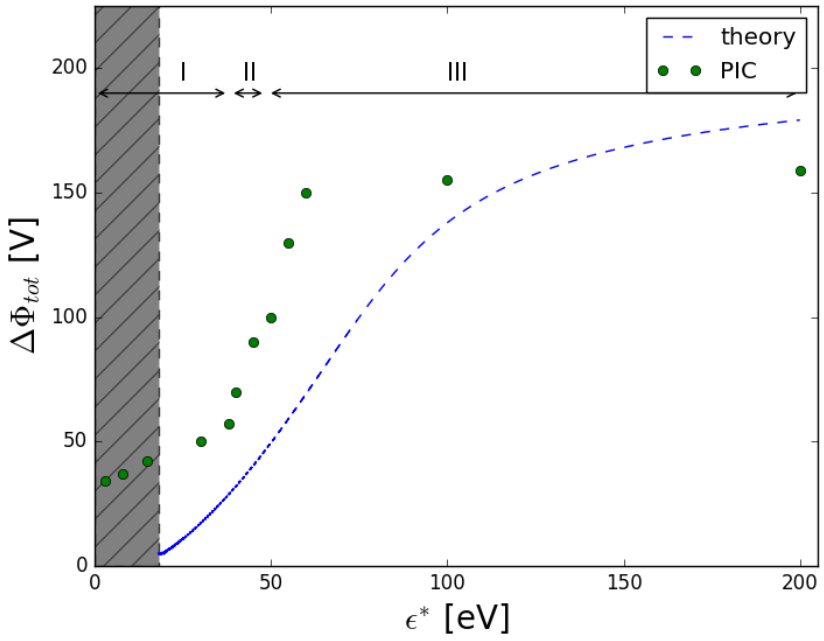

Figure 5.30 – Evolution of the plasma potential drop at steady state as a function of ϵ^*: (dashed blue) theoretical results from the global model, (green dots) PIC/MCC results. In gray, the area where the global model does not reach an equilibrium. The three arrows represent the ϵ^* ranges for each of the three Regimes identified in Section 5.3.1.

Results from this global model allows us to better understand of the plasma discharge behavior despite some disagreement between the PIC/MCC and the global model results. However this model does not allow us to reproduce the oscillating behavior observed in Section 5.3.1.

Nonetheless, the observed $P_{\text{loss,w}}/P_{\text{loss}}$ ratio as a function of ϵ^* in Figure 5.27 leads us to consider materials with a high ϵ^* value (corresponding to a low SEE yield) as a way to maximize losses in the axial direction (direction of thrust) to losses to the walls. However, this observation has to be mitigated by Figure 5.28, where the electron temperature is observed to be higher when the value of ϵ^* is higher. Indeed a high value of T_e leads to a higher proportion of multiply charged ions, not taken into account in our PIC/MCC simulations, that decreases the thruster efficiency, as detailed in Section 1.2.4. Thus results from this global model, partially validated by PIC/MCC simulations, lead us to consider medium values of ϵ^* as an optimum.

5.5 Modeling realistic SEE processes from BN walls

Once the impact of various intensities of SEE on the plasma discharge has been studied, the next step in our quest to build a realistic HET simulation model is to evaluate the diverse models available to simulate BN ceramic walls. Two models were compared: linear model, similar to the one used in Section 5.3, with a fit on experimental values, and a more complex Vaughan model, taking into account the electron incidence angle. Both are respectively described in Section 3.2.2 and Section 3.2.3.

5.5.1 Linear model

This model is the model used in the previous Section 5.3, and described in Section 3.2.2. However, it has to be fitted with experimental data in order to properly represent the behavior of BN ceramics. This has been done [96], and the obtained values are summarized in Table 3.1. After a quick comparison between the values used in this model, and the previous parameters used in the parametric study of Section 5.3, the plasma discharge is expected to present features and typical characteristics from Regime I.

As expected, this is confirmed by the simulation, as shown in Figure 5.31, where we can observe that the SEE yield does converge to a stable value $\sigma_{\text{cr}} < \bar{\sigma} < 1$. Furthermore since the value of ϵ^* is even lower than the one used as parameter in the Regime I, this simulation shows an even quicker stabilization of the SEE yield, $\bar{\sigma}$.

Since this stabilization is reached in a short time, the simulation only needs to be run for 5μs.

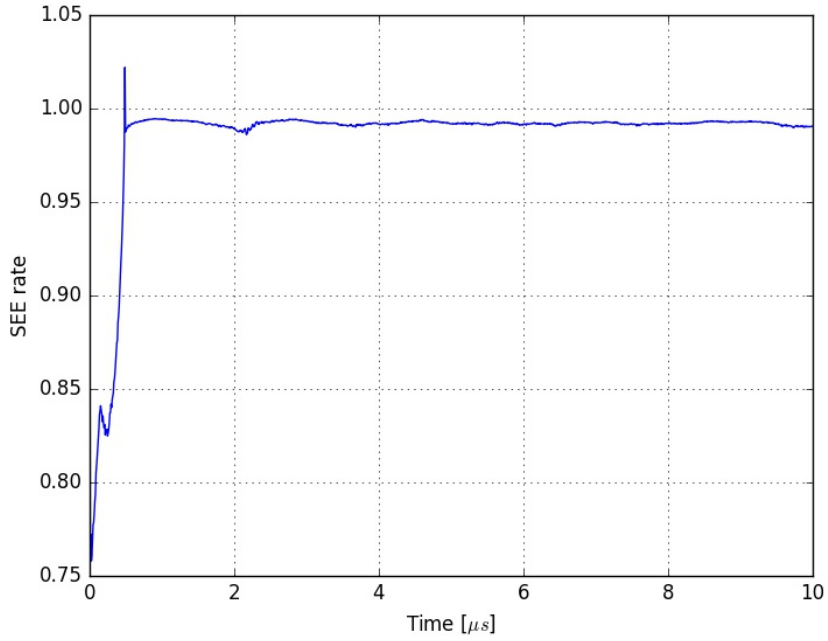

Figure 5.31 – Time evolution of the SEE yield, $\bar{\sigma}$, in the case of a linear model set-up for BN ceramics [96].

Electron drift instabilities are, as for the three previous simulations, unchanged by the presence of SEE processes, and are not precisely detailed here. Concerning the anomalous transport, the same behavior is observed as for Regime I. The radial profile of the measured mobility is illustrated in Figure 5.32 in order to compare the impacts of the SEE model on the anomalous transport.

5.5.2 Vaughan model

As described in Section 3.2.3, the Vaughan model is fitted for ceramics, and detailed in [99]. Parameters used to set-up the model are given in Table 3.1.

This model is more complex than the linear model since it takes into account the electron incidence angle, as well as its energy. This added level of complexity impacts slightly the calculation time, but is expected to give a more accurate result.

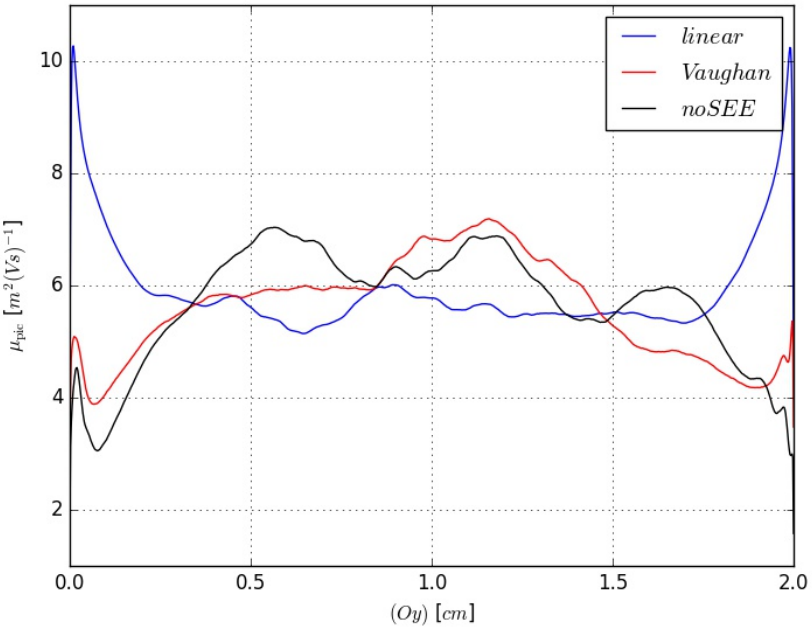

Figure 5.32 – Radial profile of the measured electron mobility, μ_{pic}, averaged in time and along (Ox): (blue) the linear model fitted for BN dielectric walls, (red) the Vaughan curve for BN walls, and (black) the case without any SEE process modeled.

However, in order to evaluate the role of the electron incidence angle, two simulations are conducted with the exact same set-up: one using the full Vaughan model, with the incidence angle dependency, the other considering every particle as hitting the wall with a normal angle of incidence. Both simulations gave the exact same result. Consequently, as already expressed in Section 3.2.4 and [73, 42], the incidence angle dependency does not play a significant role in the determination of SEE processes, at least for large channel thrusters.

Since the incidence angle is shown to not play any significant role in our case, the Vaughan curve can be simplified by considering every electron to hit the wall with an incident angle normal to the wall. This is illustrated in Figure 3.12. Yet in this case the value of the Vaughan curve for $\bar{\sigma} = 1$, which roughly corresponds to the ϵ^* value in the linear model, corresponds to an ϵ^* value for Regime III, as defined in Section 5.3.1. Consequently, the plasma discharge behavior, in the case where the Vaughan curve is used to estimate the SEE yield, is expected to show features from Regime III.

Indeed, both simulations, the one with the angle dependency and the one without, did show a stabilization of the SEE yield, $\bar{\sigma}$, to values of approximately 0.65. This is made clear in Figure 5.33.

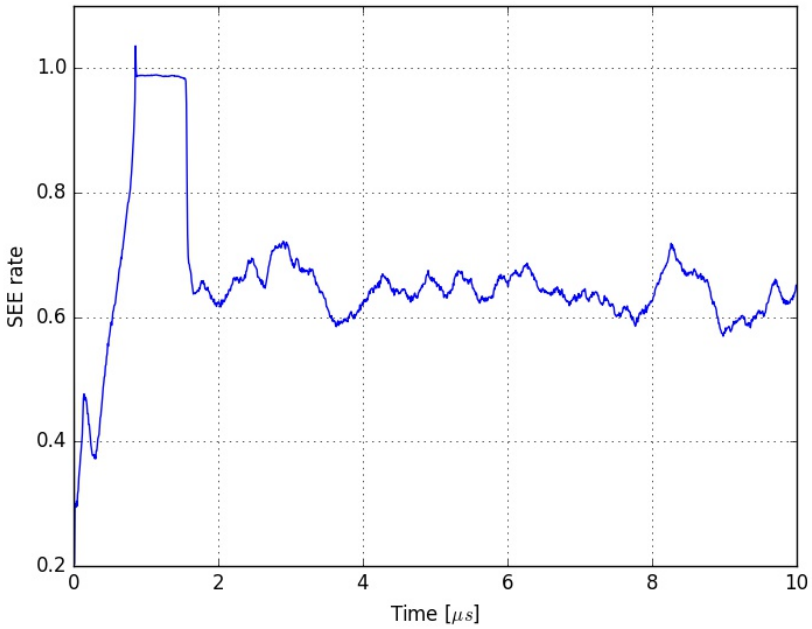

Figure 5.33 – Time evolution of the SEE yield, $\bar{\sigma}$, in the case of a SEE model set-up for BN ceramic using the Vaughan curve [99].

However concerning the electron drift instability characteristics, these are not impacted by the use of the Vaughan curve as a SEE yield model. Moreover, the plasma discharge characteristics are coherent with the characteristics observed in Regime III. Indeed the electron anomalous transport is observed to show the same behavior than Regime III, as highlighted by Figure 5.32.

5.6 Conclusion

This chapter has been focused on presenting the results obtained from a simplified $(Ox - Oy)$ PIC/MCC model of a HET plasma discharge, with diverse SEE models implemented. Some first results were obtained with the constant yield model and allowed first verifications and insights into the plasma sheath behavior. Then the linear model was used to conduct a parametric study over the material's crossover energy, ϵ^*. Since a low value

of ϵ^* corresponds to a material easily emitting secondary electrons, and a high value to a material emitting a low amount of electrons, the parametric study over ϵ^* corresponds to a study over the intensity of the SEE.

Thanks to this parametric study, we identified three different regimes of the plasma discharge behavior, governed by the intensity of the SEE. Each regime is characterized by a value of the SEE yield, $\bar{\sigma}$, at saturation. Indeed while Regime I is observed to saturate with $\bar{\sigma} > \sigma_{\text{cr}}$, Regime III saturates to a lower value of $\bar{\sigma}$ (the lower the value of ϵ^*, the lower the value of $\bar{\sigma}$), and Regime II features a relaxation oscillation (RO) between the two precedent regimes. This RO presents an $\approx 2\,\mu$s pseudo-period, steady over long time scales, and impacting plasma potential as well as $\bar{\sigma}$, and the electron energy.

While in the absence of the electron drift instability, 1D results can quite properly be rediscovered, the superposition of the electron drift instability and SEE processes leads to an alteration of some of the near-wall properties. Indeed the SCL is observed to be perturbed, where the condition $\bar{\sigma} > \sigma_{\text{cr}}$ is not sufficient anymore in order to obtain a sheath inversion. This perturbation is expected to be due to some impacts of the electron drift instability on the sheath, or to be a relaxation sheath oscillation (RSO) [95, 97].

SEE processes are not observed to perturb the electron drift instability, even in the most oscillating case, where RO are observed. Indeed the electron drift instability is superimposed, without any alteration of its properties.

Concerning anomalous electron transport, in the case where no electron instability is present, we observe, as expected, a value of electron mobility coherent with the classical diffusion theory in the plasma bulk. Furthermore the near-wall mobility is also observed to be one order of magnitude higher than the mobility in the plasma bulk. This enhanced near-wall mobility is coherent with past simulations [97, 73, 95].

When both the electron drift instability and the SEE processes are modeled, the anomalous mobility has been quantified in all three plasma discharge regimes. This allowed us to study the electron mobility with different SEE intensities. This study firstly showed that the electron anomalous transport is not impacted by SEE processes in this set-up. Secondly, using results from the kinetic theory [69], it was possible to estimate the respective contributions of the SEE processes (through near-wall mobility) and of the electron drift instability (through an electron/ion friction force defined in Section 4.3.3). This highlighted that the higher the SEE intensity, the lower the contribution of the electron drift instability, and thus the higher the contribution of SEE processes.

Consequently, SEE and the electron drift instability appears to affect the electron anomalous transport in a coupled way. Indeed, an increase of SEE means an increase of the electron mobility, but also a decrease of the

electron temperature in the plasma. Since a decrease of the electron temperature means a decrease of the instability strength, this means a decrease of the electron mobility due to the instability. It appears that the increase of mobility due to the SEE compensates almost perfectly the decrease due to the weakened instability. However, the precise mechanisms at the root of this coupling are still unclear.

Although not enabling further understanding of the SEE yield oscillations, a global model has been developed in order to take the SEE processes into account. This global model has been able to reproduce some of the HET characteristics over a wide range of ϵ^* values, allowing a better understanding of the HET operation in function of the wall material. Indeed, this global model has been able to quantify the radial losses, main topic on the development of future HETs.

Finally, it was observed that for two different models fitted to model SEE processes of xenon on BN walls, two very different plasma discharge behaviors are obtained. This asks the question of the experimental verification of these simulations. Moreover the further investigation of the Vaughan model highlighted the fact that SEE processes in our case are not dependent on the electron incident angle [73, 42]. This non-dependency over the incidence angle can be a feature of HETs, but should be verified with a curved channel, in particular for small HETs.

However, since the focus of this chapter was to highlight the impact of SEE processes, the model used is simplified, and grounded metallic walls are still a strong approximation limiting these results.

Chapter 6

Modeling floating dielectric walls

Contents

6.1 Simulation set-up

In the previous chapters, the HET system was modeled with grounded metallic walls. Walls that are able to re-emit secondary electrons like ceramics, as detailed in Chapter 5, but still potentially grounded like metallic walls. This simplification of the studied system is a significant limitation of our goal to realistically model a HET.

Using the dielectric wall model presented in Section 3.3 and the parameters from Table 3.3 with $n_0 = 3 \times 10^{17}\mathrm{m}^{-3}$, LPPic2D has been used to model the plasma discharge with various values of the dielectric width, L_{diel}, and the dielectric relative permittivity, $\epsilon^r_{\mathrm{diel}}$ (with $\epsilon^r_{\mathrm{diel}} = \epsilon_{\mathrm{diel}}/\epsilon_0$, where ϵ_0 is the vacuum permittivity). Values of $\epsilon^r_{\mathrm{diel}}$ and L_{diel} used are summed up in Table 6.1, with the case names they will be referred to in the following.

Table 6.1 – Values of ϵ^r_{diel} and L_{diel} used in LPPic2D.

Case	ϵ^r_{diel}	L_{diel} [mm]
1	25	3
2	25	10
3	1	10
4	1	3
Me	1	0

It is important to note that the model presented in Section 3.3, and schematically detailed in Figure 3.16, is set-up with two dielectric walls, one on the upper side of the system, and one on the lower side, of equal thickness and permittivity, separating the plasma from grounded electrodes. These walls close the plasma domain in the (Oy) direction, while periodic boundaries are applied along the (Ox) axis.

Moreover, as detailed in Section 3.3, the charges accumulating at the surface are taken into account twice in the PIC/MCC algorithm: (1) into the solving of the Poisson equation, and (2) into the counting of couples to be re-injected.

Values used to investigate the impact of the dielectric on the plasma discharge behavior are chosen in order to investigate a plausible range. Indeed the ceramic thickness in HETs are of the order of mm [12, 4]. Moreover the relative permittivity of the dielectric has been chosen so that $\epsilon^r_{\text{diel}} = 25$, since modern HETs most often use thin Boron Nitride (BN) as ceramic component for dielectric walls. Furthermore, this case is compared to a case with $\epsilon^r_{\text{diel}} = 1$, which means $\epsilon_{\text{diel}} = \epsilon_0$, in order to expand the investigation range to an extreme case.

Finally, the corresponding case using grounded metallic walls will be in the following referred to as case Me. This case corresponds to a simulation using the exact same parameters, but modeling grounded metallic walls instead of floating dielectric ceramics. Thus, this case has been already detailed and studied in Chapter 4 as the n_0 case, and in Chapter 5 as the $noSEE$ case.

6.2 Electron drift instability characteristics

6.2.1 Observation of the electron drift instability

The electron drift instability, already highlighted in Chapter 4 for simulations using grounded metallic walls, is observed in each of the cases given in Table 6.1. Saturation does appear after $1-2\,\mu$s in the case of floating dielectric walls, which is consistent with the observations made in the case of grounded metallic walls. This can be seen in Figures 6.1 and 6.2, which are taken from a simulation of case 1.

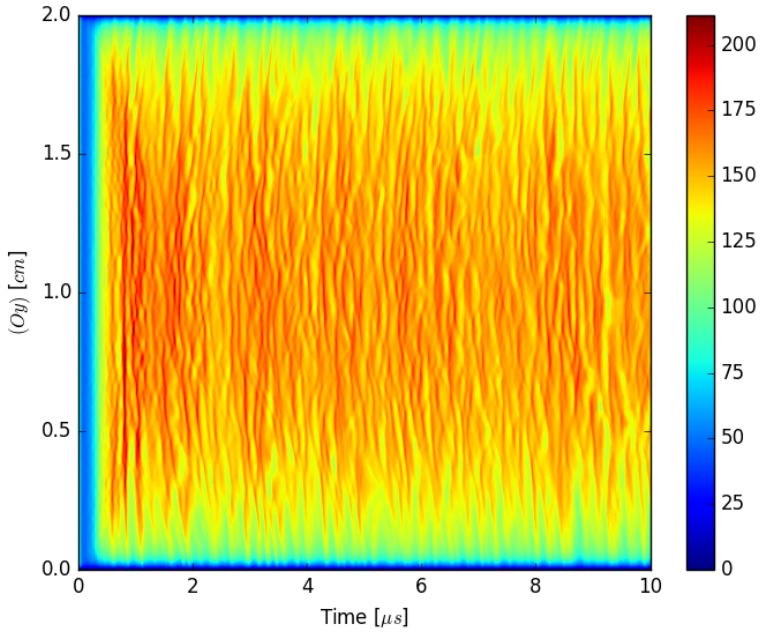

Figure 6.1 – Time evolution of the plasma potential profile taken from 1D cuts of the 2D $(Ox-Oy)$ simulation domain taken along (Oy), at $x=L_x/2$. With dielectric floating walls set-up from case 1 in Table 6.1.

6.2.2 Comparison of instability characteristics

Some instability characteristics such as the wavelength, λ, the frequency, f, and the phase velocity, v_{ph}, are measured directly from the simulations, as well as the fluctuations $|\delta\widetilde{n}_e|/n_e$ and $|\delta\widetilde{\Phi}|/T_e$. They can then be compared

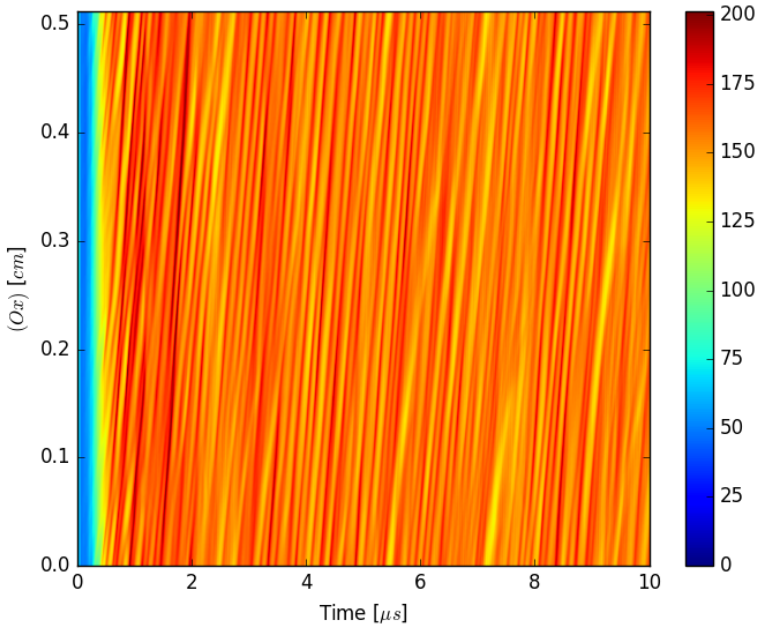

Figure 6.2 – Time evolution of the plasma potential profile taken from 1D cuts of the 2D $(Ox - Oy)$ simulation domain taken along (Ox), at $y = L_y/2$. With dielectric floating walls set-up from case 1 in Table 6.1.

to the analytical values taken from the kinetic theory [69, 11]. Comparisons are summarized in Table 6.2.

All values presented in Table 6.2 are averaged during the last 5μs of the simulation, when the instability is saturated, in order to lower the noise level. The values of λ and f summed up in Table 6.2 are measured with the same methods, and thus exposed to the same error margins, as the ones summed up in Table 4.1. Consequently, the error margin is estimated as $\approx \pm 0.5$ [MHz] for the frequency, and $\approx \pm 0.1$ [mm] for the wavelength.

The uncertainty on the T_e measurement (which is obtained from the measurement of ϵ_e) is about $\approx \pm 5$ [eV]. This uncertainty is then echoed in the subsequent estimates, which are giving us the analytical values presented in Table 6.2. The value of T_e measured in these simulations using dielectric walls is 47eV, slightly lower than the 53eV measured in simulations using metallic walls.

Nevertheless, concerning the estimation of the phase velocity, v_{ph}, from the PIC simulation, a more systematized method than for Table 4.1 is used. This method consists to measure the correlation function between each 2D

Table 6.2 – Comparison between physical values measured from the simulation and predictions from the kinetic theory about the instability characteristics for various dielectric wall characteristics.

PIC values			
Case	λ [mm]	f [MHz]	v_{ph} [10^3ms^{-1}]
1	1.0	5.0	5.0
2	1.0	5.0	6.0
3	1.0	5.0	7.0
4	1.0	5.0	7.5
Me	1.0	5.0	6.0
Case	$\lvert\delta\widetilde{n}_e\rvert/n_e$ [%]	$\lvert\delta\widetilde{\Phi}\rvert/T_e$ [%]	
1	20	60	
2	18	53	
3	19	54	
4	18	51	
Me	19	54	
Analytical values			
Case	λ [mm] (Equation 4.3)	f [MHz] (Equation 4.5)	v_{ph} [10^3ms^{-1}] (Equation 4.6)
all	0.8	5.8	5.0
Case	$\lvert\delta\widetilde{n}_e\rvert/n_e$ [%]	$\lvert\delta\widetilde{\Phi}\rvert/T_e$ [%]	
all	33	33	

spatial plot of the plasma potential (a plot is taken every N_A time-step, i.e. every $N_A\Delta t = 8$ns), then the mean value of the correlation is used in order to estimate the phase velocity. This method allows for a better measurement, with an error margin estimated to be approximately $\pm 0.5\,[10^3 \mathrm{ms}^{-1}]$.

As for v_{ph}, the diagnostics of $|\delta\widetilde{\Phi}|/T_e$ and $|\delta\widetilde{n}_e|/n_e$ have been systematized in comparison to measurements presented in Table 4.1. Consequently it gives significantly different results from Chapter 4. This is apparently due to the diagnostics method that was changed. However the error margin is not impacted and these measurements are still characterized by a ≈ 10 % error margin.

Finally, Table 6.2 highlights the fact that although the dielectric parameters are different in each case, the instability characteristics are not strongly impacted.

6.3 Anomalous electron cross-field transport

In the previous section, we observed that the introduction of dielectric floating walls did not impact significantly the instability characteristics, nor the electron temperature. Consequently, the impact of floating dielectric walls on the electron cross-field mobility can be expected not to be significant. The values measured in the cases modeled, as well as the corresponding analytical values from the kinetic theory [69, 11], are summarized in Table 6.3.

Table 6.3 – Comparison between physical values measured from the simulation and predictions from the kinetic theory for the electron cross-field mobility for various dielectric walls set-ups.

Case	PIC values		Analytical values	
$[\mathrm{m}^2\mathrm{V}^{-1}\mathrm{s}^{-1}]$	μ_{pic}	μ_{eff}	μ_{eff}^{sat}	$\mu_{\mathrm{classical}}$
(Equation)	(4.9)	(4.10)	(4.15)	(4.7)
1	6.0	5.2	3.7	0.2
2	6.3	5.7	3.7	0.2
3	6.6	5.8	3.7	0.2
4	6.9	6.0	3.7	0.2
Me	6.5	5.8	3.7	0.2

Values summarized in Table 6.3 are averaged during the last 5μs of the simulation, when the instability is saturated, in order to lower the noise level.

Nonetheless, despite this averaging, the PIC values are characterized by an error margin of $\approx \pm 0.5\,[\mathrm{m^2V^{-1}s^{-1}}]$, while the analytical values have an error margin of $\approx \pm 0.1\,[\mathrm{m^2V^{-1}s^{-1}}]$.

As already detailed the measured electron temperature $T_e = 47 \pm 5\mathrm{eV}$, lower than the electron temperature measured for metallic walls (which was $T_e = 53 \pm 5\mathrm{eV}$). This leads to a higher value of the estimated mobility at saturation, μ_{eff}^{sat}, as detailed by Equation 4.15. This difference in electron temperature and the error margins over the estimates presented in Table 6.3 clarify the observed difference between the results of the n_0 case from Table 4.2 and the present Me case.

Values given in Table 6.3 show us that the floating dielectric walls do not impact significantly the electron mobility in the case where no secondary electron emission is modeled, despite a lowered electron temperature. Nonetheless this conclusion is obtained in the given case where walls of equal thickness and permittivity separating the plasma on each side from grounded metallic electrodes.

6.4 Dielectric walls and secondary electron emission processes

We have investigated the impact of the floating dielectric walls on the plasma discharge by comparing to a case using grounded metallic walls. We now introduce SEE processes in a system modeling floating dielectric walls. The combination of the two effects are investigated in this section.

6.4.1 Dielectric walls in a RO regime

In order to verify the accuracy of the floating dielectric walls, it is necessary to model a case where the secondary electron emission processes are included as well. Thus it has been chosen to use LPPic2D with the dielectric wall set-up, and model the case where RO are observed. This case, detailed with metallic walls in Section 5.3.1, has been chosen since it is one of the most complex and thus one of the most appropriate cases to verify the model quality.

Consequently LPPic2D has been set-up using the parameters from Table 3.3 with $n_0 = 3 \times 10^{17}\mathrm{m^{-3}}$. Additionally the linear model, as given for Regime II in Table 5.2, is used. Finally, floating dielectric walls are set-up with $\epsilon_{\mathrm{diel}}^r = 25$ and $L_{\mathrm{diel}} = 3\mathrm{mm}$ (corresponding to case 1 from Table 6.1).

These values of thickness and relative permittivity are chosen since they are considered as the most realistic values for a HET using BN dielectric

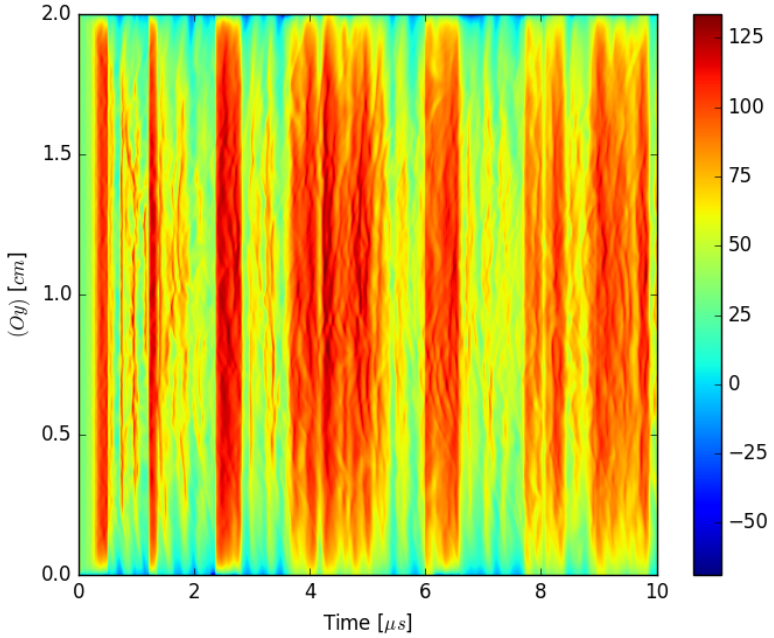

Figure 6.3 – Time evolution of the plasma potential from a 1D cut into the 2D domain. Cut taken along (Oy), at $x = L_x/2$. Dielectrics are set-up from case 1, and linear SEE in order to observe RO.

walls.

The features from the simulation with grounded metallic walls, detailed in Section 5.3.1, are observed in the simulation using floating dielectric walls. Anomalous transport and electron drift instability characteristics are not impacted by the introduction of floating dielectric walls. In this case, these features are comparable in the case of the RO regime with grounded walls and in the case of floating walls. Nonetheless, the plasma potential shows a more chaotic behavior as illustrated in Figure 6.3.

Figure 6.3 shows the impact of the dielectric walls on the plasma discharge behavior. Indeed the potential oscillations easily identified in Figure 5.5, are not so defined. However the oscillations are still visible on the plasma potential. Moreover the presence of floating dielectric walls enables the possibility of a strong sheath inversion, observed during some oscillations.

Concerning the SEE yield, $\bar{\sigma}$, the oscillation behavior observed in the Regime II from Section 5.3.1 is observed despite the chaotic behavior introduced by the dielectric floating walls, as highlighted by Figure 6.4. Indeed the pseudo-periodicity of the oscillations and their amplitude are perturbed

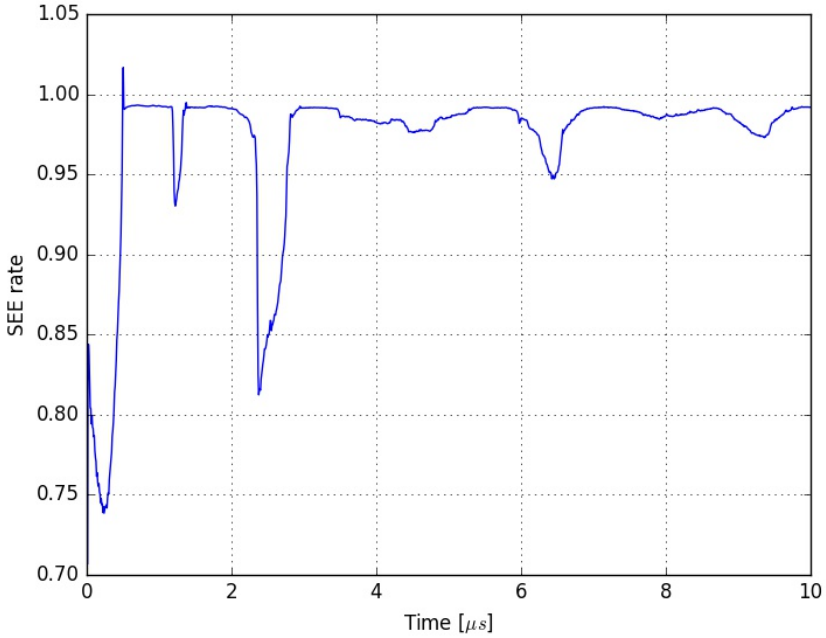

Figure 6.4 – Time evolution of the SEE yield, $\bar{\sigma}$, in the case of a SEE model set-up as Regime II from Section 5.3.1 and with dielectric parameters corresponding to the case 1 from Table 6.1.

by the introduction of floating dielectric walls. This can be a consequence from the way the electric field at the plasma/wall boundary is computed, as detailed in Section 3.2.6, or by the impact of surface charges on the plasma discharge behavior.

The introduction of floating dielectric walls does significantly impact the plasma discharge behavior as observed in this case, illustrated by Figures 6.3 and 6.4. The presence of a floating dielectric with surface charges impacts the RO regime by altering the pseudo-periodicity observed in the case with grounded metallic walls. While the main features are preserved, the introduction of a floating dielectric induces a source of chaotic behavior, thus adding complexity to the investigation. However, this implementation allows a more realistic modeling of the HET system.

6.4.2 Realistic model of a HET

Once the ceramic dielectric walls are set-up with realistic values, $\epsilon^r_{\text{diel}} = 25$ and $L_{\text{diel}} = 3\text{mm}$ (case 1), the model set-up used can be perfected to

realistically model a HET. This is done by using the parameters given in Table 3.3 with $n_0 = 3 \times 10^{17}\text{m}^{-3}$, the dielectric walls with a realistic set-up, and the linear SEE model with realistic values, as given by [96]. Indeed the linear SEE model has been fitted with experimental values, giving: $\epsilon^* = 35.04$ eV and $\sigma_0 = 0.578$.

This model shows a saturation of the SEE yield as observed in Section 5.5 with grounded metallic walls, and expected after the parametric study presented in Section 5.3.1. This is illustrated by Figure 6.5.

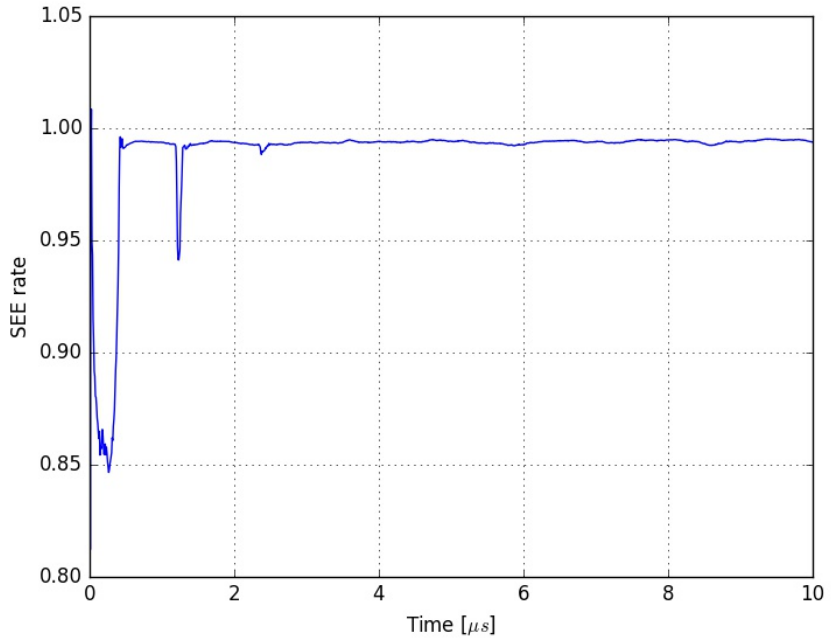

Figure 6.5 – Time evolution of the SEE yield, $\bar{\sigma}$, in the case of a realistic SEE model for BN walls and with dielectric parameters corresponding to the case given by [96].

Concerning the plasma potential, its evolution as a function of time illustrated in Figure 6.6 shows a lowered potential in comparison to the simulation with grounded walls, and the one with dielectric walls but no SEE processes. Moreover, this simulation features comparable electron drift instability characteristics. Indeed, as for previous studies, the electron drift instability is superimposed on other plasma oscillations without being strongly affected in its characteristics. Furthermore, the saturation of the SEE yield at a value higher than σ_{cr}, allows the presence of sheath inversion, as observed in Figure 6.6.

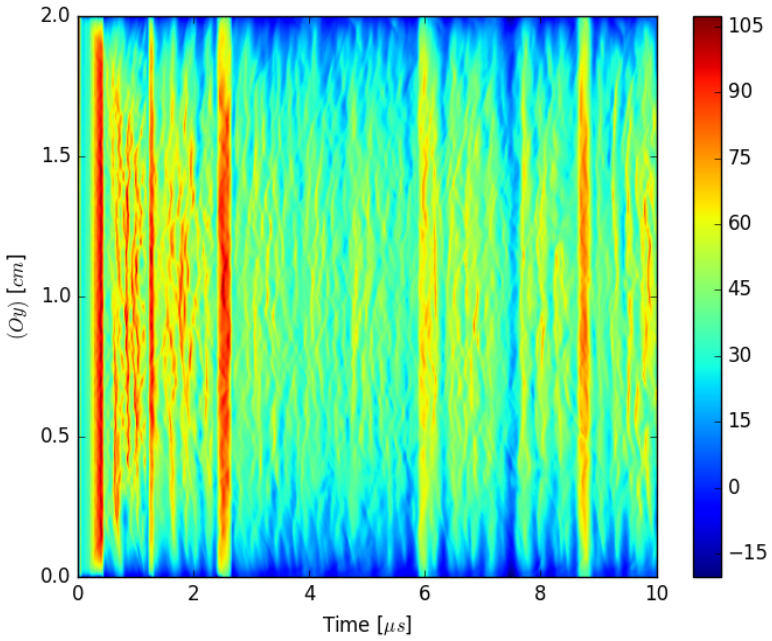

Figure 6.6 – Time evolution of the plasma potential from a 1D cut into the 2D domain. Cut taken along (Oy), at $x = L_x/2$. In the case of a realistic SEE model for BN walls and with dielectric parameters corresponding to the case given by [96].

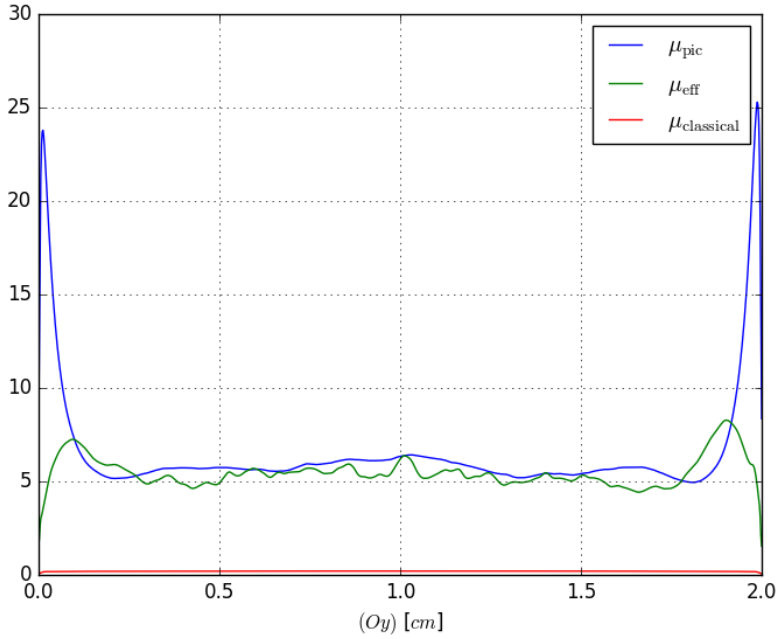

Figure 6.7 – Radial profiles, i.e. along (Oy), of all three measured mobilities: (blue) μ_{pic}, (green) μ_{eff}, and (red) $\mu_{\text{classical}}$). The given mobilities are averaged in time and averaged along (Ox).

The electron anomalous transport is consistent with previous observations. The mean measured value of the electron transport, given by Equation 4.9, is $\mu_{\text{pic}} = 6.5\,\text{m}^2(\text{Vs})^{-1}$, while the effective mobility obtained from Equation 4.10 gives us $\mu_{\text{eff}} = 5.5\,\text{m}^2(\text{Vs})^{-1}$. This shows a significant contribution of the electron drift instability to the anomalous transport, as well as the better approximation constituted by the kinetic theory from [69], since the mobility obtained from classical diffusion gives us $\mu_{\text{classical}} = 0.19\,\text{m}^2(\text{Vs})^{-1}$.

Nevertheless, as already highlighted in Section 5.3.4, the SEE contribution to the anomalous transport is due to the enhanced near-wall mobility. This can be properly observed in Figure 6.7, where the radial profiles of all three mobilities (μ_{pic}, μ_{eff}, and $\mu_{\text{classical}}$) are plotted.

6.5 Conclusion

In this chapter, the model of floating dielectric walls presented in Section 3.3 was used to conduct a parametric study over the values of the dielectric permittivity and thickness. These results have shown some impact of

the floating walls on the plasma discharge by lowering the plasma potential. However, the electron drift instability shows no sign of significant perturbation, and consequently the anomalous transport stays as well not impacted.

Once the investigation had been conducted without SEE processes, allowing proper comparison with the well-known metallic walls case, SEE processes were added to the system, using the linear model detailed in Section 3.2.2. While, with grounded metallic electrodes, the RO regime shows pseudo-periodic oscillation of the plasma potential oscillations, as well as of the SEE yield, the case using floating walls shows a more noisy behavior. Moreover, the sheath inversion is observed to be more pronounced, while the SEE yield shows lower amplitude fluctuations.

The validated system using floating walls and a linear SEE model was then configured to model realistically a HET [96]. This model allowed a reliable verification of the kinetic theory [69], and highlighted the effects of the electron drift instability and the SEE on the anomalous transport. This shows that while the SEE processes effectively contribute to the near-wall enhanced electron mobility, the main contribution to the electron transport is brought by the electron drift instability. This confirms the observations made with simpler model set-ups presented in the previous chapters.

The dielectric wall model with symmetric thicknesses has been chosen in order to model what can be considered as a realistic cut along the $r - \theta$ plane in a HET [12]. However, further studies could be conducted with asymmetric geometries, or dielectric walls separating the plasma from floating electrodes, or inserting an area filled with vacuum between the dielectrics and the electrodes (as it is in large scale HETs). Nevertheless, the present work focuses on the HET channel mechanisms, and thus uses a simpler geometry to isolate each mechanisms.

Another limitation is in the way the potential is imposed. If solving the Poisson equation inside the dielectric layer up to the grounded metallic structure can be an accurate approximation of the $r - \theta$ cut of a HET, it does not take into account the evolution of the potential inside the dielectric in the axial direction.

Consequently LPPic2D has been set-up to almost realistically model a large radius HET along a 2D cut of the plasma channel near the thruster exit.

Chapter 7

Impact of alternative propellants on the plasma discharge

Contents

7.1 Simulation set-up

As detailed in Section 1.3, efficient use of alternative propellants is a key issue in the further development of HET technologies. Thus LPPic2D was designed in order to model a plasma discharge using other noble gases than xenon.

Xenon and helium collision processes

As described in Sections 2.2.3 and 3.1.6, LPPic2D has already been implemented in order to model a helium or a xenon plasma. However for each gas a dedicated version of LPPic2D was used. A first step was to unify the different versions of LPPic2D.

LPPic2D was modified in order to efficiently use cross-sections given in the *lx-cat* database format. In the case of helium, collisional processes and corresponding cross-sections are the ones given in Section 2.2.3, while in the case of xenon the cross-sections and processes used are described in Section 3.1.6.

Argon collision processes

However for argon the cross-sections used are taken respectively from [114] for ion/neutral cross-sections, and from [115] for electron/neutral cross-sections. The corresponding collisional processes are summarized below:

$$e^- + Ar \rightarrow e^- + Ar \quad \text{(Elastic scattering)} \tag{7.1}$$
$$e^- + Ar \rightarrow e^- + Ar^* \quad (\epsilon = 11.55\text{eV, Excitation}) \tag{7.2}$$
$$e^- + Ar \rightarrow e^- + Ar^* \quad (\epsilon = 13.00\text{eV, Excitation}) \tag{7.3}$$
$$e^- + Ar \rightarrow e^- + Ar^* \quad (\epsilon = 14.00\text{eV, Excitation}) \tag{7.4}$$
$$e^- + Ar \rightarrow e^- + Ar^+ + e^- \quad (\epsilon = 15.7\text{eV, Ionization}) \tag{7.5}$$

$$Ar^+ + Ar \rightarrow Ar + Ar^+ \quad \text{(Backscattering)} \tag{7.6}$$
$$Ar^+ + Ar \rightarrow Ar^+ + Ar \quad \text{(Isotropic)} \tag{7.7}$$

Krypton collision processes

Concerning the krypton plasma discharge, the collisional processes modeled are given in the following:

$$e^- + Kr \rightarrow e^- + Kr \quad \text{(Elastic scattering)} \tag{7.8}$$
$$e^- + Kr \rightarrow e^- + Kr^* \quad (\epsilon = 9.915\text{eV, Excitation}) \tag{7.9}$$
$$e^- + Kr \rightarrow e^- + Kr^* \quad (\epsilon = 11.30\text{eV, Excitation}) \tag{7.10}$$
$$e^- + Kr \rightarrow e^- + Kr^* \quad (\epsilon = 11.998\text{eV, Excitation}) \tag{7.11}$$
$$e^- + Kr \rightarrow e^- + Kr^* \quad (\epsilon = 12.75\text{eV, Excitation}) \tag{7.12}$$
$$e^- + Kr \rightarrow e^- + Kr^+ + e^- \quad (\epsilon = 13.99\text{eV, Ionization}) \tag{7.13}$$

$$Kr^+ + Kr \rightarrow Kr + Kr^+ \quad \text{(Backscattering)} \tag{7.14}$$
$$Kr^+ + Kr \rightarrow Kr^+ + Kr \quad \text{(Isotropic)} \tag{7.15}$$

These collisions are taken, in the *lx-cat* format, from [67] concerning the ion/neutral backscattering process, from [116] for the ion/neutral elastic collisions, and from [115] for electron/neutral collisional processes.

Implementation in LPPic2D

Besides xenon, with an ion mass of 131.3 AMU, alternative propellants can be modeled in LPPic2D: argon (39.95 AMU), helium (4.003 AMU), and krypton (83.8 AMU).

These adaptations of LPPic2D allows a continuous verification of the simulation code through development by being able to run the CCP helium benchmark from [75] as well as documented xenon cases with the same version of LPPic2D. This is an important point for the development of LPPic2D as a reliable simulation tool.

In the following sections, simulation parameters were taken from Table 3.3, using a plasma density of $n_0 = 3 \times 10^{17}\mathrm{m}^{-3}$. Some simulations were done with secondary electron emission processes, and some without. The models used for SEE are described in Section 3.2, yet only the linear model configured for BN ceramics is used. Parameters used to set-up this model are taken from [96], and summed up in Table 3.1.

In order to study the effects of collisional processes, some of the simulations did not use the actual cross-sections, but the collision processes corresponding to a xenon chemistry (i.e. only the ion mass is changed, not the modeled chemistry). Simulations not using the chemistry corresponding to the modeled ions will be referred to as "fake" simulations. In an effort to avoid confusion, those simulations will be noted with an "f" prefix (i.e. "fKr" for a krypton simulation with the xenon chemistry).

Finally, in order to lower the calculation time, and simplify the results analysis, most of the simulations were performed with grounded metallic walls. As shown in Chapter 6, this does not impact too heavily the plasma discharge behavior, thus allowing us to keep, in a first attempt, this simplification. When modeled, floating dielectric walls are modeled with realistic parameters given in Section 6.5, in Section 7.4.1, along with the modeling secondary electron emission from the walls described in Section 3.2.2.

7.2 Electron drift instability characteristics

In a first attempt to investigate the impacts of alternative propellants on the electron drift instability, the simulations are done without SEE processes or dielectric walls.

Four simulations were conducted with the collisional processes corresponding to the modeled ion. Furthermore, in order to study the impact of collisional processes on the plasma discharge, three simulations were conducted with the mass of the modeled ion, but the collisional processes of

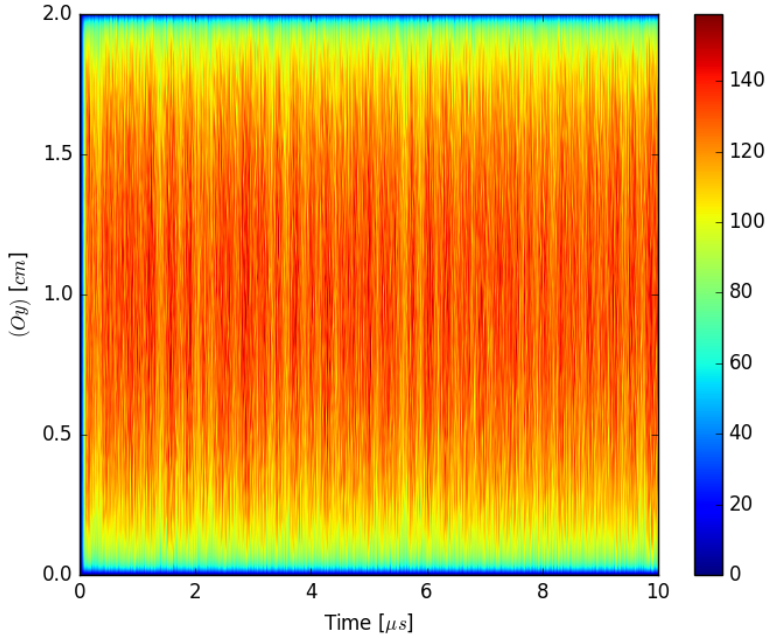

Figure 7.1 – Time evolution of the plasma potential profile taken from 1D cuts of the 2D $(Ox - Oy)$ simulation domain taken along (Oy), at $x = L_x/2$. Propellant modeled is helium with parameters from Table 3.3, without SEE and with metallic walls.

xenon(fHe, fAr, and fKr).

The instability is observed in each of the modeled cases. The growth time of the instability, τ_g, is difficult to measure precisely, however it is observed to be shorter with a lighter propellant. This can be observed by comparing Figures 7.2 and 7.1, where helium is used as propellant, to the Figures 4.4 and 4.3, where xenon is used. This observation is coherent with Equation 4.2 and confirms the kinetic theory [68].

As expressed in Section 4.2.2, instability saturation is often due to particle-wave trapping [108]. In the cases of alternative propellants modeled in this Section, the instability saturation is, as for the xenon plasma discharge, due to the ion trapping. Indeed the phase plot of ions shows the same typical form of ions wave trapping as the ones described in Section 4.2.2. Figures of this particle-wave trapping are not shown for the sake of brevity.

Other electron drift instability features such as frequency, f, or wave-length, λ, are measured and compared to the theoretical values estimated

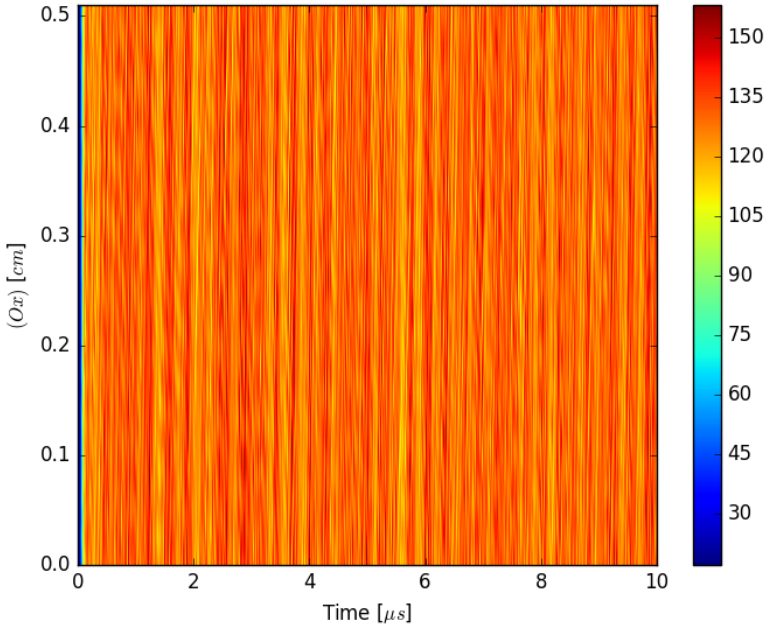

Figure 7.2 – Time evolution of the plasma potential profile taken from 1D cuts of the 2D $(Ox - Oy)$ simulation domain taken along (Ox), at $y = L_y/2$. Propellant modeled is helium with parameters from Table 3.3, without SEE and with metallic walls.

Table 7.1 – Physical values measured from the simulation about the instability characteristics in the case of alternative propellants in a simplified model.

PIC values				
Case	m_i [AMU]	λ [mm]	f [MHz]	v_{ph} [10^3ms^{-1}]
He	4.003	1.0	30.0	30.0
Ar	39.95	1.0	9.0	10.0
Kr	83.80	1.0	8.0	8.0
Xe	131.3	1.0	5.0	5.0
fHe	4.001	1.0	30.0	29.0
fAr	39.95	1.0	10.0	11.0
fKr	83.80	1.0	8.0	8.0
Case	m_i [AMU]	$\lvert\delta\widetilde{n}_e\rvert/n_e$ [%]	$\lvert\delta\widetilde{\Phi}\rvert/T_e$ [%]	
He	4.003	15	21	
Ar	39.95	15	25	
Kr	83.80	19	53	
Xe	131.3	18	42	
fHe	4.001	16	22	
fAr	39.95	18	33	
fKr	83.80	17	38	

thanks to the equations presented in Section 4.3.2. Those comparisons are summarized in Tables 7.1 and 7.2.

Values summarized in Tables 7.1 and 7.2 have been obtained using the same measurement methods than the ones used to obtain the values presented in Table 6.2. Consequently, the error margins are the same, and the values were averaged during the last 5μs of the simulation. The electron temperature, T_e, is obtained from the measurement of the mean electron energy, and is therefore exposed to a $\approx \pm 5$ eV error margin. The value of T_e measured from the PIC simulations is $\approx 47 \pm 5$eV, a value comparable to the one measured with dielectrics in Section 6.2. Detailed values of T_e for each simulation will be detailed in the following.

As for the values from Table 6.2, the uncertainty for v_{ph} is in a range of $\approx \pm 0.5\,[10^3\text{ms}^{-1}]$, while being $\approx \pm 0.5\,[\text{MHz}]$ for the frequency, and $\approx \pm 0.1\,[\text{mm}]$ for the wavelength. Concerning $|\delta\widetilde{\Phi}|/T_e$ and $|\delta\widetilde{n}_e|/n_e$ the error margin is ≈ 10 %.

Table 7.2 – Predictions from the kinetic theory about the instability characteristics in the case of alternative propellants in a simplified model.

Analytical values

Case	m_i [AMU]	λ [mm] (Equation 4.3)	f [MHz] (Equation 4.5)	v_{ph} [10^3ms^{-1}] (Equation 4.6)
He	4.003	0.8	33.0	27.0
Ar	39.95	0.8	10.0	9.0
Kr	83.80	0.8	7.2	6.0
Xe	131.3	0.8	5.8	5.0
fHe	4.001	0.8	33.0	27.0
fAr	39.95	0.8	10.0	9.0
fKr	83.80	0.8	7.2	6.0
Case	m_i [AMU]	$\lvert\delta\widetilde{n}_e\rvert/n_e$ [%]	$\lvert\delta\widetilde{\Phi}\rvert/T_e$ [%]	
He	4.003	33	33	
Ar	39.95	33	33	
Kr	83.80	33	33	
Xe	131.3	33	33	
fHe	4.001	33	33	
fAr	39.95	33	33	
fKr	83.80	33	33	

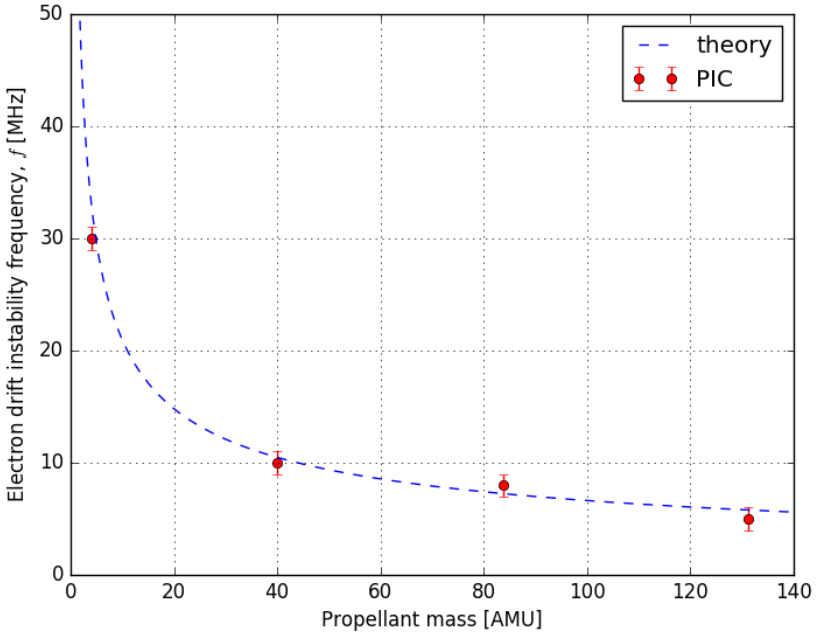

Figure 7.3 – Comparison between: (dashed blue line) the theoretical value of the electron drift instability frequency, f, obtained from Equation 4.5, and (red points) the values obtained from the PIC simulations.

Error margins in the measurement as well as the PIC variability are accounting for the slight differences observed between the Xe case from Table 7.1, the n_0 case from Table 4.1, and the Me case from Table 6.2.

The electron drift instability frequency, f, can be directly compared to the results from the kinetic theory [69]. This is illustrated in Figure 7.3, where the PIC results, with the corresponding error-bars, show good agreement with the kinetic theory.

Furthermore, as already demonstrated in Chapter 4 for the xenon plasma discharge, collision processes are observed to play only a minor role on the instability characteristics. Indeed simulations modeling a xenon plasma discharge, with or without collision processes, showed comparable results. In the same way, the comparison between Ar and fAr simulations, as well as between He and fHe simulations, or Kr and fKr, shows a good agreement between the cases modeling the real chemistry and the cases modeling a "fake" chemistry (the chemistry of xenon as expressed in Section 7.1, but the corresponding ion mass). This agreement confirms that ion/neutral and

electron/neutral collisions do not play a major role on the instability.

7.3 Anomalous electron cross-field transport

Following the Equations presented in Section 4.3.3, the mobilities obtained from the simulations: μ_{pic} and μ_{eff}, can be compared to the analytical values: μ_{eff}^{sat} and $\mu_{\text{classical}}$, taken from [11].

The comparison for each simulation is given in Table 7.3. Simulations using the changed mass without the corresponding chemistry are presented as well in order to complete the study.

Table 7.3 – Comparison between physical values measured from the simulation and predictions from the kinetic theory for the electron cross-field mobility.

Case		PIC values		Analytical values	
	m_i	μ_{pic}	μ_{eff}	μ_{eff}^{sat}	$\mu_{\text{classical}}$
(Unit)	[AMU]		$[\text{m}^2\text{V}^{-1}\text{s}^{-1}]$		
(Equation)		(4.9)	(4.10)	(4.15)	(4.7)
He	4.003	4.6	4.1	3.5	0.02
Ar	39.95	5.3	4.7	3.7	0.1
Kr	83.80	5.4	4.7	3.7	0.2
Xe	131.3	5.8	5.1	3.7	0.2
fHe	4.003	5.0	4.4	3.6	0.2
fKr	83.80	6.0	5.2	3.7	0.2
fAr	39.95	5.6	4.9	3.7	0.2

Values given in Table 7.3 are mean values averaged during the last 5μs of the simulation. Thus these values are averaged at a period of the simulation when the instability is saturated. Error margin of mobilities are estimated to be $\approx \pm 0.5[\text{m}^2\text{V}^{-1}\text{s}^{-1}]$ for PIC values, and $\approx \pm 0.1[\text{m}^2\text{V}^{-1}\text{s}^{-1}]$ for analytical results.

As detailed in Equation 4.15, μ_{eff}^{sat} depends on the ion exit velocity, v_{zi}, which depends on the ion mass. Since the ion is accelerated by a constant electric field along (Oz), E_z, and collisions are not playing a significant role, and the ions are injected at a very low temperature, the exit velocity can be estimated as:

$$v_{zi} = \sqrt{\frac{2qE_zL_z}{m_i}} \tag{7.16}$$

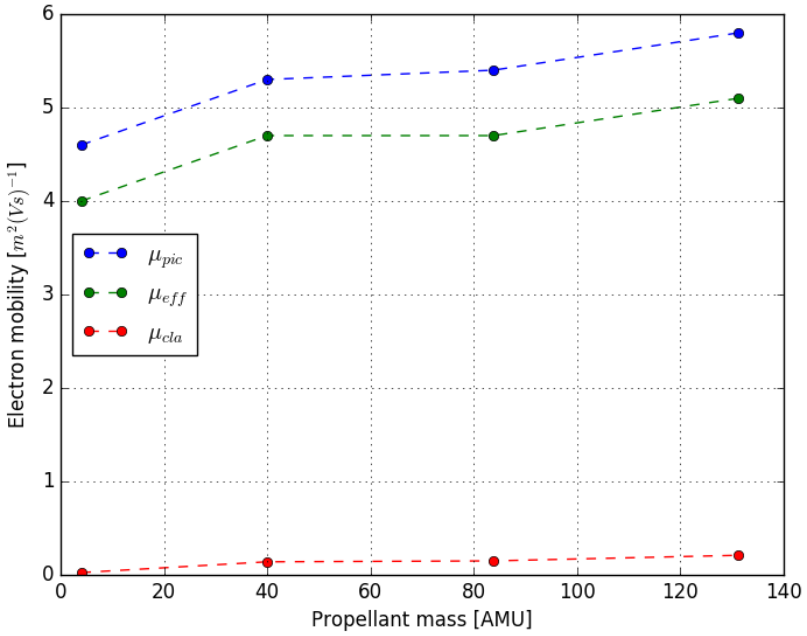

Figure 7.4 – Evolution of the mobility estimates and results from the PIC simulation, summarized in Table 7.3: (blue) μ_{pic} given by Equation 4.9, (green) μ_{eff} given by Equation 4.10, and (red) $\mu_{\text{classical}}$ given by Equation 4.7.

Measurements from the simulations have confirmed the validity of this estimate for xenon simulations, thus Equation 7.16 is used for the alternative propellants.

The evolution of the mobility estimates with the propellant mass, summarized in Table 7.3, is illustrated in Figure 7.4, where we can easily observe the very slight increase of the electron cross-field mobility with the propellant mass.

As shown in Table 7.3, the enhanced mobility measured in the simulation, μ_{pic}, is not heavily impacted by the propellant change. Indeed, as expressed by the kinetic theory, the electron mobility is mostly impacted by the electron temperature, T_e. Yet the electron temperature does not change significantly with the propellant, as highlighted by Table 7.4.

Although the electron temperature, T_e, does not vary with the propellant, the collision frequency, ν_m, is impacted in particular in the case of Helium. These values are expressed in Table 7.4. This can be explained by looking at one of the model specificities. As detailed in Section 3.1.4, macro-particles

Table 7.4 – Physical values measured in the simulations.

Case	m_i [AMU]	ν_m [$m^{-3}s^{-1}$] (Equation 4.8)	T_e [eV]	n_{couples} [macro-particles/Δt]
He	4.001	1.70×10^7	47	75
Ar	39.95	1.50×10^7	48	25
Kr	83.80	1.53×10^7	49	17
Xe	131.3	1.54×10^7	47	17
fHe	4.001	1.50×10^7	45	70
fAr	39.95	1.52×10^7	47	18
fKr	83.80	1.54×10^7	47	17

are re-injected from the walls in order to compensate losses and ensure the system neutrality. Thus in the case of Helium, the number of macro-particles re-injected, n_{couples}, is much higher than with other gases.

As for values in Table 7.3, values given in Table 7.4 are mean values averaged during the last 5μs of the simulation, when the instability is saturated.

7.4 Alternative propellants and secondary electron emission

The impact of alternative propellants has been studied in the simplistic case where SEE is not modeled and walls are considered grounded, the simulation set-up can be made more complex by adding SEE processes as well as floating dielectric walls into the model.

7.4.1 Alternative propellants in a realistic HET model

As expressed in Section 6.5, the set-up chosen for the dielectric walls is $\epsilon^r_{\text{diel}} = 25$ and $L_{\text{diel}} = 3$mm, representing a realistic set-up for modern HETs.

Concerning the SEE model, it is chosen to keep the linear model from [96]. Indeed this model is considered as a relevant compromise in term of complexity and calculation time versus accuracy. However the SEE yield shows the same behavior for the studied alternative propellants as for xenon in Section 5.5: Indeed in each case, $\bar{\sigma}$ shows a saturation at a given value, so that $\sigma_{\text{cr}} < \bar{\sigma} < 1$. This is expected since the electron temperature, T_e, is the same for all the propellant, as detailed in Table 7.6, and the SEE is mainly determined by the electrons.

Using this set-up, LPPic2D was used in order to model the plasma discharge for the three alternative propellants: argon, krypton, and helium. Thus comparisons could be made with a similar simulation using xenon as propellant.

Results are summed up in Table 7.5 concerning the instability characteristics, and Table 7.6 concerning mobility comparisons.

Table 7.5 – Comparison between physical values measured from the simulation and predictions from the kinetic theory about the instability characteristics for alternative propellants in a realistic HET model.

PIC values				
Case	m_i [AMU]	λ [mm]	f [MHz]	v_{ph} [10^3ms^{-1}]
He	4.003	1.0	30.0	30.0
Ar	39.95	1.0	8.0	9.0
Kr	83.80	1.0	6.0	7.5
Xe	131.3	1.0	5.0	5.5
Case	m_i [AMU]	$\lvert\delta\widetilde{n}_e\rvert/n_e$ [%]	$\lvert\delta\widetilde{\Phi}\rvert/T_e$ [%]	
He	4.003	17	37	
Ar	39.95	20	40	
Kr	83.80	19	41	
Xe	131.3	18	56	
Analytical values				
Case	m_i [AMU]	λ [mm] (Equation 4.3)	f [MHz] (Equation 4.5)	v_{ph} [10^3ms^{-1}] (Equation 4.6)
He	4.001	0.8	33	27.0
Ar	39.95	0.8	10.0	9.0
Kr	83.80	0.8	7.2	6.0
Xe	131.3	0.8	5.8	5.0
Case	m_i [AMU]	$\lvert\delta\widetilde{n}_e\rvert/n_e$ [%]	$\lvert\delta\widetilde{\Phi}\rvert/T_e$ [%]	
He	4.001	33	33	
Ar	39.95	33	33	
Kr	83.80	33	33	
Xe	131.3	33	33	

Measurements presented in Tables 7.5 and 7.6 are exposed to the same error margin as the results presented in Tables 7.1, 7.2, and 7.3 since they

Table 7.6 – Comparison between physical values measured from the simulation and predictions from the kinetic theory for the electron cross-field mobility.

Case			PIC values		Analytical values	
	m_i	T_e	μ_{pic}	μ_{eff}	μ_{eff}^{sat}	$\mu_{\text{classical}}$
	[AMU]	[eV]		$[\text{m}^2\text{V}^{-1}\text{s}^{-1}]$		
(Equation)			(4.9)	(4.10)	(4.15)	(4.7)
He	4.001	33	5.5	4.7	3.0	0.026
Ar	39.95	35	5.9	5.0	3.2	0.14
Kr	83.80	34	5.8	4.9	3.1	0.14
Xe	131.3	37	6.5	5.5	3.3	0.19

share the same measurement methods. These values are averaged during the last 5μs of the simulation, when the instability is saturated, in order to lower the statistical noise level.

While the replacement of metallic grounded walls by floating dielectric walls does not impact significantly the plasma discharge behavior as shown in Chapter 6, the introduction of secondary electron emission from the walls has an important cooling effect, as described in Chapter 5. This conclusions are confirmed by these simulations, introducing SEE processes as well as dielectrics, in comparison with simulations from Section 7.2.

These simulations confirm those from Section 7.2, showing that the mobility is not impacted by the propellant used. Even in a more realistic model simulating more properly the ceramic closing the system, this conclusion is still valid.

7.4.2 SEE yield oscillations regime

Another investigation consists of a study of the effects of alternative propellants in the case of the SEE yield oscillations regime, identified in Section 5.3.1. Indeed, as the propellant is changed, it is necessary to study whether the RO appear at the same ϵ^* parameter or if this parameter is impacted. Since the electron temperature is not significantly modified by the propellant change (cf. Table 7.6), the consequence on ϵ^* is expected to be very low.

This study has been conducted on the same propellants as in Section 7.4.1, modeling krypton, argon, and helium plasma discharges.

Two gases featured a SEE yield oscillations regime similar to the xenon case from Section 5.3.1: krypton and argon. Indeed these two gases showed

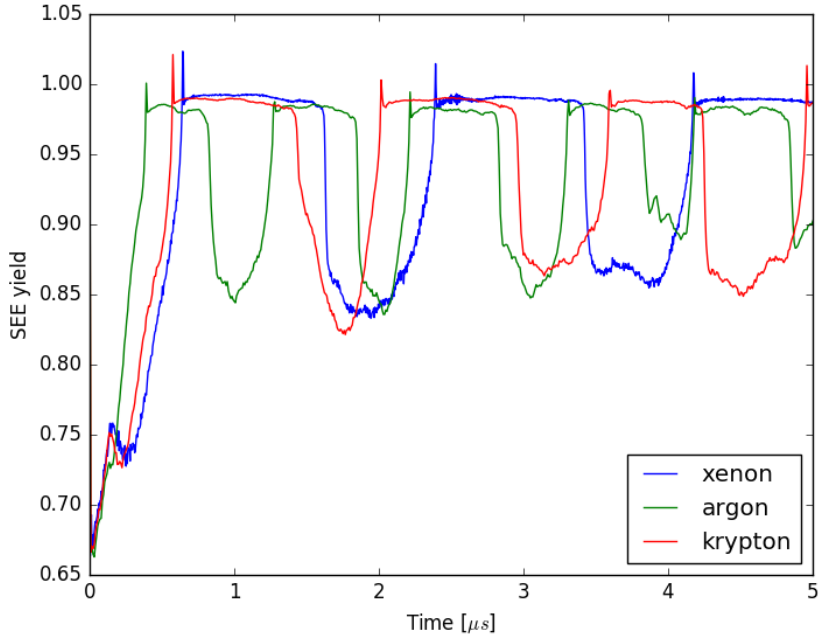

Figure 7.5 – Temporal evolution of the SEE yield in the case of argon (green), xenon (blue), and krypton (red) with a linear SEE model leading to a SEE yield oscillations regime. This superposition, despite being difficult to read, allows a proper comparison of the different pseudo-period lengths and oscillation amplitudes.

expected oscillations of the SEE yield as highlighted by Figure 7.5.

While these two gases showed typical temporal evolution of their SEE yield, two notable features are significant:

— The values of the SEE yield between which it is oscillating are the same for the three gases. Indeed in Figure 7.5, the SEE yield oscillates pseudo-periodically from a lower value of ≈ 0.85, and a higher value slightly higher than σ_{cr}. Since this value is obtained from Equation 5.3, the lower the ion mass, the lower the value of σ_{cr}.

— The pseudo-periodicity observed in the three figures seems to present a longer pseudo-period the lower the ion mass. Indeed, while xenon shows a pseudo-period of $\approx 2\mu$s, krypton has a pseudo-period of $\approx 1.2\mu$s, and argon $\approx 1.0\mu$s.

Finally in the case with helium, a significantly lighter gas, the set-up of the SEE model with the same parameters features a SEE yield oscillations regime with higher frequency oscillations. So high in fact that the oscillations

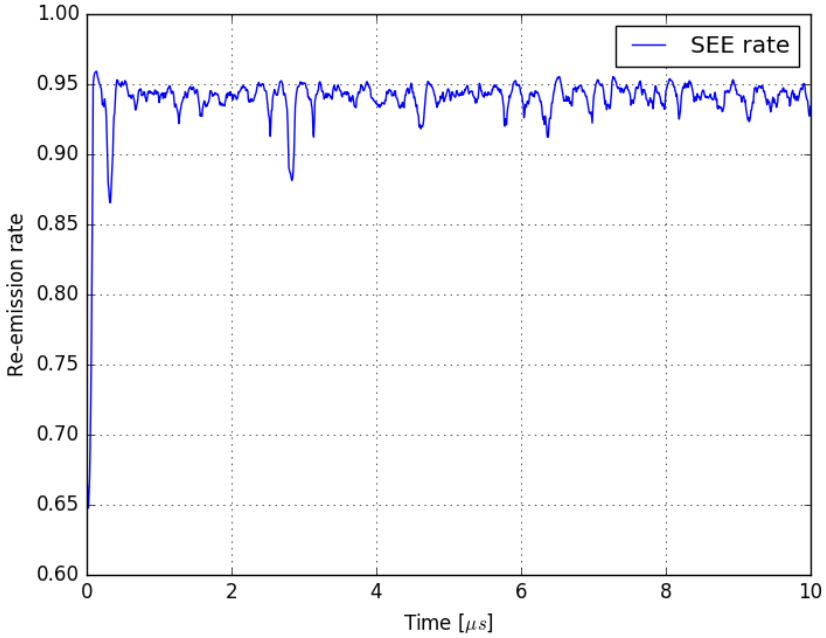

Figure 7.6 – Temporal evolution of the SEE yield in the case of helium with a linear SEE model set-up for a SEE yield oscillations regime.

observed are difficult to identify, and do not oscillate between the same values. This behavior is illustrated in Figure 7.6.

7.5 Global model

The global model presented in Section 5.4 is adapted to the alternative propellant results presented previously. The global model is used with the corresponding ion masses in order to compare the PIC/MCC simulations with the global model results. Since the critical value of ϵ^* for which the global model does not reach an equilibrium changes as a function of the mass, the plots of each gases are traced from this lower critical value.

The PIC/MCC simulations used to do these comparisons are the ones presented in Section 7.4.2, with $\sigma_0 = 0.5$, $\epsilon^* = 45$eV, and $\sigma_{\max} = 2.9$, and simulations done in the same conditions but with $\epsilon^* = 30$eV, and with $\epsilon^* = 60$eV.

Firstly the electron temperature is compared in Figure 7.7. This comparison shows the same difference between the global model and the PIC/MCC simulations for each gas, keeping the relative order of the gases. As observed

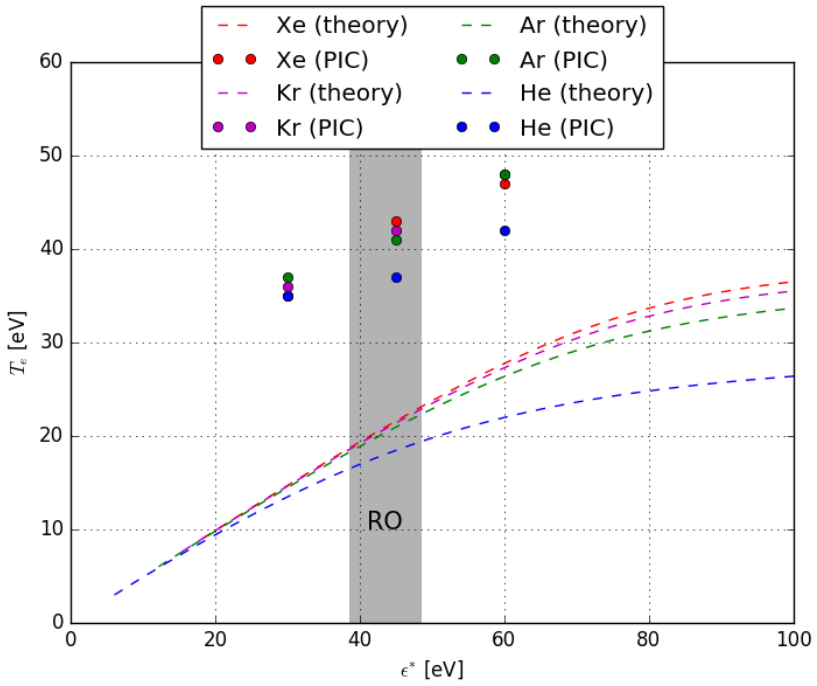

Figure 7.7 – Evolution of the electron temperature at steady state as a function of ϵ^*: (dashed lines) theoretical results from the global model, (dots) PIC/MCC results. Each color corresponds to a given propellant: (red) xenon, (blue) helium, (green) argon, and (purple) krypton. The range of ϵ^* for which ROs are observed is highlighted by a light gray rectangle.

in Figure 7.7, the electron temperature is expected to be lower the lighter the propellant.

Secondly the potential drop at the walls is compared in Figure 7.8. As for the electron temperature, the relative order between gases is kept between PIC/MCC and global model results. Moreover it is confirmed that the lighter the propellant the lower the expected plasma potential.

Thirdly the SEE yield, $\bar{\sigma}$ is compared in Figure 7.9. This shows a bad agreement, with results from the global model being very different from PIC/MCC simulations results, in particular for $\epsilon^* = 60$eV. This can be explained, for the case where $\epsilon^* = 45$eV, by the difficulty to reliably measure $\bar{\sigma}$ in a case where SEE yield oscillations are present. Concerning values obtained at $\epsilon^* = 30$eV and $\epsilon^* = 60$eV, these observations confirm the deviation from the global model already observed for xenon in Section 5.4.

Finally the ratio $P_{\text{loss,w}}/P_{\text{loss}}$ is plotted in Figure 7.10. In this figure we can observe that the lighter the propellant, the higher the ratio, mostly for

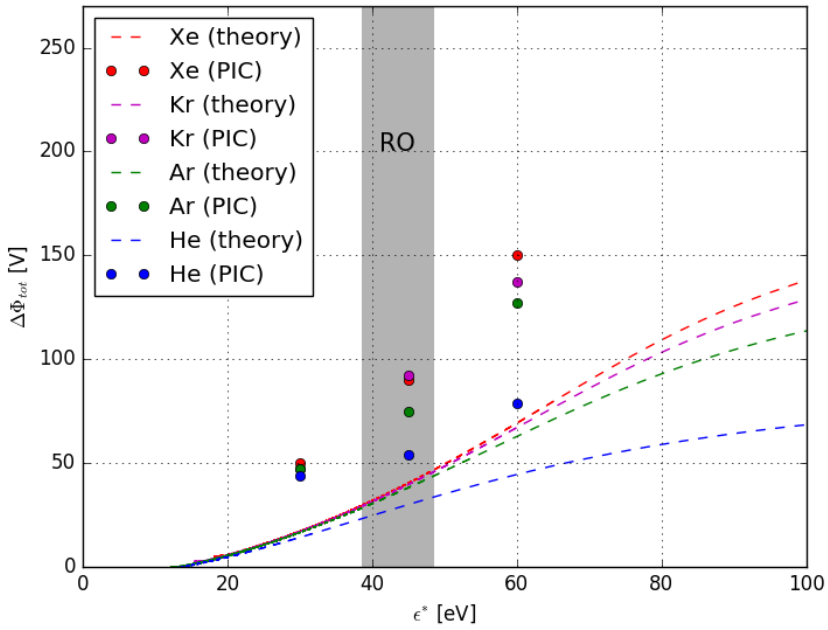

Figure 7.8 – Evolution of the plasma potential drop at the walls at steady state as a function of ϵ^*: (dashed lines) theoretical results from the global model, (dots) PIC/MCC results. Each color corresponds to a given propellant: (red) xenon, (blue) helium, (green) argon, and (purple) krypton. The range of ϵ^* for which ROs are observed is highlighted by a light gray rectangle.

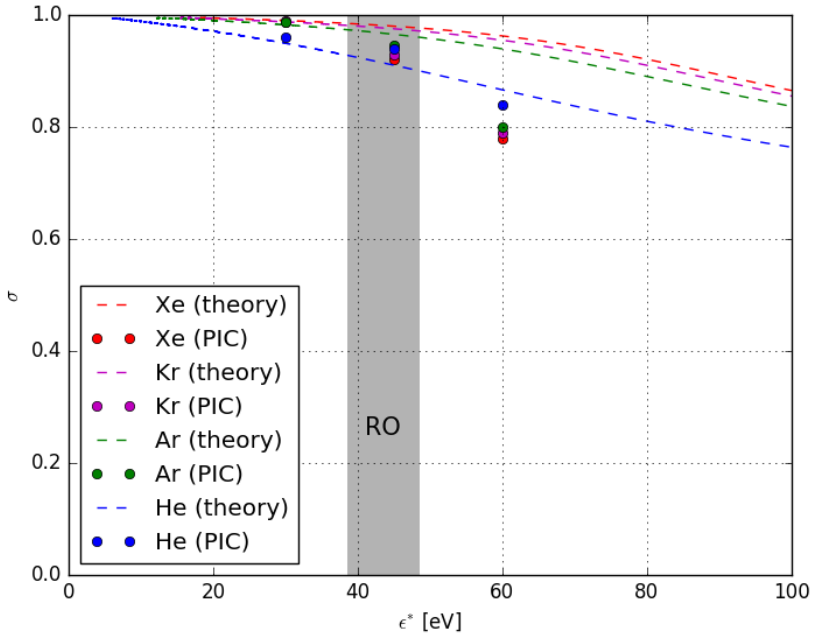

Figure 7.9 – Evolution of the SEE yield at steady state as a function of ϵ^*: (dashed lines) theoretical results from the global model, (dots) PIC/MCC results. Each color corresponds to a given propellant: (red) xenon, (blue) helium, (green) argon, and (purple) krypton. The range of ϵ^* for which ROs are observed is highlighted by a light gray rectangle.

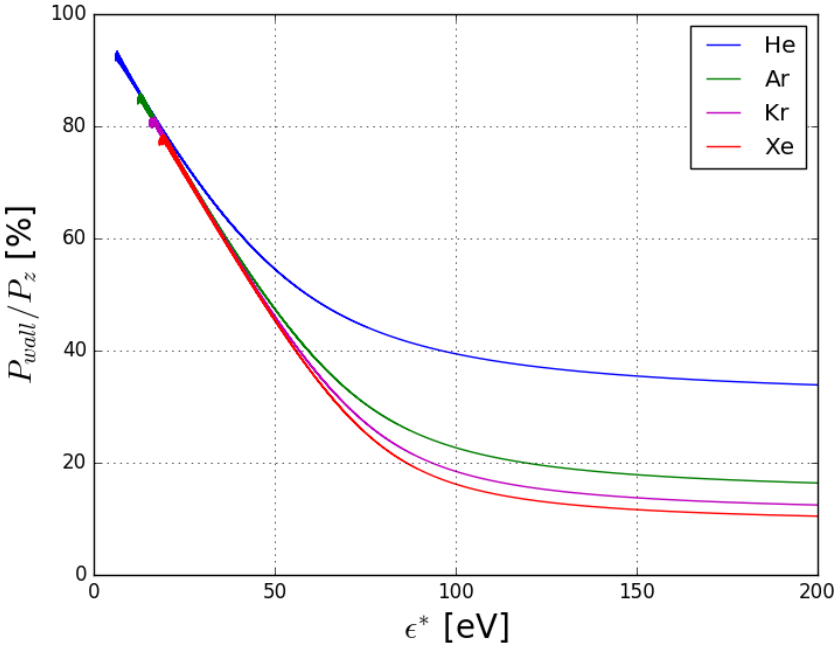

Figure 7.10 – Evolution of the $P_{\text{loss,w}}/P_{\text{loss}}$ ratio at steady state as a function of ϵ^*: (red) xenon, (blue) helium, (green) argon, and (purple) krypton.

high values of ϵ^*. Thus xenon is, as experimentally confirmed, expected to provide the best thruster efficiency. However, for mid-range values of ϵ^*, already highlighted as optimal values in Section 5.4.3, the difference between xenon, argon and krypton does not seem significant.

7.6 Conclusion

This chapter has presented results obtained by the implementation in LP-Pic2D of various noble gases than can be used as propellants in the plasma discharge. Thus it is possible to study the impact of propellant change in the modeled system. Firstly in a simplified geometry with metallic grounded walls, we were able to confirm the minor impact of collisional processes, as already highlighted in Section 4.2.1, and test the kinetic theory [69] for various propellants. Indeed, as predicted, the lighter the propellant, the shorter the growth time, and the higher the electron drift instability frequency. Moreover the anomalous electron transport is not, or only weakly, impacted by the propellant change. This is mainly due to the fact that the electron temperature is not impacted by the propellant change in our simulation set-up,

and is coherent with the kinetic theory [69, 11].

In a second time, the use of a more realistic model allowed us to better characterize, and confirm, the previous conclusions in a more credible model.

Thirdly the impact of propellant change on the SEE yield oscillations regime allowed quick, but meaningful, insights in the characteristics governing this complex plasma discharge behavior. Indeed it appears that this regime is correctly oscillating between a value of ≈ 0.85 and a value slightly higher than σ_{cr} corresponding to the modeled gas. Moreover the pseudo-period of the oscillations was observed to be shorter with lighter propellants. However these observations do not seem to apply to the helium discharge, where its significantly lighter ion mass shows an unexpected behavior.

Finally the use of the global model has allowed us to verify its results with various propellants. This has brought us to the conclusion that for the considered ϵ^* range, the expected $P_{\mathrm{loss,w}}/P_{\mathrm{loss}}$ ratio is not expected to be significantly altered by the use of krypton or argon instead of xenon.

However since the focus of this work has been to study mono-propellant plasma discharge in HETs, further studies should include the possibility to investigate a mix of gases, as well as negative ions. This should allow the study of HETs using iodine, atmospheric propellants [64], or the impact of the H_2/Xe mixture on the electron drift instability [117].

Another limitation is the fact that LPPic2D has been implemented to only follow singly positively charged ions. This assumption can be justified in the case of xenon, as it has been detailed along the previous chapters, but is perhaps not confirmed in the case of alternative propellants.

Moreover the present simulation set-up does not allow to self-consistently obtain the electron temperature. Indeed, as shown in the global model, the electron temperature is obtained from the simulation parameters and not from the axial fluxes. Thus the impacts of alternative propellants cannot be completely covered.

Finally a less obvious limitation is due to the geometry used in these simulations. Indeed the $r-\theta$ cut used in LPPic2D to model the HET plasma discharge does not allow a proper self-consistent solving of the propellant flow rate or the ion trajectories. Consequently, if such a geometry is adapted to investigate the coupled effects of the electron drift instability as well as the plasma/wall interactions, as it has been done in the previous chapters, it does not allow a proper model of the thruster performance.

Chapter 8

Conclusion and future works

8.1 Conclusions

Following previous 2D PIC/MCC $z-\theta$ simulations, the electron drift instability has been highlighted as the electron anomalous transport main driver [40, 58]. However, plasma/wall interactions, while not being the main driver of the electron anomalous transport [39, 48, 49, 50, 51, 52], have been experimentally observed to play a significant role on the plasma discharge behavior [7, 27, 37, 47]. Consequently, in order to investigate the impacts of both the electron drift instability as well as the SEE on the electron transport, 3D or 2D PIC/MCC $r-\theta$ simulations are needed. Although 3D simulations are geometrically accurate, they are computationally costly, needing geometrical scaling to model a slice of a HET channel [70], thus impacting some of the plasma discharge characteristics [71]. In contrast, 2D $r-\theta$ models are computationally more friendly, yet they lose some of the geometrical accuracy.

Indeed, previous 2D PIC/MCC $r-\theta$ simulations [73, 42], despite a proper modeling of the dielectric walls, SEE processes, and electron drift instability, were unable to obtain a saturation of the instability through the system set-up. Consequently this work has consisted to generalize and take advantage of a method introduced by 1D PIC/MCC simulations [74, 68] in order to mimic a direction orthogonal to the simulation. This has allowed us to introduce a so-called "fake" (Oz) length, which is able to ape the channel axial length.

However the $r-\theta$ cut, while being completed by a "fake" (Oz) direction, is placed near the HET channel exit plane, since this region is characterized by both a large electron drift instability, and a strong SEE. Moreover, since the electron drift instability features short wavelength (of the order of the mm) oscillations [13], the curvature has been neglected, enabling the model

to use Cartesian coordinates, but restricting its results to large radius HETs.

The development of LPPic2D, the 2D PIC/MCC simulation tool used to model the exit plane of a large radius HET in the $r - \theta$ direction has taken advantage of recent HPC development, and has aimed to efficiently use the newly available calculation power in order to create a versatile and flexible simulation tool. Thanks to this development, inspiration from previous similar kinetic simulations [42, 73, 68], and inputs from an appropriate kinetic theory [69], we were able to investigate numerous topics, in particular plasma/wall interactions and anomalous cross-field electron transport.

The development process has been characterized by a special attention paid to the verification and validation of the simulation tool. Indeed, unitary test cases from [78], or tailor made, were systematically used at each step of the development in order to verify each new feature implemented in LPPic2D. Complementing these unitary tests, a global benchmark [75] was used to regularly verify the proper functioning of LPPic2D's PIC/MCC core algorithm. Development of LPPic2D from scratch to a 2D-3V PIC/MCC model able to realistically simulate a HET exit plane was detailed in Chapter 2 and Chapter 3.

The obtained tool has then been used to study numerous physical cases of a HET exit plane, taking the opportunity of LPPic2D's computational efficiency to conduct diverse parametric studies. A first parametric study has been conducted in a simplified model, without floating dielectric walls, or SEE processes. The kinetic theory from [69] correctly predicted the anomalous transport, as well as the electron drift instability characteristics, for various plasma densities. The enhanced cross-field electron mobility is observed to depend on an "electron density/electric field" correlation term, which represents an electron/ion friction force that is strongly enhanced by the electron drift instability. Although the instability occurs in the azimuthal direction, the presence of the magnetic field couples this with the axial direction. The results of this investigation have been detailed in Chapter 4.

Then, the model was completed by adding SEE models. Numerous models of electron induced SEE were used, and a parametric study over the SEE intensity was conducted. This study showed the auxiliary impact of SEE on the electron transport in HETs compared to the electron drift instability contribution, and allowed us to identify three different regimes of the plasma discharge behavior, one of them featuring pseudo-periodic relaxation oscillations. Moreover a comparison between two SEE models for BN ceramics was realized, and showed significantly different results, both realistic models featuring a different discharge regime. However concerning the electron anomalous transport, the SEE was shown to produce an enhanced near-wall transport (as it was highlighted by simulations without the electron drift

instability included), but the parametric study over the SEE strength highlighted that this increase is negligible compared to the effect of the electron drift instability. From this investigation a global model has been developed. While not enabling proper detail of the relaxation oscillations, this model has allowed a precise quantification of the radial losses in the system. Chapter 5 describes the results of these investigation.

Once SEE processes have been investigated, floating dielectric walls were implemented in the study. Modeling these floating potential walls are increasing the model quality and precision, however, while the main conclusions of the previous studies were not impacted by this change, dielectric walls are observed to affect the general behavior of the plasma discharge, adding noise to the observations. The introduction of dielectric walls, coupled to SEE processes allowed us to realistically model HETs, and observe key behaviors. The anomalous transport in a realistic HET model with SEE and dielectrics has been shown to feature a near-wall conductivity, as expected only playing an auxiliary role on the electron anomalous transport, which finds its deepest roots into the electron drift instability. These results were detailed in Chapter 6.

Finally using this realistic model of a HET exit plane in the $r-\theta$ direction, a parametric study was done over the propellant used in the plasma discharge. Using realistic collisional cross-sections, three propellants other than xenon were modeled: argon, helium, and krypton. This showed a good agreement with the kinetic theory [69], and highlighted the fact that neither the electron anomalous transport nor the electron drift instability appear to be impacted by the propellant change. Study over alternative propellant has been detailed in Chapter 7.

Nevertheless an important limitation is affecting the studied system: since Poisson's equation is only solved in the $(Ox - Oy)$ plane, but not along the (Oz) direction, the wavenumber of any fluctuations along (Oz) are zero. This implies that convection of the instability away from the simulation plane is not correctly modeled. We have tried to account for this by using a finite axial length, and by removing particles which cross the boundaries in this direction, mimicking the axial dimension of the system. But this still only represents an approximation, since the wave propagation along (Oz) cannot be properly modeled without solving Poisson's equation along this axis.

Another geometrical limitation, due to the mimicking of the (Oz) dimension, is that the electric field inside the dielectrics is also solved only along the $(Ox - Oy)$ plane, neglecting the evolution of the potential in the axial direction.

Unfortunately both of these limitations are inherent to the 2D model and the way the third dimension is only mimicked. A proper solving of these

limitations can only come through the solving of Poisson's equation along (Oz), and thus through the development of a 3D PIC/MCC model.

8.2 Future works

The present work has been focused on the mechanisms at the root of the electron anomalous cross-field transport: the electron drift instability and the SEE. To reach this goal a 2D PIC/MCC parallelized code was developed from scratch, complemented along the way, keeping a strong focal point on the code's reliability. While results have been obtained in an almost realistic system, numerous topics of interest can be identified to complement this work and enhance our understanding of HETs.

Firstly, as HETs are expected to be miniaturized for always smaller satellites, the channel curvature is expected to play a role on the plasma discharge behavior. For these extremely small geometries, sometimes with even purely cylindrical channels, the large radius approximation allowing us to use Cartesian coordinates is no longer valid. In such cases, the implementation of a cylindrical coordinates system in LPPic2D core is a crucial need. Nonetheless, the geometrical scales at which such thrusters are expected to operate (typically in the order of the cm or less), could allow an unscaled 3D PIC/MCC simulation of their discharge channel. Consequently extension of the set-up to cylindrical coordinates and/or a 3D simulation tool is an important step in our quest to better understand HETs.

Secondly while LPPic2D is able to model a noble gas discharge, complex chemistries needing negatively charged ions, multiply charged ions, or mix of gases are not modeled. This is a limitation to test some of the possible alternative propellants, such as atmospheric mixtures [64], H_2/Xe mixtures [117], or iodine [61, 62]. It is a limitation as well to model very high power HETs where the proportion of Xe^{2+} can be significant [7].

Finally, as already highlighted, the electron temperature is in the $r - \theta$ simulation obtained from the simulation parameters. The geometry of the simulation does not allow us to study the propellant flow rate or the ion trajectories. Consequently the thruster performance cannot be properly assessed, since neither the thruster efficiency nor the thruster divergence can be estimated. In order to access these values a 3D PIC/MCC code can be developed. This can be a solution for very small HETs as already detailed, however for medium and large HETs this solution is known to be computationally too costly. The solution could be the adaptation of the "fake" length method to the r direction in a $z - \theta$ simulation. Emphasizing observations from the $r - \theta$ model presented in this work, a "fake" r length

model can be developed in order to keep the 2D computational efficiency while obtaining accurate values of thruster performance.

I would like to conclude this work, as well as these three years of research, on a quote from a well-known plasma scientist, and sometimes philosopher, Trevor Lafleur: *"Life is like a PIC simulation"*[1]: chaotic, complex, perhaps sometimes unexpected, but always fruitful.

1. the 22nd of May, 2017, Presqu'île de Giens

Appendix A

LPPic2D structure and characteristics

The LPPic2D simulation tool has been designed in order to take advantage of modern informatics. Thus, it has been encoded in Fortran 2003 and in C language. This has structured the code and required some implementations.

A.1 Data structure

For the sake of code readability and efficiency, the data is structured using the latest *Fortran 2003* standards. Thus both the values at the grid-point as well as the values associated with the particle are stored in specifically designed derived type. The derived type for the particle is given in Code sample A.1 while the derived type used for grid-points is given in Code sample A.2.

```
type particle
  integer                          :: numero = 0
  integer                          :: charge = 0
  double precision, dimension(3) :: V      = [0,0,0]
  double precision                 :: X      = 0
  double precision                 :: Y      = 0
  double precision                 :: Z      = 0
  double precision, dimension(2) :: Ei     = [0,0]
  double precision, dimension(3) :: B      = [0,0,0]
end type particle
```

Code sample A.1 – Derived type for particle data storage.

Where numero is an identification number used in order to follow the particle individually, and the values stored are normalized following Section 2.1.2.

```
type grid
  double precision                 :: Rho  = 0
  double precision, dimension(2)   :: Ej   = [0,0]
  double precision                 :: Phi  = 0
  double precision                 :: p    = 0
  double precision, dimension(3)   :: B    = [0,0,0]
  double precision                 :: Nume = 0
  double precision                 :: Numi = 0
end type grid
```

Code sample A.2 – Derived type for grid-point data storage.

Where Rho is the unnormalized value of the charge density and p the normalized one. Nume and Numi are respectively the electron and ion density around the grid-point.

Once those derived types are defined, the data corresponding to the system can be stored in different vectors and arrays.

Thus particles are sort in vectors, each specie having its own. The vector is not full, allowing the use stack algorithms (described in Appendix B.3). However if the vector becomes too small to store all the particles present in the CPU domain, it can be enlarged. Adding a new particle type (neutrals, meta-stables,...) hence requires to create a new vector.

Grid-points are stored in a bi-dimensional array, defined from 0 to $y_{\max}$ in the (Oy) direction and from 0 to $x_{\max}$ in the (Ox) direction. Since the Poisson equation is not solved in the (Oz) direction, this array does not need to represent and store data along (Oz).

Finally the permittivity of the grid-point is stored thanks to a different derived type, defined in Code sample A.3, which is organized on a different bi-dimensional array. This array is different from the one for the grid-points, since it does not represent the full system and it is not needed when no dielectric walls are modeled. This was done in order to preserve the memory efficiency of LPPic2D.

```
type permittivity
  double precision :: n=1 !Northern permittivity
  double precision :: s=1 !Southern permittivity
end type permittivity
```

Code sample A.3 – Derived type for dielectric permittivity data storage.

Furthermore since particles need to be exchanged between CPU domains in the parallel version of LPPic2D, a corresponding *MPI* data type is created following the *Fortran 2003* derived type defined in Code sample A.1. This is done in Code sample A.4.

```
subroutine type_derives
implicit none

  integer,dimension(8) :: types,longueur_blocs
  integer(kind=MPI_ADDRESS_KIND), dimension(8) ::
     deplacements, adresses
  type(particle) :: particule
  integer :: i

  types(1:2) = MPI_INTEGER
  types(3:8) = MPI_DOUBLE_PRECISION

  longueur_blocs = (/ 1,1,3,1,1,1,2,3 /)

  call MPI_GET_ADDRESS(particule%numero,adresses(1),code)
  call MPI_GET_ADDRESS(particule%charge,adresses(2),code)
  call MPI_GET_ADDRESS(particule%V, adresses(3),code)
  call MPI_GET_ADDRESS(particule%X, adresses(4),code)
  call MPI_GET_ADDRESS(particule%Y, adresses(5),code)
  call MPI_GET_ADDRESS(particule%Z, adresses(6),code)
  call MPI_GET_ADDRESS(particule%Ei,adresses(7),code)
  call MPI_GET_ADDRESS(particule%B, adresses(8),code)

  do i=1,8
    deplacements(i) = adresses(i)-adresses(1)
  end do

  call MPI_TYPE_CREATE_STRUCT(8,longueur_blocs,
     deplacements,types,type_particle_mpi,code)

  call MPI_TYPE_COMMIT(type_particle_mpi,code)

end subroutine type_derives
```

Code sample A.4 – Derived type for parallel particle exchange.

In the same way, since CPU have each a closed domain, it is important to store the boundaries of every CPU domain in order to allow each CPU to be aware of its neighbors in case of an exchange of particles. Thus LPPic2D initialized the domain decomposition then store in each CPU an array, called

topogrid, that stores the boundaries along (Ox) and (Oy) of every domain using their ranks.

A.2 LPPic2D organization

LPPic2D is attempting to obtain high performances on modern massively parallel clusters. Consequently the way of writing the code has to respect modern standards. Structured programming as well as modular programming methods are necessary to reach this goal. However the organization and structure of LPPic2D should be done in order to minimize the dependencies and maximize the code performance while keeping the readability to an acceptable level.

An example of the code structure is detailed in Figure A.1. However the structure is not fixed in time, and continuous developments are ensuring that this Figure A.1 is not up-to-date anymore.

A.3 Initializations

A.3.1 Random seed

Numerous subroutines and functions of LPPic2D use the *Fortran 2003* random number generator. This generator allows the code to obtain a random number from an uniform distribution defined on $[0, 1]$. However this random number generator needs to be initialized differently between every processor and between different simulations, in order to prevent the observation of patterns. This is done by using the internal clock of every CPU used by LPPic2D as described in Code sample A.5.

```
subroutine mon_germe
implicit none

  integer, allocatable  :: seed(:)
  integer               :: un, istat, n

  call random_seed(size = n)
  allocate(seed(n))

  un = 97
```

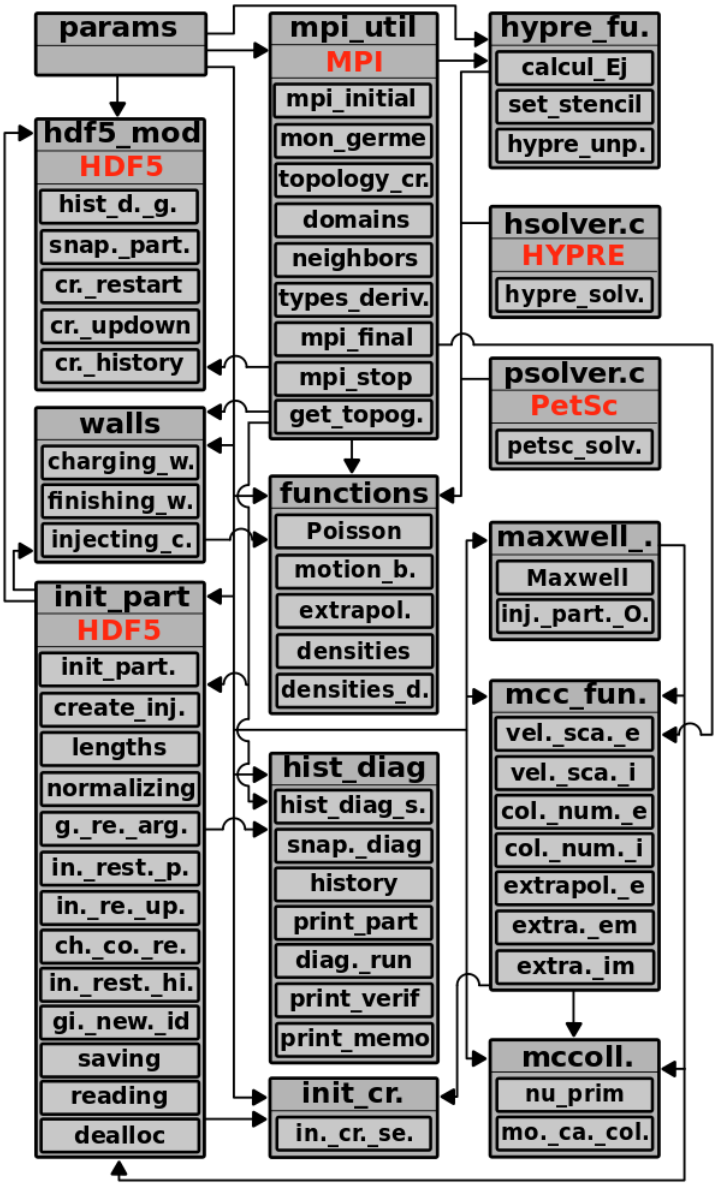

Figure A.1 – Hierarchy between the different modules constituting LPPic2D. In a sake for clarity, the main module of the program is not represented despite every module being affiliated to it. At the top of each module figure its name, in red eventually the library linked with the module, in gray boxes the subroutines and functions of the module. Arrows represent links between modules.

```
  open(unit=un, file="/dev/urandom", access="stream",
     form="unformatted", action="read", status="old",
     iostat=istat)

  if (istat == 0) then
    read(un) seed
    close(un)
  else
    print  *, "RNG_not_seeded_well"
    seed =124126
  endif

  seed(:) = abs(seed(:))
  call random_seed(put=seed)

n distribution end subroutine mon_germe
```

Code sample A.5 – Initialization of the random number generator seed.

A.3.2 Maxwellian distribution

Once the seed for the random number generator has been initialized, we have to be able to obtain velocities from a Maxwellian distribution at a given temperature (T_e for electrons, T_n for neutrals, T_i for ions). This is obtained by Code sample A.6 from [118].

```
subroutine Maxwell(tabps)
implicit none

  type(particle), intent(inout) :: tabps
  double precision              :: v_Te, v_Ti, v_Tn, W,
     X1, X2
  integer                       : j

  v_Te = sqrt(q*Te/me)       !used to scale velocities
  v_Ti = sqrt(q*Ti/mi)
  v_Tn = sqrt(q*Tn*kb/mi/q)

  do j=1,3
      W = 1
      do while(W .GE. 1 .OR. W .LE. 0)
          call random_number(X1)
          call random_number(X2)
```

```
            X1 = dble(2.0*X1 - 1.0)
            X2 = dble(2.0*X2 - 1.0)
            W = X1*X1 + X2*X2
        end do

        W = sqrt( (-2.0*LOG(W)) /W)

        !getting scaled velocities
        if(tabps%charge == -1) then
            tabps%V(j) = v_Te*X1*W
        else if(tabps%charge == 1) then
            tabps%V(j) = v_Ti*X2*W
        else if(tabps%charge == 0) then
            tabps%V(j) = v_Tn*X2*W
        else
            print *,'error_in_particle_charge_definition'
        end if
    end do
end subroutine Maxwell
```

Code sample A.6 – Obtaining velocities from a Maxwellian distribution at a given temperature.

Indeed in Code sample A.6, the algorithm is able to obtain using uniformly distributed random numbers, here noted $X1$ and $X2$, a scaled velocity from a Maxwellian distribution.

A.3.3 Maxwellian flux distribution

When particles are injected from a wall or a boundary, along the (Oz) or (Oy) directions, the velocity components of the particle need to be taken from a Maxwellian flux distribution. Obtaining a Maxwellian flux distribution from an uniform distribution is described in [118]. An example is given for the injection of particles in the (Oz) direction (corresponding to ions and electrons being re-injected after having hit the fake axial length boundary) Code sample A.7.

```
subroutine injecting_particles_Oz(part)
implicit none

  type(particle), intent(inout) :: part
  double precision              :: V_thermal, R
```

```
  !first getting normalized velocities from a Maxwellian
     distribution
  call Maxwell(part)
  part%V(:) = part%V(:)*dT/dX

  !getting the thermal velocity
  if(part%charge == -1) then
    V_thermal = sqrt((2.d0*q*Te)/me)
  else if(part%charge == 1) then
    V_thermal = sqrt((2.d0*q*Ti)/mi)
  else
      V_thermal=0
    print *,part%charge,'error'
  end if

  !Getting the Maxwellian flux velocity in the Oz
     direction
  call random_number(R)
  if(part%charge == -1) then
    part%V(3) = -abs(V_thermal*sqrt(-log(R))*dT/dX)
  else if(part%charge == 1) then
    part%V(3) =  abs(V_thermal*sqrt(-log(R))*dT/dX)
  else
    print *,part%charge,'error'
  end if

end subroutine injecting_particles_Oz
```

Code sample A.7 – Obtaining velocities from a Maxwellian flux distribution at a given temperature.

In this particular case the velocities along (Ox) and (Oy), orthogonal to the injection direction, are obtained from a classical Maxwellian distribution as detailed in the previous section. Only the way the velocity along the injection direction, here (Oz), is impacted.

Appendix B

Parallel operation of LPPic2D

LPPic2D has been parallelized thanks to a distributed memory scheme with spatial domain decomposition in order to use the power of modern high performance computing (HPC). The operating of key subroutines and functions of LPPic2D was deeply impacted by this choice, and significantly differ from the sequential version.

B.1 Initializing the spatial domain decomposition

The spatial domain decomposition [84] is obtained thanks to the *MPI* library. However LPPic2D presents a limitation due to the re-injection of particles that have hit the (Oz) fake boundary, as described in Section 3.1.3. This limits the number of domains in the (Ox) direction to only three. Thus when created, the *MPI* topology has to take this limitation into account as described in Code sample B.1.

```
subroutine topology_creation
implicit none

  logical,parameter          :: reOrganization = .false.

  if(Nprocs == 1 .OR. Nprocs == 2) then
    dims(:) = (/ 0,0 /)
  else
    dims(:) = (/ 3,0 /)
  endif
  call MPI_DIMS_CREATE(Nprocs,ndims,dims,code)
```

```
  !creation of the topology
  period(:) = (/ .true. , .false. /)
  call MPI_CART_CREATE(MPI_COMM_WORLD, ndims, dims,
     period, reOrganization, comm2d, code)

end subroutine topology_creation
```

Code sample B.1 – Creating the topology.

This limitation can be overcome by using an hybrid parallelization approach, using both *MPI* and *OpenMP* libraries at the same time. Such a hybrid version was tested for LPPic2D with a coarse method, [89]: In this method no spatial decomposition between the *OpenMP* threads is done, and they all share the same memory as well as the same domain and particles. While it showed promising results with high number of CPUs [85], a fine grain method should be more adapted to the LPPic2D set-up. In this case it would be needed to further decompose each *MPI* domain between all the *OpenMP* threads it is containing.

However the added complexity, and the needed informatics engineering, represented a significant hurdle to adopt this hybrid approach in a daily use. Indeed such hybrid version requires fine set-up to optimize the number of *OpenMP* threads per *MPI* processes. Consequently this hybrid version has not been used to produced results detailed in this work, and will not be further detailed.

B.2 Solving the Poisson equation

As detailed in Section 2.3.2, solving the Poisson equation amounts to solve a matrix equation detailed in Equations 2.49 and 2.50. This is done using libraries freely available.

In the sequential version of LPPic2D, before any parallelization, the *MUMPS* library [81]. However this library does not efficiently use the spatial domain decomposition initiated with the parallelization of LPPic2D.

Consequently LPPic2D has been interfaced with libraries allowing the efficient use of parallel computational ressources. The two that are implemented in LPPic2D are: *PetSc* [82], and *HYPRE* [83]. Since these libraries are encoded in *C* language, an interface needs to be created. This interface is designed as a *Fortran 2003* subroutine that passes the relevant informations to a *C* functions that calls the library. This is done in a separate module that needs to be compiled using a *C* compiler. Such modules are seen in Figure A.1 as hsolver.c and psolver.c.

This interfacing between *Fortran 2003* and *C* does not create too much complexity, nevertheless obvious differences (array indexation, memory usage,...) between the two languages have to be properly addressed in order to prevent time consuming errors.

B.3 Exchanging particles

The equation of motion integration in its principle is not impacted by the parallelization. Yet the parallelization brings to this function the need to exchange particles between CPU domains. Indeed once the particle has been moved, it can appears that its position is no longer inside the CPU domain on which it is stored. Consequently the particle, and all its informations, has to be passed to the relevant CPU domain.

In order to describe this exchange we firstly have to describe the stack algorithm developed to efficiently move the particles. As explained in Appendix A.1, the particles are stored in vectors. One vector per specie. This vector, tab, is not full and has empty slots at its end. Thus in order to store the number of particles stored in the vector, an integer, compt, is defined. When particles are moved, the algorithm begins with the particle in the last slot of tab and moves particles until it reaches the slot 0 of tab. However if a particle is absorbed or needs to be passed to another domain, the slot occupied by the particle becomes empty. Thus the slot is exchanged with the particle at the last position in tab. This keeps tab sorted, and is summed up in Figure B.1.

Once the particles have been moved and sorted in tab, a temporary vector is created in which are stored the particles that need to be passed to another domain. This exchange used the *sendrecv* function from the *MPI* library in order to deal with deadlocks. This is done by simultaneously receiving and sending in a defined order, as described in Figure B.2. Note that the CPUs can only exchange particles with its 8 direct neighbors.

This rotating exchange is done in two phases where the CPU exchanges with all its neighbors. Firstly the CPU exchanges one integer, which is the number of particles the CPU is going to passes to its neighbor. Secondly the exchange itself can happen. This two steps exchange is given in Code sample B.2. Since every CPU domain is exchanging with all its neighbors, all the particles are exchanged.

```
do i=1,8
  !exchange the number of paticles to be exchanged during
      next step
```

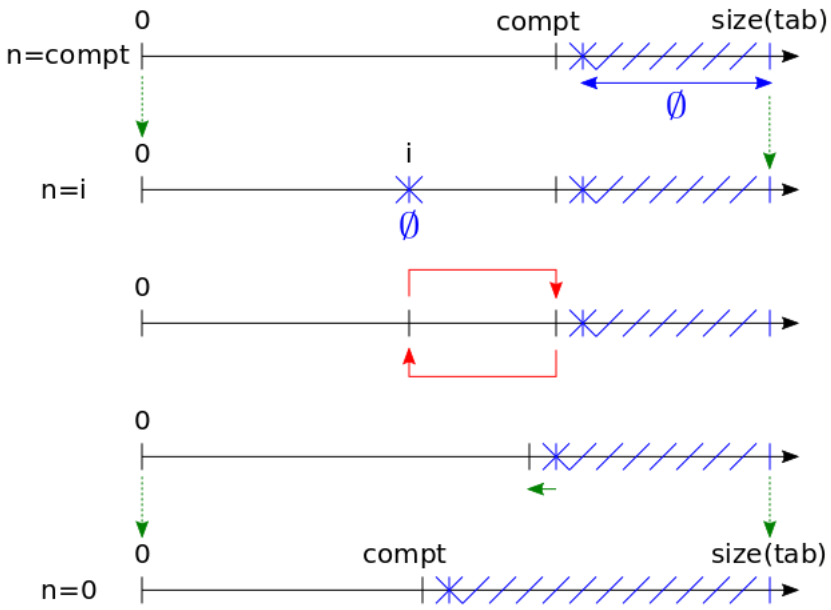

Figure B.1 – Stack algorithm used to efficiently move the particles. When the algorithm reaches a particle, at position i in the tab vector, that needs to be absorbed or passed to another CPU, an exchange is done in order to keep the stack sorted.

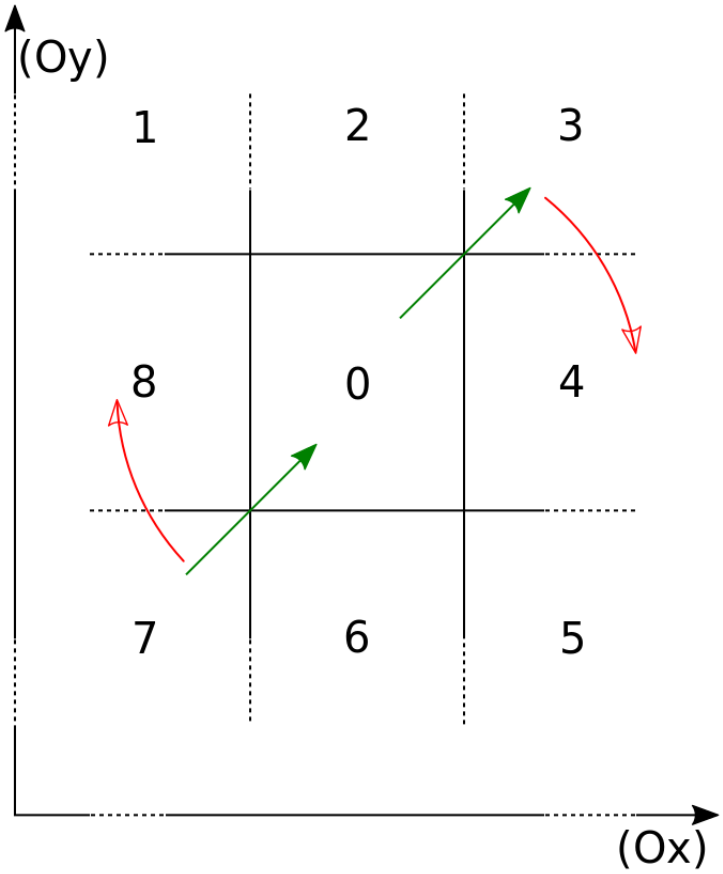

Figure B.2 – Schematic of the algorithm used in order to pass particles between domains. While the CPU 0 receives particles from 7 (green), it sends to 3 (green) then the operation is repeated clockwise (red) in the next direction.

```
  toex(:)   = (/ to(i,1),to(i,2) /)
  fromex(:) = 0

  call MPI_SENDRECV(toex(1),2,MPI_INTEGER,voisins_to(i),
                    etiq_1,fromex(1),2,MPI_INTEGER, &
                    voisins_fr(i),etiq_1,comm2d, &
                    statut,code)

  if(voisins_fr(i) == MPI_PROC_NULL) fromex(:) = (/ 0,0
     /)
  from(i,1) = fromex(1)
  from(i,2) = fromex(2)

  !exchange the particles themselves (ions and electrons)
  tabe_ex(to(i,1)+1:to(i,1)+to(i,2),i) = tabi_ex(1:to(i
     ,2),i)
    call MPI_SENDRECV(tabe_ex(1,i),to(i,1)+to(i,2), &
                      type_particle_mpi,voisins_to(i), &
                      etiq_2,tab_in(1,i),from(i,1)+ &
                      from(i,2), type_particle_mpi, &
                      voisins_fr(i),etiq_2,comm2d, &
                      statut,code)

  !get the number of elec/ions to be injected afterwards
     in the tabe/i vectors
  e_injected = e_injected + from(i,1)
  i_injected = i_injected + from(i,2)
end do
```

Code sample B.2 – Two steps exchange of particles between CPU domains.

B.4 Exchanging ghost cells values

As described in Section 2.3.3, each CPU domain has the grid-points values on its own domain as well as in the first cells of its direct neighbors. This is summed in Figure B.3.

In order to optimize this exchange in a sense of computational time, asynchronous communications are used to carry out these communications. Using asynchronous communications allows us to cover some of the exchanges by calculations. Indeed, while the CPUs are exchanging the peripheral data concerning the ghost cells (data being sent or received), the data at the center of the domain is not requested by communications. Thus it is possible to perform calculations on this memory space during the asynchronous commu-

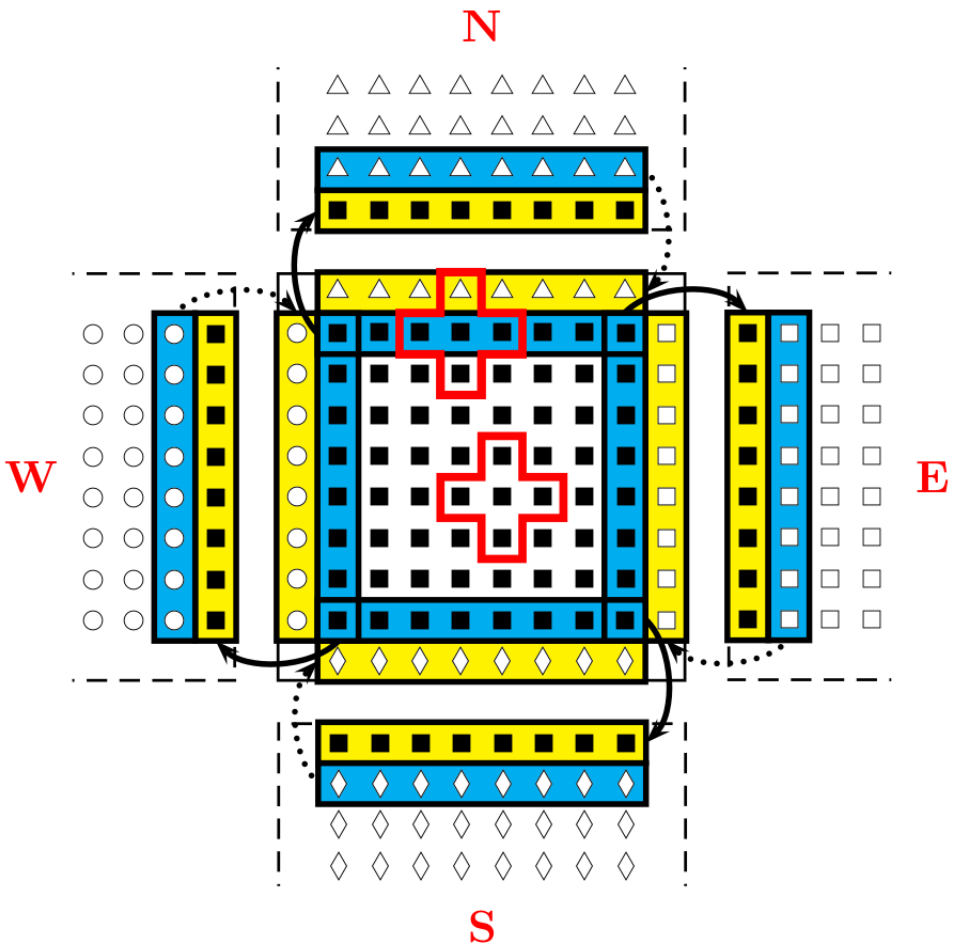

Figure B.3 – Exchange of values between neighbors domains in order to fill the so-called "ghost cells". In blue the cells inside the domain that are exchanged with the neighbors. In yellow the ghost cells that need to be received from the neighbors. In red the five-points stencil. Scheme from [84].

nications, which allows optimization of the code performance by decreasing the waiting time.

Appendix C

The restart capability

In order to guarantee the operating of LPPic2D on modern clusters, it is required to be able to stop the code after a given calculation time, the so-called "wall-time", and restart the code afterwards. Such a restart procedure can happen several times per simulations (typical wall-times are set between 6 and 12h while our simulations can last for more than 30h) and should not impact the physical results.

Thus all important values needed to restart the code have to be correctly and efficiently stored in adapted files. Moreover LPPic2D needs to be able to simultaneously know the wall-time corresponding to the cluster it is running on, as well as if the current run is starting from scratch or from a restart point. Both these difficulties have been solved by adding corresponding arguments in the launching script of LPPic2D.

Then LPPic2D needs to be able to restart from a given point without disturbing the physical results. Thus the restart needs to be done only when the diagnostics have been done, otherwise it would disturb the averaging of the physical values on the grid. Consequently the restart can only be done every N_A time-steps, when the diagnostics that have been measuring during the last N_A time-steps are averaging and dumping the data in their corresponding files.

Furthermore the physical values needed to restart LPPic2D need to be stored. This is done through two files.

Particles are all stored in a *HDF5* file that is organized so that it does not need to be fully opened by the CPU to restart: The particles from a given CPU are stored in a given dataset so that the CPU only opens his dataset in the file. Otherwise the CPU would be unable to open the totality of the file in its memory. Nevertheless this is a limitation since the number of CPUs used in the simulation cannot be changed during a restart. The general values of LPPic2D (number

of time-steps already done,...) are stored in a specific dataset opened by every CPU.

Walls values are stored in an appropriate *HDF5* file. Since all the values concerning the walls are stored in the master-processor there is no need for a complex file structure.

Since LPPic2D is modeling an electrostatic system, there is no need to store the physical values at the grid-points. The charge density can be obtained directly from the particles positions at the beginning of the restart.

Appendix D

Performance and scalability

Once LPPic2D is parallelized, solutions used in the simulation tool have to be tested in term of HPC performances. Most part of this work have been detailed in [85].

D.1 Comparison of Poisson solvers

Since LPPic2D has two libraries available to solve the Poisson equation, each of these libraries offering a vast choice of solvers and pre-conditioners, a comparative study has to be done in order to chose the most efficient set-up.

A first study was conducted on a downscaled system (100 times less cells), however since the efficiency of the solvers depends strongly on the system size, the study had to be conducted on the real size system as described in Table 3.3.

Such a comparison between set-ups is presented in Figure D.1 and has been taken from [85].

These comparisons proved the efficiency of *HYPRE* for the modeled system in LPPic2D. Yet not the most efficient set-up was kept for LPPic2D simulations of HETs since it appeared that some areas could be wrongly solved. Consequently the set-up finally chosen for LPPic2D simulations presented in this work is to use the *PFMG* solver from *HYPRE* without any pre-conditioner.

D.2 Scalability of LPPic2D

Using the parameters given by Table 3.3, a strong scaling test has been conducted with LPPic2D. This means that for a given system (typically 25×10^6 particles and 255×1000 grid-points) the number of CPUs used is

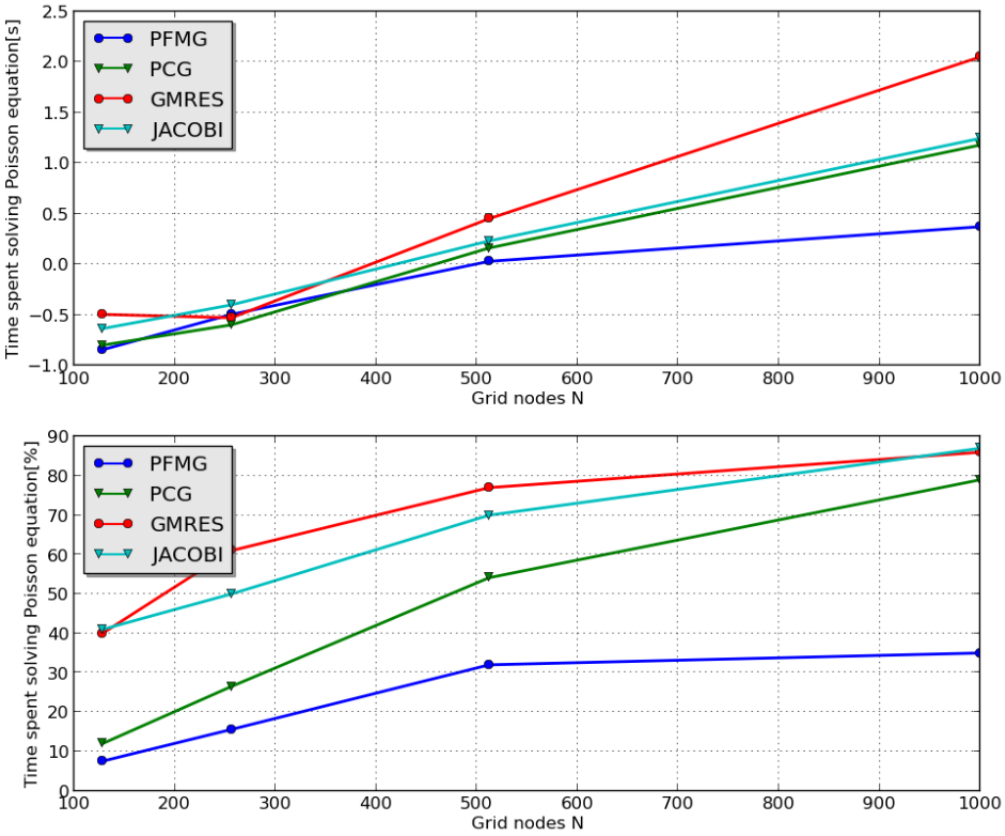

Figure D.1 – Performance comparison between *HYPRE* solvers from [85]. In this comparison, *PFMG* appears to be the most effective solver.

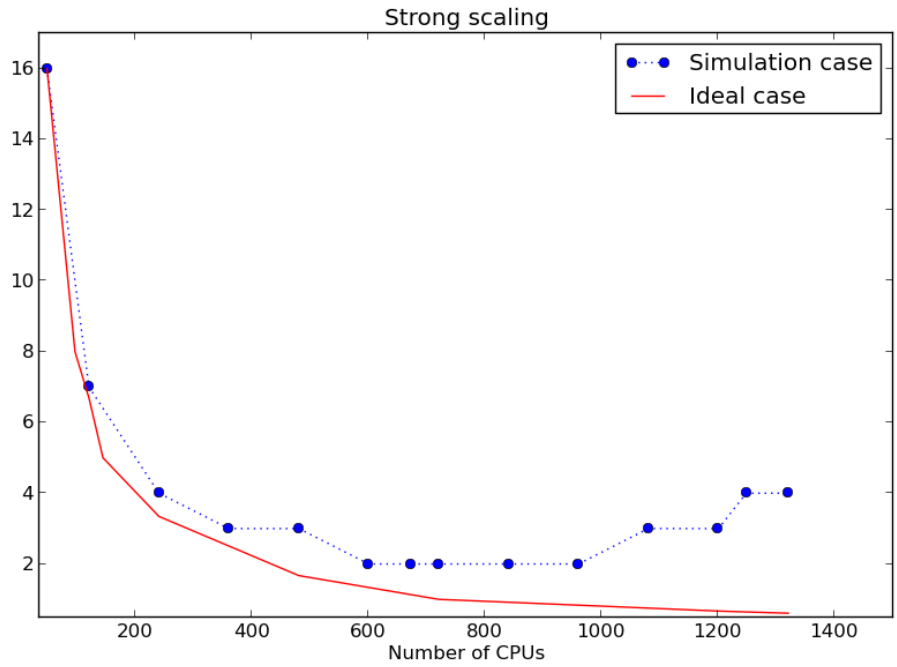

Figure D.2 – Strong scalability test. Performance comparison of LPPic2D (blue) and the ideal scaling factor (red) with the lowest number of CPUs used being 48 [85].

increased step-by-step. For a given number of CPUs the computational time needed to carry on a given number of time-steps (typically some 1000s) is measured. This allows us to compare the code's performance to the ideal scaling. This comparison is graphically given in Figure D.2.

As made explicit by Figure D.2, LPPic2D shows an optimum near 600 CPUs. Therefore LPPic2D is mainly used with 360 CPUs.

This limitation is due to the limitation of 3 CPUs along the (Ox) direction given in Appendix A.3. Indeed due to this limitation, the width of a given domain along the (Oy) direction becomes smaller and smaller while the number of CPUs increases. This leads to domains being significantly thin, with only a width of some grid-points along (Oy).

Hence exchanges of particles as well as communications inside the Poisson solver become significant and slow down LPPic2D performances.

As already expressed in Appendix A.3, a solution to overcome this algorithmic limitation is to develop a hybrid version of LPPic2D, taking advantage of both *MPI* and *OpenMP* libraries, of both distributed and shared memory programming. These programming methods are nearer from the

modern architecture of cluster, but adds an important level of complexity to the code's readability and sustainability.

Appendix E

The CCP Helium benchmark

The CCP Helium benchmark defined in [75] has been used to verify MiniPIC and LPPic2D quality. As said the benchmark defined in [75] is comprised of four test-cases. The first test-case is described in Section 2.2.3 and in particular with parameters defined in Table 2.1. In these four test-cases the simulation tool (MiniPIC or LPPic2D) has to model a plasma closed between two absorbing electrodes. One grounded, the other at a fixed sinusoidally varying potential, so that $\Phi(x = 0) = 0\text{V}$ and $\Phi(x = x_{\max}) = V_0 \sin(\Omega_0 t)$. Furthermore those cases are characterized by a number of time-step modeled, N_S, as well as a number of time-step at the end of the simulation, where the results are averaged, N_A. These simulations can be done one-dimensionally with MiniPIC, or bi-dimensionally with LPPic2D as described in Figure 2.12.

These four test-cases given by [75] share the same structure, however the parameters used to set-up the simulation change in order to test the code differently. The set of parameters used for the first test-case is given in Table 2.1. For the three last cases, the set-up parameters are summed up in Table E.1.

Once the N_S time-steps are exectuted, the results, averaged on N_A time-steps, are output from the simulation and compared to the corresponding benchmark values given by [75]. Numerous physical values are given in [75], however only some were compared on a regular basis as quality indicators.

— The time-averaged ionization source term profile from one electrode to another.
— The time-averaged ion density distribution profile from one electrode to another.
— Ion density in the mid-plane of the discharge.
— Electron temperature in the mid-plane of the discharge.
— Ion current collected at each electrodes.
— On MiniPIC, the time averaged power density coupled to electrons

Table E.1 – Simulation environment used for the three last cases of the CCP benchmark [75]

Test case		2	3	4
Physical Parameters				
Electrode separation	$L\,(cm)$		6.7	
Neutral density	$n_{\mathrm{g}}\,(10^{20}m^{-3})$	32.1	96.4	321
Neutral temperature	$T_g\,(K)$		300	
Frequency	$f\,(MHz)$		13.56	
Voltage	$V_0\,(V)$		450	
Simulation time	$t_s\,(s)$	$5120/f$	$5120/f$	$15360/f$
Averaging time	$t_A\,(s)$	$32/f$	$32/f$	$32/f$
Physical constants				
Electron mass	$m_e\,(kg)$		9.109	
Helium ionic mass	$m_i\,(kg)$		6.67	
Initial conditions				
Plasma density	$n_0\,(10^{14}m^{-3})$	5.12	5.12	3.84
Electron temperature	$T_e\,(K)$		30.000	
Ion temperature	$T_i\,(K)$		300	
Particles per cell	$N_{/C}$	256	128	64
Numerical parameters				
Cell size	$\Delta x\,(m)$	$L/256$	$L/512$	$L/512$
Time step	$\Delta t\,(s)$	$(800f)^{-1}$	$(1600f)^{-1}$	$(3200f)^{-1}$
Steps to execute	N_S	4 096 000	8 192 000	49 152 000
Steps to average	N_A	25 600	51 200	102 400

was monitored. This diagnostic was abandoned on LPPic2D.
It is important to note that some of these diagnostics are not overlapping with the diagnostics presented in Section 2.3.3. Indeed some of the diagnostics used for the benchmark were only used for it, and are not "switched on" in normal production use of LPPic2D, while some diagnostics of LPPic2D are not used when benchmarking the code with this CCP discharge cases.

Despite the fact that the benchmark [75] does not offer an analytical solution, this benchmark does offer a global testing of a PIC code. This completes adequately the unitary tests realized to confirm the accurate operating of some key subroutines.

Appendix F

Secondary electron emission yield

The secondary electron emission (SEE) is obtained as detailed in Equation 5.17, as:

$$\bar{\sigma} = \frac{\Gamma_{e,\text{see}}}{\Gamma_{e,w}} = \frac{\int_\Omega \sigma(v_x) v_x f(\mathbf{v}) d^3\mathbf{v}}{\int_\Omega v_x f(\mathbf{v}) d^3\mathbf{v}}$$

where $f(\mathbf{v})$ is a Maxwellian distribution defined as:

$$f(\mathbf{v}) = f(v_x, v_y, v_z) = n_e \left(\frac{m_e}{2\pi T_e}\right)^{3/2} \exp\left(-\frac{m_e}{2T_e}(v_x^2 + v_y^2 + v_z^2)\right) \quad \text{(F.1)}$$

and Ω is the domain on which the integrals are defined. As the electron velocity is defined on the half-space closed by the wall, Ω corresponds to $v_x \geq 0$, and $v_y, v_z \in [-\infty, \infty]$. Thus the two integrals, $\Gamma_{e,w}$ and $\Gamma_{e,\text{see}}$, have to be estimated separately.

Let us firstly concentrate on $\Gamma_{e,w}$. By expressing $\mathbf{v} = v_x\mathbf{u}_x + v_y\mathbf{u}_y + v_z\mathbf{u}_z$, we can decompose $\Gamma_{e,w}$ along the Ω domain as:

$$\Gamma_{e,w} = B \int_{-\infty}^{\infty} dv_y \exp\left(-Av_y^2\right) \int_{-\infty}^{\infty} dv_z \exp\left(-Av_z^2\right) \int_0^{\infty} v_x dv_x \exp\left(-Av_x^2\right) \quad \text{(F.2)}$$

with:

$$A = \frac{m_e}{2T_e} \quad \text{(F.3)}$$

$$B = n_e \left(\frac{m_e}{2\pi T_e}\right)^{3/2} \quad \text{(F.4)}$$

By integrating Equation F.2, we easily obtain:

$$\Gamma_{e,w} = \frac{\pi B}{2A^2} \tag{F.5}$$

Let us now estimate $\Gamma_{e,\text{see}}$ as given by Equation 5.17. By using the definition of $\sigma(\epsilon)$ given by Equation 3.24, and keeping in mind that $\forall \epsilon, \sigma(\epsilon) \leq \sigma_{\max}$, we obtain:

$$\begin{aligned}\Gamma_{e,\text{see}} = B \int_0^\infty v_x dv_x \int_{-\infty}^\infty dv_y \\ \int_{-\infty}^\infty dv_z min_\epsilon(\sigma_{\max}, \sigma_0 + \frac{\epsilon}{\epsilon^*}[1-\sigma_0]) \exp\left(-A(v_x^2+v_y^2+v_z^2)\right)\end{aligned} \tag{F.6}$$

As the minimum function is defined over $\epsilon = \frac{1}{2} m_e (v_x + v_y + v_z)^2$, a change of variable is needed in order to properly decompose Equation F.6.

From the definition of σ, we observe that, in the velocity space, σ is defined from the linear Equation 3.24 inside a half-sphere centered in 0, defined for $v_x \geq 0$, and with a radius $\epsilon_{\max}$. While outside this half-sphere, for $\epsilon \geq \epsilon_{\max}$, $\sigma = \sigma_{\max}$.

Thus $\epsilon_{\max}$ is the minimum value of ϵ for which $\sigma(\epsilon) = \sigma_{\max}$. This can be easily estimated from σ saturated linear expression, as:

$$\epsilon_{\max} = \frac{\sigma_{\max} - \sigma_0}{1 - \sigma_0} \epsilon^* = R \tag{F.7}$$

with R the notation used in the following for the sake of brevity.

Consequently, by changing to spherical variables in the velocity space in Equation F.6, so that $v_x = r\, sin\phi\, cos\theta$, $v_y = r\, sin\phi\, sin\theta$, and $v_z = r\, cos\phi$, and decomposing the integrals, we obtain:

$$\begin{aligned}\Gamma_{e,\text{see}} = B \Bigg[\int_0^R r^2\, dr \int_{-\pi/2}^{\pi/2} d\theta \int_0^\pi sin\phi\, d\phi\, r\, sin\phi\, cos\theta (\sigma_0 + Cr^2) e^{-Ar^2} \\ + \int_R^\infty r^2\, dr \int_{-\pi/2}^{\pi/2} d\theta \int_0^\pi sin\phi\, d\phi\, r\, sin\phi\, cos\theta \sigma_{\max} e^{-Ar^2}\end{aligned} \tag{F.8}$$

with:

$$C = \frac{1}{2} \frac{1-\sigma_0}{\epsilon^*} m_e \tag{F.9}$$

Integration of Equation F.8 directly gives us:

$$\begin{aligned}\frac{\Gamma_{e,\text{see}}}{\pi B} &= \sigma_0 \frac{1-e^{-AR^2}(AR^2+1)}{2A^2} \\ &+ C\frac{2-e^{-AR^2}(AR^2(AR^2+2)+2)}{2A^3} \\ &+ \sigma_{\max}\frac{e^{-AR^2(AR^2+1)}}{2A^2}\end{aligned} \tag{F.10}$$

By re-arranging Equation F.10, we obtain:

$$\begin{aligned}\Gamma_{e,\text{see}} &= \sigma_0 \frac{\pi B}{2A^2} + \frac{1}{2}\frac{1-\sigma_0}{\epsilon^*} m_e \frac{1}{A}\frac{\pi B}{2A^2} \\ &+ (\sigma_{\max}-\sigma_0)e^{-AR^2}(AR^2+1)\frac{\pi B}{2A^2} \\ &- \frac{C}{A}e^{-AR^2}(AR^2(AR^2+2)+2)\frac{\pi B}{2A^2}\end{aligned} \tag{F.11}$$

By substituting the value of Equation F.2 into Equation F.11, and simplifying, we obtain:

$$\begin{aligned}\bar{\sigma} = \frac{\Gamma_{e,\text{see}}}{\Gamma_{e,w}} &= \sigma_0 + \frac{1-\sigma_0}{\epsilon^*}2T_e \\ &+ (\sigma_{\max}-\sigma_0)\,e^{-AR^2}\,(AR^2+1) \\ &+ T_e\frac{\sigma_0-1}{\epsilon^*}\,e^{-AR^2}\,(AR^2(AR^2+2)+2)\end{aligned} \tag{F.12}$$

with:

$$AR^2 = \frac{m_e}{2T_e}\left(\frac{\sigma_{\max}-\sigma_0}{1-\sigma_0}\,\epsilon^*\right)^2 \tag{F.13}$$

The expression obtained in Equation F.12 is then used in the global model developed in Section 5.4.1. However, it is important to note that if we neglect the saturation of the SEE model, and consider an infinitely increasing SEE yield (i.e. $\sigma_{\max} \mapsto \infty$), then Equation F.12 simplifies to:

$$\bar{\sigma}_{unsaturated} = \sigma_0 + \frac{1-\sigma_0}{\epsilon^*}2T_e \tag{F.14}$$

Since the saturated part of Equation F.12, which corresponds to $\bar{\sigma}-\bar{\sigma}_{unsaturated}$, is strongly dependent to e^{-AR^2}, the saturation of the SEE model presented in Section 3.2.2 appears not to play a significant role on the global model behavior.

Bibliography

[1] Astro-note.org, "liste des lancements de satellites artificiels depuis 1957 ." http://astro-notes.org/list_sat.htm, June 2016.

[2] Euroconsult, "Satellite Value Chain – snapshot 2015," *Euroconsult Executive Report*, February 2016.

[3] Space generation advisory council, "Space generation advisory council," *Space Generation Advisory Council*, 2015.

[4] A. Bouchoule, A. Cadiou, A. Heron, M. Dudeck, and M. Lyszyk, "An overview of the French research program on plasma thrusters for space applications," *Contrib. Plasma Phys.*, vol. 41, no. 573, 2001.

[5] E. Y. Choueiri, "A critical history of electric propulsion: The first 50 years (1906-1956)," *J. Propul. Power*, vol. 20, no. 2, pp. 193–203, 2004.

[6] S. Mazouffre, "Electric propulsion for satellites and spacecrafts: Established technologies and novel approaches," *Plasma Sources Sci. Technol.*, vol. 25, no. 3, 2016.

[7] D. M. Goebel and I. Katz, *Fundamentals of Electric Propulsion: Ion and Hall Thrusters*. Wiley, 2008.

[8] I. Newton and E. Halley, *Philosophiae naturalis principia mathematica*. [Streater, J., Smith, S.] Imprimatur Pepys, S., Regalis Societas praeses, 1687.

[9] K. Tsiolkovsky, *Issledovanie Mirovykh Prostransty Reaktivnymi Priborami*. Naootchnoye Obozreniye, 1903.

[10] J. R. Wertz and W. J. Larson, *Space mission analysis and design*. Torrance, California: Microcosm Press, 1999.

[11] V. Croes, T. Lafleur, Z. Bonaventura, A. Bourdon, and P. Chabert, "2D particle-in-cell simulations of the electron drift instability and associated anomalous electron transport in Hall-effect thrusters," *Plasma Sources Sci. Technol.*, vol. 26, no. 034001, 2017.

[12] D. King, K. de Grys, R. Aadland, D. Tilley, and A. Voigt, "Magnetic flux shaping in ion accelerators with closed electron drift," Mar. 27 2001. US Patent 6,208,080.

[13] J. C. Adam, J. P. Boeuf, N. Dubuit, M. Dudeck, L. Garrigues, D. Gresillon, A. Heron, G. Hagelaar, V. Kulaev, N. Lemoine, S. Mazouffre, J. Perez-Luna, V. Pisarev, and S. Tsikata, "Physics, simulation, and diagnostics of Hall effect thrusters," *Plasma Phys. Control. Fusion*, vol. 24, no. 124041, 2008.

[14] J.-P. Boeuf, "Tutorial: Physics and modeling of Hall thrusters," *Journal of Applied Physics*, vol. 121, no. 1, p. 011101, 2017.

[15] Eutelsat, "operation of Hall Effect Thrusters," 2016.

[16] Y. Raitses, J. Ashkenazy, and M. Guelman, "Propellant utilization in Hall thrusters," *Journal of Propulsion and Power*, vol. 14, no. 2, pp. 247–253, 1998.

[17] C. Boniface, G. J. M. Hagelaar, L. Garrigues, J. P. Boeuf, and M. Prioul, "Modeling of double stage Hall effect thruster," *IEEE Transactions on Plasma Science*, vol. 33, pp. 522–523, April 2005.

[18] R. R. Hofer, P. Y. Peterson, and A. D. Gallimore, "A high specific impulse two-stage Hall thruster with plasma lens focusing," in *IEPC-01-036*, 2001.

[19] E. Ahedo, "Plasmas for space propulsion," *Plasma Phys. Control. Fusion*, vol. 53, no. 124037, 2011.

[20] I. Katz, G. Jongeward, V. Davis, M. Mandell, I. Mikellides, R. Dressler, I. Boyd, K. Kannenberg, J. Pollard, and D. King, *A Hall effect thruster plume model including large-angle elastic scattering.* Joint Propulsion Conferences, American Institute of Aeronautics and Astronautics, July 2001. doi:10.2514/6.2001-3355.

[21] B. Boyd, "Review of Hall Thruster Plume Modeling," *Journal of Spacecraft and Rockets*, vol. 38, no. 3, pp. 381–387, 2001.

[22] F. Taccogna, S. Longo, and M. Capitelli, "Particle-in-Cell with Monte Carlo Simulation of SPT-100 Exhaust Plumes," *Journal of Spacecraft and Rockets*, vol. 39, no. 3, pp. 409–419, 2002.

[23] V. Vial, S. Mazouffre, M. Prioul, D. Pagnon, and A. Bouchoule, "CCD images of Hall effect thruster plume dynamics after ultrafast current ignition," *IEEE Transactions on Plasma Science*, vol. 33, pp. 524–525, April 2005.

[24] V. Kim, "Main physical features and processes determining the performance of stationary plasma thrusters," *J. Propulsion Power*, vol. 14, no. 736, 1998.

[25] A. I. Morozov and V. V. Savelyev, *Fundamentals of stationary plasma thruster theory*, vol. 21. Dordecht: Kluwer, 2000.

[26] E. Ahedo and V. de Pablo, "Combined effects of electron partial thermalization and secondary emission in Hall thruster discharges," *Phys. Plasmas*, vol. 14, no. 083501, 2007.

[27] I. D. Kaganovich, Y. Raitses, D. Sydorenko, and A. Smolyakov, "Kinetic effects in a Hall thruster discharge," *Phys. Plasmas*, vol. 14, no. 057104, 2007.

[28] E. Y. Choueiri, "Plasma oscillations in Hall thrusters," *Phys. Plasmas*, vol. 8, no. 1411, 2001.

[29] S. Barral, K. Makowski, Z. Peradznski, and M. Dudeck, "Transit-time instability in Hall thrusters," *Phys. Plasmas*, vol. 12, no. 073504, 2005.

[30] J. Vaudolon and S. Mazouffre, "Observation of high-frequency ion instabilities in a cross-field plasma," *Plasma Sources Sci. Technol.*, vol. 24, no. 032003, 2015.

[31] S. Barral and E. Ahedo, "Low-frequency model of breathing oscillations in Hall discharges," *Phys. Rev.*, vol. E 79, no. 046401, 2009.

[32] A. I. Morozov, V. V. S. e. b. B. B. Kadomtsev, and V. D. Shafranov, *Reviews of plasma physics*. New-York: Springer Science+Business Media, 2000.

[33] N. B. Meezan, W. A. J. Hargus, and M. A. Cappelli, "Anomalous electron mobility in a coaxial Hall discharge plasma," *Phys. Rev., E 63, 026410*, vol. 63, no. 2, 2001.

[34] N. B. Meezan, *Electron transport in a coaxial Hall discharge*. Ph.d., Department of Mechanical Engineering, Stanford University, 2002.

[35] L. Garrigues, J. Pérez-Luna, J. Lo, G. J. M. Hagelaar, J. P. Boeuf, and S. Mazouffre, "Empirical electron cross-field mobility in a Hall effect thruster," *Appl. Phys. Lett.*, vol. 95, no. 141501, 2009.

[36] I. Katz, I. G. Mikellides, B. A. Jorns, and A. L. Ortega, "Hall2De simulations with an anomalous transport model based on the electron cyclotron drift instability," in *IEPC-2015-402*, 2015.

[37] D. Sydorenko, A. Smolyakov, I. Kaganovitch, and Y. Raitses, "Electron kinetic effects and beam related instabilities in Hall thrusters," *Phys. Plasmas*, vol. 15, no. 053506, 2008.

[38] F. Taccogna, S. Longo, M. Capitelli, and R. Schneider, "Anomalous transport induced by sheath instability in Hall effect thrusters," *Appl. Phys. Lett.*, vol. 94, no. 251502, 2009.

[39] M. Hirakawa, "Electron transport mechanism in a Hall thruster," in *IEPC-97-021*, 1997.

[40] J. C. Adam, A. Héron, and G. Laval, "Study of stationary plasma thrusters using two-dimensional fully kinetic simulations," *Phys. Plasmas*, vol. 11, no. 295, 2004.

[41] A. Ducrocq, J. C. Adam, A. Héron, and G. Laval, "High-frequency electron drift instability in the cross-field configuration of Hall thrusters," *Phys. Plasmas*, vol. 13, no. 102111, 2006.

[42] A. Héron and J. C. Adam, "Anomalous conductivity in Hall thrusters : Effects of the non-linear coupling of the electron-cyclotron drift instability with secondary electron emission of the walls.," *Phys. Plasmas*, vol. 20, no. 082313, 2013.

[43] A. Morozova, Y. Esipchuk, A. Kapulkin, V. Nevrovskii, and V. Smirnov, "Effect of the magnetic field on a closed-electron-drift accelerator," *Sov. Phys.: Tech. Phys.*, vol. 17, no. 482, 1972.

[44] D. Escobar and E. Ahedo, "Low frequency azimuthal stability of the ionization region of the Hall thruster discharge," *Phys. Plasmas*, vol. 21, no. 043505, 2014.

[45] W. Frias, A. I. Smolyakov, I. D. Kaganovitch, and Y. Raitses, "Long wavelength gradient drift instability in Hall plasma devices. I. Fluid theory," *Phys. Plasmas*, vol. 19, no. 072112, 2012.

[46] W. Frias, A. I. Smolyakov, and I. D. Kaganovitch, "Long wavelength gradient drift instability in Hall plasma devices. II. Applications," *Phys. Plasmas*, vol. 20, no. 052108, 2012.

[47] N. Gascon, M. Dudeck, and S. Barral, "Wall material effects in stationary plasma thrusters. I. Parametric studies of an SPT-100," *Phys. Plasmas*, vol. 10, no. 4123, 2003.

[48] C. Boniface, L. Garrigues, G. J. M. Hagelaar, J. P. Boeuf, D. Gawron, and S. Mazouffre, "Anomalous cross-field electron transport in a Hall thruster," *Appl. Phys. Lett.*, vol. 89, no. 161503, 2006.

[49] G. J. M. Hagelaar, J. Bareilles, L. Garrigues, and J. P. Boeuf, "Role of anomalous electron transport in a stationary plasma thruster simulation," *J. Appl. Phys.*, vol. 93, no. 67, 2003.

[50] N. B. Meezan and M. A. Capelli, "Kinetic Study of Wall Collisions in a Coaxial Hall Discharge," *Phys. Rev.*, vol. E 66, no. 036401, 2002.

[51] F. I. Parra, E. Ahedo, J. M. Fife, and M. Martinez-Sanchez, "A two-dimensional hybrid model of the hall thruster discharge," *J. Appl. Phys.*, vol. 100, no. 023304, 2006.

[52] A. N. Smirnov, Y. Raitses, and N. J. Fisch, "Electron cross-field transport in a miniaturized cylindrical Hall thruster," *IEEE Trans. Plasma Sci.*, vol. 34, no. 132, 2006.

[53] S. Yoshikawa and D. J. Rose, "Anomalous Diffusion of a Plasma across a Magnetic Field," *Phys. Fluids*, vol. 5, no. 334, 1962.

[54] E. Y. Choueiri, "Fundamental difference between the two Hall thruster variants," *Phys. Plasmas*, vol. 8, no. 1411, pp. 5025–5033, 2001.

[55] A. W. Smith and M. A. Cappelli, "Time and space-correlated plasma potential measurements in the near field of a coaxial Hall plasma discharge," *Phys. Plasmas*, vol. 16, no. 073504, 2009.

[56] M. K. Scharfe, N. Gascon, M. A. Cappelli, and E. Fernandez, "Comparison of hybrid Hall thruster model to experimental measurements," *Phys. Plasmas*, vol. 13, no. 083505, 2006.

[57] J. Cavalier, N. Lemoine, G. Bonhomme, S. Tsikata, C. Honore, and D. Gresillon, "Hall thruster plasma fluctuations identified as the E x B electron drift instability : Modeling and fitting on experimental data.," *Phys. Plasmas*, vol. 20, no. 082107, 2013.

[58] P. Coche and L. Garrigues, "A two-dimensional (azimuthal-axial) Particle-In-Cell model of a Hall thruster," *Phys. Plasmas*, vol. 21, no. 023503, 2014.

[59] R. Betzendahl, "The 2014 rare gases market report," *Cryogas International*, vol. 52, no. 28, 2014.

[60] A. Kieckhafer and L. B. King, "Energetics of propellant options for high-power Hall thrusters," *J. Propul. Power*, vol. 23, pp. 21–26, 2007.

[61] R. Dressler, Y. H. Chiu, and D. Levandier, "Propellant alternatives for ion and Hall effect thrusters," in *AIAA-2000-0602*, 38th Aerospace Sciences Meetings, American Institute of Aeronautics and Astronautics, jan 2000.

[62] J. Szabo, B. Pote, S. Paintal, M. Robin, A. Hillier, D. R. Branam, and R. E. Huffmann, "Performance evaluation of an iodine-vapor Hall thruster," *Journal of Propulsion and Power*, vol. 28, no. 4, pp. 848–857, 2012.

[63] P. Grondein, T. Lafleur, P. Chabert, and A. Aanesland, "Global model of an iodine gridded plasma thruster," *Phys. Plasmas*, vol. 23, no. 033514, 2016.

[64] Proceedings of Space Propulsion, Bordeaux, *Completion of HET and RIT characterization with atmospheric propellants*, 2012.

[65] L. Rezeau and G. Belmont, "Quelques proprietes des plasmas." lpp.fr, January 2007.

[66] J. Szabo, *Fully kinetic numerical modeling of a plasma thruster*. PhD thesis, MIT, 2001.

[67] M. Lieberman and A. Lichtenberg, *Principles of plasma discharges and materials processing*. Wiley, 1994.

[68] T. Lafleur, S. D. Baalrud, and P. Chabert, "Theory for the anomalous electron transport in Hall effect thrusters: I Insights from particle-in-cell simulations," *Phys. Plasmas*, vol. 23, no. 053502, 2016.

[69] T. Lafleur, S. D. Baalrud, and P. Chabert, "Theory for the anomalous electron transport in Hall effect thrusters: II. Kinetic model," *Phys. Plasmas*, vol. 23, no. 053503, 2016.

[70] F. Taccogna and P. Minelli, "Three-dimensional fully kinetic particle-in-cell model of Hall-effect thruster," in *Presented at the 32nd International Electric Propulsion Conference*, November 2011.

[71] F. Taccogna, S. Longo, M. Capitelli, and R. Schneider, "Self-similarity in Hall plasma discharges: Applications to particle models," *Physics of Plasmas*, vol. 12, no. 5, p. 053502, 2005.

[72] V. Kindratenko and P. Trancoso, "Trends in high-performance computing," *Computing in Science Engineering*, vol. 13, no. 3, pp. 92–95, 2011.

[73] F. Taccogna, R. Schneider, S. Longo, and M. Capitelli, "Kinetic simulations of a plasma thruster," *Plasma Sources Science and Technology*, vol. 17, no. 2, p. 024003, 2008.

[74] J. P. Boeuf, "Rotating structures in low temperature magnetized plasmas—insight from particle simulations," *Front. Phys.*, vol. 2, no. 74, 2014.

[75] M. Turner, A. Derzsi, Z. Donko, and T. Lafleur, "Simulation benchmarks for low pressure plasmas: capacitive discharges," *Phys. Plasmas*, vol. 20, no. 1, 2013.

[76] C. K. Birdsall and A. B. Langdon, *Plasma Physics via Computer Simulation*. New-York: McGraw-Hill, 1985.

[77] H. Ueda, Y. Omura, H. Matsumoto, and T. Okuzawa, "A study of the numerical heating in electrostatic particle simulations," *Computer Physics Communications*, vol. 79, pp. 149–259, April 1994.

[78] M. M. Turner, "Verification of particle-in-cell simulations with Monte Carlo collisions," *Plasma Sources Science and Technology*, vol. 25, no. 5, p. 054007, 2016.

[79] H. R. Skullerud, "Longitudinal diffusion of electrons in electrostatic fields in gases," *J. Phys. B (Atom. Molec. Phys.)*, vol. 2, pp. 696–705, 1969.

[80] V. Vahedi and M. Surendra, "A Monte Carlo collision model for the particle-in-cell method: applications to argon and oxygen discharges," *Comp. Phys. Commun.*, vol. 87, no. 179, 1995.

[81] P. Amestoy, I. Duff, and J. Excellents, "Multifrontal parallel distributed symmetric and unsymmetric solvers," *Computer Methods in Applied Mechanics and Engineering*, vol. 184, no. 2-4, pp. 501–520, 2000.

[82] S. Balay, S. Abhyankar, M. F. Adams, J. Brown, P. Brune, K. Buschelman, L. Dalcin, V. Eijkhout, W. D. Gropp, D. Kaushik, M. G. Knepley, L. C. McInnes, K. Rupp, B. F. Smith, S. Zampini, H. Zhang, and H. Zhang, "PETSc Web page."

[83] R. Falgout and U. Yang, *hypre: a Library of High Performance Preconditioners*. 2002.

[84] D. Lecas, I. Dupays, and M. Flé, *Message Passing Interface (MPI)*. IDRIS, 2016.

[85] A. W. Mainassara, "Optimisation et amélioration d'un code PIC 2D plasma froid pour la propulsion des satellites," Master's thesis, Polytech Lyon, 2017.

[86] T. H. Group, "Hierarchical Data Format, version 5," 1997.

[87] J. Frederiksen, G. Lapenta, and M. Pessah, "Particle Control in Phase Space by Global K-Means Clustering," *arXiv*, vol. 1504.03849, Nov. 2015.

[88] M. Vranic, T. Grismayer, J. Martins, R. Fonseca, and L. Silva, "Particle merging algorithm for PIC codes," *Computer Physics Communications*, 2014.

[89] P. Lavalle and P. F. Wautelet, "Programmation hybride mpi-openmp," 2013.

[90] G. S. Janes and R. Lowder, "Anomalous electron diffusion and ion acceleration in a low density plasma," *Phys. Fluids*, vol. 9, no. 115, 1966.

[91] J. Boris, "Relativistic plasma simulation-optimization of a hybrid code," in *Proceeding of Fourth Conference on Numerical Simulations of Plasmas*, November 1970.

[92] V. Croes, R. Lucken, A. Tavant, A. W. Mainassara, Z. Bonaventura, T. Lafleur, A. Bourdon, and P. Chabert, "Particle-In-Cell/Monte Carlo collisions methods: Bi-dimensional computations of various plasma thrusters," *Journal of Computational Physics*, in preparation.

[93] P. Chabert and N. Braithwaite, *Physics of Radio-Frequency Plasmas*. Cambridge press, February 2011.

[94] A. V. Phelps, "Compilation of atomic and molecular data," 2005.

[95] S. Barral, K. Makowski, Z. Peradznski, N. Gascon, and M. Dudeck, "Wall material effects in stationary plasma thrusters. II. Near-wall and in-wall conductivity," *Phys. Plasmas*, vol. 10, no. 4137, 2003.

[96] A. N. Smirnov, Y. Raitses, and N. J. Fisch, "Electron cross-field transport in a low power cylindrical Hall thruster," *Phys. Plasmas*, vol. 11, no. 4922, 2004.

[97] D. Sydorenko, I. D. Kaganovich, Y. Raitses, and A. I. Smolyakov, "Breakdown of a space charge limited regime of a sheath in a weakly collisional plasma bounded by walls with secondary electron emission," *Phys. Rev. Let.*, vol. 103, no. 145004, 2009.

[98] P. Dawson, "Secondary Electron Emission Yields of some Ceramics," *J. Appl. Phys.*, vol. 37, no. 3644, 1966.

[99] J. Vaughan, "A new formula for secondary emission yield," *IEEE Trans./Electron Devices*, vol. 36, pp. 1963–1967, 1989.

[100] M. A. Furman and M. T. F. Pivi, "Probabilistic model for the simulation of secondary electron emission," *Phys. Rev. ST Accel. Beams*, vol. 5, p. 124404, 2002.

[101] R. Cimino, I. R. Collins, M. A. Furman, M. Pivi, F. Ruggiero, G. Rumolo, and F. Zimmermann, "Can low-energy electrons affect high-energy physics accelerators?," *Phys. Rev. Lett.*, vol. 93, p. 014801, Jun 2004.

[102] J. R. Dennison, A. Sim, and C. D. Thomson, "Evolution of the electron yield curves of insulators as a function of impinging electron fluence and energy," *IEEE Transactions on Plasma Science*, vol. 34, pp. 2204–2218, Oct 2006.

[103] S. Clerc, J. R. Dennison, R. Hoffmann, and J. Abbott, "On the computation of secondary electron emission models," *IEEE Transactions on Plasma Science*, vol. 34, no. 5, pp. 2219–2225, 2006.

[104] A. Shih and C. Hor, "Secondary emission properties as a function of the electron incidence angle," *IEEE Transactions on Electron Devices*, vol. 40, no. 4, pp. 824–829, 1993.

[105] D. Sydorenko, *Particle-in-cell simulations of electron dynamics in low pressure discharges with magnetic fields.* PhD thesis, University of Saskatchewan, June 2006.

[106] E. McDaniel, *Collision phenomena in ionized gases.* John Wiley & Sons, Dec 1964.

[107] T. Lafleur, P. Chabert, and J. P. Booth, "Electron heating in capacitively coupled plasmas revisited," *Plasma Sources Sci. Technol.*, vol. 23, no. 035010, 2014.

[108] R. L. Dewar, "Saturation of kinetic plasma instabilities by particle trapping," *Phys. Fluids*, vol. 16, no. 431-435, 1973.

[109] S. Mazouffre, "Laser-induced fluorescence diagnostics of the cross-field discharge of Hall Thrusters," *Plasma Sources Sci. Technol.*, vol. 22, no. 013001, 2012.

[110] T. Lafleur, S. D. Baalrud, and P. Chabert, "Characteristics and transport effects of the electron drift instability in Hall-effect thrusters," *Plasma Sources Science and Technology*, vol. 26, no. 2, p. 024008, 2017.

[111] G. D. Hobbs and J. A. Wesson, "Heat flow through a Langmuir sheath in the presence of electron emission," *Plasma Physics*, vol. 9, pp. 85–87, 1967.

[112] V. Croes, T. Lafleur, A. Tavant, A. Bourdon, and P. Chabert, "2D particle-in-cell simulations of Hall-effect thrusters: effects of the secondary electron emission on the electron drift instability and associated anomalous electron transport," *Phys. Plasmas*, in preparation.

[113] G. D. Hobbs and J. A. Wesson, "Heat flow through a Langmuir sheath in the presence of electron emission," *Plasma Phys. Control. Fusion*, vol. 9, no. 102111, 1967.

[114] www.lxcat.net, "Phelps database." retrieved on November 16, 2016.

[115] www.lxcat.net, "Biagi-v7.1 database." retrieved on November 16, 2016.

[116] S. Sakabe and Y. Izawa, "Simple formula for the cross sections of resonant charge transfer between atoms and their positive ions at low impact velocity," *Physical Review*, vol. 45, February 1992.

[117] J. Cavalier, *Modèles cinétiques et caractérisation expérimentale des fluctuations électrostatiques dans un propulseur à effet Hall.* PhD thesis, Université de Lorraine, Oct 2013.

[118] K. Cartwright, J. Verboncoeur, and C. Birdsall, "Loading and injection of maxwellian distributions in particle simulations," *Journal of Computational Physics*, vol. 162, pp. 483–513, 2000.

université PARIS-SACLAY | ÉCOLE DOCTORALE Ondes et Matière (EDOM)

ÉCOLE POLYTECHNIQUE UNIVERSITÉ PARIS-SACLAY

Titre : Modélisation de la décharge plasma d'un propulseur à effet Hall.

Mots clefs : Propulsion spatiale, simulation numérique, instabilités, plasmas froids, PIC/MCC, ergols alternatifs.

Résumé : Alors que les applications spatiales prennent une place de plus en plus cruciale dans nos vies, les coûts d'opération des satellites doivent être réduits. Ceci peut être obtenu par l'utilisation de systèmes de propulsion électrique, plus efficients que leurs homologues chimiques traditionnellement utilisés. Une des technologies de propulsion électrique la plus performante et la plus utilisée est le propulseur à effet Hall. Toutefois ce système reste complexe et peu compris. En effet de nombreuses questions, concernant le transport anormal des électrons ou les interactions plasma/paroi, sont encore ouvertes.
Les réponses à ces questions sont basées sur des mécanismes cinétiques et donc ne peuvent être obtenues grâce à des modèles fluides. De plus les caractéristiques géométriques et temporelles de ces mécanismes les rendent difficilement observables expérimentalement. Par conséquent nous avons, pour répondre à ces questions, développé un code cinétique bi-dimensionnel.
Grâce à un modèle simplifié de propulseur à effet Hall, nous avons observé l'importance de l'instabilité de dérive électronique pour le transport anormal. Ensuite, en utilisant un modèle réaliste de propulseur, nous avons pu étudier les effets des interactions plasma/paroi sur la décharge plasma. Nous avons également pu quantifier les effets intriqués des émissions électroniques secondaires et de l'instabilité de dérive sur le transport anormal. Par une étude paramétrique sur les émissions électroniques secondaires, nous avons pu identifier trois régimes de décharge plasma. Finalement l'impact des ergols alternatifs a pu être étudié en utilisant des processus collisionnels réalistes.

Title : Plasma discharge modeling of a Hall-effect thruster.

Keywords : Space propulsion, numerical simulations, instabilities, cold plasma, PIC/MCC, alternative propellants.

Abstract : As space applications are increasingly crucial in our daily life, satellite operating costs need to be decreased. This can be achieved through the use of cost efficient electric propulsion systems. One of the most successful and competitive electric propulsion system is the Hall effect thruster, but this system is characterized by its complexity and remains poorly understood. Indeed some key questions, concerning electron anomalous transport or plasma/wall interactions, are still to be answered.
Answers to both questions are based on kinetic mechanisms, and thus cannot be solved with fluid models. Furthermore the temporal and geometrical scales of these mechanisms make them difficult to be experimentally measured. Consequently we chose, in order to answer those questions, to develop a bi-dimensional fully kinetic simulation tool.
Using a simplified simulation of the Hall effect thruster, we observed the importance of the azimuthal electron drift instability for anomalous cross-field electron transport. Then, using a realistic model of a Hall effect thruster, we were able to study the effects of plasma/wall interactions on the plasma discharge characteristics, as well as to quantify the coupled effects of secondary electron emission and electron drift instability on the anomalous transport. Through parametric study of secondary electron emission, three plasma discharge regimes were identified. Finally the impact of alternative propellants was studied.

Université Paris-Saclay
Espace Technologique / Immeuble Discovery
Route de l'Orme aux Merisiers RD 128 / 91190 Saint-Aubin, France